A Dedicated Search for Low Frequency Radio Transient Astrophysical Events using ETA

Kshitija B. Deshpande

Thesis submitted to the Faculty of the

Virginia Polytechnic Institute and State University

in partial fulfillment of the requirements for the degree of

Master of Science

in

Electrical Engineering

S. W. Ellingson, Chair

J. H. Simonetti

C. D. Patterson

November 9, 2009

Blacksburg, Virginia

Keywords: Low Frequency Radio Transients, Eight-meter-wavelength Transient Array, Crab Giant Pulses, Gamma Ray Bursts, Primordial Black Holes

A Dedicated Search for Low Frequency Radio Transient Astrophysical Events using ETA

Kshitija B. Deshpande

ABSTRACT

Astrophysical phenomena such as self-annihilation of primordial black holes (PBHs), gamma ray bursts (GRBs), and supernovae are expected to produce single dispersed pulses detectable in the low end of the radio spectrum. Analysis of these pulses could provide valuable information about the sources, and the surrounding and intervening medium. The Eight-meter-wavelength Transient Array (ETA) is a radio telescope dedicated to the search for these pulses in an 18 MHz bandwidth centered at 38 MHz. ETA consists of 10 dual-polarized active dipoles providing an all-sky field of view. This thesis describes the results of a search campaign using ETA, namely, a Crab giant pulse (CGP) search. CGPs are already known to exist, and thus provide an excellent diagnostic for system performance. We found 11 CGP candidates in 14 hours of data. Although there has not been a single compelling detection (signal-to-noise ratio > 6), our analysis shows that at least a few of these candidates may be CGPs. We also explain the analysis preparation for PBH and GRB searches. Additionally, we describe the instrument and a software "toolchain" developed for the analysis of data that includes calibration, radio frequency interference (RFI) mitigation, and incoherent dedispersion. A dispersed pulse simulation code was developed and used to test the toolchain. Finally, improvements are suggested.

Dedication

I dedicate this thesis to my parents.

Acknowledgments

I would like to sincerely thank my advisor Dr. Steven Ellingson for his support and patience with me during the research and writing of this work. I am thankful to Dr. John Simonetti, Dr. Cameron Patterson and the entire ETA group for their help and support. Thanks to Sean Cutchin for his inputs and comments during the research on ETA. This work was funded by the National Science Foundation under Grant No. AST-0504677, and by the Pisgah Astronomical Research Institute.

It is a great pleasure to acknowledge the MPRG group including all the students and Hilda Reynolds, Jenny Frank and James Dunson. I am extremely grateful to my *other mother* Nancy Goad for her endless love and support. I would like to thank my colleagues Chris Headley, Mahmud Harun, S. M. Hasan, Kyehun Lee, Joseph Gaeddert, Carlos Aguayo, Chris Phelps, Jesse Reed, Sahana Raghunandan and Harpreet Singh Dhillon for discussions on various topics on communications and electromagnetics.

I am blessed to have many wonderful people around. Thanks to Dr. Claudio da Silva for introducing me to a more intense world of stochastic signals and systems. I enjoyed working with him as a teaching assistant. My special thanks goes to John Haris for all his support. I am thankful to Drs. Gary Brown, Scott Bailey and Kathaleen Meehan for their guidance. I would like to thank Yogesh Maan for the useful discussions on pulsars and transients. I am glad to have my extended family in Blacksburg and in US: my roommates, Kalyani Nagaraj, Shvetha Soundararajan and Kalyani Tipnis and all my friends; I thank you all. Thanks to

Maitrayee for her help and push during many occasions. Kalyani and Shvetha, thanks a ton for all your support, especially during some of those stressful days. Prakash, Mugdha, I am looking forward to many more trips and fun times ahead.

I am immensely grateful to my family: Aai, Baba and Shreya for their infinite love and unshakable confidence in me. I am blessed to have them. Baba, thanks for being there for me, always. Parag, I cannot thank you enough for your unconditional love and unfailing support. You have been a great brother, friend, philosopher and guide. I would like to thank Prasun Dada for his guidance. His *remote* teaching has helped me learn many things during my graduate school. I am thankful to all my cousins: Sameer dada, Wasim dada and Amod dada for all their love and encouragement.

Contents

List of Figures

List of Tables

Chapter 1

Introduction

In the radio spectrum, pulses of astronomical origin might provide observable signatures of some of the exotic and as-yet undetected astronomical phenomena in the universe. These phenomena are introduced in Section 1.1 ("Astronomical Radio Transients"). Some past, present, and future transient searches are discussed in Section 1.2 ("Radio Transient Searches"). The Eight-meter-wavelength Transient Array (ETA) is a radio telescope dedicated to the search for transients at low frequencies, and is briefly introduced in Section 1.3 ("The Current Work"). The objective of this work is to report a search "campaign" using ETA, namely, a Crab giant pulse (CGP) search. The research contributions of this thesis are summarized in Section 1.4 ("Contributions"), and the remainder of this thesis is outlined in Section 1.5 ("Organization of this Thesis").

1.1 Astronomical Radio Transients

Several known or theorized astrophysical sources of radio transients are described in detail in this section. A more general discussion of this topic can be found in [1].

1.1.1 Giant Pulses from Pulsars

Pulsars are spinning neutron stars that emit beams of electromagnetic (EM) radiation. When the beams intersect Earth, radio telescopes can detect them as pulses. Some pulsars are observed to produce "giant pulses" (GPs); that is, pulses with strengths 100 to 1000 times the mean pulse intensity. GPs may serve as a useful diagnostic of the system performance for any transient instrument. The first pulsar found to exhibit GPs is the Crab pulsar (PSR B0531+21) which was discovered in 1968 by Staelin and Reifenstein [2]. The GPs emitted by the Crab pulsar are referred to in this thesis as CGPs. These are apparent throughout the radio spectrum [3]. Notable observations of CGPs at frequencies $\lesssim$ 300 MHz include those at 23 MHz using the UTR-2 radio telescope [4], and at 200 MHz using the Murchison Widefield Array's Low Frequency Demonstrator (MWA-LFD) [5]. Chapter 5 of this thesis reports on observations of CGPs at 38 MHz using ETA. Low frequency detections of GPs from pulsars other than Crab have been reported for PSR B1112+50 [6] and PSR B0031-07 [7] at 111 MHz.

1.1.2 Primordial Black Holes (PBHs)

PBHs are believed to be the result of inhomogeneities in the density of matter in the early universe. Black holes (BHs) with critical mass $\lesssim 10^{14}$ g are predicted to completely "evaporate" due to Hawking radiation [8], terminating in an explosion in our present epoch [9]. Rees [10] suggested that a burst of coherent radio emission might be a possible signature of an exploding PBH, and might be detectable by a small array of antennas operating at low frequencies.

A model typically used to describe the aftermath of PBH annihilation is the Relativistic Fireball model [10, 11] and is explained in brief as follows. An explosion can be characterized by a release of energy in the form of electron-positron pairs, which form a fireball or a conducting shell expanding into the surrounding uniform magnetic field. The charged particles along the surface of the fireball give rise to surface currents while preventing the field from penetrating it. As the fireball expands relativistically in the ambient magnetic field, a coherent EM pulse

is generated. Blandford [11] reasoned that $\sim$ 50% of the released energy is in the form of relativistic electron-positron pairs which ultimately goes into the EM pulse. The Lorentz factor γ_f of this fireball is the same as the Lorentz factor of the charged particles along its surface expanding at speed v. Thus, $\gamma_f = 1/\sqrt{1 - v^2/c^2}$. For efficient coherent radio pulse production from the expansion of the fireball, γ_f should be between $\sim 10^5$ and $\sim 10^7$. Since the ambient interstellar magnetic field is essentially uniform on the scale of the fireball, the radio pulse would be $\sim$ 100% linearly polarized.

A second scenario for a coherent pulse emission from an exploding PBH is proposed by Kavic *et al.* [12] where the PBH undergoes a topological phase transition. In presence of an extra spatial dimension (a spatial dimension in addition to the classical 3+1 spacetime dimensions), PBHs could exist in different phases. For example, in presence of a compactified extra spatial dimension (the dimension curled up on itself), a PBH could exist as a "black string", wrapping the extra dimension. When the PBH evaporates and shrinks to the length scale smaller than the extra dimension, it should eventually "snap" and become localized within the extra dimension. In contrast to the first scenario in which all the mass is converted to energy, the PBH in this case releases a few percent of its mass into energy ($\eta \cong 0.01$) during a time scale L/c, where L is the size of the extra spatial dimension that could be associated with the γ_f of the corresponding fireball. Observations with wide field of view (FOV) telescopes such as ETA operating around 38 MHz are sensitive to $\gamma_f \sim 10^4$ to 10^5, corresponding to an extra dimension length of $L \sim 10^{-17}$ to 10^{-18} m.

As explained later (Section 2.1.1), the distance d to the evaporating black hole can be estimated from the dispersion measure (DM) of the received radio pulse. Since signal-to-noise ratio (SNR) $\propto$ (pulse energy)$/d^2$, knowing the SNR of the detected pulse, the released pulse energy could be estimated. If the fireball expands to a critical radius R_c before being decelerated, the characteristic frequency is given by (See [10])

$$\nu_c \sim c\frac{{\gamma_f}^2}{R_c}. \tag{1.1}$$

The radiation emitted forms a pulse observable at frequencies lower than this critical frequency. From the estimation of energy released, it may be possible to distinguish between a standard explosion ($\eta = 1$) and a topological phase transition event ($\eta \cong 0.01$). A positive detection of the later type would indicate the presence of an extra dimension.

If there are no detections, an upper limit can be set on the rate of PBH explosions, which itself is useful information. If s_1 corresponds to the SNR for a source of a specific γ_f at a distance of 1 kpc, the maximum distance d_{max} to which a PBH explosion with SNR $= s$ could be detected is

$$d_{max} = \left(\frac{s_1}{s}\right)^{1/2} \times 1 \text{ kpc} \tag{1.2}$$

Following [13], instantaneous volume surveyed is

$$V = \frac{d_{max}^3 \Omega}{3} \tag{1.3}$$

where Ω is the solid angle of the area of the sky surveyed. If T is the total observing time, then the limit on PBH detections is $R = (VT)^{-1}$.

1.1.3 Gamma Ray Bursts (GRBs)

GRBs are energetic and short or long duration bursts of gamma rays speculated to be emanating from neutron star/neutron star (NS/NS) [14] or neutron star/black hole (NS/BH) merger events [15], or a cataclysmic collapse of a massive star [16].

It has been proposed that GRBs may be accompanied by very short duration low-frequency radio emission, called "prompt emission". Most of the energy in this emission is expected to occupy frequencies from 0.1 to 1 MHz [17], and therefore detectable only from space-based radio telescopes since observations from ground at these frequencies are limited by the ionosphere. However, detectable flux might reach frequencies $\sim$ 30 MHz, and might possibly be detected by ground-based observations. Low-frequency observations of radio emissions from GRBs would

be useful in identifying and constraining the nature of the source, the physics of the burst, and the nature of the surrounding medium. Sagiv and Waxman [18] suggested an alternative model where the shock wave continuously accelerates protons and electrons to high energies in the surrounding magnetic field, also producing a low frequency radio emission.

Benz and Paesold (1998) describe a search for prompt radio emission carried out in a frequency range of 40 to 1000 MHz, but there were no positive detections [19] (See Section 1.2.1). Although the spectral coverage of this experiment was good, the instrument sensitivity was low. Thus, improved sensitivity of dedicated low-frequency instruments such as ETA is expected to be useful in detection of the prompt radio emission from GRBs, should it exist.

1.1.4 Prompt Emission from Supernovae

A relativistic fireball model has also been proposed as a source of pulse production when a supernova occurs [20]. A summary of searches for prompt emission from supernovae (all yielding negative results) can be found in [21]. To obtain improved sensitivity, Meikle and Colgate (1978) suggested using a multiple-beam array, an idea which is incorporated by most of the new generation low-frequency radio telescopes.

1.1.5 Other Sources

In addition to the sources discussed earlier, mergers of NS/NS and NS/BH systems are potential sources of low-frequency radio pulses [22]. Other sources of low-frequency radio pulses, not specifically of interest in this thesis, include cosmic ray air showers [23, 24], solar bursts [25], and Jupiter [26].

A powerful ($\approx$ 30 Jy) and highly dispersed ($\approx$ 375 pc cm^{-3}) pulse of duration $<$ 5 ms was recently detected during the analysis of archival Parkes multi-beam survey data at 1.4 GHz [27]. The direction of arrival of this pulse was located three degrees south of the center of the Small

Magellanic Cloud (SMC), but the dispersion measure of $\approx$ 375 pc cm^{-3} suggests a distance much larger than that of the SMC. Thus, it was concluded that the source of the pulse did not belong to the SMC. The source of this pulse is still unknown. Routine detection of such strong pulses is difficult for existing large radio telescopes due to limited telescope time and narrow FOV. A dedicated transient instrument such as ETA can overcome these limitations and may serve as a better instrument for transient searches.

1.2 Radio Transient Searches

As noted above, some efforts to detect radio transients have been performed in the past. A useful summary of these searches through 2003 can be found in [28]. In this section, a few searches done in the past as well as some contemporary searches are reviewed, in addition to some of the planned experiments for radio transient detections. Some of the published radio transient searches are summarized in Table 1.1. In the table, ν is the center frequency, B is the instantaneous bandwidth of the instrument, T_{obs} gives total observation time in hours (that is, total data collected in hours), and τ is the postdetection integration time which represents the minimum time resolution.

1.2.1 Past Searches

We review a few of the previously-published transient searches in this section. The search parameters corresponding to these experiments are reported in Table 1.1. Although none of the searches have confirmed transient detections (other than CGPs), each of them suggest improvements for future searches for transients.

- **Phinney and Taylor (1979) – PBH**

  Phinney and Taylor (1979) [13] re-analyzed data from a pulsar survey carried out in 1973−74 at the Arecibo observatory. They reviewed ten previously-published radio pulse

Table 1.1: Table summarizing some previously conducted and current searches. The sources for which the searches were specifically intended (if any) are written in parentheses in the first column. In the fourth column, percent bandwidth ($\triangleq B/\nu \times 100$) is also given.

Searches	Experiment/ Instrument	ν [MHz]	B [MHz]	T_{obs} [h]	τ	DM Range [pc cm^{-3}]	Comments
Phinney & Tayor, 1979. [13] (PBH)	Arecibo	430	16 (4%)	292	17 ms	0 − 640	Limit on PBH explosions is 2×10^{-9} events pc^{-3}yr^{-1} with $\gamma_f > 10^5$.
Benz & Paesold, 1998. [19] (PBH & GRB)	3×7 m dishes with frequency sweeping receivers. Sweep time equals 0.25 s.	40 − 1000	1 (2.5%− 0.1%)	4643	26 μs	1−10	No detections. Limit on PBH explosions is 5×10^{-3} events pc^{-3}yr^{-1} with $\gamma_f > 10^4$.
Balsano, 1999. [29] (GRB)	FLIRT: 128 element phased array	74	2.2 (3%)	16.5	2 ms	8 − 1795	One unconfirmed detection.
Katz *et al.*, 2003. [30]	STARE: 3 detectors 100s of km apart providing an anticoincidence system	611	4 (1%)	12960	0.125 s	Not applicable (Not a search for dispersed pulses).	All astronomical events detected were of solar origin.
Becker, 2005. [31] (Cyclotron maser emission from extrasolar planets).	Arecibo	327	50 (15%)	15	128 μs	Not applicable (Not a search for dispersed pulses).	No detection.
Wilson, 2005. [32]	PLFM: A single dipole	46	18 (39%)	0.33	20 ms	15 − 70	9 candidate pulses $> 6.5\sigma$.
Morales *et al.*, 2005. [33] (GRB)	GASE: 8 dipole antennas	30	4 (13%)	Not Reported	Not Reported	Not Reported	In progress.
Siemion *et al.*, 2008. [34]	Astropulse: Arecibo	1420	2.5 (0.2%)	Not Reported	0.4 μs	55 − 830	Analysis results at early stage.
Siemion *et al.*, 2008. [34]	Fly's eye: ATA [35], 26×6 m dishes.	1430	210 (15%)	450	0.625 ms	0 − 200	3 pulsars & 6 CGPs $> 7\sigma$ detected.
This work CGP Search (Chapter 5)	ETA: 10 dual-polarized dipoles [36]	38	3.75 (10%)	24.7	498 ms	54 − 59.6	11 CGP candidates detected. (3.3−5.3σ)
This work PBH Search	ETA: 10 dual-polarized dipoles [36]	38	3.75 (10%)	27.2	136 μs	10 − 1000	Analysis not done yet.

surveys, and compared the results to their work. This search at 430 MHz was sensitive to $\gamma_f > 10^5$ over 260 kpc distances. There were no detections. The upper bound on PBH rate-density was estimated as 2×10^{-9} events pc^{-3} yr^{-1}.

- **Benz and Paesold (1998) − PBH and GRB Prompt Emission**

  Benz and Paesold (1998) [19] performed a search for PBHs and prompt radio emission from GRBs in the data of three solar radio spectrographs. When the Burst And Transient Source Experiment (BATSE) orbiting instrument reported a burst identified to be different from a solar flare, the spectrographs recorded the data. These observations covered

a frequency range of $40 - 1000$ MHz, and were sensitive to $\gamma_f > 10^4$. There were no positive detections, implying a PBH rate-density limit of 5×10^{-3} events pc^{-3} yr^{-1}. It was concluded that a detectable radio emission would be produced only when the source was relatively close within our galaxy (less than at about 1 kpc distance) or if γ_f is greater than $\sim 10^4$.

- **Fallbrook Low Frequency Immediate Response (FLIRT) Experiment**

  A dedicated search for GRB prompt radio emissions [29] was performed at 74 MHz (bandwidth of 2.2 MHz) using a phased array with 8000 m^2 effective aperture located in Fallbrook, California [37]. The telescope consisted of 128 elements, each of which was a small array of eight full-wave dipole antennas. The telescope was remotely operated and was designed to respond to notices by NASA's GRB Coordinate Network (GCN). One transient was detected as a possible prompt emission from GRB980329. Later analysis suggested that although the candidate pulse indicated a source with DM ~ 66 pc cm^{-3}, astrophysical nature of the source could not be confirmed.

- **Survey for Transient Astronomical Radio Emission (STARE)**

  STARE [30] was a search for transients at 611 MHz in a 4 MHz bandwidth, incorporating an anticoincidence system with three detectors at geographically separated sites. In an anticoincidence system, an event recorded by all the sites simultaneously would be considered as a confirmed detection. Thus, it provides an effective method to discriminate against the RFI from local sources. In 18 months of round-the-clock observations, STARE found 3898 events $>$ 27 kJy, all of which were determined to be associated with solar activity. 173 GRBs occurred during their observations. Although 7 candidate transients were found within ± 1 hr of a GRB event, all of them were later attributed to solar radio bursts as well [38]. From the non-detection of extrasolar transients, it was concluded that there are probably no sources within 1 kpc that produce undispersed transient radio emission detectible in this wavelength regime.

- **Becker (2005)**

  Becker (2005) [31] carried out a search for cyclotron maser emission from extrasolar planets at 327 MHz in a 50 MHz bandwidth at the Arecibo observatory. Four extrasolar planetary systems were observed for non-thermal radio emission similar to that emitted by magnetized planets from our solar system such as Jupiter. No detections were made in 15 hours of observation.

- **Pisgah Low Frequency Monitor (PLFM) Experiment**

  In the PLFM experiment, a search for transients was carried out using a single dipole operating in an 18 MHz bandwidth centered at 46 MHz [32]. A sensitivity of $\sim$1 MJy was achieved, with an ability to resolve $\sim$ 20 ms wide pulses. 9 pulse candidates greater than 6.5σ corresponding to DMs ranging from 15 to 70 pc cm^{-3} were detected in a 20 minutes long observation. The possibility of association of these pulse candidates with known pulsars was considered. RFI tends to saturate the search for pulses over a range of dispersion measures, and may cause spurious detections. The possibility that these candidate pulses could be a result of this saturation due to RFI could not be ruled out, because of an inability to completely discriminate against RFI. Thus the pulse candidates were not considered to be confirmed detections. This experiment served as a pilot experiment for ETA. Several improvements to the instrumentation and survey technique were suggested that were later incorporated in ETA.

1.2.2 Current Searches

In this section, we briefly introduce the searches for transient radio emission contemporary to ETA. Most of them use arrays of wide FOV antennas such as dipoles. These experiments have not discovered any confirmed detections yet.

- **GRB All-sky Spectrometer Experiment (GASE)**

  GASE is an experiment in progress designed to search for prompt radio emission coinci-

dent with GRBs at a frequency of 30 MHz using an array of 8 dipole antennas [33]. No results have been reported as yet.

- **Astropulse**

  Astropulse is a survey conducted using the Arecibo telescope at 1420 MHz [34]. A search for dispersed μs- and ms-time scale radio pulses is carried out over a DM range of $55 - 830$ pc cm^{-3}. Astropulse's multibeam data are distributed publicly to volunteers who download a program which performs the analysis on their home computers. Analysis of results from Astropulse is at a very early stage.

- **Fly's Eye Experiment**

  A dispersed radio pulse search called the Fly's Eye experiment [34], is being carried out using the Allen Telescope Array (ATA) [35]. A 100 square degree field is observed by pointing each 6 m ATA antenna in a different direction. About 450 hours of data has been collected through 2008, and 9 transients including 6 CGPs have been detected in the preliminary data. No detections in the actual survey data have been reported yet.

- **ETA**

  ETA is a dedicated transient search instrument operating at 38 MHz with a 3.75 MHz processed bandwidth. The instrument is discussed in detail in Section 3.1. Data collection and analysis are described in Chapters 3–5.

1.2.3 Future Projects

For a successful transient search, large FOV is desirable in addition to good sensitivity. The upcoming radio telescopes discussed in this section will provide large FOV as well as better sensitivity and angular resolution.

- **Murchison Widefield Array (MWA)**[1]

  The MWA is being designed to operate in $80 - 300$ MHz, and will consist of 8000 dual-polarization dipole antennas organized into 512 "tiles", each a 4×4 array of dipoles [39]. A portion of the array called Low Frequency Demonstrator (LFD) is currently operational. Recent CGP detections at 200 MHz, and an attempted but unsuccessful search at 100 MHz, are discussed in [5].

- **Low Frequency Array (LOFAR)**[2]

  LOFAR, when completed, will contain 25000 dipole-type antennas operating in a frequency range of 30 to 200 MHz. The detailed telescope specifications can be found in [40]. LOFAR proposes to search for transients [41, 42].

- **Long Wavelength Array (LWA)**[3]

  The LWA will eventually consist of 53 electronically-steered phased-array "stations", each consisting of 256 pairs of crossed-dipole antennas. The operating frequency range of LWA is $10 - 88$ MHz. Construction of the first station (LWA-1) is currently underway. Details on the design, specifications, and science goals of LWA, which includes transient searches, can be found in [43].

1.3 The Current Work

The searches for radio transient events carried out in the past suffered one or more of the following shortcomings: Limited FOV, limited sensitivity, limited observation time, inability to discriminate against RFI, and so on. It was attempted to address many of these issues while building ETA, the details of which can be found in Chapter 3. ETA is an array of 10 dual-polarized dipoles operating in frequency range of 29 to 47 MHz. It provides a FOV of

[1] http://www.mwatelescope.org/
[2] http://www.lofar.org/
[3] http://lwa.unm.edu/

$\approx$ 2.6 sr. We have recorded and archived about 68 hours of data as part of different search campaigns.

In this thesis, CGP search campaign data are analyzed. The results are presented in Chapter 5. We found 11 CGP candidates in 14 hours of data. In Section 5.2, we discuss and analyze these results. Although none of the detections is compelling (SNR > 6), our analysis suggests that at least a few of these detections are possibly CGPs. The telescope sensitivity is ~ 1 kJy (5σ) for dispersed pulses with pulse width ≈ 0.5 s (see Section 3.2.3 for specific estimates.) The CGP search serves as a useful commissioning test for the system and also for the software toolchain developed as a part of targeted DM pulse search (Chapter 5). We propose and use an algorithm to mitigate RFI (Section 4.1.5) in this thesis.

In Chapter 6, we discuss a planned PBH search using data already collected. ETA observations are most sensitive to PBH explosions with γ_f between $\sim 10^4$ and $\sim 10^5$. In the absence of detections, an event rate-density limit could be set to $\sim 10^{-7}$ pc^{-3}y^{-1} at 38 MHz. This is at least an order of magnitude better than the existing limits obtained from other low-frequency observations for comparable γ_f. We have also collected 8 hours of GRB data in response to 7 GCN triggers. The analysis preparation for both these campaigns is discussed in detail in Chapter 6.

1.4 Contributions

The specific contributions of this work include the following items.

- Results from a CGP search campaign using ETA. Chapter 5 ("Crab Giant Pulse Campaign") presents these results.
- A new software "toolchain" was developed to analyze these data, and is described in Section 4.1 ("The Toolchain"). This toolchain is employed in our CGP search.

- A major problem in low-frequency radio astronomy is radio frequency interference (RFI). In Appendix C ("RFI Mitigation Algorithm for the Eight-meter-wavelength Transient Array"), we propose an algorithm to mitigate the RFI and demonstrate its use. This algorithm is employed in our CGP search.

1.5 Organization of this Thesis

The reminder of this thesis is organized as follows: The propagation effects on the pulse as it traverses through interstellar medium (ISM) are reviewed in Chapter 2 ("Theory"). An instrument signal path model is also developed in the same chapter. In Chapter 3 ("The Eight-meter-wavelength Transient Array (ETA)"), the telescope used in this study is described along with the science and technical specifications. The data processing software is described in Chapter 4 ("Data Analysis"). Using this software, datasets from the two campaigns are analyzed. The results of the CGP campaign are presented in Chapter 5 ("Crab Giant Pulse Campaign"). In Chapter 6 ("Conclusions"), we summarize the findings of this thesis and outline future work; in particular, the analysis of the data already collected in search of PBH explosions and GRB prompt emission.

Chapter 2

Theory

Presented in this chapter is the theoretical background required for subsequent chapters of this thesis. The propagation effects affecting the signal as it travels through the interstellar medium (ISM) are discussed in Section 2.1 ("Propagation Effects"). The analog path of the signal received by the telescope is discussed in Section 2.2 ("System Model"). The sensitivity of a telescope is determined in Section 2.3 ("Sensitivity").

2.1 Propagation Effects

As a radio pulse travels through the ISM, propagation effects such as dispersion and scattering take place. These effects are more prominent in observations at low frequencies.

2.1.1 Pulse Dispersion

Dispersion is a phenomenon in which low frequency components of a pulse propagate slower than the high frequency components due to the presence of free electrons in the ionized ISM.

This leads to a frequency-dependent delay called the dispersion delay, which is given by

$$\delta t = \frac{\mathrm{DM}}{\alpha}\left(\frac{1}{\nu^2}\right) \tag{2.1}$$

where for frequency of observation ν in Hz and dispersion measure (DM) in pc cm^{-3} (1 pc = 1 parsec = 3.26 light-years), α is 2.410×10^{-16} Hz^{-2} pc cm^{-3} s^{-1}. DM is defined as the column density of electrons along the line of sight to a source, that is,

$$\mathrm{DM} = \int_0^{d_s} n_e(l)dl \tag{2.2}$$

where n_e is the electron density and d_s is the distance to the source. The distance to the source of the pulse can therefore be estimated as DM/n_e, using the measured DM and a model for the integrated electron density along the line of sight [44, 45]. For sources in our Galaxy, the maximum DM is $\sim$ 20 pc cm^{-3} (perpendicular to the Galactic plane) and $\sim$ 1400 pc cm^{-3} (through the Galactic center).

The dispersion delay between two frequencies, ν_1 and ν_2, is:

$$\Delta t_{2\to1} = \frac{\mathrm{DM}}{\alpha}\left(\frac{1}{\nu_1^2} - \frac{1}{\nu_2^2}\right). \tag{2.3}$$

Pulse dispersion is illustrated in Figure 2.1. This figure shows a spectrogram (an intensity plot displaying the power spectral density (PSD) as a function of both time and frequency) of a simulated dispersed pulse.

2.1.2 Pulse Broadening

Independently of dispersion, pulses are typically broadened to durations on the order of milliseconds to seconds due to scattering by inhomogeneities in the ISM (for example see [3, 46]). When a pulse traverses the ISM, it is scattered by irregularities in the ISM; that is, by vari-

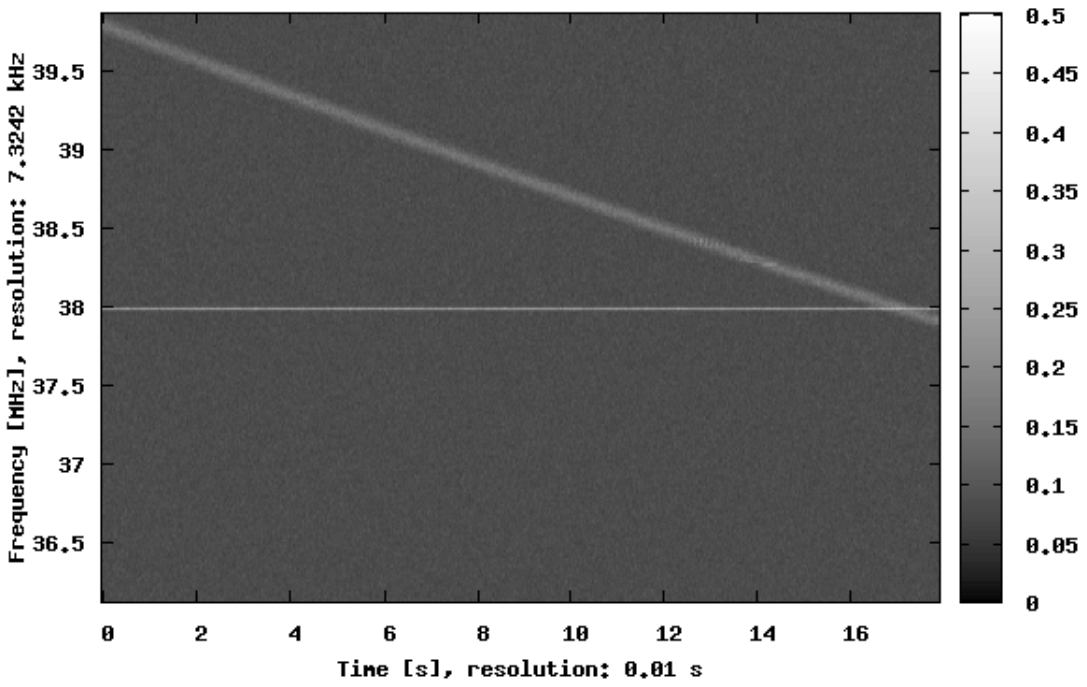

Figure 2.1: A spectrogram showing a simulated dispersed pulse with DM = 56.791 pc cm^{-3}. Time resolution = 8.738 ms, frequency resolution = 7.324 kHz. (The line at the center represents uncorrected DC bias (non-zero mean value).)

ation in the electron density as a function of distance. The multipath components combine to broaden the original pulse. The resultant pulse broadening is quantified in terms of pulse broadening time, τ_d. In general, τ_d is proportional to $\nu^{-\alpha}$ where $\alpha = 2\beta/(\beta - 2)$, and where β parameterizes the statistics of the ISM irregularities [4, 47]. For example, if a Kolmogorov spectrum is assumed, $\beta = 11/3$, thus giving $\alpha = 4.4$. Using various models to obtain the frequency dependence and some previous observations, τ_d can be anticipated for observations at different frequencies. Broadening determined from these observations reveals details about the ISM. Thus, monitoring these scattered-broadened pulses may provide a method to study electron density distributions as well as to estimate the distance to the source [48].

A matched filtering approach should be used in single pulse detection (for example, see [28, 31]). Thus, it is necessary to consider broadening for optimal pulse detection.

2.2 System Model

The purpose of this section is to develop a mathematical model to obtain the sensitivity of the telescope. As explained in Section 2.3, computation of sensitivity requires a determination of the system noise temperature, T_{sys}, which is also done in this section.

The analog signal path for a radio telescope of the type employed in this research can be modeled as shown in Figure 2.2. The principal components of the signal path are an antenna, a preamplifier, and a feedline connecting the preamplifier to an analog receiver. The analog receiver is connected to the analog to digital converter (ADC) which converts the receiver output into a digital signal.

Antenna temperature, T_A, is defined as follows: Let P be the power that the antenna delivers to a conjugate-matched load. Then place the antenna inside an ideal blackbody enclosure. T_A is the physical temperature of the enclosure material that results in the same power P being delivered to the conjugate-matched load. For ETA (and other low-frequency telescopes), T_A usually depends primarily on power collected from the sky. This point is discussed in more detail in Section 2.3. The equivalent noise temperatures of the preamplifier, the feedline, and the receiver are T_{pre}, T_f, and T_R, respectively. The gains of the preamplifier, the feedline, and the receiver are G_{pre}, G_f, and G_R, respectively.

The amount of power transferred to the preamplifier from the antenna terminals is governed by the impedance mismatch efficiency (IME), $1 - |\Gamma|^2$, where Γ is the voltage reflection coefficient at the antenna terminals looking into the preamplifier. Γ is given by

$$\Gamma = \frac{Z_{pre} - Z_A^*}{Z_{pre} + Z_A^*} \tag{2.4}$$

where Z_{pre} is the input impedance of the preamplifier and Z_A^* is the conjugate of the antenna impedance.

Following an analysis described in [49], the power spectral density (PSD) of the external noise

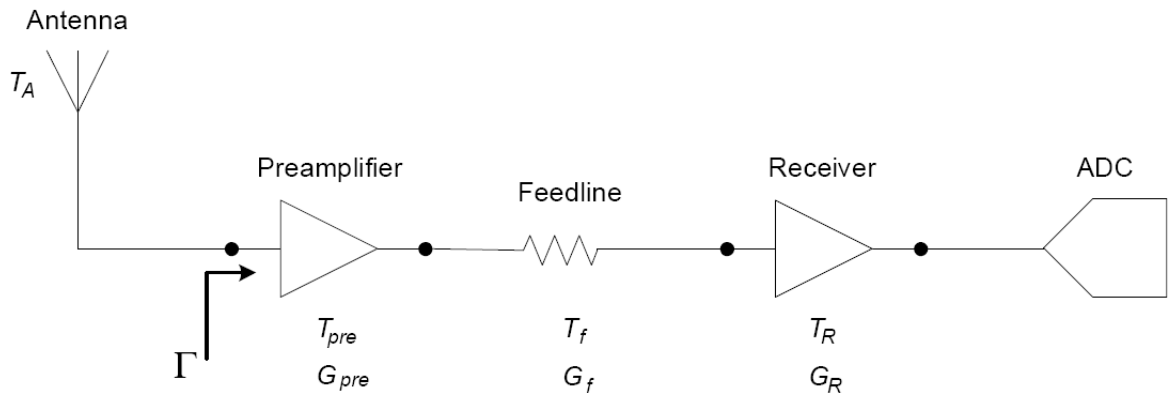

Figure 2.2: Signal path for a low-frequency radio telescope.

measured at the output of the receiver is obtained as

$$S_{ext} = \frac{1}{2} e_r k T_A (1 - |\Gamma|^2) G_{pre} G_f G_R \tag{2.5}$$

where e_r is the antenna radiation efficiency which for our purposes is the fraction of power captured by the antenna, assuming lossless conditions, which is captured by the antenna under actual (potentially lossy) conditions. The radiation efficiency is less than one due primarily to ground loss; that is, loss due to absorption by the non-perfectly-conducting ground. The factor of 1/2 accounts for the fact that any given polarization can capture at most half of the available power. The PSD due to internal noise of the system measured at the output of the receiver has a contribution from the thermal noise generated by the preamplifier, the feedline, and the receiver. The noise PSD generated by the preamplifier and measured at the output of the receiver is given by

$$N_p = k T_{pre} G_{pre} G_f G_R. \tag{2.6}$$

The noise associated with the feedline at the output of the receiver is

$$N_f = k T_f (1 - G_f) G_R. \tag{2.7}$$

Finally, the noise generated by the receiver is given by

$$N_R = kT_R G_R. \tag{2.8}$$

Thus, the total internal noise PSD is

$$\begin{aligned} S_{int} &= kT_{pre}G_{pre}G_f G_R + kT_f(1-G_f)G_R + kT_R G_R \\ &= kG_{pre}G_f G_R\left(T_{pre} + \frac{T_f}{G_{pre}}\left(\frac{1}{G_f}-1\right) + \frac{T_R}{G_{pre}G_f}\right). \end{aligned} \tag{2.9}$$

The total PSD at the output of the receiver can be expressed as

$$\begin{aligned} S_{out} &= S_{ext} + S_{int} \\ &= kG_{pre}G_f G_R\left(\frac{1}{2}e_r T_A(1-|\Gamma|^2) + T_{pre} + \frac{T_f}{G_{pre}}\left(\frac{1}{G_f}-1\right) + \frac{T_R}{G_{pre}G_f}\right). \end{aligned} \tag{2.10}$$

If the system noise temperature T_{sys} is defined at the antenna terminals on the preamplifier side of the antenna-preamplifier interface, the total PSD at the output of the receiver can also be expressed as

$$S_{out} = kG_{pre}G_f G_R T_{sys}. \tag{2.11}$$

Thus:

$$T_{sys} = \frac{1}{2}e_r T_A(1-|\Gamma|^2) + T_{pre} + \frac{T_f}{G_{pre}}\left(\frac{1}{G_f}-1\right) + \frac{T_R}{G_{pre}G_f}. \tag{2.12}$$

Let $T_{ext} = e_r T_A(1-|\Gamma|^2)/2$ and $T_{int} = T_{sys} - T_{ext}$ in Equation 2.12. If $T_{ext} >> T_{int}$, then the system is limited by Galactic noise, and we can ignore the contributions to T_{sys} from other components giving

$$T_{sys} \approx \frac{1}{2}e_r T_A(1-|\Gamma|^2). \tag{2.13}$$

If instead $T_{ext} \lesssim T_{int}$, then the system is not external noise-dominated, and then we cannot use

Equation 2.13. This situation can be quantified using a ratio γ_r of the external noise captured by the system to the total internal noise of the system ($\gamma_r \triangleq T_{ext}/T_{int}$):

$$\gamma_r = \frac{\frac{1}{2}e_r T_A(1-|\Gamma|^2)}{T_{pre} + \frac{T_f}{G_{pre}}\left(\frac{1}{G_f}-1\right) + \frac{T_R}{G_{pre}G_f}}. \tag{2.14}$$

Galactic noise-dominated operation is achieved when $\gamma_r >> 1$. For a low-frequency radio telescope, it is possible to have the system sensitivity limited by the Galactic noise and not by the internal noise. This will be demonstrated for ETA in Section 3.2.3.

2.3 Sensitivity

In this section, we derive estimates of the minimum detectable flux by a radio telescope, and its sensitivity to dispersed and undispersed pulses. In this analysis, it is assumed that the sources emit 100% linearly-polarized pulses, which is in fact the case for sources of interest described in Section 1.1.

The PSD received by an antenna due to a linearly-polarized signal, measured at the antenna terminals on the preamplifier side of the antenna-preamplifier interface, is given by

$$P_s = SA_e(\theta,\phi,\lambda)\cos^2(\Delta\psi) \tag{2.15}$$

where S is the source flux density (W m^{-2} Hz^{-1}), and $A_e(\theta,\phi,\lambda)$ is the effective aperture of the antenna (including ground loss and IME), which is a function of the zenith angle θ, azimuthal angle ϕ and wavelength λ. The factor of $\cos^2(\Delta\psi)$ accounts for the polarization mismatch between the linearly-polarized incident signal and the dipole. $\Delta\psi$ is the angle between the incident electric field vector, $\boldsymbol{E_i}$, and the vector effective length of the antenna, $\boldsymbol{l_e}$. The vector effective length determines the voltage V_{oc} induced on the open-circuit terminals of the antenna when a wave is incident on it; that is, $V_{oc} = \boldsymbol{E_i}\cdot\boldsymbol{l_e}$ [50].

The noise PSD, referenced to the terminals of the antenna on the preamplifier side of antenna-preamplifier interface, and assuming T_{sys} defined as in Equation 2.12, is

$$P_n = kT_{sys}. \tag{2.16}$$

Thus, the signal-to-noise ratio (SNR) is given by

$$\text{SNR} = \frac{P_s}{P_n} = \frac{SA_e(\theta, \phi, \lambda)\ \cos^2(\Delta\psi)}{kT_{sys}}. \tag{2.17}$$

The flux density that will produce a detection of SNR = 1 is

$$S_{min} = \frac{kT_{sys}}{A_e(\theta, \phi, \lambda)\ \cos^2(\Delta\psi)}. \tag{2.18}$$

This is true for $B\tau = 1$, where τ is the postdetection integration time, and B is the bandwidth of the observed signal or of the receiver channel, whichever is less. If either B or τ is increased, the sensitivity improves according to:

$$S_{min} = \frac{kT_{sys}}{A_e(\theta, \phi, \lambda)\sqrt{\tau B}\ \cos^2(\Delta\psi)} \tag{2.19}$$

This is an expression for continuum sensitivity. If perfect dedispersion is assumed, the sensitivity to a dedispersed pulse will be given by

$$S_{min} = \frac{kT_{sys}}{A_e(\theta, \phi, \lambda)\sqrt{\tau_p B}\cos^2(\Delta\psi)} \tag{2.20}$$

where τ_p is the pulse duration at the source, assuming τ_p is also the integration time. The highest SNR is obtained when the integration time in Equation 2.17 is matched to the pulse duration. If scatter broadening is considered, τ_p should be replaced by an effective pulse length that includes the scatter-broadened duration. In case of scatter broadening, the highest SNR is obtained when matched filters of appropriate pulse shapes are used in detection (see Section 2.1.2 for details).

Sensitivity improves by a factor of N when the outputs from N antennas are combined coherently; and by a factor of $\sqrt{N}$ when the outputs are combined incoherently, assuming uncorrelated noise in both the cases. It has been demonstrated in [51] that the Galactic noise received by two antennas separated by a few wavelengths is significantly correlated. If the outputs of antennas are combined incoherently when the noise is partially correlated, the improvement in the sensitivity will be less than $\sqrt{N}$.

Going forward we will assume that noise correlation does not significantly affect the sensitivity, based on the observation from [51] that the associated correlation "temperature" is small compared to the antenna temperature for antennas spaced at least a wavelength apart.

If the antennas are not copolarized with the incoming signal of interest, there will be a polarization loss governed by the factor $\cos^2(\Delta\psi)$. We know that the incoming signal is polarized, but it is difficult to know its polarization *a priori*. An antenna will receive 100% power if the signal is copolarized with it, or zero power if the signal is orthogonal to it. To obtain estimates in the absence of *a priori* polarization information, we assume the intermediate case where $\Delta\psi = \pi/4$, and hence, only half of the available signal power is received by each antenna. This is a useful choice as it also corresponds to the case where the incoming signal is unpolarized. For N such antennas, the signal can be added either coherently or incoherently as described above. The sensitivity of an array of N antennas is thus

$$S_{min} \geq \frac{2kT_{sys}}{A_e(\theta,\phi,\lambda)\sqrt{\tau B N}} \qquad \text{(Coherent Combining)}, \tag{2.21}$$

$$S_{min} \geq \frac{2kT_{sys}}{A_e(\theta,\phi,\lambda)\sqrt{\tau B}\sqrt{N}} \qquad \text{(Incoherent Combining)}. \tag{2.22}$$

Calculation of T_{sys} in the expressions above requires T_A. It is possible to estimate $T_A(\lambda)$ knowing the antenna pattern and the brightness temperature distribution in the sky. It is given by

$$T_A(\lambda) = \frac{1}{\Omega_A}\int_0^{2\pi}\int_0^{\pi} T_B(\theta,\phi,\lambda)\ P_n(\theta,\phi)\ \sin\theta\ d\theta\ d\phi, \tag{2.23}$$

where Ω_A is the antenna beam solid angle; $T_B(\theta, \phi, \lambda)$ is sky brightness temperature distribution, and $P_n(\theta, \phi)$ is the normalized (maximum value unity) antenna power pattern.

We now turn our attention to a useful metric of sensitivity in terms of apparent brightness temperature, proposed in [30]. For a source of solid angle Ω, and uniform spatial brightness temperature, the flux density observed at a frequency ν in the Rayleigh-Jeans limit ($h\nu << kT_B$ where T_B is the corresponding brightness temperature of the source (true for radio wavelengths)) is given by

$$S = \frac{2kT_B\nu^2\Omega}{c^2}. \tag{2.24}$$

If the source has a diameter l and is at distance d, then

$$\Omega \sim \frac{\pi}{4}\left(\frac{l}{d}\right)^2. \tag{2.25}$$

Thus, by rearranging Equation 2.24, we find the minimum brightness temperature detected by the instrument is

$$T_{B,min} \approx \frac{2c^2 S_{min}}{\pi k\nu^2}\left(\frac{d}{l}\right)^2 \tag{2.26}$$

where S_{min} is computed using Equation 2.21 or Equation 2.22. The above expression can be used to determine whether radio pulses from the sources discussed in Section 1.1 can be reliably detected by the instrument. It can be used to estimate the apparent brightness temperature of the source with a prior knowledge of flux, distance and extent of the source.

Chapter 3

The Eight-meter-wavelength Transient Array (ETA)

The Eight-meter-wavelength Transient Array (ETA) is a low-frequency radio telescope consisting of 10 dual-polarized active dipoles. It is a joint project of the departments of Electrical & Computer Engineering and Physics at Virginia Polytechnic Institute and State University. The telescope is designed to continuously monitor almost the entire sky for radio transients such as primordial black holes (PBHs), gamma ray bursts (GRBs), and Crab giant pulses (CGPs) in the frequency range $29 - 47$ MHz. The telescope was located at the Pisgah Astronomical Research Institute (PARI) ($35°12'$ N, $82°52'$ W) in a mountainous region near Balsam Grove, NC from 2005 to 2008. Additional information about this project, its science goals, and its current status are available at the project website[1].

The ETA dipoles are resonant at about 38 MHz. The dipoles are individually instrumented and digitized. The data collected from each dipole are sampled at 120 million samples per second (MSPS) 12 bits real, but recorded at 7.5 MSPS with 7-bit I and 7-bit Q.

The instrument is described in detail in Section 3.1 ("System Description"). The science spec-

[1] http://www.ece.vt.edu/swe/eta/

ifications of ETA are discussed in Section 3.2 ("Science Specifications"). A summary of data collected is given in Section 3.3 ("Data Collected To Date").

3.1 System Description

We describe the ETA system in this section. A simplified block diagram of ETA system is shown in Figure 3.1. Each subsystem is described in detail below.

3.1.1 Antenna System and RF Front End

ETA is an array of 10 dual-polarized dipoles, which we call "stands". The stands are arranged as a circle with diameter equal to 2 wavelengths at 38 MHz, with one stand located in the center. Shown in Figure 3.2 are the stand positions and numbering.

Inverted "V" dipoles are used in ETA, the details of which can be found in [52]. To make the dipole resonant at approximately 38 MHz, the total length of the dipole is selected to be 3.8 m. Ground screens were installed around July 2007 in order to improve stability with respect to weather-dependent ground conditions. Some of the data analyzed in this thesis were taken before the ground screens were installed, and some were taken after. The ground screen used for ETA is 4 m^2 wire mesh "poultry netting", made of galvanized steel with 1-inch hexagonal grid.

Each dipole is connected to a preamplifier having an input impedance of 100 Ω. The preamplifier is also referred to as an active balun. The output of the preamplifier is connected to RG-58 (50Ω) coaxial cable which conveys signal to the electronics building. At the other end, the cable running from each preamplifier is connected to an analog receiver of custom design which amplifies and filters the signal. The relevant specifications of these components are presented in Section 3.2.2.

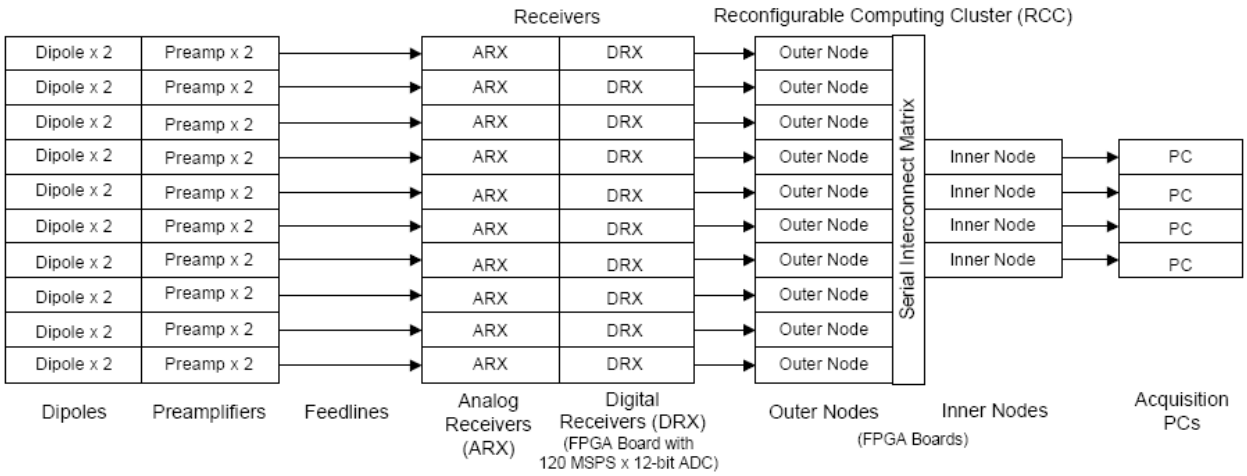

Figure 3.1: A system-level block diagram of ETA.

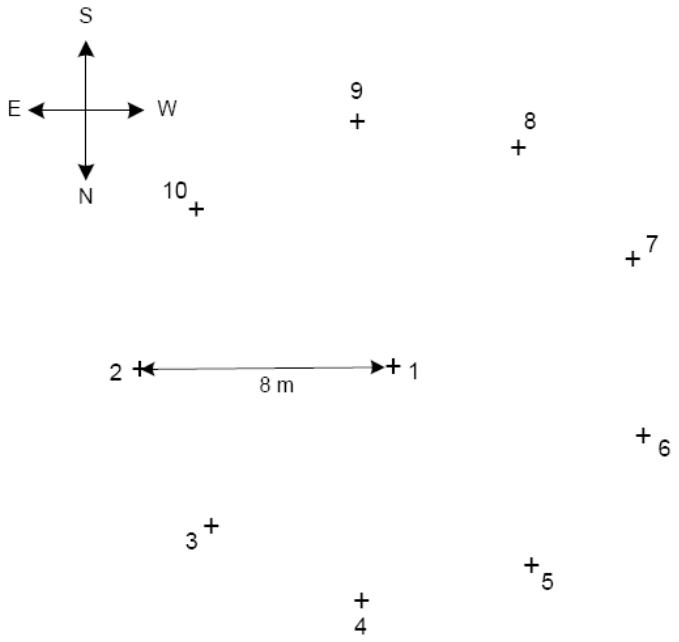

Figure 3.2: Placement of the stands in the array.

The output of the analog receiver is sampled at the ADC using direct sampling. Further processing on the signal is performed in the digital domain and is described in the next section.

3.1.2 Digital Signal Processing and Data Recording

As shown in Figure 3.1, the output of analog receiver is digitized in the digital receiver and routed through a reconfigurable computing cluster (RCC) node to the PCs for recording. See complete details in [36]: Here we provide just a summary. Each digital receiver is an Altera Stratix FPGA development board, which we refer to as an "S25". The main functions of the digital receivers are to digitize, downconvert and channelize the analog signal. The signal from each dipole is digitized using a 12-bit ADC on an S25 at 120 MSPS, as shown in Figure 3.3.

The digitized real-valued data centered at 38 MHz with 18 MHz bandwidth is passed through an "$F_s/4$ Shift Left" block. This downconverts the passband signal by 30 MHz by demultiplexing the real-valued samples into I and Q streams, and alternating signs as necessary. The I and Q streams are passed through a 21 MHz low-pass multirate FIR filter, which also reduces the sampling rate by a factor of 2, to 60 MSPS. A numerically-controlled oscillator (NCO) and a complex tuner shift the center frequency, typically 38 MHz, to the desired value of 0 Hz. A second stage of low-pass multirate FIR filters reduce the bandwidth to 3.75 MHz, and output data as 7-bit I, and 7-bit Q. This stage of filters also reduces the sampling rate from 60 MSPS to 7.5 MSPS. The output formatter prepares a data stream which is transmitted to the RCC.

The RCC consists of 14 Xilinx FPGA boards divided into 10 outer nodes which are directly connected to the digital receivers, and 4 inner nodes that are connected to the acquisition PCs. The outer and inner nodes are interconnected using a serial interconnect matrix. The RCC acts as a reconfigurable, high speed router for the antenna streams. The inner nodes synchronize and aggregate data from the outer nodes and transmit the resultant data stream to the acquisition PCs.

A data acquisition PC is a Dell SC430 server-class PC, and is capable of recording data contin-

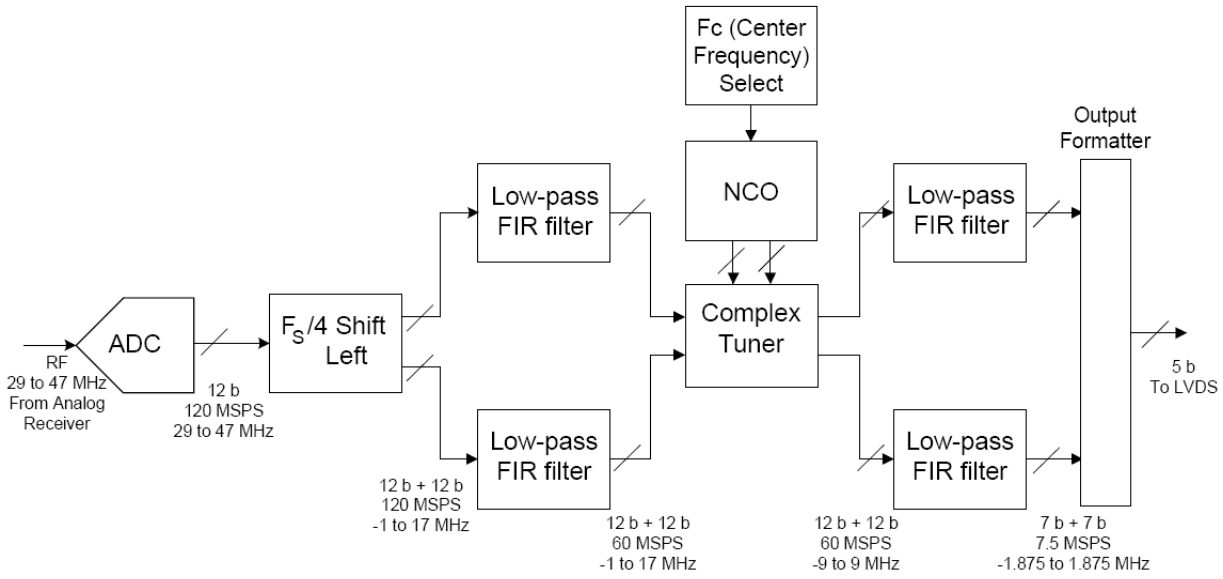

Figure 3.3: Signal flow for the signal from one dipole on an S25 board.

uously for up to two hours, resulting in approximately 400 GB. The recorded data is archived on tapes. The data are stored in raw data format in a file of 1 GB size, each containing ∼18 s of simultaneous acquisition from maximum 4 dipoles. Currently, an individual tape contains about 2 datasets where each is a collection of 200 files corresponding to a one-hour observation. Additional dipole outputs are recorded using the other PCs in the same manner.

3.2 Science Specifications

The knowledge of A_e and system temperature T_{sys} is required in computing the sensitivity. In this section, we first compute these two quantities and then the pulse sensitivity of the telescope.

3.2.1 Effective Area

The effective area and beam solid angle for the ETA dipole are calculated as follows. The effective area can be written as

$$A_e(\theta, \phi, \lambda) = \frac{\lambda^2}{4\pi} G(\theta, \phi, \lambda) e_r (1 - |\Gamma|^2) \tag{3.1}$$

where $G(\theta, \phi, \lambda)$ is the directivity assuming a perfectly matched antenna with no ground loss, e_r is the radiation efficiency which includes the ground loss, and $(1-|\Gamma|^2)$ represents the impedance mismatch efficiency (IME) (See Section 2.2). The directivity can be modeled as $G(\lambda)\cos^{\alpha}\theta$ where $G(\lambda)$ is the zenith directivity, and the factor $\cos^{\alpha}\theta$ gives zenith angle dependence. The complicated patterns of the inverted V dipole used for ETA can be approximated to be $\cos^{1.34}\theta$ in the E-plane and $\cos^{1.88}\theta$ in the H-plane [53]. For simplicity, α is taken to be equal to 1.6, the geometric mean of 1.34 and 1.88. Thus, Equation 3.1 can be modified for ETA to be

$$A_e(\theta, \phi, \lambda) = \frac{\lambda^2}{4\pi} G(\lambda) e_r (1 - |\Gamma|^2) \cos^{1.6}\theta. \tag{3.2}$$

Using 4NEC2, a method-of-moments software, the co-polarized zenith gain of the ETA dipole at 38 MHz is obtained to be 6.8 dBi (for a perfect ground). The gain including ground loss using 4NEC2 for a realistic ground is noticed to be about 2.5 to 3 dB lower than that obtained with a perfect ground. The variation depends on the choice of conductivity and permittivity. In this analysis, we consider the worst case value of -3 dB for e_r for a lossy ground. With an IME of -1.0 dB at 38 MHz, Equation 3.1 gives A_e at zenith equal to 9.4 m^2 for a lossy ground and 18.8 m^2 for a perfect ground; that is with ground screens installed (assuming $e_r = 0$ dB). The beam solid angle is given by $\Omega_A = 4\pi/G(\lambda) \approx 2.6$ sr at 38 MHz.

3.2.2 System Temperature

T_{sys} can be calculated according to Equation 2.12, which requires knowledge of the ground loss, IME, the temperatures and the gains of each components in the antenna and RF system. These values are presented below.

The IME for this antenna varies considerably over the frequencies of interest. IME is -1.0 dB at 38 MHz, and it is ~ -7.5 dB and ~ -3 dB at 29 and 47 MHz, respectively. e_r is assumed to be -3 dB for real ground and 0 dB for the case when ground screens are installed. The measured gain of the preamplifier is $G_{pre} = 23.25 \pm 0.15$ dB over 29 to 47 MHz frequency range. The noise temperature of the preamplifier T_{pre} is estimated to be roughly 300 K. All these parameters are reported and discussed in [52] in detail. The feedline loss for cable of length 32 m (from Stand 1) was measured to be 3.2 dB at 38 MHz, and a $\nu^{-0.5}$ frequency dependence was assumed to calculate the loss at other frequencies. The maximum cable length is about 40 m running from the array to the building with the electronics. It is found that 10 dB/100 m feedline loss does not change T_{int} by much (as shown later), and the telescope maintains the external noise-dominated operation. The analog receiver provides gain $G_R = 52.2$ dB at 38 MHz. G_R is -1.2 dB and -1.8 dB down at 29 and 47 MHz, respectively. The receiver noise figure is 6 dB [54]. Thus, the receiver noise temperature is 864 K. Table 3.1 summarizes these values for 38 MHz. An approximate range of values for T_{int} is found using Equation 2.12.

T_A is calculated using a MATLAB code that implements Equation 2.23. Sky brightness temperatures were obtained using a low frequency sky map generating program called *LFmap* developed at the U.S. Naval Research Laboratory [55].

The worst case value of T_{int} is obtained for the feedline loss of -7.2 dB for the cable of maximum length. Figure 3.4 shows the variation of γ_r with respect to T_A, for T_A in range of daily expected values for different cases. The variation of γ_r indicates Galactic noise-dominated operation of the ETA telescope in all cases. Figure 3.5 shows the corresponding values of T_{sys} found using

Table 3.1: Summary of T_{int} computation at 38 MHz. We have used Equation 2.12 for the calculations.

$(1-\|\Gamma\|^2)$	-1 dB
T_{pre}	300 K
G_{pre}	23.25 dB
T_f	290 K
G_f	-3.2 dB – -7.2 dB
T_R	864 K
T_{int}	310 K – 327 K

Equation 2.13 for all T_A values varying over the daily range.

3.2.3 Sensitivity

Table 3.2 presents the sensitivity values for ETA, computed using Equations 2.21 and 2.22. The antenna temperature variation over a day (7800 − 16000 K) is considered. From Equations 2.13 and 3.1, it is seen that for Galactic noise-dominated operation, the effect of ground screen and IME; i.e. the factor $e_r(1-|\Gamma^2|)$, does not affect the ratio A_e/T_{sys}, and therefore does not affect the sensitivity. We also have bandwidth $B = 3.75$ MHz. We find pulse sensitivities (with signal to noise ratio (SNR) = 5) at different integration times, namely, $\tau = \tau_p = 136$ μs and 498 ms. 136 μs is the minimum achievable time resolution after 1K FFT on the ETA data, while 498 ms is a typical scatter-broadened pulse width for CGPs expected at these frequencies.

Using Equation 2.26, and the sensitivity values for 2 stands combined incoherently, a plot of source brightness temperature sensitivity (T_B) as a function of distance to the source and extent of the source can be obtained. Figure 3.6 shows the resulting plot. With light travel-time argument, a pulse detected with 136 μs time resolution corresponds to the extent of the emission region of 41 km. Similarly, 498 ms wide dedispersed pulse leads to a source extent of 0.2 times the radius of the Sun. This plot enables us to speculate the distances to which an astrophysical event could be detected by ETA. As an illustration, we show that CGPs ($T_B \sim 10^{31.8}$ K) are detectable by ETA.

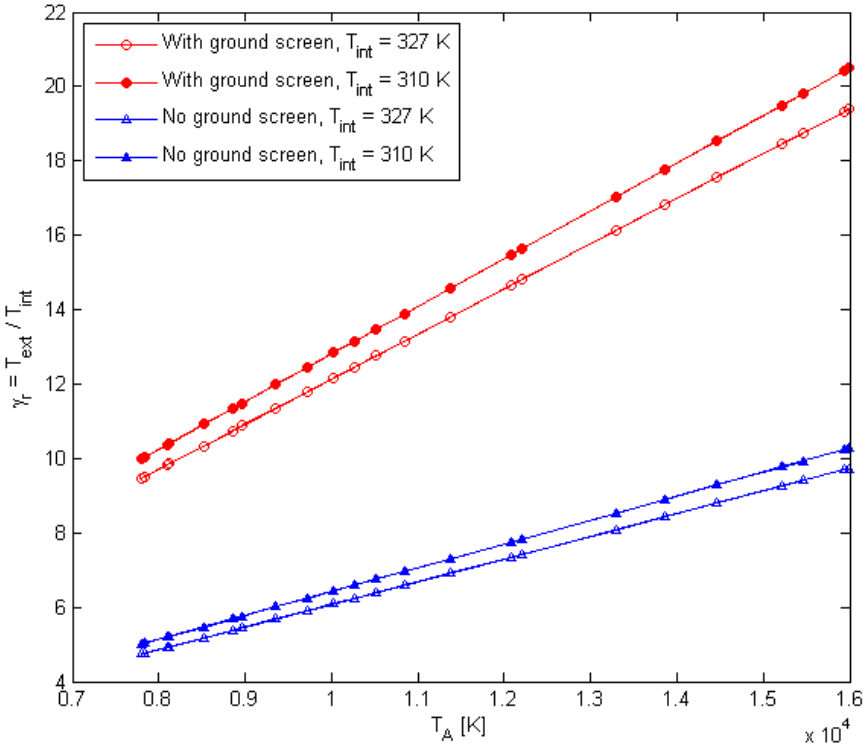

Figure 3.4: Variation of γ_r over a range of daily T_A values.

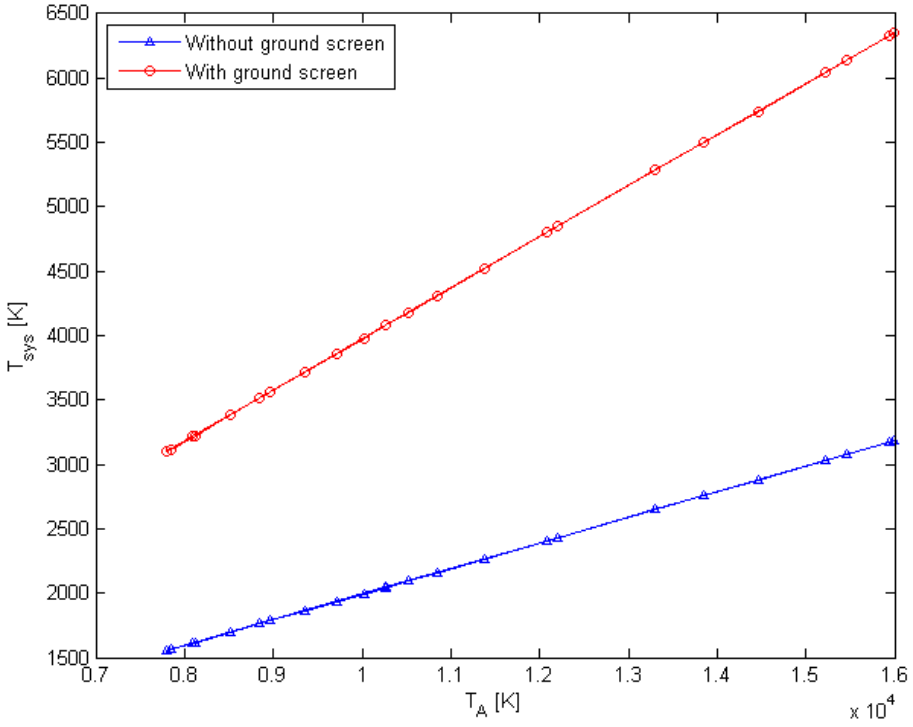

Figure 3.5: Variation of T_{sys} over the range of daily T_A values.

Table 3.2: Pulse sensitivity of ETA with different numbers of dipoles. Range shown to account for daily variation of T_A. As discussed in the text, the presence of ground screens does not affect the sensitivity.

		Pulse Sensitivity ($\tau = 136$ μs)	Pulse sensitivity ($\tau = 498$ ms)
1 Dipole (assuming no polarization mismatch)		50.302 kJy – 103.183 kJy	831 Jy – 1705 Jy
1 Stand (=2 Crossed-dipoles)	Coherent Combining	50.302 kJy – 103.183 kJy	831 Jy – 1705 Jy
	Incoherent Combining	71.138 kJy – 145.923 kJy	1176 Jy – 2411 Jy
2 Stands (=4 Crossed-dipoles)	Coherent Combining	25.151 kJy – 51.592 kJy	416 Jy – 853 Jy
	Incoherent Combining	50.302 kJy – 103.183 kJy	831 Jy – 1705 Jy
4 Stands (=8 Crossed-dipoles)	Coherent Combining	12.575 kJy – 25.796 kJy	208 Jy – 426 Jy
	Incoherent Combining	35.569 kJy – 72.962 kJy	588 Jy – 1206 Jy
10 Stands (=20 Crossed-dipoles)	Coherent Combining	5.030 kJy – 10.318 kJy	83 Jy – 171 Jy
	Incoherent Combining	22.496 kJy – 46.145 kJy	372 Jy – 763 Jy

3.3 Data Collected To Date

Table 3.3 summarizes the data collected by ETA while it was located at PARI. Three major transient searches were carried out with ETA, namely, the PBH campaign, the GCN-triggered campaign, and the CGP campaign. Table 3.3 also lists the observing time in hours for individual campaigns. The table also lists the total number of acquisitions for each campaign, and the time span over which the data for a particular campaign was collected. Note that the total observing time is not necessarily the sum of all acquired data because some datasets serve multiple campaigns. Several datasets collected that are not part of the PBH, CGP, and GCN-triggered campaigns are summarized under the name "Other" in the campaign column. A detailed version of Table 3.3 can be found in Appendix D.

For the search campaign for GRBs, ETA acquired 7 datasets as a response to 7 triggers received

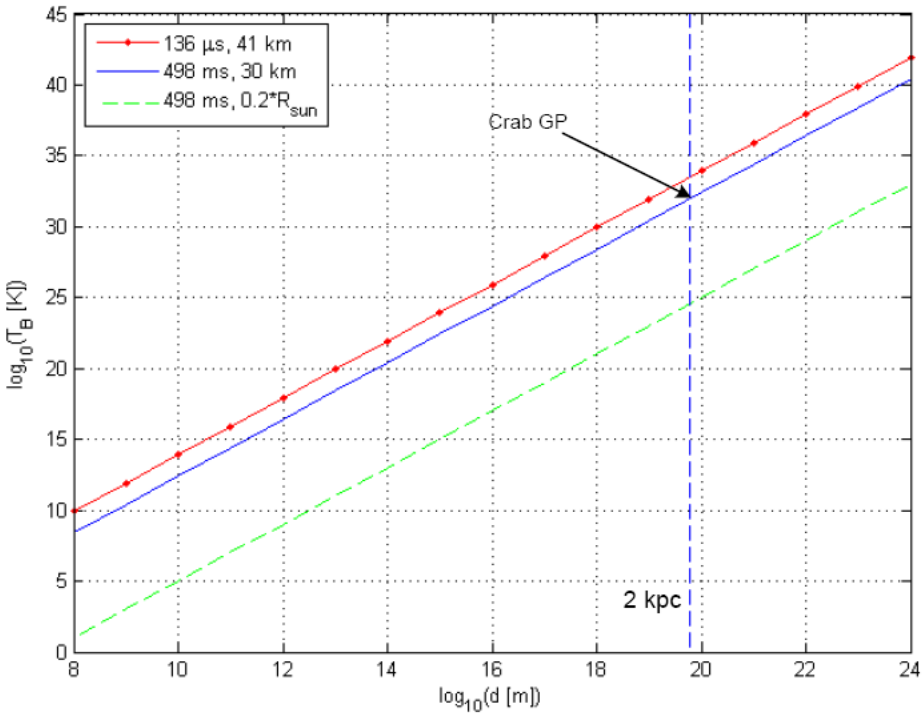

Figure 3.6: 5σ sensitivity of ETA at 38 MHz (2 stands combined incoherently) in terms of source brightness temperature at various distances for pulses of different widths. T_A (assumed) = 7800 K.

Table 3.3: Summary of ETA data collected so far. The dates are in yymmdd (year-month-day) format.

Campaign	Observing Time [h]	# GCN triggers	# Acquisitions	Range of Dates of Observation
PBH	27.18		35	061221 - 070402
CGP	24.68		28	070212 - 071205
GCN-triggered	7.70	7	7	070129 - 071201
Other	11.64		39	070213 - 071122
Total	67.89		107	061221 - 071205

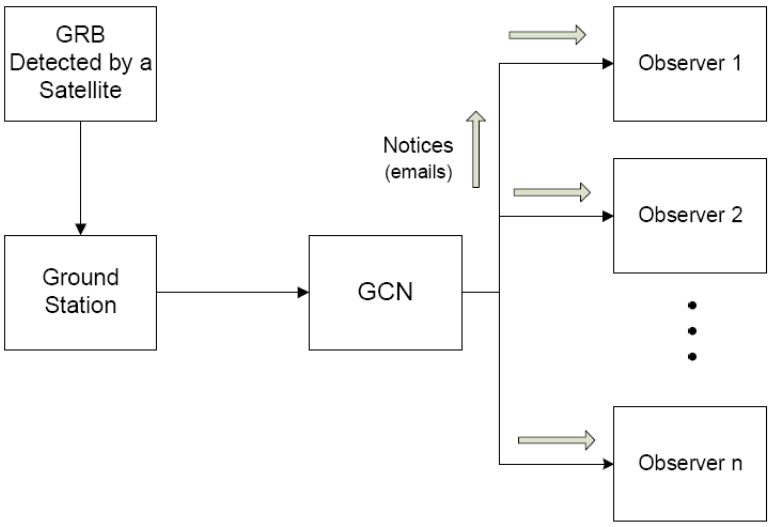

Figure 3.7: A block diagram of GCN-trigger system.

from the GRB Coordinate Network (GCN)[2]. GCN is a system which promptly sends notices to ground-based observers in the form of emails when a burst is detected by one of its associated satellites [56]. A simple block diagram in Figure 3.7 illustrates the GCN-trigger system. This system allows ground-based telescopes to conduct follow-up observations of the bursts by conveying them the information about the coordinates of the burst at the earliest. ETA can acquire $1-2$ hours of data in response to notices received from GCN. GCN-triggered data was collected by ETA for the following 7 GRBs: GRB 070129, GRB 070208, GRB 070219, GRB 070220, GRB 070223, GRB 070309 and GRB 071122.

[2] http://gcn.gsfc.nasa.gov/

Chapter 4

Data Analysis

Transient search algorithms and software are active topics; a recent example is [57]. Data analysis software for single dispersed radio pulse searches at low frequencies include corrections for instrumental effects (such as spectral ripple) and diurnal variation of the Galactic background, RFI mitigation, and incoherent dedispersion. In this chapter, we present the "toolchain" developed for the ETA Crab giant pulse (CGP) search campaign. The toolchain is described in detail in Section 4.1 ("The Toolchain"). We simulated a dispersed pulse to test the toolchain. The simulation and its results are discussed in Section 4.2.1 ("Simulated Dataset"). The analysis of actual field data is presented in Section 4.2.2 ("Real Dataset").

Non-DM-specific searches such as those required for the gamma ray burst (GRB) and primordial black hole (PBH) campaigns require a search over a range of DM values. Modification of the toolchain to achieve this is suggested in Chapter 6.

4.1 The Toolchain

The toolchain and the tasks it carries out during the data analysis are described in this section. The toolchain consists of codes written in C and running from the command-line interface in

Linux. There are two sets of codes: p's and q's. q codes call p codes to perform a task on each file of the dataset. Table 4.1 summarizes the toolchain, listing the codes and the tasks they carry out. A flowchart describing the toolchain is shown in Figure 4.1.

4.1.1 Data Integrity Check

The purpose of this step is to identify data which are corrupted or otherwise unusable either due to internal system errors or due to excessive radio frequency interference (RFI). Code $q1$ performs the data integrity check. The output files contain diagnostic summaries, along with sample value histograms. The histograms of the "I" and "Q" samples both are examined and verified to be approximately Gaussian with the same variance and with negligible DC offsets. The statistics of the data are analyzed to find the number of "clips" (extreme data values), which is useful in identifying files that are badly corrupted with RFI. The diagnostic output from this step also provides a quick verification of coherency inside a file and across the files. This is done by examining the diagnostic "counter bits", described in Section 5 of [36].

4.1.2 Creating Raw Spectrograms

Spectrograms (intensity plots displaying the power spectral density (PSD) as a function of both time and frequency) are generated by Fourier transforming the raw data. The transform is implemented on the data sampled originally with 7.5 MSPS, using a triangle-windowed 1K FFT. This yields frequency resolution of 7.324 kHz and time resolution 136 μs. The spectrogram corresponding to one file spans 17.896 s in time and 3.75 MHz in frequency. This step is carried out by $q4$, which calls $p2$ to perform the FFT on each file, and $q2$ to get the time-frequency, time, and frequency domain results.

Table 4.1: Toolchain summary. "Requires" means the indicated code is called.

Code Name	Requires	Section Where Discussed	Description
$q1$	$p1$	4.1.1	Verifies data coherency inside a file and across files, and helps to find files that are highly corrupted with RFI.
$q2$		4.1.2	Generates spectrograms, time series, and frequency domain results and summaries.
$q4$	$p2, q2$	4.1.2	Generates raw spectrograms.
$q5$	$p3$	4.1.3	Generates a baseline spectrogram, which is used to calibrate all the spectrograms in the dataset.
$q6$	$p4, q2$	4.1.4	Calibrates the raw spectrograms.
$q8\_p1$ (variation of $q8$)		4.1.5	Removes the "dropouts" (Step 1 of RFI mitigation. See Appendix C for details).
$p8$		4.1.5	Performs step 3 of RFI mitigation.
$q8$		4.1.5	Performs steps 2, 4, 5 and 6 of RFI mitigation.
$q7$	$p5$	4.1.6	Incoherently dedisperses the RFI-mitigated spectrograms at the targeted DM and generates a time series.
$p6$		4.1.7	Downsamples the time series to coarser time resolutions.
$p9$		4.1.8	Removes baseline fluctuations from the time series.
$p10$		4.1.9	Incoherently combines two or more outcomes.
$p14$		4.1.10	Searches for pulses of various widths.
$q12$	$q7, p6, p9$ $p10, p14\_p2$ (variation of $p14$)	4.1.11	For a candidate pulse, performs a DM "sweep test".

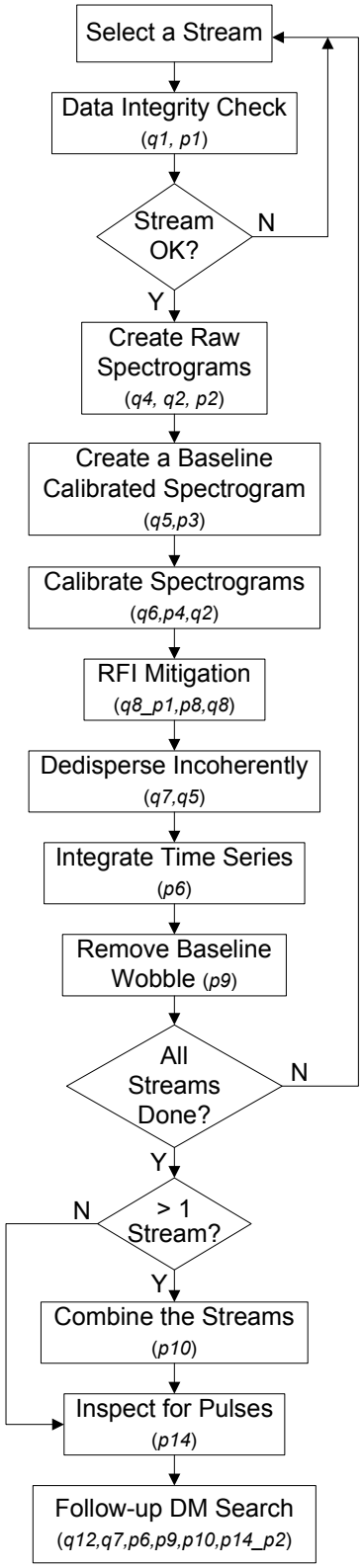

Figure 4.1: Data analysis flowchart. The toolchain codes concerning a task are also mentioned.

4.1.3 Creating a Baseline Spectrogram

Raw spectrograms are calibrated to remove the frequency response of the instrument and the time domain variation in the total power which is due to the diurnal variation of the Galactic background radiation. This is done by first constructing a "baseline spectrogram" which represents the frequency response and time variation over an entire dataset. The procedure is as follows: first manually select one sufficiently-RFI-free file every 7.5 minutes so as to track the Galactic background variation. Code $p3$ determines a baseline fit to integrated spectra in each of these files. It uses median filtering to remove the peak at 0 Hz (associated with DC bias) and narrowband RFI. Code $q5$ then linearly interpolates over this set of frequency responses to give the baseline spectrogram.

4.1.4 Calibration of Spectrograms

All the raw spectrograms in the dataset are calibrated using the baseline spectrogram created in the previous step. Code $q6$ reads a baseline spectrum for a file from the baseline spectrogram and then calls $p4$ to divide each column (frequency) of the related raw spectrogram, pixel-by-pixel, by the baseline spectrum. Each calibrated spectrogram thus obtained has a flat frequency response with mean value equal to 1.

4.1.5 RFI Mitigation

RFI degrades sensitivity and generates false detections. To mitigate the effects of RFI, an algorithm described in a detailed report included in Appendix C is used. The algorithm also removes "dropouts", which are instances of gain compression in the receiver due to high-power out-of-band RFI.

$q8\_p1$ is used in step 1 of RFI mitigation to remove the dropouts. In the next step, $q8$ removes strong RFI by replacing a fraction of the largest magnitude pixels in the time-frequency domain

by the mean PSD value. The output of this is used to find the standard deviation values (using $p8$), which are then given as inputs to $q8$ for the subsequent steps in RFI excision.

4.1.6 Incoherent Dedispersion

To remove dispersion, either coherent or incoherent dedispersion can be used. Coherent dedispersion performs "de-chirping" of the received signal, using all available phase information [46]. Since, for our purposes, it was simpler to implement RFI mitigation on incoherent data, we incorporate *incoherent* dedispersion in our toolchain. Moreover, the computational burden of incoherent dedispersion is less when compared with that of coherent dedispersion.

Incoherent dedispersion operates on the PSD values in baseline-calibrated spectrograms. It involves shifting of frequency channels or "columns" (all bins representing a single frequency across all spectra) by the dispersion delay for that frequency relative to the highest frequency in the frequency range computed using Equation 2.3 presented in Section 2.1.1. Code $q7$ calls $p5$, which individually dedisperses all spectrograms, to get time series each 17.896 s long. $q7$ then stitches these time series together to obtain a single larger time series.

The optimum time resolution for spectrograms going into incoherent dedispersion is determined by the minimum time required by a pulse to traverse one frequency bin. The lowest DM normally considered is 10 pc cm^{-3}, since for DM lower than 10 pc cm^{-3}, the dedispersed data is likely to be severely affected by RFI which might cause spurious detections. The lowest frequency bin for ETA data, when tuned to a center frequency of 38.0 MHz, represents 36.125 to 36.132 MHz. This gives $\Delta t_{2\to1} = 12.88$ ms at the lowest DM. The highest frequency bin represents 39.867 to 39.875 MHz, indicating $\Delta t_{2\to1} = 9.589$ ms at this DM, and is therefore the minimum time resolution of interest. In practice, 8.738 ms is a convenient time resolution, as this gives 2048 spectra in each 17.896 s long file.

4.1.7 Integrate Time Series

To account for the scatter broadening, the dedispersed time series obtained from the previous step is averaged in the time domain to the expected resolution of the scattered-broadened pulse. This greatly improves sensitivity in pulse detection (see Section 4.1.10). The limits on the appropriate width (τ_d) of dispersed pulses observed at ETA frequencies are obtained as mentioned briefly in Section 2.1.2. For illustrative purpose, we describe the limits on τ_d for CGPs in detail here. Assuming the ISM is distributed according to the Kolmogorov spectrum, the duration of a scatter-broadened pulse is proportional to $\nu^{-4.4}$ [44]. Using this to scale a reference observation from [3] (pulse width of 0.5 ms at 0.3 GHz) to 38 MHz, we get $\tau_d = 4.4$ s. Popov *et al.* [4] presented a model $\tau_d = 20(\nu/100\text{ MHz})^{-3.5\pm0.1}$ ms for the frequency dependence of the pulse width. Using this model and an observation reported in the same paper (pulse width of 3 s at 23 MHz), we obtain $\tau_d \approx 0.6$ s at 38 MHz. Thus,

$$0.6\ s \leq \tau_d \leq 4.4\ s. \tag{4.1}$$

Therefore, for CGP searches, using code *p6* we average in the time domain to reduce the time resolution from 8.738 ms to about 498 ms; i.e., a multiple of 8.738 ms close to 0.6 s.

4.1.8 Removal of Baseline Wobble

As mentioned earlier, the PARI site for ETA is located in a mountainous region. The terrain causes significant multipath, which in turn causes "wobble" in the baseline as various multipath components go in and out of phase as the Earth rotates. (An example is shown in Figure 4.11(b).) It is desired to remove this wobble so that it does not bias the pulse detection. To correct this baseline wobble, an estimate of the time domain variation is subtracted from the original time series. This estimate is obtained by taking a moving average over the dedispersed time series with a suitable-sized window. Our experiments suggested that 50 s is a

reasonable window size for averaging. The effect of baseline removal can be seen by comparing Figure 4.11(b) to Figure 4.13. Code $p9$ performs this task.

4.1.9 Incoherent Combining of the Streams

Currently, this toolchain supports only *incoherent* combining of antennas as opposed to coherent combining (as in beamforming). Let $W_1(t)$ and $W_2(t)$ be two time series to be combined in this manner. Then the result is:

$$\begin{aligned} W_{12}(t) &= \frac{W_1(t) + W_2(t)\ V_2^{(1)}(t)}{2}, \\ \text{where}\quad V_2^{(1)}(t) &= \left\langle \frac{W_1(t)}{W_2(t)} \right\rangle_{t_w} \end{aligned} \tag{4.2}$$

and where $<>_{t_w}$ stands for boxcar averaging performed over the whole observation using a window of length t_w. t_w is determined as follows. In a dedispersed time series, the "zero crossings"– i.e., the points where the baseline crosses the mean value – occur on the order of 10 minutes or so. Thus, we choose t_w equal to 1 minute; i.e., a small fraction of this period.

For $N > 2$ streams, the procedure implied by Equation 4.2 can be generalized as follows:

$$\begin{aligned} W_{fin}(t) &= \frac{\sum_{i=1}^{N} W_i(t)\ V_i^{(s)}(t)}{N}, \\ \text{where}\quad V_i^{(s)}(t) &= \left\langle \frac{W_s(t)}{W_i(t)} \right\rangle_{t_w} \end{aligned} \tag{4.3}$$

and where s is the stream (selected manually) as the desired reference. The reference stream should be the one with the least RFI and the least variations in its baseline. Although not currently implemented, one could also consider averaging all the "good" streams and then to use that result as the reference stream.

4.1.10 Inspection for Pulses

The procedure for detecting pulses in a dedispersed time series consists of following steps:

1. The "local" mean, m_l, and "local" standard deviation, σ_l, of the time series are computed. m_l and σ_l are defined as the mean and the standard deviation over an interval t_p less than the total time of observation such that both m_l and σ_l track residual variations in the data over this timescale. An appropriate window size t_p for computing m_l and σ_l is suggested below.

2. In the time series, for a trial pulse length, a sample x_{max} is detected such that the detection metric d (defined below) is maximum. The detection metric in terms of m_l and σ_l is defined as

$$d = \frac{x_{max} - m_l}{\sigma_l}; \tag{4.4}$$

   i.e., the number of local standard deviations above the local mean value.

3. Time of occurrence and d are noted. Since this process is repeated from the shortest to the longest pulse lengths (as explained below) there is a possibility that the same pulse might be detected at different pulse lengths. In order to avoid this repetition, the detected event is masked temporarily, that is, pixels corresponding to the event are temporarily set to 1.

4. All detections exceeding $3\sigma_l$ are noted.

5. Because there is a large uncertainty in the widths of pulses due to scatter broadening, Steps 1–4 are repeated for different trial pulse lengths. Given a starting pulse length of y seconds, subsequent pulse lengths chosen are $2y, 4y, 8y \ldots$ until the upper limit of the expected pulse width is exceeded. In each case, the data are averaged to the corresponding pulse lengths to improve sensitivity. For CGP searches, the starting pulse length is 498 ms and the maximum pulse length considered is about 8 s.

There is a trade-off in determining the size of the window t_p used to compute m_l and σ_l. It should be large enough to give a reasonable estimate of the mean and standard deviation but should not be so large that the estimate is biased by residual variations in the time series. Our trials suggest $t_p = 600$ s is a reasonable choice.

Code $p14$ performs this task.

4.1.11 Follow-up DM Search

Pulses detected in the previous step are subjected to a "follow-up" search over a range of DM values about the discovery DM. The purpose of this step is to confirm that the detection metric is maximum at the desired DM and this is not a spurious detection or a result of saturation. An appropriate DM spacing for this procedure is $\delta\mathrm{DM} \lessapprox \mathrm{DM}(\Delta\nu_{\mathrm{MHz}}/\mathrm{B}_{\mathrm{MHz}})$ where $\Delta\nu_{\mathrm{MHz}}$ is the width of a frequency channel, and $\mathrm{B}_{\mathrm{MHz}}$ is the bandwidth. This expression is derived in Appendix A.

The DM search for a particular detection begins at the discovery DM and moves higher and lower until the detection metric d decreases by at least a factor of 2.

The time of occurrence of each detection obtained from the output of above step is written in an input file along with other input parameters. Using these inputs, code $q12$ performs dedispersion at various DM values about the DM of interest, averages the time series, and removes the baseline wobble for each stream. It then combines all streams and finally calls $p14\_p2$ to find the detection metric within a window around the specified event time. For the CGP search, we choose a window of 20 s length centered at the event time. For each event, $q12$ outputs the detection metrics as a function of DM for various trial pulse lengths.

4.2 Examples

In this section we present the use of the toolchain for analyzing a simulated dataset and a real observation. The purpose of Section 4.2.1 is to illustrate the analysis in the case of ideal (simulated, RFI- and multipath-free) data known to contain a pulse. The example in Section 4.2.2 illustrates results in the case of actual field data which may or may not contain pulses.

4.2.1 Simulated Dataset

The dataset used in this example contains a simulated pulse dispersed at DM = 56.791 pc cm^{-3} (the DM value for the Crab pulsar) plus simulated Gaussian noise. The dedispersed pulse has a full width at half maximum (FWHM) of 1 s and a signal to noise ratio of ∼7.8. The generation of the dispersed, scattered-broadened pulse is discussed in detail in Appendix B. Table 4.2 summarizes the dataset and the results. In this simulation, we assume that ground screens are not present.

The analysis of this dataset is described below. Note that the simulated data has neither frequency nor time domain variations. It is also free from the effects of multipath. Thus, steps from Sections 4.1.3, 4.1.4 and 4.1.8 are not necessary and hence are not included in this analysis. Also, as only one stream is simulated, incoherent combining (Section 4.1.9) was bypassed.

- **Creating Raw Spectrograms:** All 9 raw spectrograms were generated using $q4$. They were stitched together to obtain the raw spectrogram shown in Figure 4.2.
- **RFI mitigation:** RFI mitigation was performed using the proposed algorithm in order to account for any potential "toxicity" of the proposed RFI mitigation algorithm (refer to Appendix C for more details).
- **Incoherent Dedispersion:** Dedispersion was performed incoherently using $q7$ at the Crab DM.

Table 4.2: Summary of the simulated dataset.

1	Tape ID	Not recorded to tape. Demo only.
2	Tape position	NA
3	Campaign	Crab GP
4	Dataset Name	(Simulated dataset)
5	Start	(Simulated dataset)
6	Duration (hh:mm:ss)	00:02:41
7	Center Frequency	38.000 MHz
8	Processed Bandwidth	3.750 MHz
9	System Temperature	1550 K (assumed)
10	Antennas Used	1 (simulated)
11	Data Format	Consisting of 9 files of 1 GB each

- **Integrate Time Series:** We integrated the time series to a time resolution of 498 ms. Figure 4.3 shows the output.

- **Inspection for Pulses:** The time series was inspected using the pulse detection algorithm from Section 4.1.10. Table 4.3 shows the output of $p14$. Estimated flux was found by scaling the minimum detectable flux (computed using Equation 2.22 from Section 2.3) by the detection metric. As seen in Table 4.3, the simulated pulse shows up as a $\sim 7.8\sigma$ detection at a trial pulse length of 1 s. The expected rate of occurrence of a $d\sigma$ pulse is defined as the probability of this detection assuming ideal noise in per unit time. This quantity represents the probability that the detection is a spurious, noise-induced detection, and is expected to be low. The probability of a spurious detection in a given integration time τ is $p = (\mathrm{erfc}(d/\sqrt{(2)}))/2$. Thus, the probability of occurrence of that detection in time T or in $n = T/\tau$ number of integration times is given by $np(1-p)^{n-1}$. Therefore, the probability of the detection per unit time is $np(1-p)^{n-1}/T$.

- **Follow-up DM Search:** A follow-up DM search was performed over a range of DM values until the detection metric decreased by at least a factor of 2. The output of $q12$ is plotted as shown in Figure 4.4. The value of DM spacing (1.109×10^{-1} pc cm^{-3}) was obtained from Equation A.5 in the Appendix A. The curve for 0.5 s in Figure 4.4 shows that the detection metric approximately peaks around the Crab DM and goes down

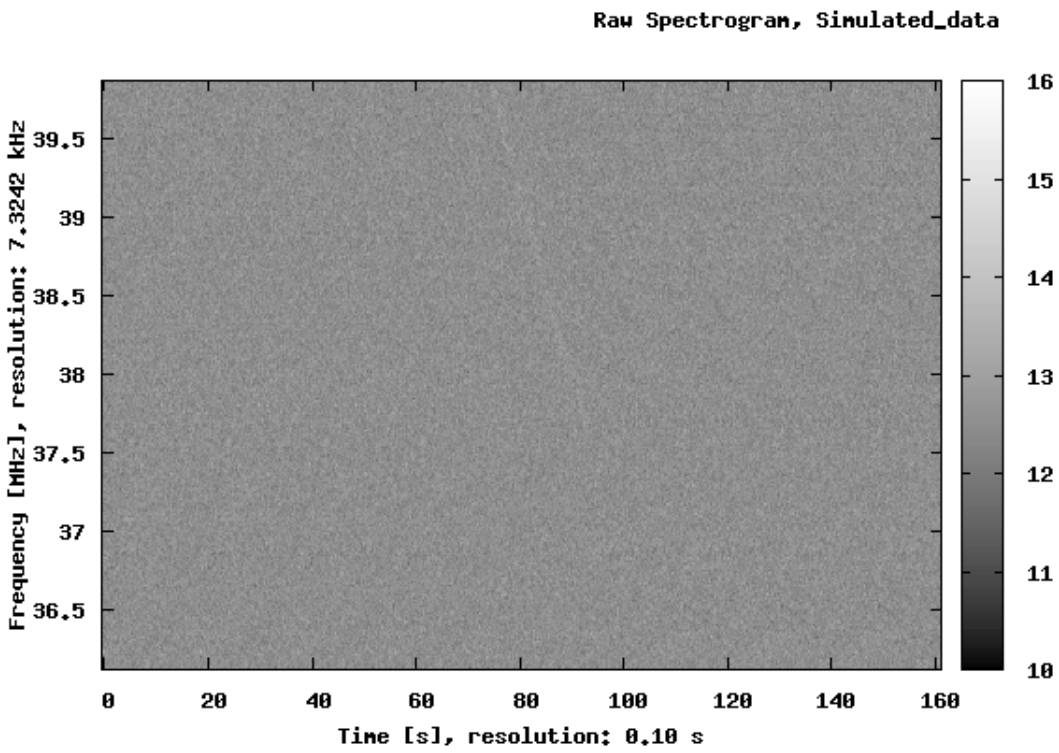

Figure 4.2: Raw spectrogram (Simulated Dataset). Power spectral density (PSD) in arbitrary units. The pulse is visible from about 75 s to 90 s.

significantly at other DM values.

4.2.2 Real Dataset

The dataset used as an example here is known as Crab_070212, observed on February 12, 2007. This dataset contains relatively little RFI compared to other observations, hence was chosen for illustration purposes. It is an hour-long observation using 2 antennas, as indicated in Table 4.4.

The analysis of this dataset proceeds as follows:

- **Data Integrity Check:** The raw data was checked for data integrity using $q1$ with satisfactory results.
- **Creating Raw Spectrograms:** All 200 raw spectrograms of each stream were generated using $q4$. They were stitched together to obtain the raw spectrograms shown in

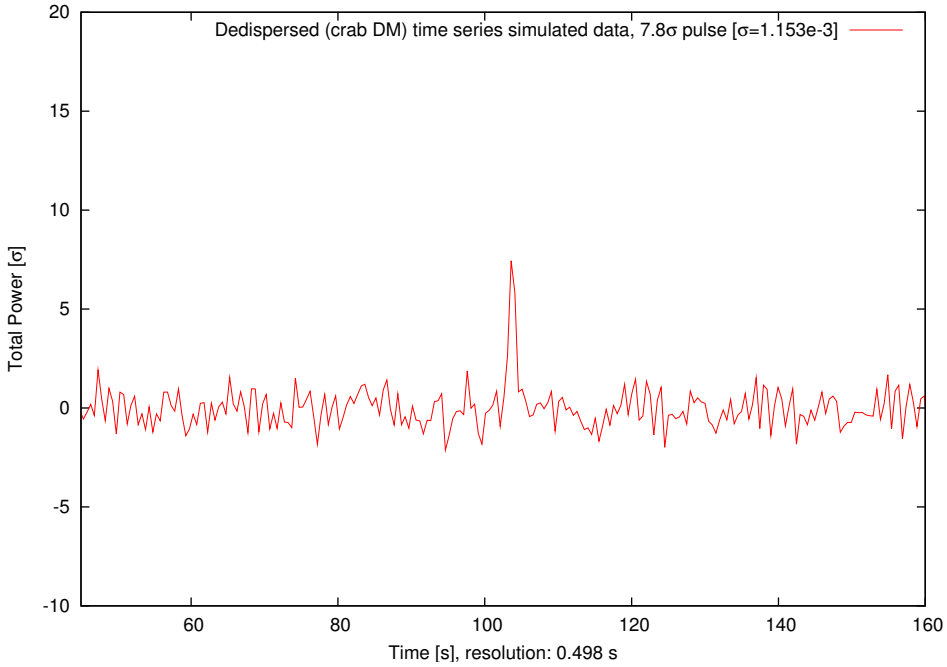

(a)

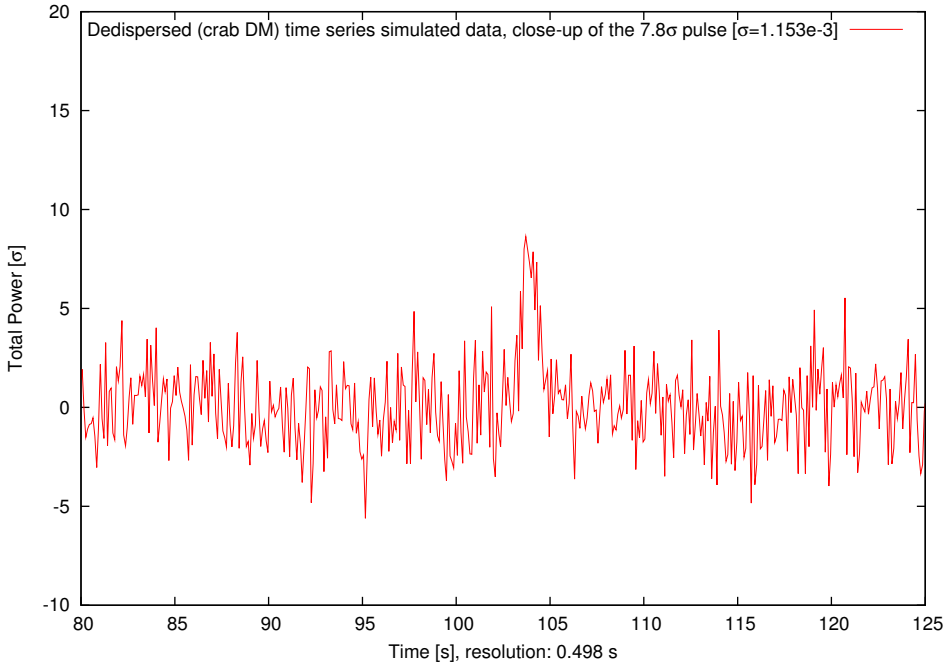

(b)

Figure 4.3: (a): Dedispersed time series at Crab DM (Simulated Dataset). Time resolution: 498 ms. (b): Close-up from (a).

Figures 4.5 and 4.6.

- **Creating a Baseline Spectrogram:** We selected files 3, 31, 50, 76, 101, 125, 150,

Table 4.3: Maximum detection at Crab DM= 56.791 pc cm^{-3}.

Trial Pulse Length [s]	Max Detection [σ_l]	Event Time [s]	Estimated Flux [Jy]	Expected Rate [h^{-1}]	Follow-up DM Sweep Test
1	7.8	104.1	1825	8.06×10^{-12}	Passed

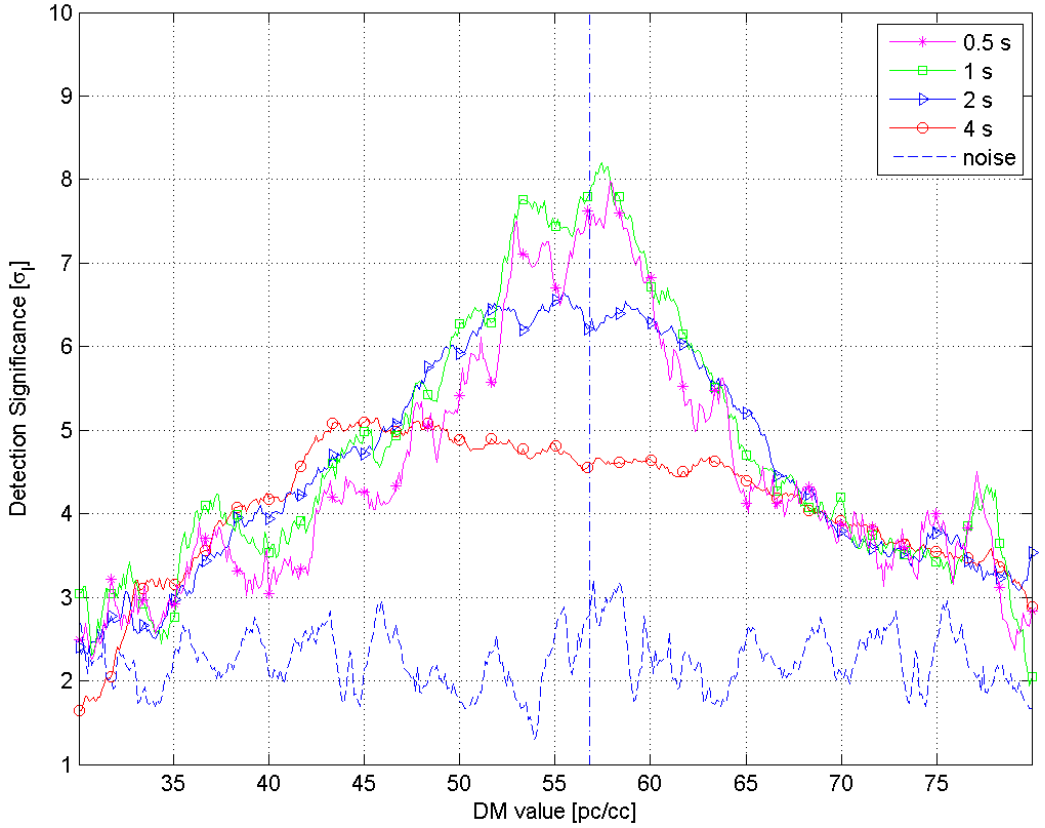

Figure 4.4: Results of DM sweep for the detection at 104.1 s (Simulated Dataset). Curves represent different trial pulse lengths. Vertical dashed line is 56.791 pc cm^{-3} (Crab DM). The dashed line shows result when the same procedure is used on data in which the pulse is excluded.

175 and 193 using the criteria discussed in Section 4.1.3. A baseline spectrogram was generated using $q5$ with these files as inputs.

- **Calibration of Spectrograms:** The baseline spectrogram generated in previous step was used to reduce the dataset to calibrated spectrograms using code $q6$. The calibrated spectrograms for both streams are shown in Figures 4.7 and 4.8.

- **RFI mitigation:** In step 1 of RFI mitigation, $q8\_p1$ removed the dropouts from both the

Table 4.4: Crab_070212 dataset summary.

1	Tape ID	t003
2	Tape position	1
3	Campaign	Crab GP
4	Dataset Name	Crab_070212
5	Start	UT 2007 Feb 13 00:58
6	Duration (hh:mm:ss)	01:00:00
7	Center Frequency	38.000 MHz
8	Processed Bandwidth	3.750 MHz
9	System Temperature	1940 K
10	Antennas Used	6B, 6Y
11	Data Format	Consisting of 200 files of 1 GB each
12	Summary Findings	Two pulses (4.42σ, 4.50σ) satisfied initial detection criteria. The 4.42σ pulse passed a "Follow-up" DM sweep test.
13	Remarks	Relatively clean dataset. All streams are usable. Antenna temperature estimated from an all-sky map using a model for the antenna pattern.

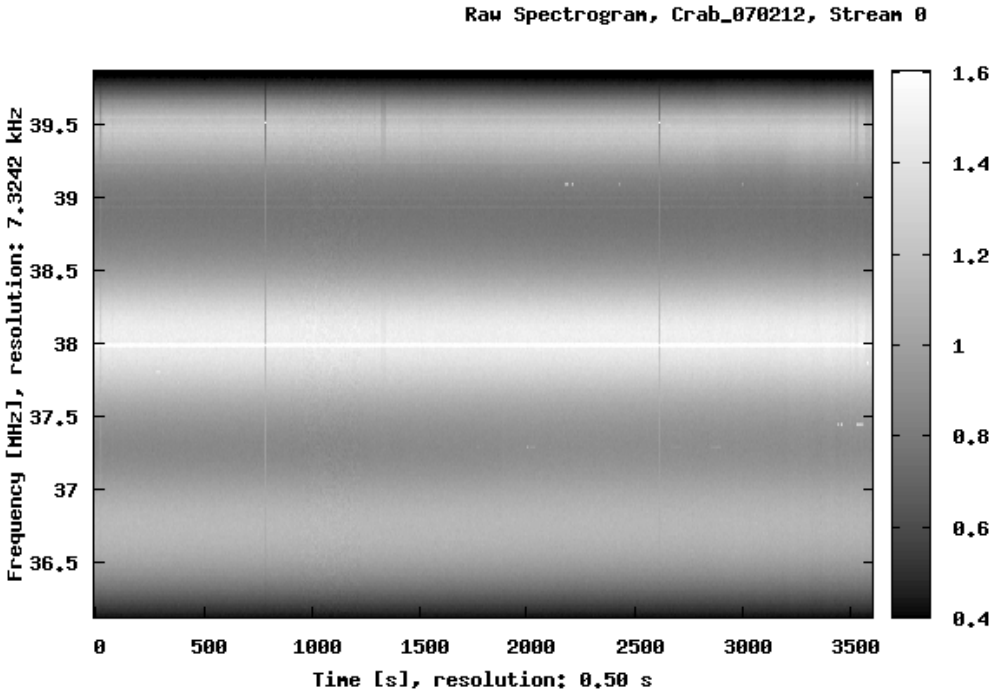

Figure 4.5: Raw spectrogram, stream 0 (6B).

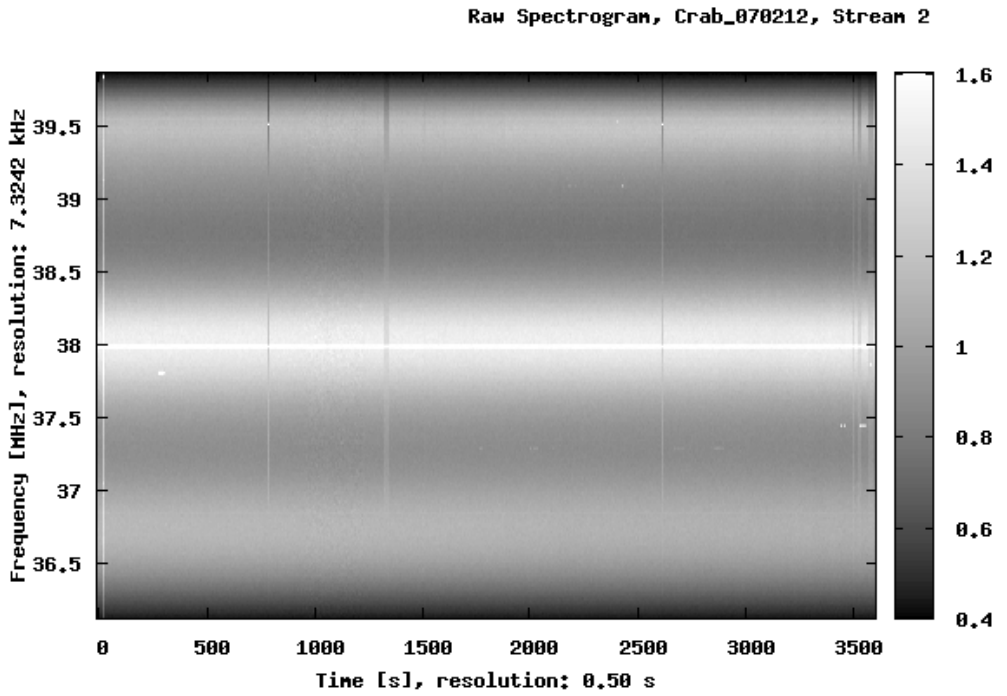

Figure 4.6: Raw spectrogram, stream 2 (6Y).

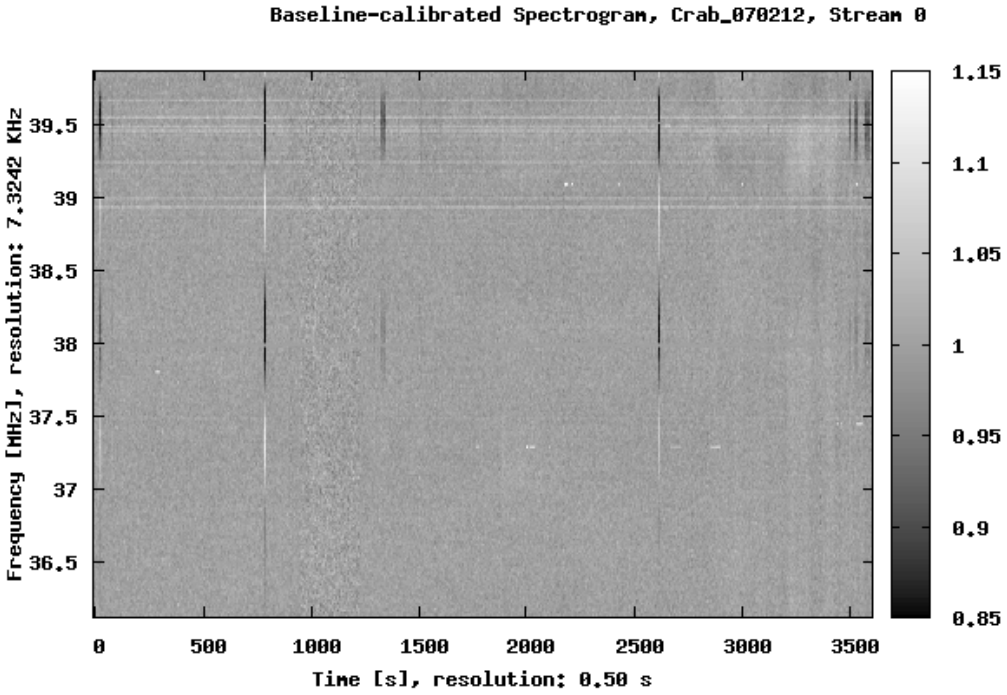

Figure 4.7: Calibrated spectrogram, stream 0 (6B).

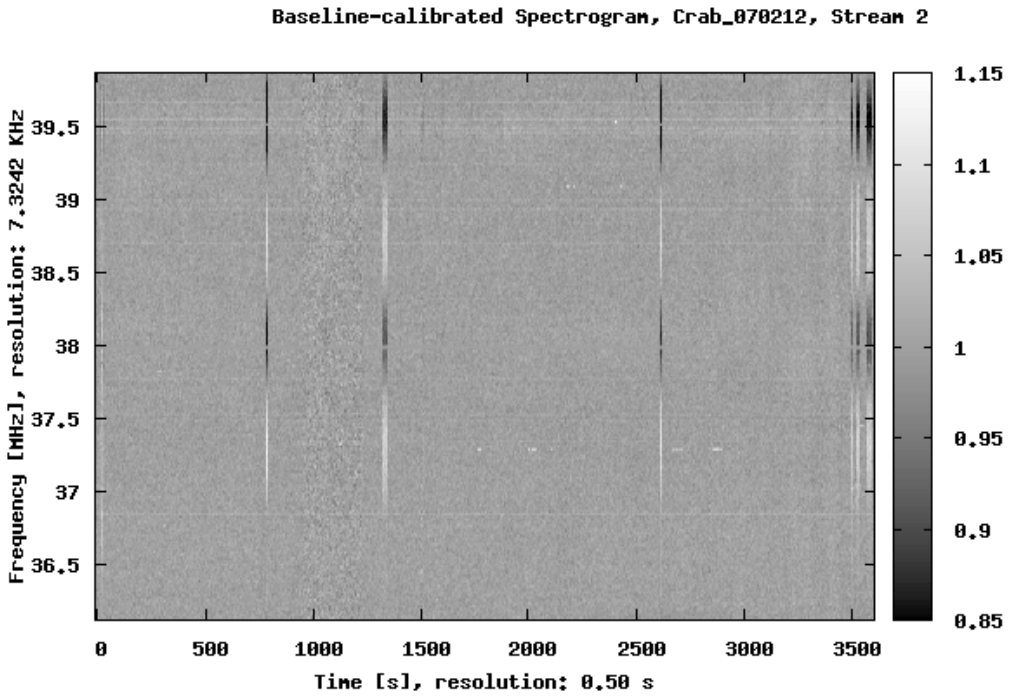

Figure 4.8: Calibrated spectrogram, stream 2 (6Y).

streams. 1% of data was removed from the time-frequency domain using $q8$ and then code $p8$ was used to obtain the standard deviation values to be used in the subsequent steps of RFI mitigation. The output of $p8$ for stream 0 is shown in Table 4.5. The standard deviation values required by the RFI mitigation algorithm were obtained by averaging the standard deviation values in corresponding domains for the set of files selected above. The results of application of the next RFI mitigation step are shown in Figures 4.9 and 4.10.

- **Incoherent Dedispersion:** Dedispersion was performed incoherently using $q7$ at the Crab DM. Figures 4.11(a) and 4.12(a) show the results of dedispersion.

- **Integrate Time Series:** As explained in Section 4.1.7, the dedispersed time series for each stream was averaged using $p6$ to a resolution of 498 ms. Figures 4.11(b) and 4.12(b) show the results of averaging. Notice the baseline wobble in these time series. This wobble is removed in the next step.

- **Removal of Baseline Wobble:** Figures 4.13 and 4.14 show the output of $p9$ after

Table 4.5: Averaged standard deviation values from the files used for baseline calibration and RFI mitigation, stream 0.

File Number	σ_{tf}	σ_t	σ_f
3	1.193×10^{-1}	7.152×10^{-3}	5.307×10^{-3}
31	1.191×10^{-1}	7.017×10^{-3}	5.591×10^{-3}
50	1.192×10^{-1}	6.831×10^{-3}	5.555×10^{-3}
76	1.193×10^{-1}	6.889×10^{-3}	5.620×10^{-3}
101	1.191×10^{-1}	6.921×10^{-3}	5.314×10^{-3}
125	1.193×10^{-1}	7.026×10^{-3}	5.514×10^{-3}
150	1.192×10^{-1}	6.922×10^{-3}	5.802×10^{-3}
175	1.192×10^{-1}	7.134×10^{-3}	5.288×10^{-3}
193	1.192×10^{-1}	7.039×10^{-3}	5.623×10^{-3}
Average	$\sigma_{tf} = 1.192 \times 10^{-1}$	$\sigma_t = 6.992 \times 10^{-3}$	$\sigma_f = 5.513 \times 10^{-3}$

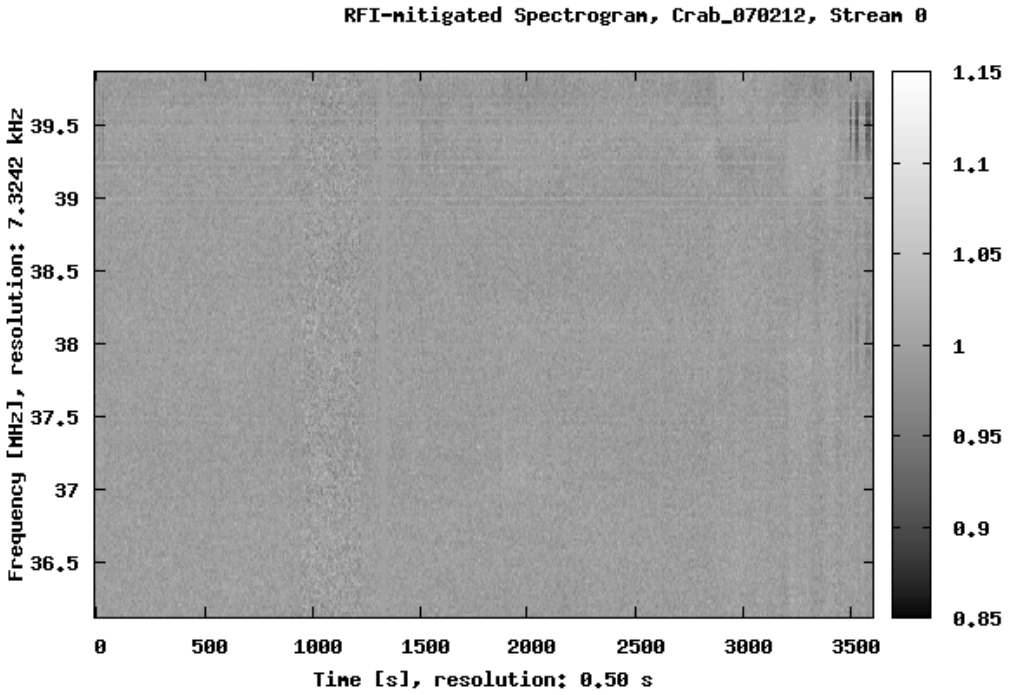

Figure 4.9: Spectrogram with RFI mitigation, stream 0 (6B).

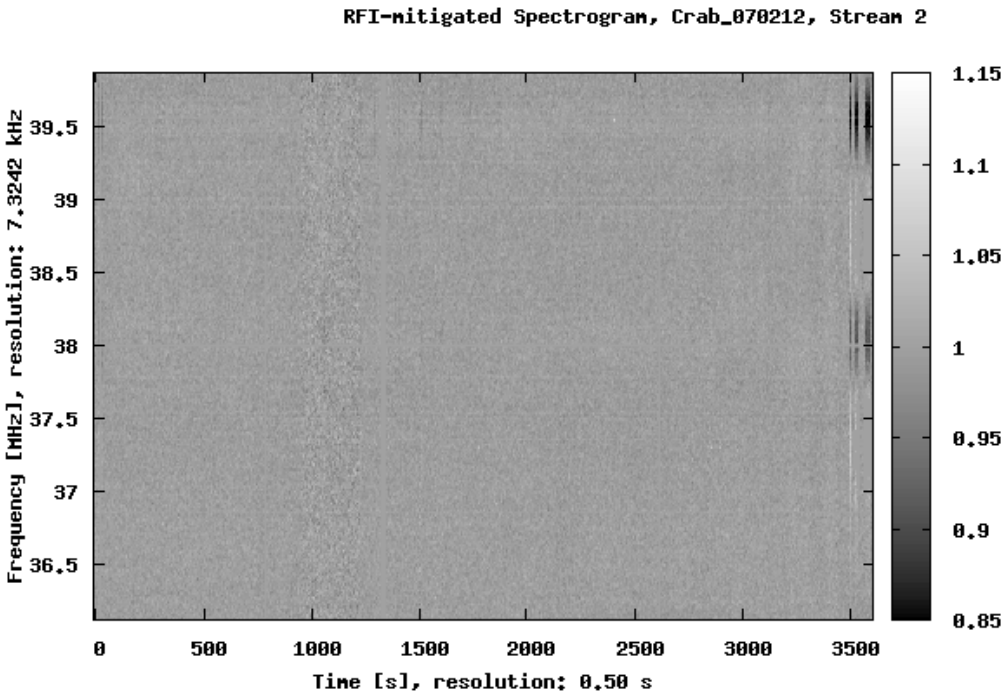

Figure 4.10: Spectrogram with RFI mitigation, stream 2 (6Y).

removal of the wobble.

- **Incoherent Combining of the Streams:** Figures 4.15 and 4.16 show the output of $p10$ after incoherently combining the two streams as described in Section 4.1.9.

- **Inspection for Pulses:** The incoherently-combined time series is inspected using the pulse detection algorithm from Section 4.1.10. Table 4.6 shows the output of $p14$. The estimated flux was found by scaling the minimum detectable flux by the detection metric.

- **Follow-up DM Search:** As seen in Table 4.6, there is a $\sim 4.5\sigma$ detection at a trial pulse length of 1 s. A close-up of this pulse candidate is shown in Figure 4.17. The candidate seems to have a width of $\sim$2 s, which is well within the limits for a CGP mentioned in Section 4.1.7. The candidate pulse was further investigated by doing a follow-up DM search until the detection metric decreased at least by a factor of 2. The result is shown in Figure 4.18. The DM resolution was obtained from Equation A.5 in Appendix A, giving 1.109×10^{-3} pc cm^{-3}. It is seen that the peak DM value is obtained at trial pulse length

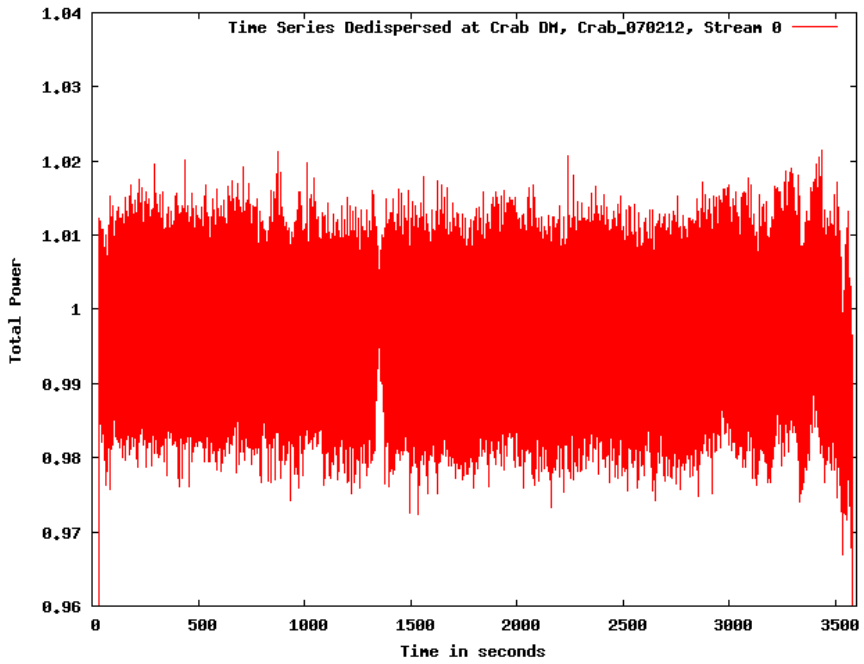

(a) Time resolution = 8.7381 ms

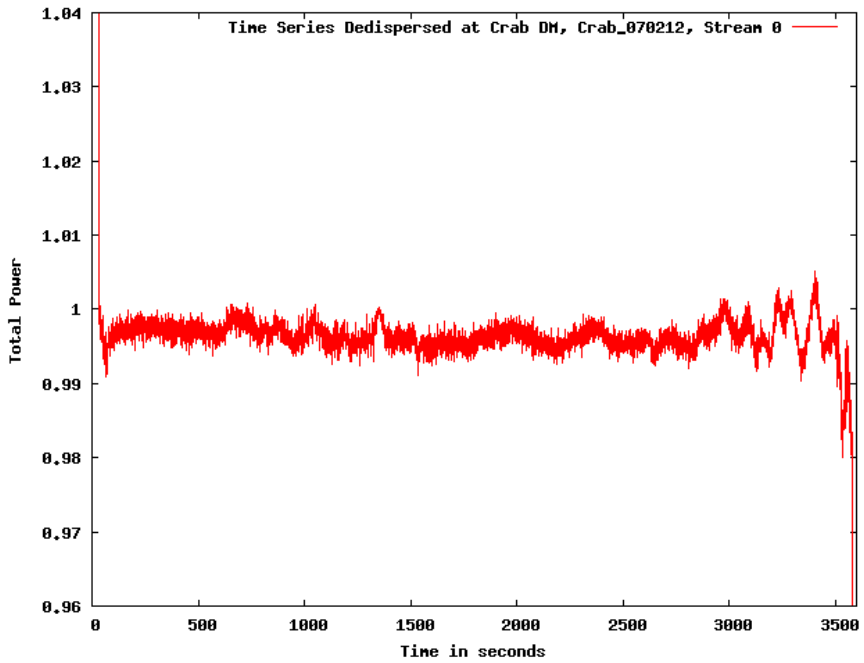

(b) Time resolution = 498 ms

Figure 4.11: Dedispersed time series at various time resolutions, stream 0 (6B).

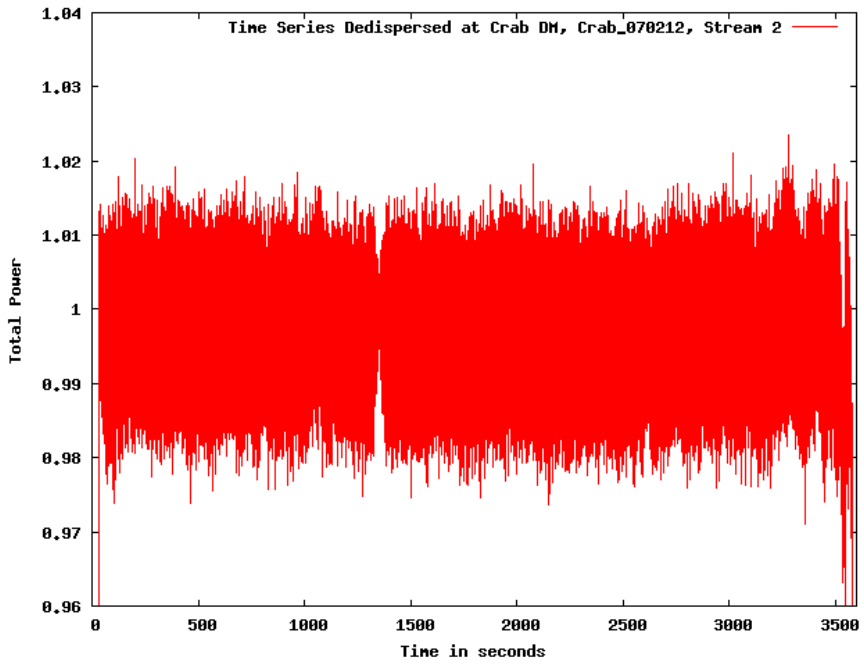

(a) Time resolution = 8.7381 ms

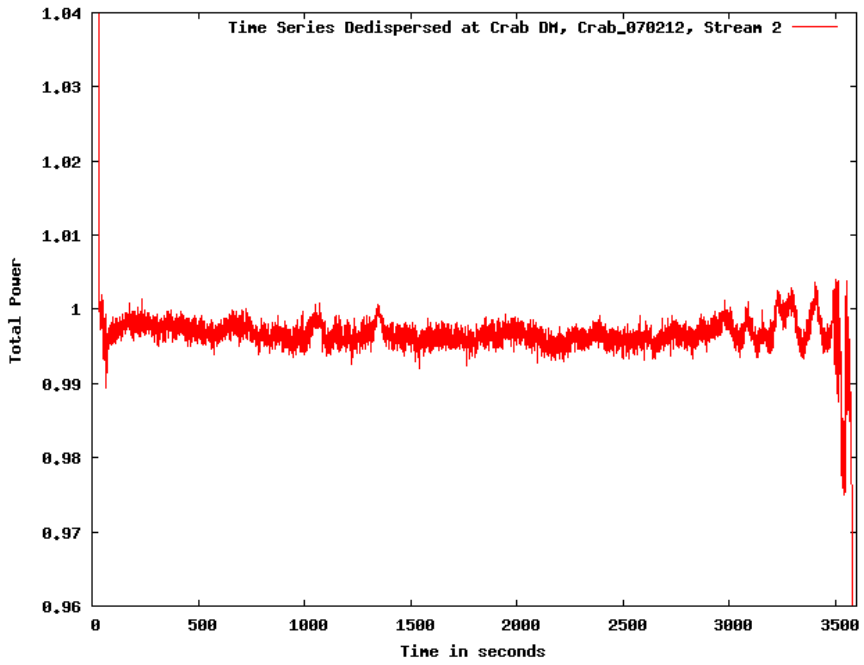

(b) Time resolution = 498 ms

Figure 4.12: Dedispersed time series at various time resolutions, stream 2 (6Y).

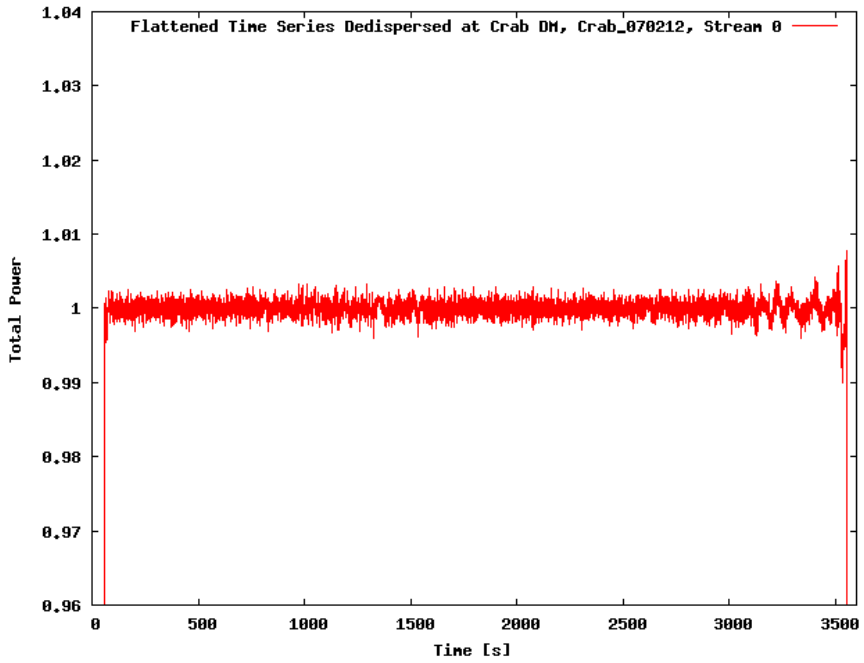

Figure 4.13: Dedispersed time series after removal of baseline wobble, stream 0 (6B)

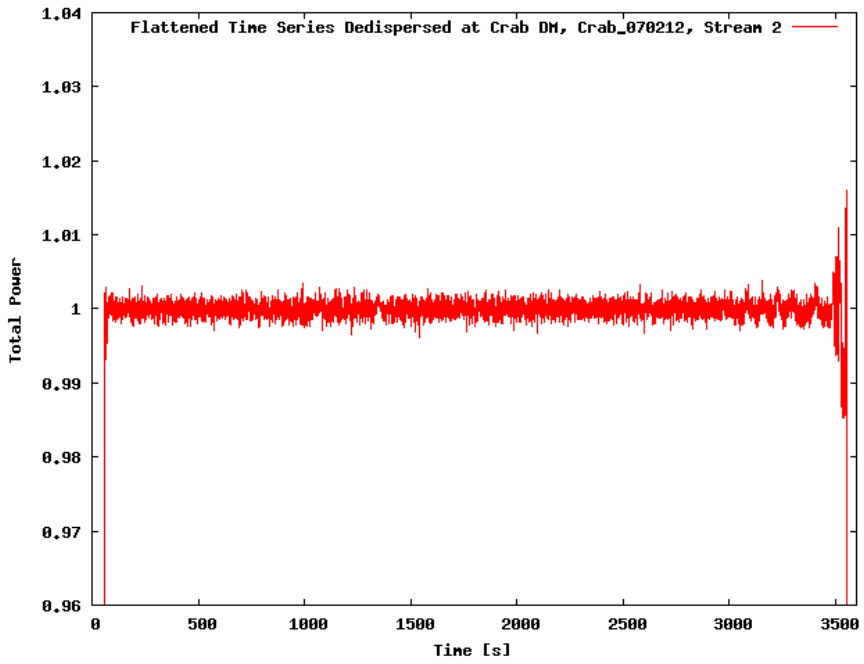

Figure 4.14: Dedispersed time series after removal of baseline wobble, stream 2 (6Y).

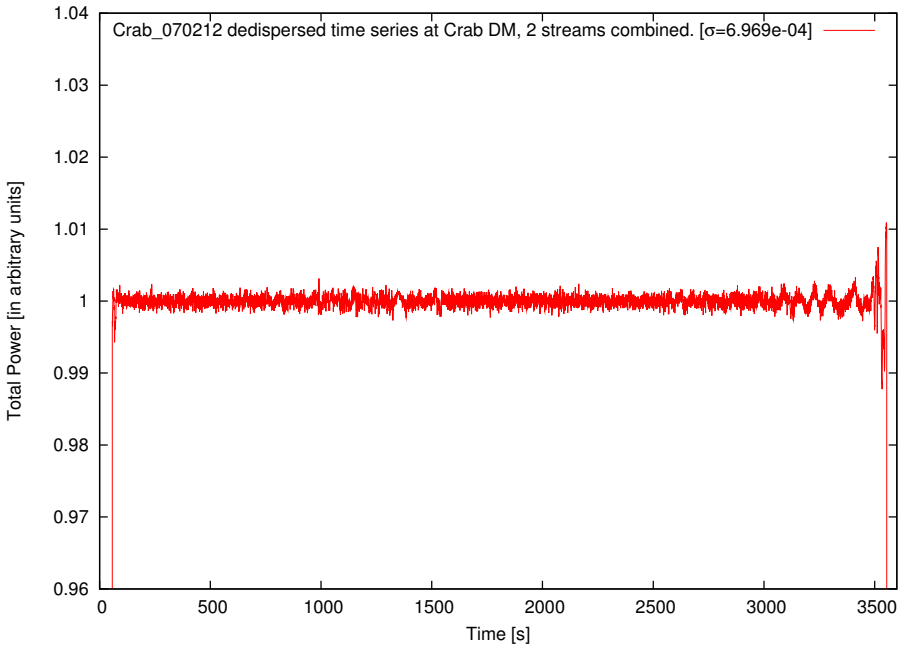

Figure 4.15: Dedispersed time series at Crab DM, 2 streams combined.

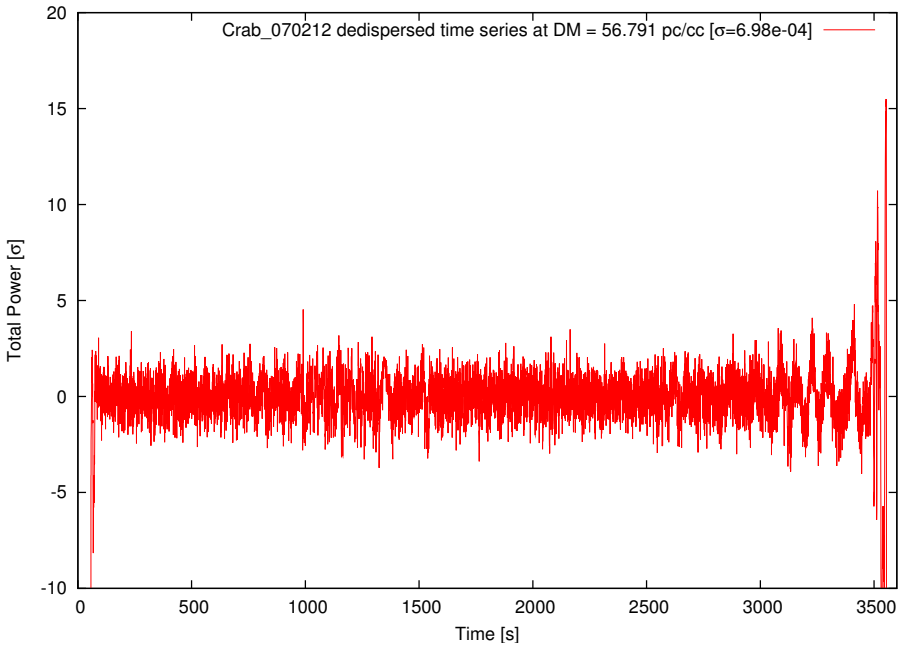

Figure 4.16: Same as Figure 4.15 but with power now expressed in terms of σ.

Table 4.6: Detections at Crab DM = 56.791 pc cm^{-3}.

Trial Pulse Length [s]	Max Detection [σ_l]	Event Time [s]	Estimated Flux [Jy]	Expected Rate [h^{-1}]	Follow-up DM Sweep Test
2.00	4.5	990.7	661	2.34×10^{-2}	Failed
1.00	4.4	235.6	915	1.73×10^{-2}	Passed

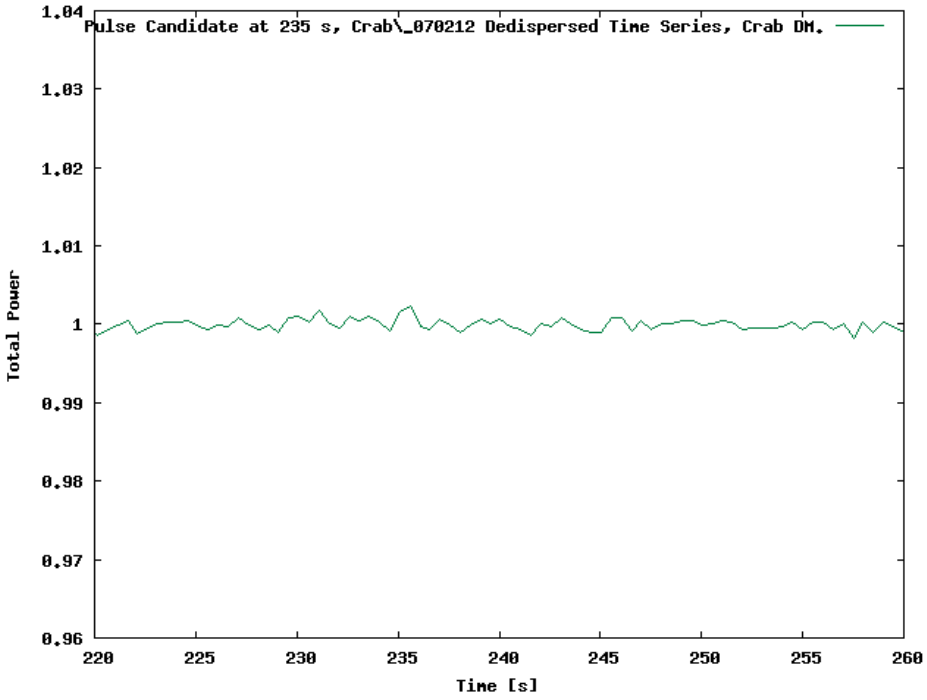

Figure 4.17: Close-up of the candidate pulse at 235.6 s from Figure 4.15.

equal to 1 s, and it lies between the Crab DM and 56.902 pc cm^{-3}, which is still within 0.2% of the Crab DM value. Based on these observations, this pulse candidate cannot be ruled out as a CGP. In contrast, the follow-up DM search done on the second detection (at 990.7 s), shown in Figure 4.19, does not peak at the Crab DM, and thus is ruled out as a CGP candidate.

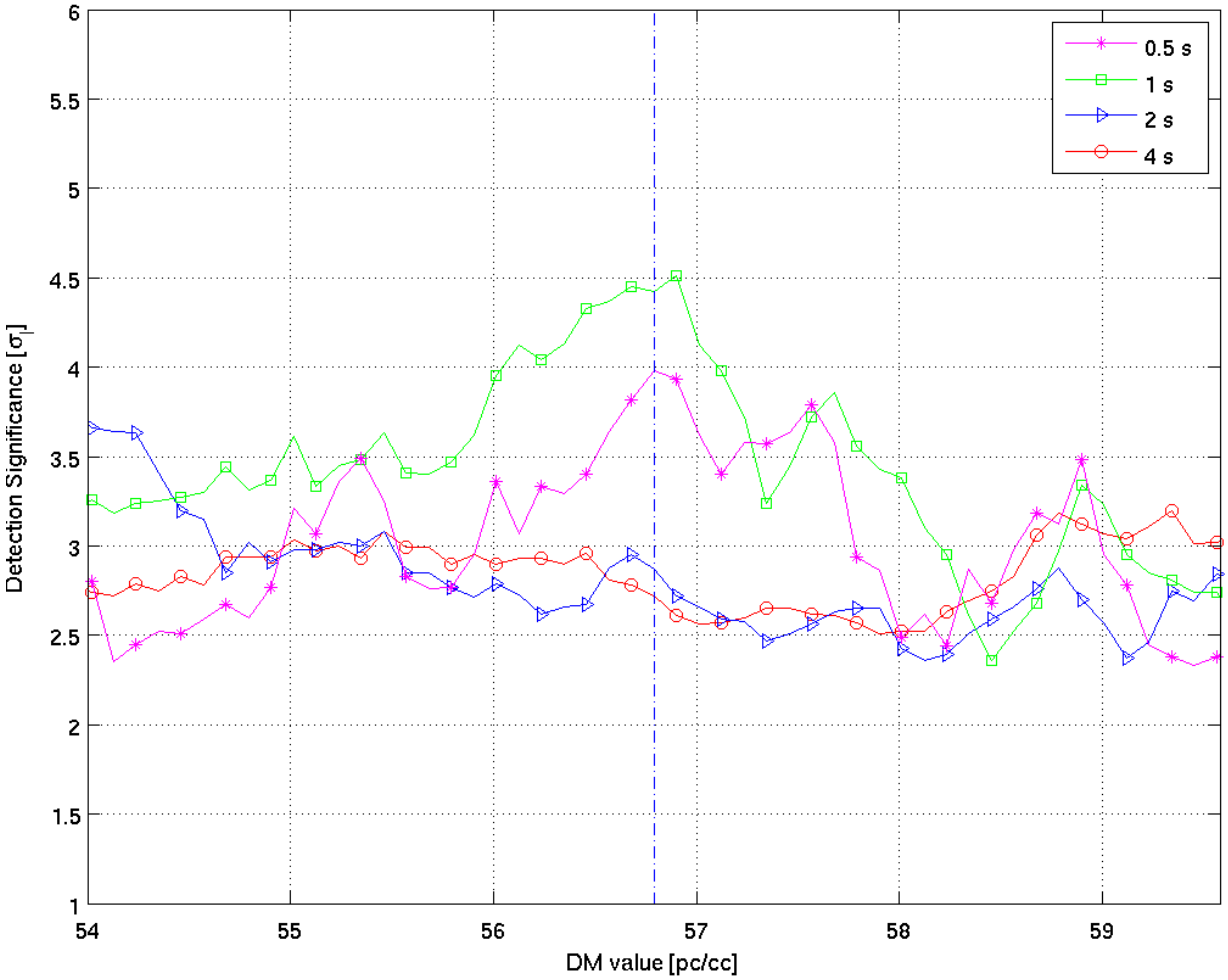

Figure 4.18: Results of DM sweep for the detection at 235.6 s. Curves represent different trial pulse lengths. Vertical dashed line is 56.791 pc cm^{-3} (Crab DM).

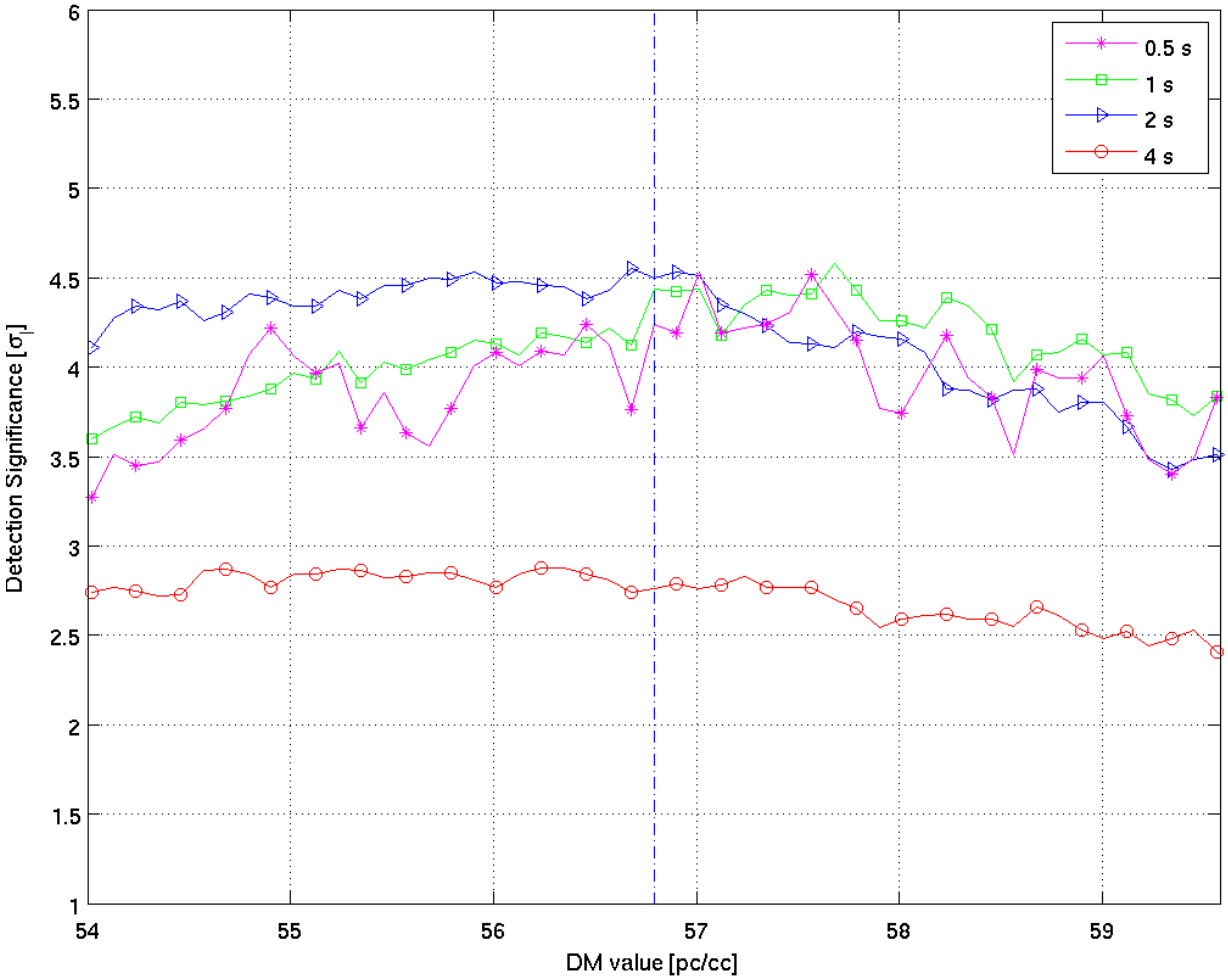

Figure 4.19: Results of DM sweep for the detection at 990.7 s. Curves represent different trial pulse lengths. Vertical dashed line is 56.791 pc cm^{-3} (Crab DM).

Chapter 5

Crab Giant Pulse Campaign

In this chapter, we present the results of one of the search campaigns by ETA, the Crab giant pulse (CGP) search campaign. The datasets analyzed in this campaign are introduced in Section 5.1 ("Introduction"). The results are presented in Section 5.2 ("Results").

5.1 Introduction

In this thesis, we consider observations made at 38 MHz with ETA as a part of the CGP search campaign. We collected about 24.6 hours of data during the campaign, as indicated in Table 3.3. The datasets collected are listed in Table D.1 in Appendix D. We analyzed 23.6 hours of data of which about 40% were determined to be unusable due to RFI, and hence were not processed further. The remaining 14 hours of data, as indicated in Table 5.1, were searched for CGPs using the targeted DM pulse search toolchain described in Chapter 4. In the following section, we present the results.

Table 5.1: Summary of ETA CGP search campaign. Antennas excluded from the analysis are written in parentheses. Additional detail about each dataset can be found in Table D.1.

Dataset	SNR	Detected Pulse Width [s]	1 σ sensitivity [Jy]	Estimated Flux	Expected Rate of Occurrence [hr^{-1}]	Observation Time [hr]	Detections per hour	Antennas
Crab_070212	4.4	1	208	915	1.73×10^{-2}	1	1	6B, 6Y
Crab_070218	No detections					0.75	0	2B, 6B
Crab_070221	No detections					0.75	0	2B, 6B
Crab_070228b	4.4 3.3	0.5 0.5	400	1760 1320	4.34×10^{-2} 7.58×10^{-2}	1	2	6Y
Crab_070323	4.2 3.5	0.5 0.5	207	869 724	8.60×10^{-2} 7.13×10^{-1}	0.5	4	1B,4B,6B,2B
Crab_070324	3.3	0.5	292	964	7.12×10^{-2}	1	1	1B, 6B, (4B, 2B)
Crab_070326	4.0	0.5	292	1168	1.79×10^{-1}	1	1	1B, 6B, (4B, 2B)
071118_0600	4.2	0.5	129	542	1.03×10^{-1}	1	1	1B, 8B, 6B, 2B, 9B, 4Y, 3Y, (1Y)
071118_0845	No detections					0.5	0	1B, 8B, 6B, 2B, 9B, 4Y, 3Y, (1Y)
071120_0200	No detections					1	0	1B, 2B, 1B, 8B, 6B, 2B
071124_0200	3.6	0.5	153	551	4.87×10^{-1}	0.75	1.33	8B, 6B, 2B, 9B, 4Y, 1Y, 3Y, (1B)
071201_0100	No detections However, see Section 5.2.2					1	0	1B, 8B, 6B, 2B, 9B, 4Y, 1Y, 3Y
071202_0056	5.3	0.5	156	827	4.76×10^{-4}	0.95	1	1B, 8B, 6B, 2B, 4Y, 1Y, 3Y, (9B)
071203_0052	No detections					1	0	1B, 8B, 6B, 2B, 9B, 4Y, 1Y, 3Y
071204_0048	No detections					1	0	1B, 8B, 6B, 2B, 9B, 4Y, 1Y, 3Y
071205_0044	3.7	0.5	156	577	3.82×10^{-1}	0.95	1	8B, 6B, 2B, 9B, 4Y, 1Y, 3Y, (9B)

5.2 Results

In this section, we present additional detail on results and the analysis of these results. A total of 11 detections in the 16 datasets satisfied the DM sweep test criterion for CGPs. We discuss these detections in the following section. In Section 5.2.2, we present an interesting case of CGP detection not included in these 11 detections.

5.2.1 CGP Fluxes and Detection Rate

The estimated fluxes depend on the antenna temperature at the time of observation as explained in Section 3.2.3. They are found to range from 542 Jy to 1760 Jy. These detections are further summarized in Table 5.2. The DM sweep test for each detection and the time series dedispersed at the Crab DM for the corresponding dataset are shown in Figures 5.1 to 5.11. Appendix E lists the calibrated and RFI-mitigated spectrograms for all the streams in the corresponding datasets.

The detection rate is determined to be around 1.35 hr^{-1}. The expected rate of occurrence of pulses can be estimated as follows. Argyle and Gower (1972) proposed that CGP intensities are distributed according to $N = (500 \times 60)S^{-2.5}$, where N is the number of pulses per hour stronger than S (in units of average pulse energy) [58]. From 74 MHz observations, the flux of the Crab pulsar is 85 ± 3 Jy [59]. Following Bhat *et al.* (2005), if the power-law variation with the frequency at lower frequencies is taken to be $\nu^{+2.7\pm0.1}$ [5], the average pulse energy of a Crab pulse at 38 MHz is 14 ± 0.5 Jy. Thus, pulses at 38 MHz with flux density of 929 Jy, which is ≈ 66 times the mean flux density, are expected to occur at a rate of ≈ 0.85 hr^{-1}. The rate we found from our observations (1.35 hr^{-1}) is larger but close to this prediction. This increases confidence that we are detecting CGPs.

We compare our detection with other CGP observations at different frequencies in Figure 5.12. The peak flux density of the detections by Popov *et al.* at 23 MHz is 150 Jy in 12 hours [4], and those by Bhat *et al.* at 200 MHz is 50 kJy in 1 hour [5]. Log-linear extrapolation between these two values yields an expected peak flux density for CGP detections at 38 MHz of 576 Jy over about 1 hour duration. Deviations from the extrapolated CGP flux at 38 MHz can be explained by the fact that the CGP flux values are known to vary considerably. The tail statistics of the CGP distribution is not completely understood. Thus, the flux densities could be arbitrarily large at any of these frequencies. Furthermore, the minimum detectable flux by ETA is comparable to the extrapolated value. Therefore, it is not surprising that we detect

Table 5.2: Summary of CGP detections by ETA. Detections per hour ($\triangleq$ (Total Number of Detections)/(Total Observation Length in hours)) is indicated for the entire CGP search campaign.

Estimated Flux [Jy]	SNR	Dataset	Figure
1760	4.4	Crab_070228b	5.2
1320	3.3	Crab_070228b	5.3
1168	4.0	Crab_070326	5.7
964	3.3	Crab_070324	5.6
915	4.4	Crab_070212	5.1
896	4.2	Crab_070323	5.4
827	5.3	071202_0056	5.10
724	3.5	Crab_070323	5.5
577	3.7	071205_0044	5.11
551	3.6	071124_0200	5.9
542	4.2	071118_0600	5.8
Mean Flux: 929 Jy. Median Flux: 869 Jy. Standard Deviation of Flux: 371 Jy.			
Detections per hour: 1.35			

pulses primarily above this value.

5.2.2 071201_0100 Discussion

In this section, we present a special case of CGP candidate detected. This candidate is not included in the 11 detections discussed in the previous section. It was found in dataset 071201_0100 after combining antennas 9B, 4Y, 3Y and 1Y. It is shown in Figures 5.13 and 5.14. Figure 5.15 shows the result of DM sweep test for the same candidate. The peak DM value for the pulse lies between the Crab DM and 56.902 pc cm^{-3}, which is within 0.2% of the Crab DM value. Although the DM sweep suggests that this detection could probably be one of the best CGP candidates we detected, the pulse disappears when the outputs from the remaining four antennas are combined incoherently. This either could be due to some defect in the combining procedure or the candidate is a spurious detection.

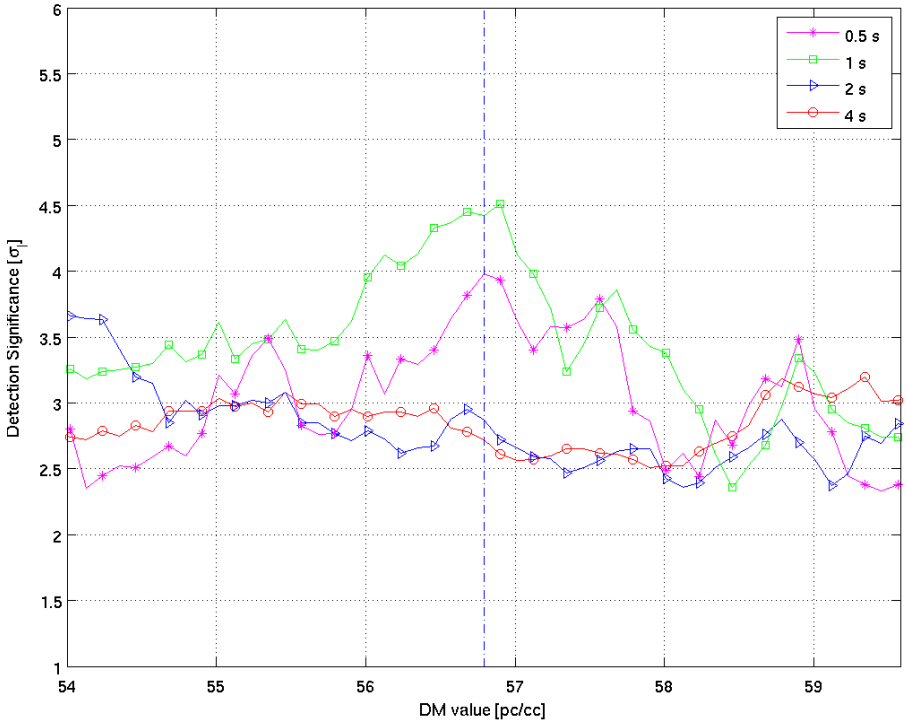

(a) Results of DM search. Dashed line represents 56.791 pc cm^{-3} (Crab DM).

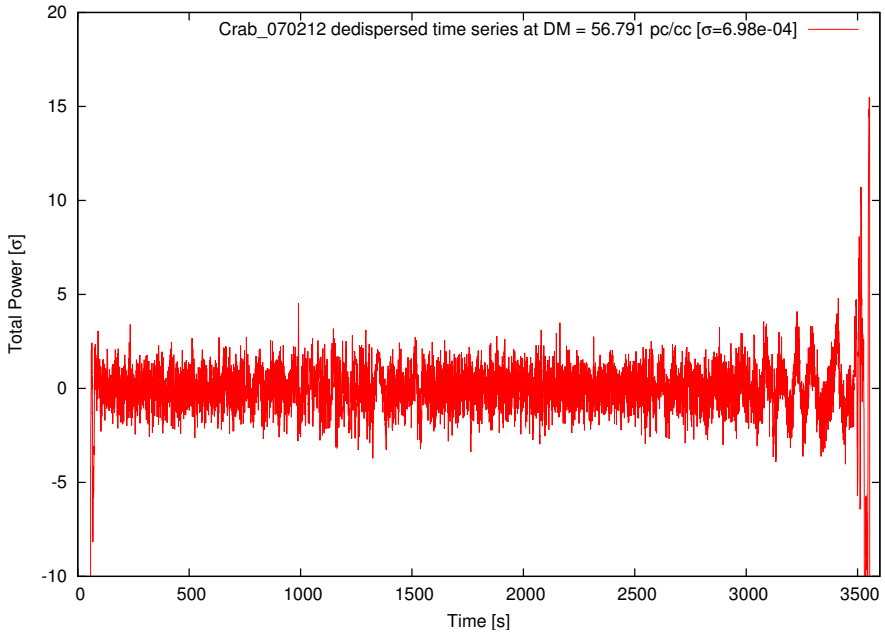

(b) Dedispersed time series. Detection at 235.6 s. Time resolution: 0.5 s.

Figure 5.1: CGP Candidate (SNR = 4.4) from Crab_070212.

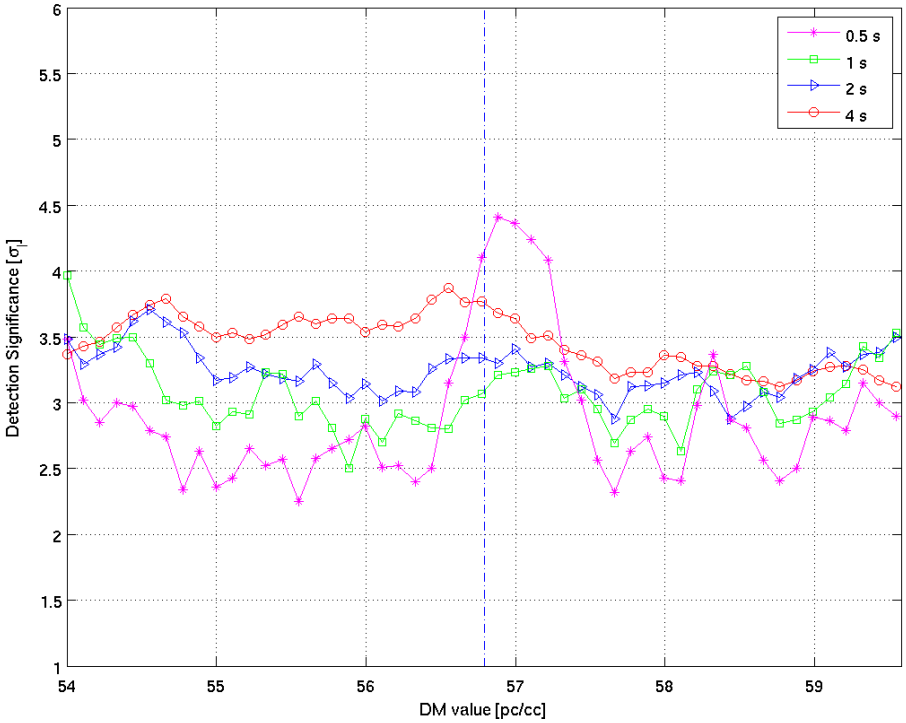

(a) Results of DM search. Dashed line represents 56.791 pc cm^{-3} (Crab DM).

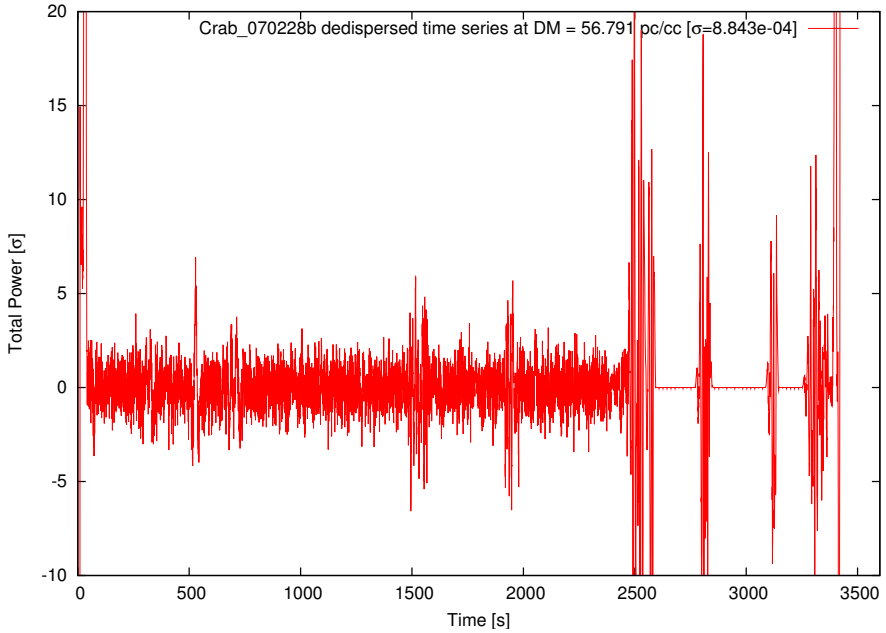

(b) Dedispersed time series. Detection at 260.5 s. Time resolution: 0.5 s.

Figure 5.2: CGP Candidate (SNR = 4.4) Crab_070228b.

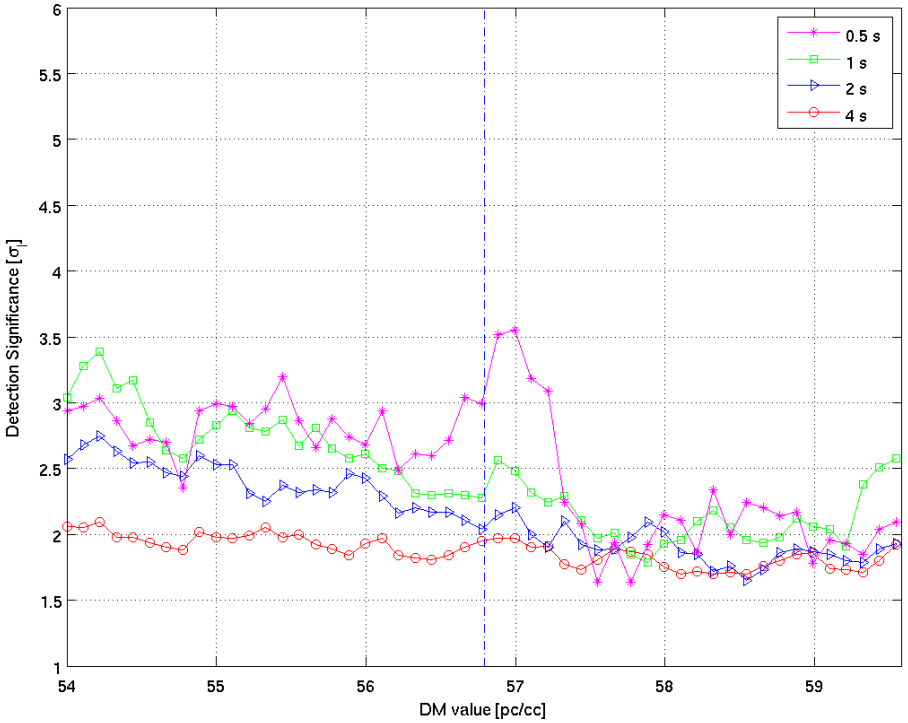

(a) Results of DM search. Dashed line represents 56.791 pc cm^{-3} (Crab DM).

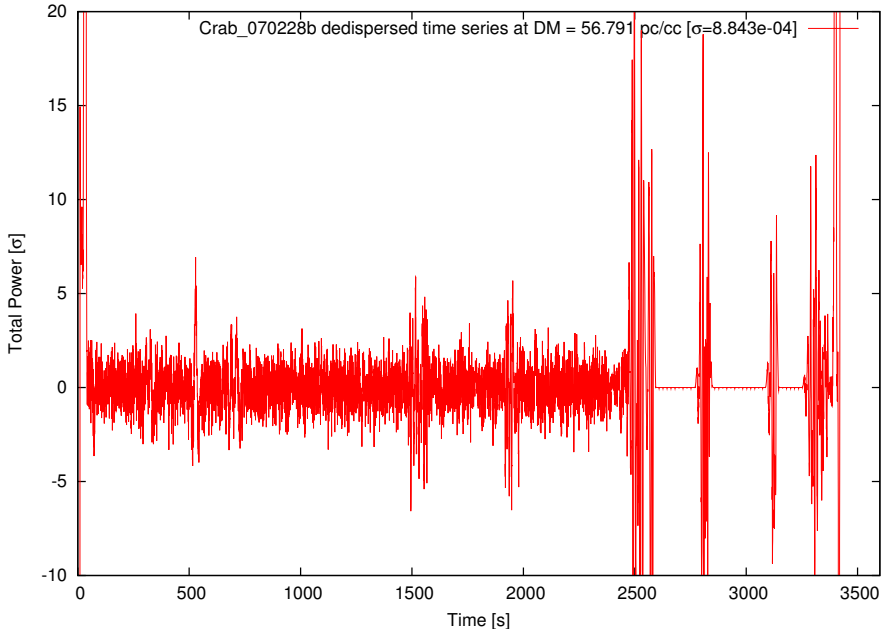

(b) Dedispersed time series. Detection at 2111.8 s. Time resolution: 0.5 s.

Figure 5.3: CGP Candidate (SNR = 3.3) Crab_070228b.

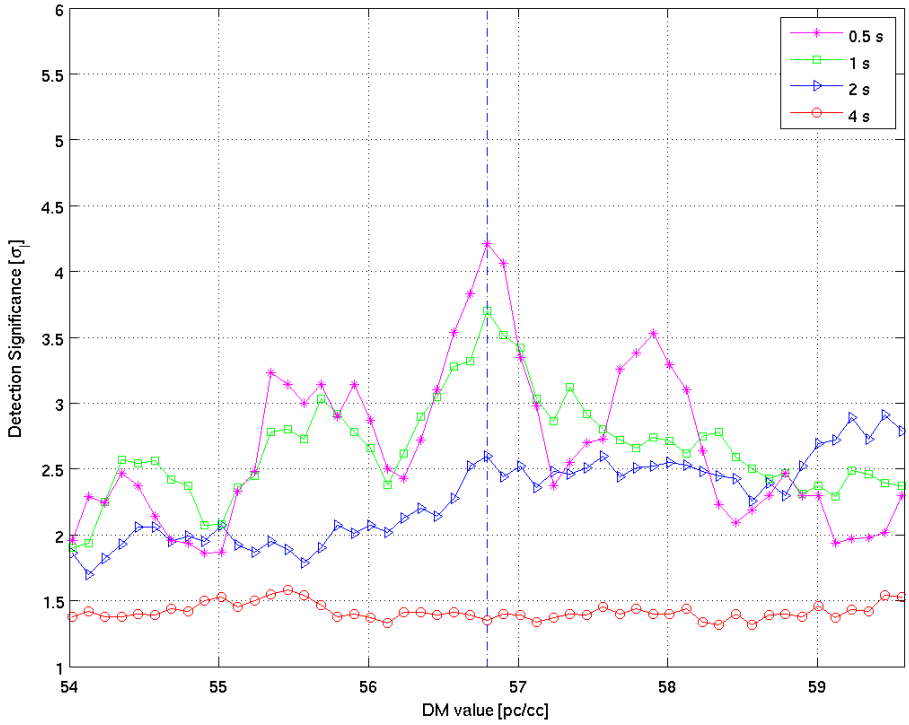

(a) Results of DM search. Dashed line represents 56.791 pc cm^{-3} (Crab DM).

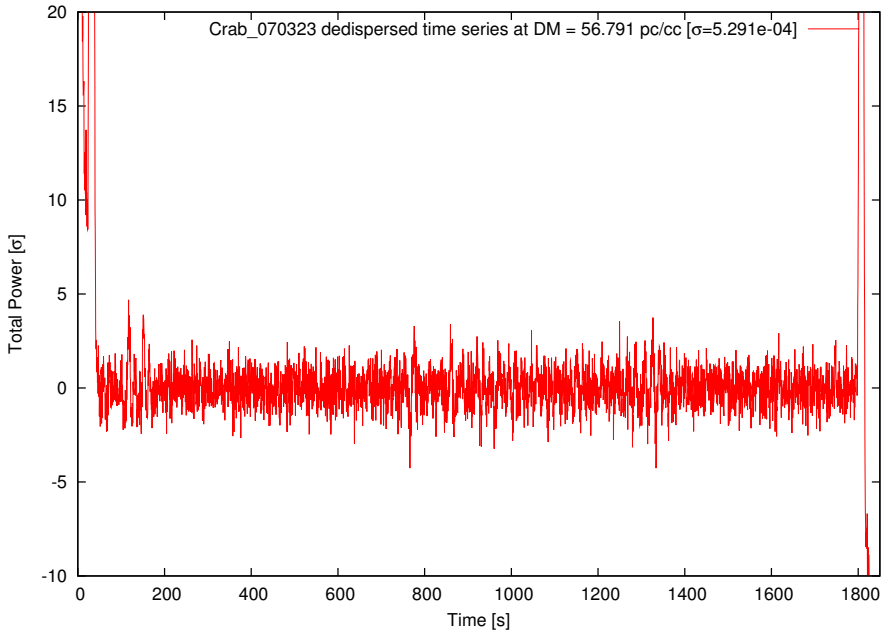

(b) Dedispersed time series. Detection at 1249.6 s. Time resolution: 0.5 s.

Figure 5.4: CGP Candidate (SNR = 4.2) Crab_070323.

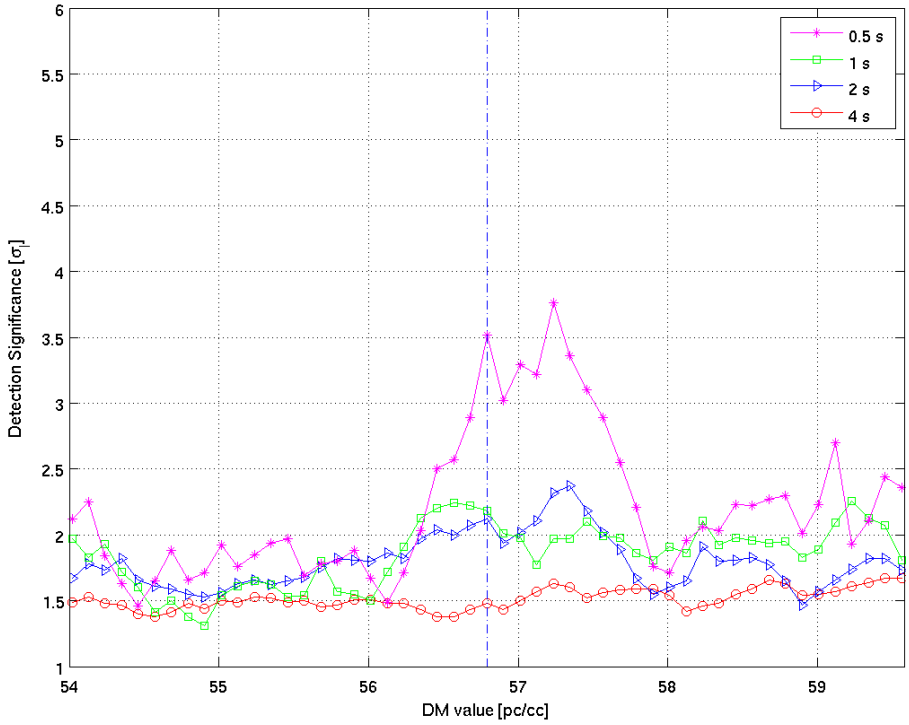

(a) Results of DM search. Dashed line represents 56.791 pc cm^{-3} (Crab DM).

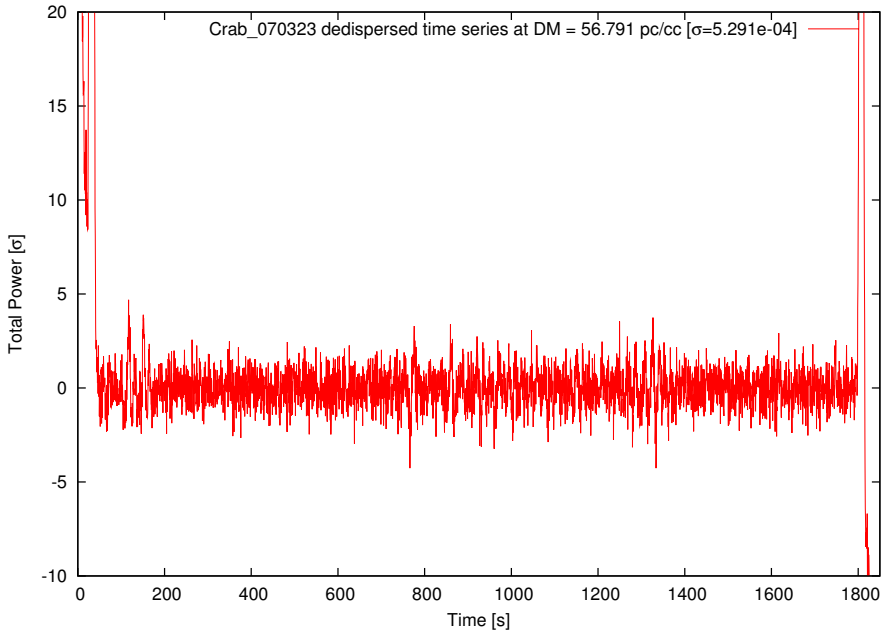

(b) Dedispersed time series. Detection at 1046.4 s. Time resolution: 0.5 s.

Figure 5.5: CGP Candidate (SNR = 3.5) Crab_070323.

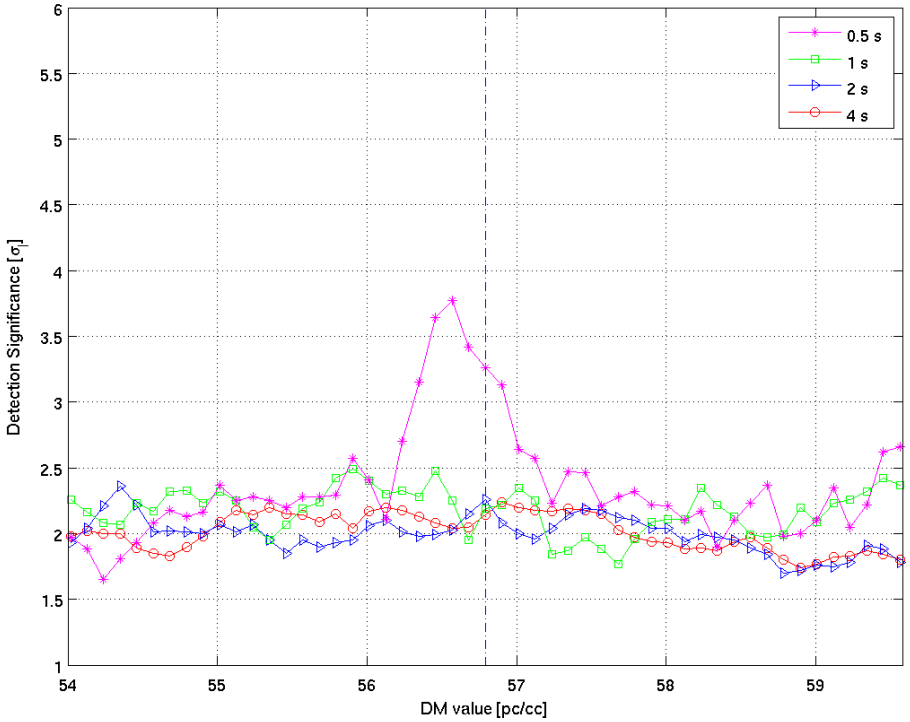

(a) Results of DM search. Dashed line represents 56.791 pc cm^{-3} (Crab DM).

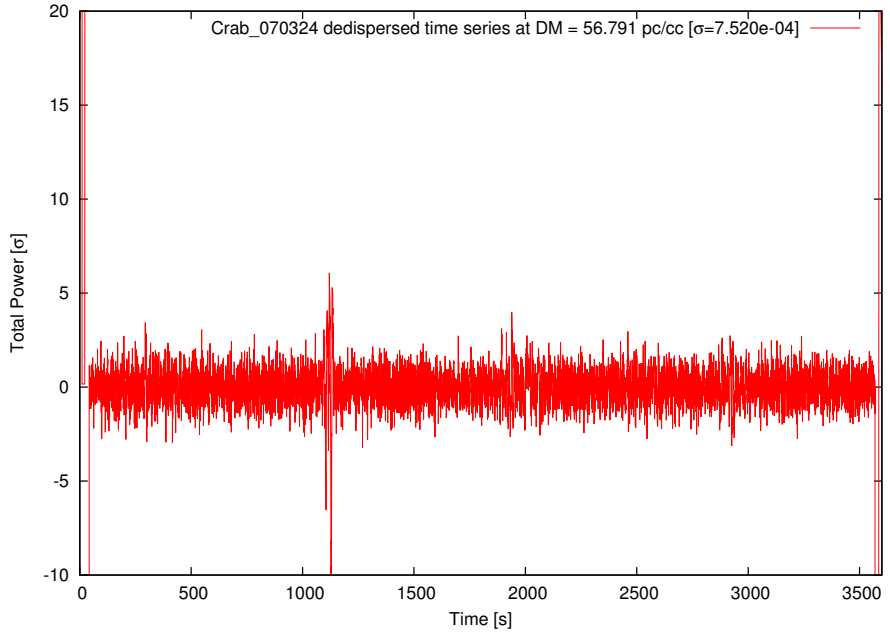

(b) Dedispersed time series. Detection at 546.9 s. Time resolution: 0.5 s.

Figure 5.6: CGP Candidate (SNR = 3.3) Crab_070324.

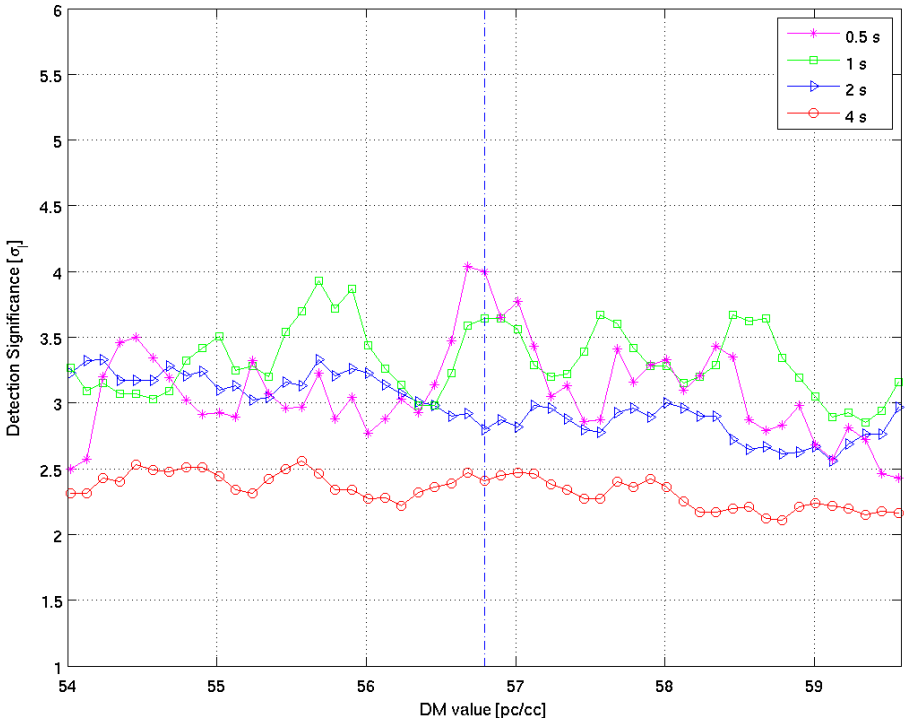

(a) Results of DM search. Dashed line represents 56.791 pc cm^{-3} (Crab DM).

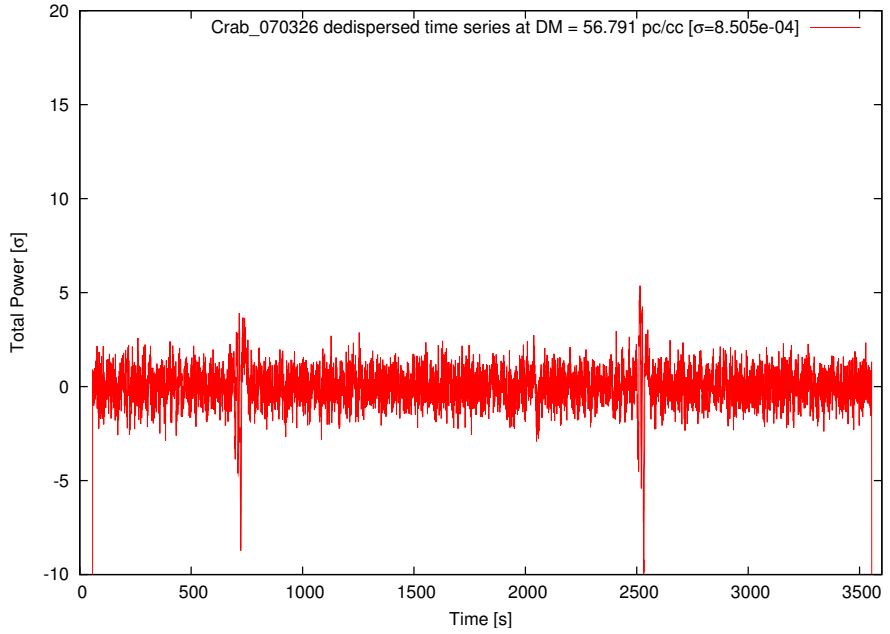

(b) Dedispersed time series. Detection at 2407.7 s. Time resolution: 0.5 s.

Figure 5.7: CGP Candidate (SNR = 4.0) Crab_070326.

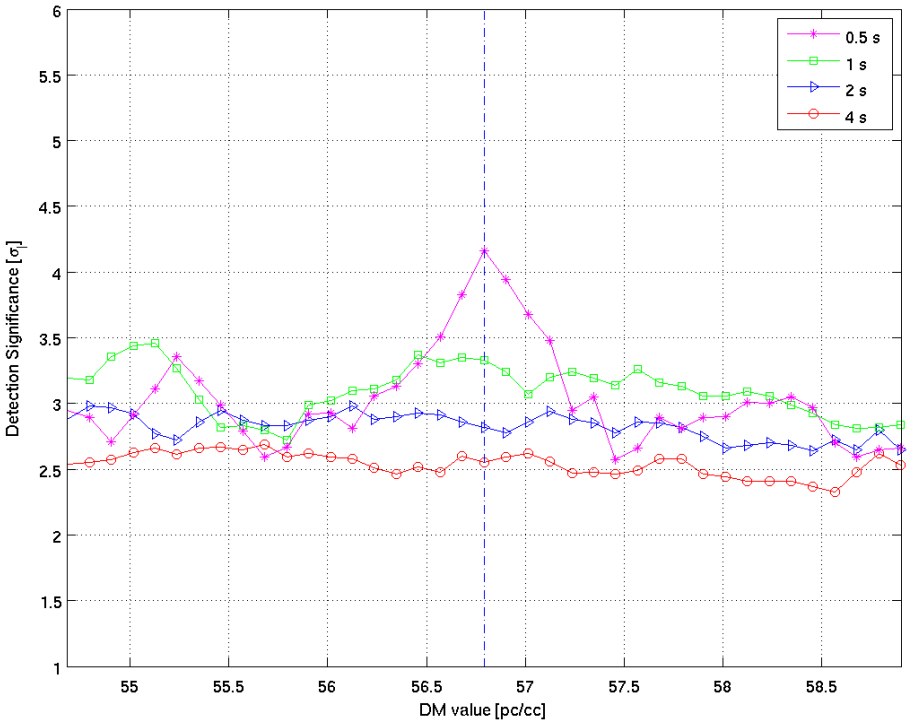

(a) Results of DM search. Dashed line represents 56.791 pc cm^{-3} (Crab DM).

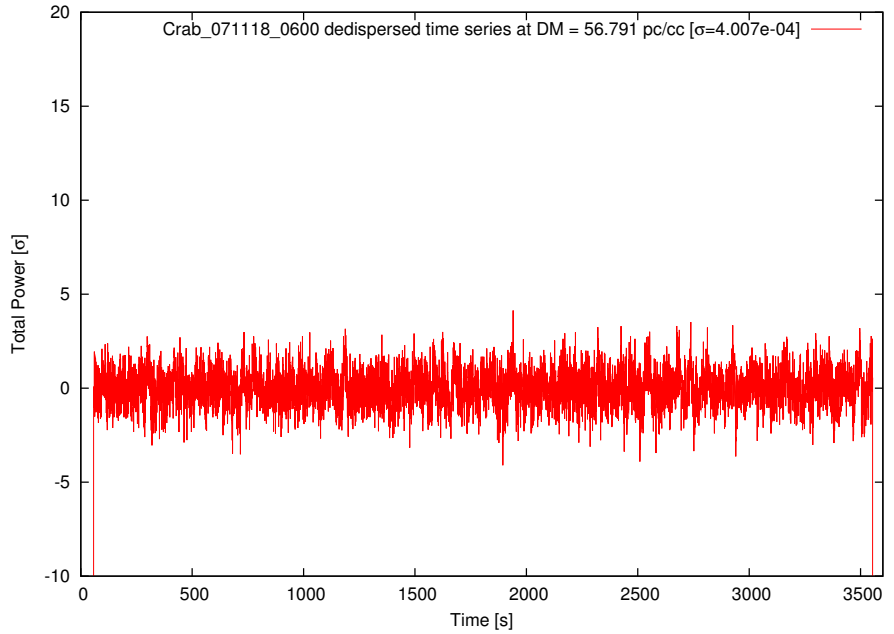

(b) Dedispersed time series. Detection at 1940.5 s. Time resolution: 0.5 s.

Figure 5.8: CGP Candidate (SNR = 4.2) Crab_071118_0600.

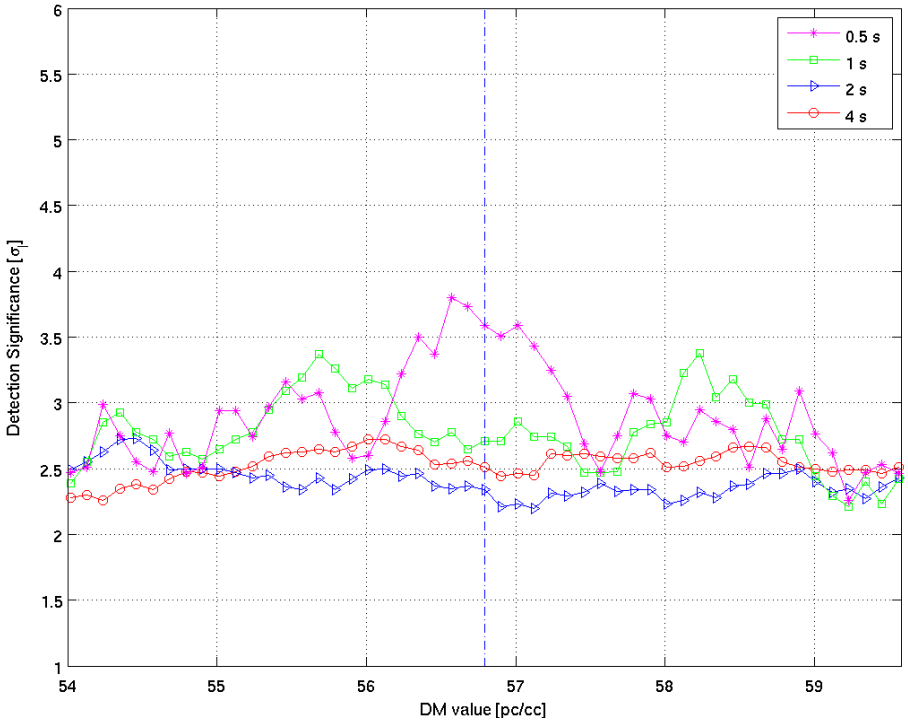

(a) Results of DM search. Dashed line represents 56.791 pc cm^{-3} (Crab DM).

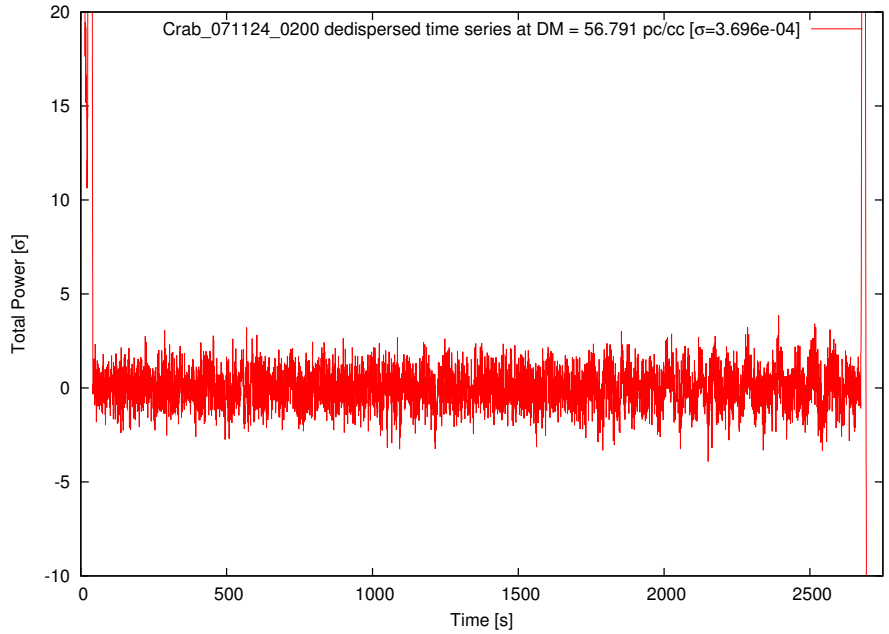

(b) Dedispersed time series. Detection at 2392.7 s. Time resolution: 0.5 s.

Figure 5.9: CGP Candidate (SNR = 3.6) Crab_071124_0200.

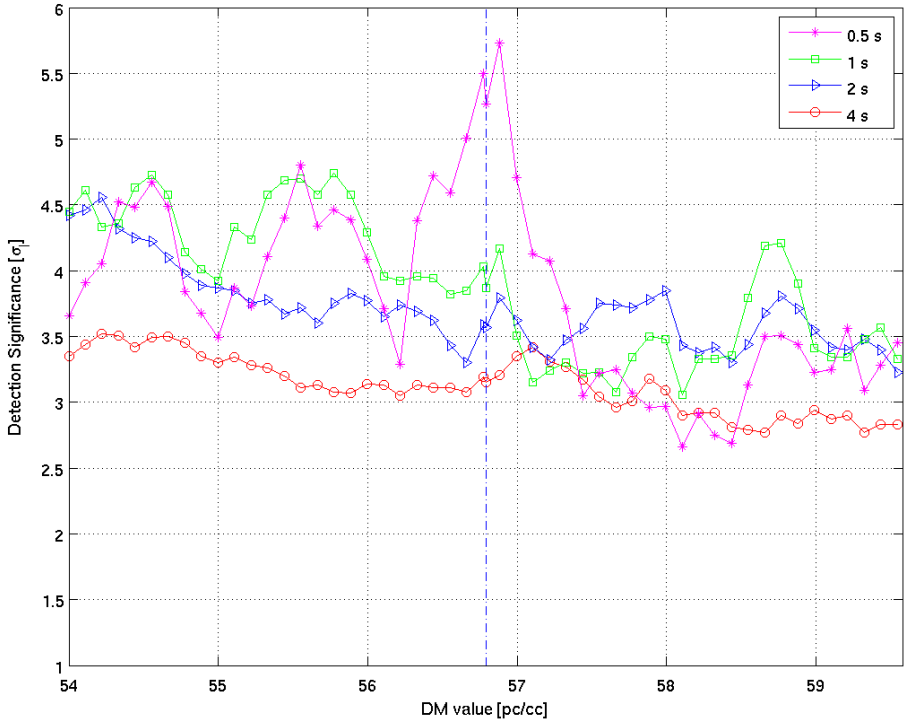

(a) Results of DM search. Dashed line represents 56.791 pc cm^{-3} (Crab DM).

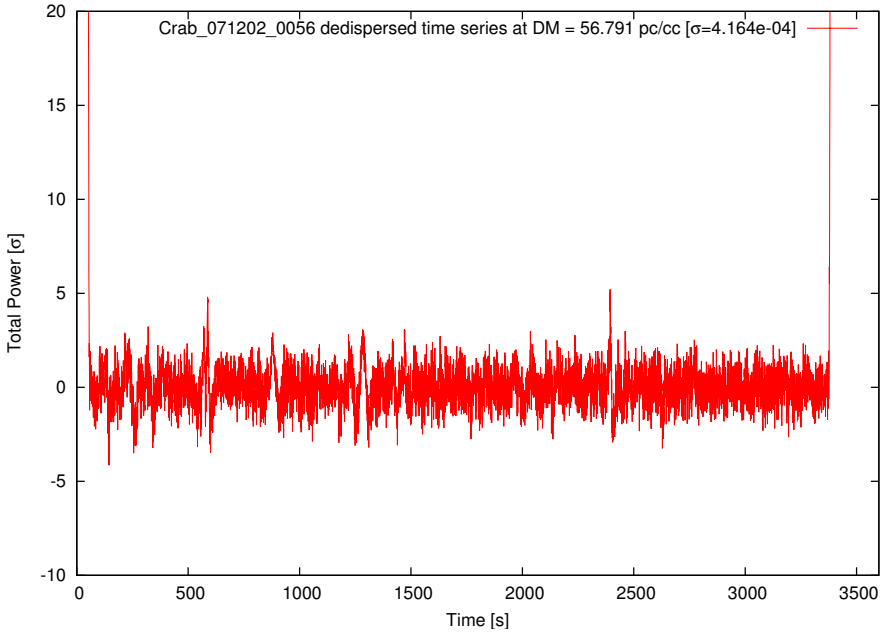

(b) Dedispersed time series. Detection at 320.3 s. Time resolution: 0.5 s.

Figure 5.10: CGP Candidate (SNR = 5.3) Crab_071202_0056.

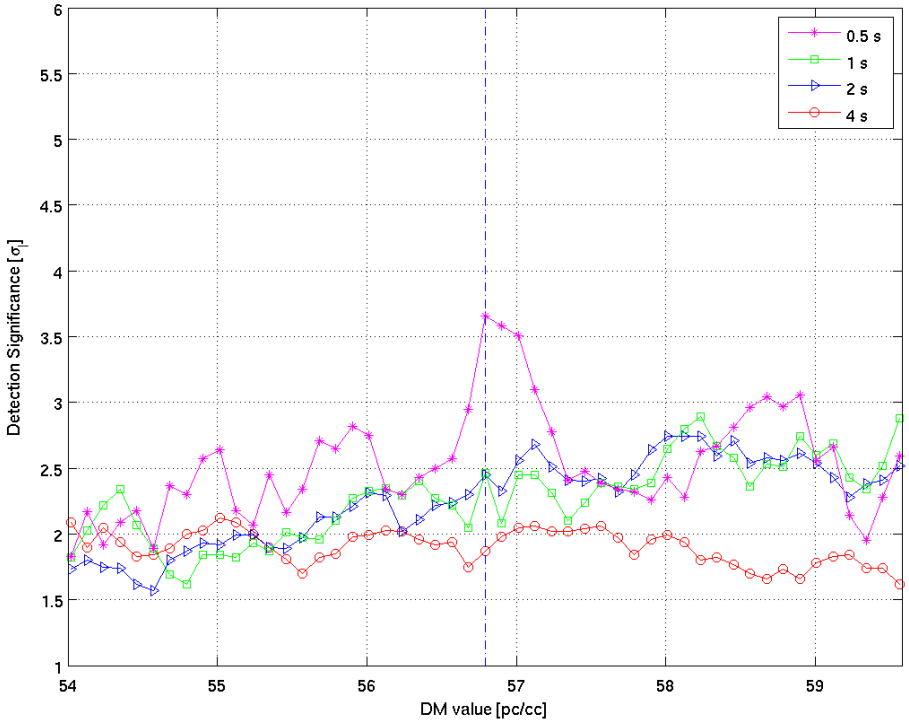

(a) Results of DM search. Dashed line represents 56.791 pc cm^{-3} (Crab DM).

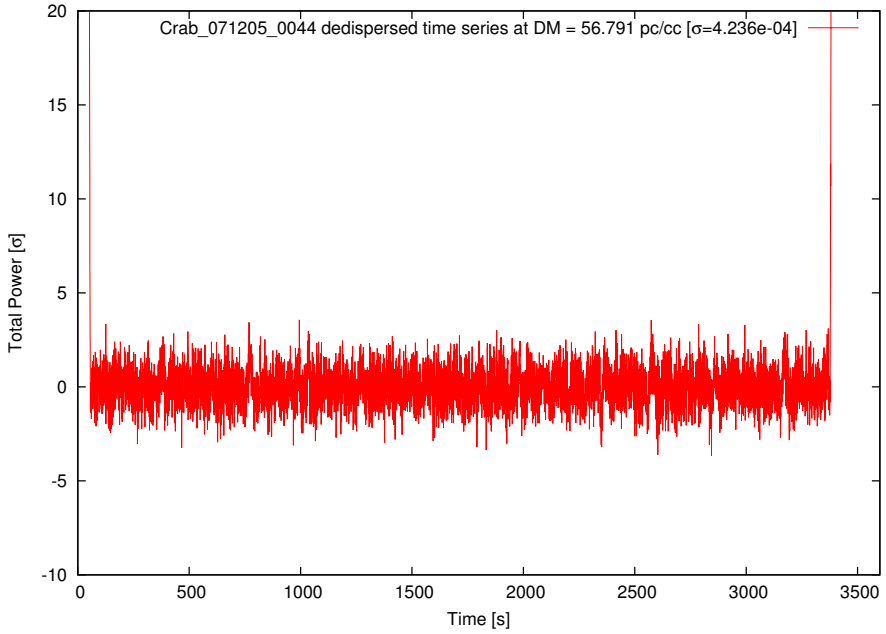

(b) Dedispersed time series. Detection at 125.5 s. Time resolution: 0.5 s.

Figure 5.11: CGP Candidate (SNR = 3.7) Crab_071205_0044.

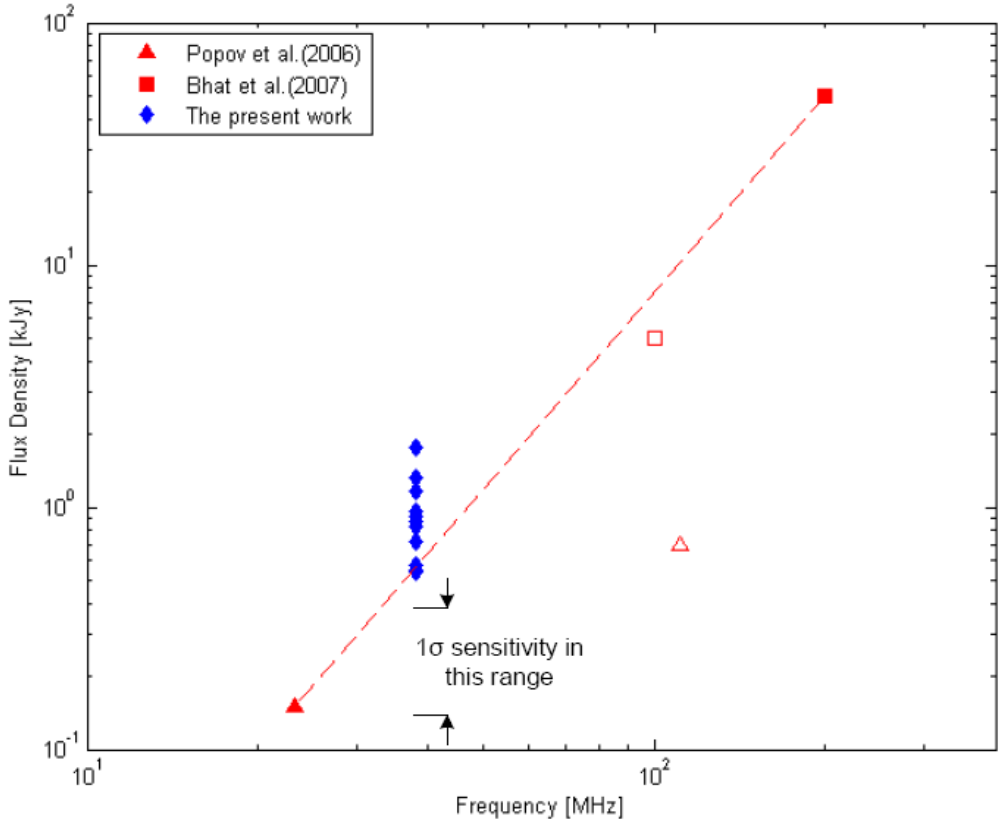

Figure 5.12: Flux densities of CGPs in this campaign compared to peak flux densities of CGP detections at 23 MHz and 200 MHz. The unfilled square at 100 MHz indicates limits derived from a nondetection with MWA-LFD [5], while the unfilled triangle at 111 MHz represents the brightest giant pulse in 15 minutes of observation by Popov *et al.* [4]. The ETA detections are represented by diamonds.

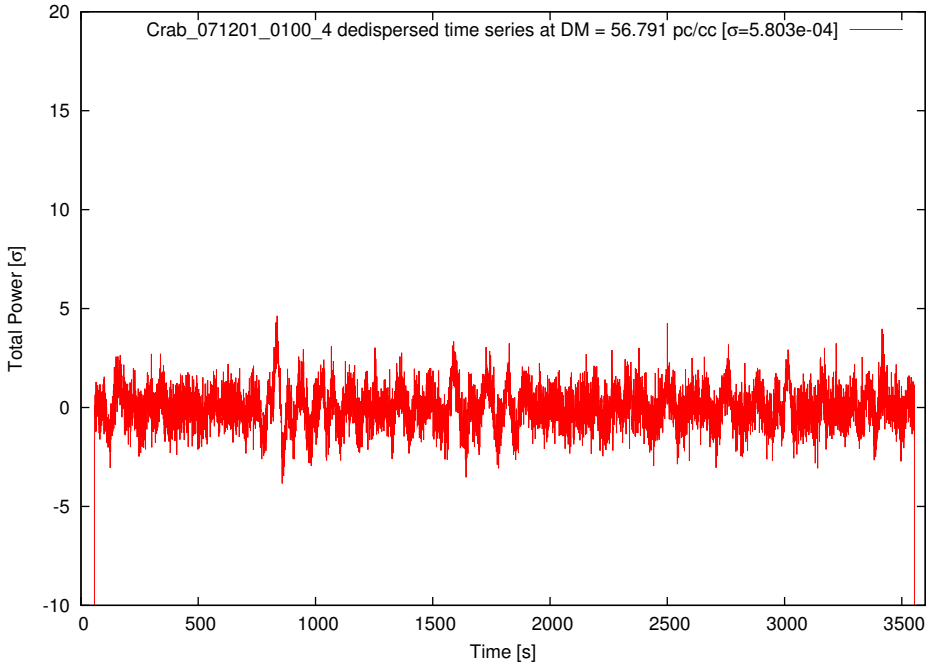

Figure 5.13: One of the best candidate pulses occurred at 2500.3 s in dataset 071201_0100_4.

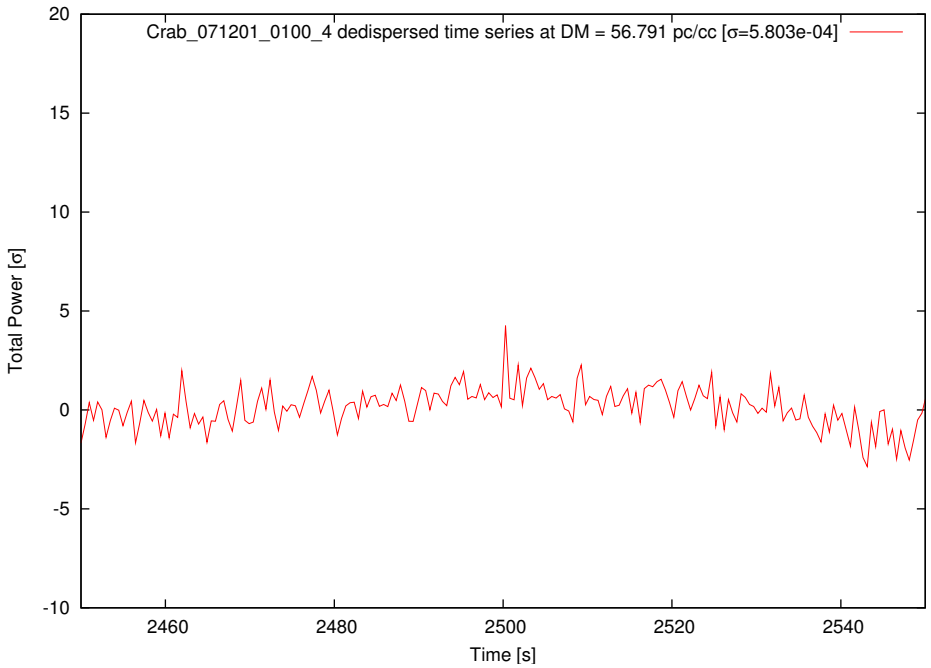

Figure 5.14: Close-up of the candidate pulse at 2500.3 s from Figure 5.13.

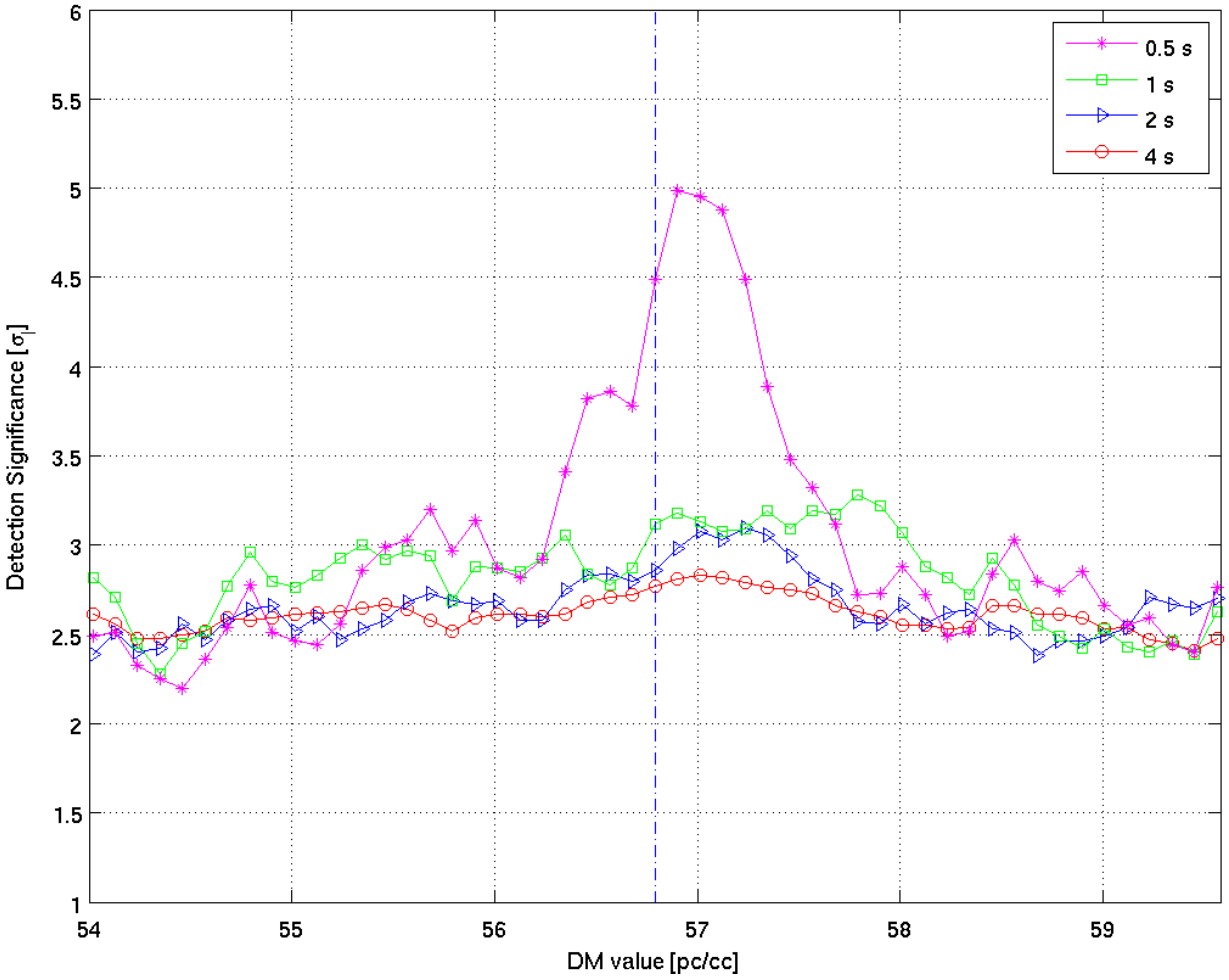

Figure 5.15: Results of DM search for the pulse candidate at 2500.3 s in dataset 071201_0100_4. Dashed line represents 56.791 pc cm^{-3} (Crab DM).

Chapter 6

Conclusions

In this chapter, we conclude the thesis and suggest some improvements. The findings of this work are summarized in Section 6.1 ("Findings"). The topics of future research are discussed in Section 6.2 ("Future Work")

6.1 Findings

In this thesis, we describe the Eight-meter-wavelength Transient Array (ETA) in detail in Chapter 3. The pulse sensitivities of ETA are reported in Table 3.2. The ETA data collection during various search campaigns is summarized in Table 3.3. The Crab giant pulse (CGP) campaign data are analyzed using the toolchain developed for targeted-DM searches. Tables 5.1 and 5.2 present the results. We detected 11 CGP candidates in 14 hours of data. The expected rate of occurrence of CGPs matches approximately with that extrapolated from the known CGP statistics. Thus, although there has not been a single compelling detection (SNR $>$ 6), it is possible that at least a few of these detections are CGPs. Estimated fluxes for detections are consistent with the mean flux density extrapolated at 38 MHz from previous observations. Apart from these 11 detections, we found a really good CGP candidate in one of the datasets. This is described in Section 5.2.2.

6.2 Future Work

The toolchain described in Section 4.1 is useful for searches where the dispersion measure (DM) is known *a priori*. For primordial black hole (PBH) and gamma ray burst (GRB) searches, a range of DM values must be examined. The analysis should be repeated over a number of DM values. A flowchart describing the modified toolchain is shown in Figure 6.1. The following issues should be considered.

1. **Selection of DM values and DM spacing:**

   As shown in Figure 6.1, the major change in the analysis process is to repeat the operations after the RFI mitigation by dedispersing the data at different DM values. The DM values can be chosen between DM_{start} to DM_{end} in steps of $\delta\mathrm{DM} \lessapprox \mathrm{DM}(\Delta\nu_{\mathrm{MHz}}/\mathrm{B}_{\mathrm{MHz}})$ where $\Delta\nu_{\mathrm{MHz}}$ is the width of a frequency channel, and $\mathrm{B}_{\mathrm{MHz}}$ is the bandwidth. Thus,

   $$\mathrm{DM}_{i+1} = \mathrm{DM}_i + \mathrm{DM}_i \, \frac{\Delta\nu_{\mathrm{MHz}}}{\mathrm{B}_{\mathrm{MHz}}} \tag{6.1}$$

   where $\mathrm{DM}_0 = \mathrm{DM}_{start}$ and i increases until DM_{end} is reached. As mentioned earlier in Section 4.1.6, the lowest DM = DM_{start} should be $\sim$10 pc cm^{-3}, since for lower DMs, the dedispersed data is likely to be severely affected by RFI which might cause spurious detections. The upper limit on DM = DM_{end} will be determined by mainly the dataset length, since if the dispersion delay exceeds the dataset length, the bandwidth of the instrument degrades the SNR as opposed to increasing it. For an ETA dataset of length 1 hour, the theoretical maximum DM can be obtained using Equation 2.3 as 6316.7 pc cm^{-3}. Since the maximum DM for sources in our Galaxy is $\sim$ 1400 pc cm^{-3}, that value may be a more reasonable upper limit. However, the computation time will also constrain the number of DM values that can be searched over.

2. **Selection of Trial Pulse Widths**

   The other unknown in non-specific-DM searches is generally the pulse width. For certain

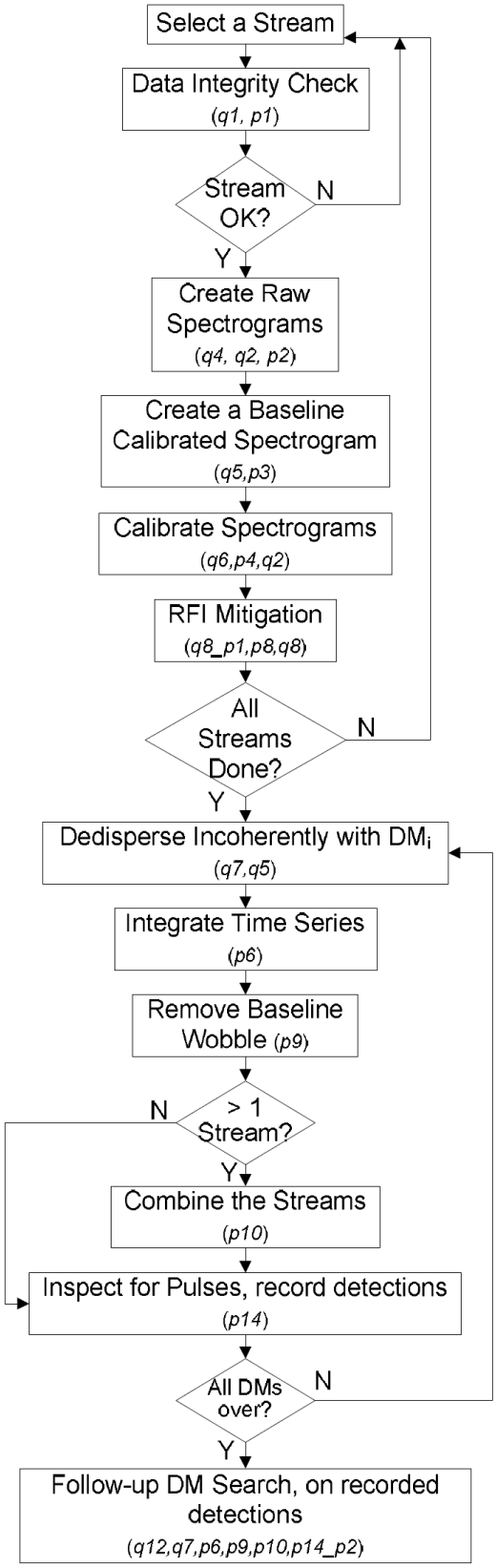

Figure 6.1: Data analysis flowchart for non-specific-DM search toolchain. The toolchain codes from Table 4.1 concerning a task are also mentioned.

searches such as CGP search, the range of possible pulse widths can be estimated as described in Section 2.1.2. In case of PBH and GRB searches, the minimum trial pulse width is equal to the minimum time resolution for the experiment. The maximum trial pulse width to be searched will be limited by the scattering in the interstellar medium (ISM). In case of ETA, the minimum time resolution is $\tau_{min} = 136$ μs. Given this as the starting pulse length, subsequent pulse lengths can be chosen to be $2\tau_{min}, 4\tau_{min}, 8\tau_{min}$ ... until an upper limit is reached.

Possible improvements for future experiments are as follows. Increased sensitivity would be useful. The acquisitions so far include maximum 8 dipoles or 4 stands. Observations using the entire array will certainly improve the sensitivity. Beamforming; i.e., coherent combining, will provide further improvement in sensitivity. Moreover, an anticoincidence system will prove useful in mitigating the effects of radio frequency interference (RFI) and will provide an ability to discriminate the transient detections against RFI.

Appendix A

Selection of Appropriate DM Spacing

Section 4.1.11 explains the need to determine an appropriate spacing $\delta\mathrm{DM}$ for the DM search. This spacing must be small enough so that the sensitivity to intermediate DM values is maintained, but not so small that computational time is wasted in computing unnecessary intermediate DMs.

First, let us modify Equation 2.1 presented in Section 2.1.1 to obtain the dispersion delay as follows:

$$t(\mathrm{DM}, \nu) = (4.2 \times 10^3)\ \mathrm{DM}\ \nu_{\mathrm{GHz}}^{-2} \qquad \mu\mathrm{s} \tag{A.1}$$

where ν_{GHz} is the observing frequency in GHz; DM is dispersion measure in pc cm^{-3}. The differential delay across a frequency channel $\Delta\nu_{\mathrm{MHz}}$ is given by (for example, see [46])

$$\begin{aligned} \Delta t(\mathrm{DM}, \Delta\nu) &= \frac{d}{d\nu_{\mathrm{GHz}}}(t(\mathrm{DM}, \nu)) \times \Delta\nu_{\mathrm{GHz}} \\ &= 8.3\ \mathrm{DM}\ \Delta\nu_{\mathrm{MHz}}\ \nu_{\mathrm{GHz}}^{-3} \qquad \mu\mathrm{s}. \end{aligned}$$

If the DM value used for dedispersion is in error by $\delta\mathrm{DM}$, the pulse will be smeared in the resulting time series. An error of $\delta\mathrm{DM}$ in the dispersion measure will produce a smear of $\Delta t(\delta\mathrm{DM}, \mathrm{B})$ in the dedispersed time series, where B is total bandwidth. $\Delta t(\delta\mathrm{DM}, \mathrm{B})$ is given

by:

$$\begin{aligned} \Delta t(\delta\mathrm{DM}, \mathrm{B}) &= 8.3\ \delta\mathrm{DM}\ \mathrm{B}_{\mathrm{MHz}}\ \nu_{\mathrm{GHz}}^{-3} \qquad \mu\mathrm{s} \\ &= \Delta t(\mathrm{DM}, \mathrm{B}) \frac{\delta\mathrm{DM}}{\mathrm{DM}} \\ &= (8.3 \times 10^{-3})\ \delta\mathrm{DM}\ \mathrm{B}_{\mathrm{MHz}}\ \nu_{\mathrm{GHz}}^{-3} \qquad \mathrm{ms}. \end{aligned} \tag{A.2}$$

If we desire δDM to produce a temporal smearing no greater than that produced by the irreducible dispersion across a frequency channel, then

$$\Delta t(\delta\mathrm{DM,B}) \approx \Delta t(\mathrm{DM}, \Delta\nu). \tag{A.3}$$

From Equations (A.3) and (A.2), Equation (A.3) becomes:

$$(8.3 \times 10^{-3})\ \delta\mathrm{DM}\ \mathrm{B}_{\mathrm{MHz}}\ \nu_{\mathrm{GHz}}^{-3} \approx (8.3 \times 10^{-3})\ \mathrm{DM}\ \Delta\nu_{\mathrm{MHz}}\ \nu_{\mathrm{GHz}}^{-3}, \tag{A.4}$$

which can be solved for the desired DM spacing:

$$\delta\mathrm{DM} \lessapprox \mathrm{DM}\ \frac{\Delta\nu_{\mathrm{MHz}}}{\mathrm{B}_{\mathrm{MHz}}}\ . \tag{A.5}$$

Appendix B

Generation of a Coherent Dispersed Pulse by Simulation

In this appendix, we present the complete technical report "Generation of a Coherent Dispersed Pulse by Simulation" written in August 2009. This appendix is referred to from Section 4.2.1 of the thesis.

Generation of a Coherent Dispersed Pulse by Simulation

K. B. Deshpande * and S. W. Ellingson

August 6, 2009

Contents

*Bradley Department of Electrical & Computer Engineering, 432 Durham Hall, Virginia Polytechnic Institute and State University, Blacksburg, VA 24061 USA. E-mail: kshitija@vt.edu

1 Introduction

In this report, we describe a method of generating a coherent dispersed pulse by simulation. A pulse from a source is dispersed as it travels through the interstellar medium (ISM). Additionally, it is broadened to durations on the order of milliseconds to seconds due to scattering by inhomogeneities in the ISM (See for example [1]). A pulse simulated to exhibit properties that represent these propagation effects can serve as a good test for radio transient search software. We simulate a dispersed, scattered-broadened Crab giant pulse (CGP) in the Eight-meter-wavelength Transient Array (ETA) data format, and use it to verify the "toolchain" developed to analyze the data from the ETA [2]. We describe the method in Section 2 ("Methodology"), and present an illustration of CGP simulation in Section 3 ("Example").

2 Methodology

The dispersed pulse can be modeled as a "chirp" signal (where frequency is a function of time) in the time domain. It is easy to generate a dispersed pulse in the frequency domain, given knowledge of the dispersion delay at each frequency in the band of interest. The time domain signal can be then obtained by inverse Fourier transform. This procedure is described below in detail.

A pulse traveling through the interstellar medium (ISM) is dispersed; that is, the higher-frequency components of the pulse arrive earlier in time than the lower frequency ones. The dispersive delay is given by [3]:

$$\tau = \frac{\mathrm{DM}}{\alpha_0 \nu^2} \quad [\mathrm{s}] \tag{1}$$

where ν is instantaneous frequency in Hz, $\alpha_0 = 2.410 \text{ x } 10^{-16}$, and the dispersion measure (DM) has units of pc cm^{-3}. The shortest dispersion delay τ_1 will occur at the highest

frequency ν_1 in the band of interest. The dispersion delay for other frequencies ν relative to the delay at the highest frequency is given as $t_r(\nu) \triangleq \tau - \tau_1$. Thus,

$$\begin{aligned} t_r(\nu) &= \tau - \frac{\mathrm{DM}}{\alpha_0 \nu_1^2} \\ &= \frac{\mathrm{DM}}{\alpha_0 \nu^2} - \frac{\mathrm{DM}}{\alpha_0 \nu_1^2} \\ &= \frac{\mathrm{DM}}{\alpha_0} \left(\frac{1}{\nu^2} - \frac{1}{\nu_1^2} \right). \end{aligned} \tag{2}$$

Let us first consider the case of simulating a dispersed "impulse" as sketched in a "magnitude spectrogram" (intensity plot displaying the magnitude of spectrum as a function of both time and frequency) in Figure 1. Even though we start with the frequency domain signal, the final goal is to obtain the time domain signal. Let the magnitude of each value in Figure 1 be

$$\begin{aligned} a(t,\nu) &= 1 \qquad \text{for} \quad t_r(\nu) - \frac{dt}{2} < t \leq t_r(\nu) + \frac{dt}{2} \\ &= 0 \qquad \text{otherwise} \end{aligned} \tag{3}$$

where dt is equal to the sample period in the time-frequency domain. In other words, dt is the resultant time resolution after performing N-point fast Fourier transform (FFT) on the time domain data with a time resolution of δt. Thus, $dt = N\delta t$. In Figure 1, the vertical dashed line represents the frequency spectrum at time t'. The inverse Fourier transform of the spectrum at time t' gives the corresponding time domain signal for an interval of length dt.

Let us now consider the additional effect of scatter-broadening. To incorporate this effect, a Gaussian-shaped pulse can be implemented in the Fourier domain using the following equation.

$$a(t,\nu) = \exp\left(-\frac{(t - t_r(\nu))^2}{t_{1/2}^2 \beta} \right) \tag{4}$$

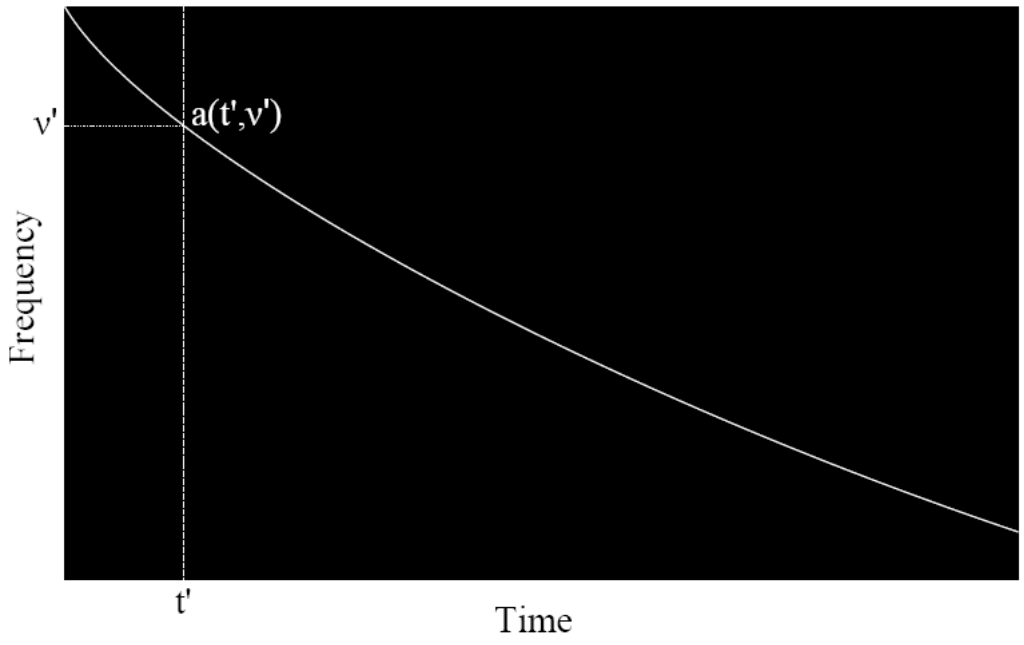

Figure 1: A sketch of a magnitude spectrogram showing a dispersed impulse in the time-frequency domain as a white solid line. Color code: black = 0, white = 1.

where $t_{1/2}$ is the full width at half maximum (FWHM) of this Gaussian-shaped pulse and β is a constant. At half maximum, the numerator in the exponent will be equal to $t_{1/2}^2$. Thus, from Equation 6 we have

$$\frac{1}{2} = \exp\left(-\frac{t_{1/2}^2}{t_{1/2}^2\beta}\right). \tag{5}$$

Solving this equation, we find $\beta = 1/\ln 2$. Substituting β in Equation 6, we obtain

$$a(t,\nu) = \exp\left(-\frac{(t - t_r(\nu))^2 \ln 2}{t_{1/2}^2}\right) \tag{6}$$

The procedure of pulse generation in this case is the same as that described in the previous case; except now with $a(t,\nu)$ from Equation 6, we get a dispersed, scattered-broadened pulse.

3 Example

To illustrate the dispersed pulse in the time-frequency domain, a raw spectrogram containing only a dispersed "impulse" is shown in Figure 2. Next, a dispersed CGP (DM = 56.791 pc cm^{-3}) of FWHM = 1 s is generated in the ETA data format described in detail in [4], and is shown in the raw spectrogram of Figure 3. The signal-to-noise ratio (S/N) of this pulse after dedispersion is ~ 20 at a time resolution of 8.738 ms as seen in the dedispersed time series in Figure 4. Analysis of a simulated 7.8 σ CGP similar to the pulse in Figure 3 embedded in a small dataset is done using the ETA toolchain, and is discussed in Section 4.1 of [2].

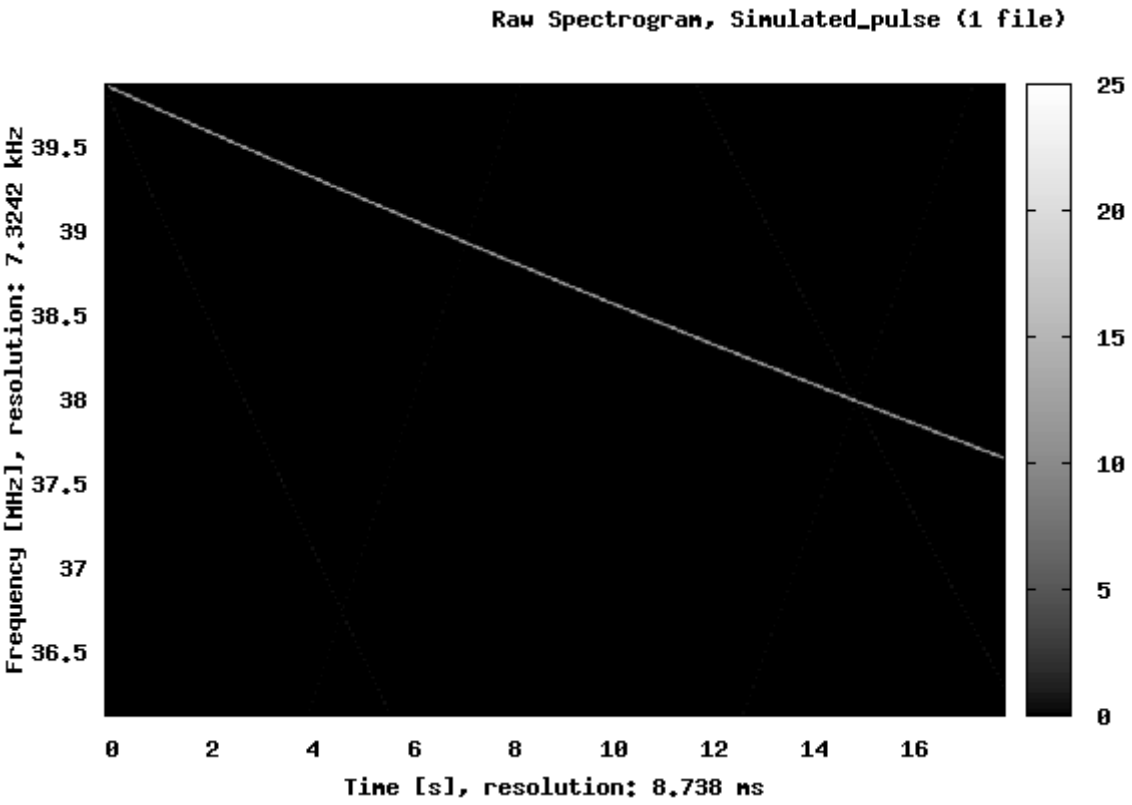

Figure 2: Spectrogram of a simulated impulse dispersed at 56.791 pc cm^{-3} without noise. Intensity of each point on the plot represents the power spectral density (PSD) in arbitrary units. The pulse spans from 39.875 MHz to 37.675 MHz in 17.9 s, which is the same result found theoretically using Equation 2.

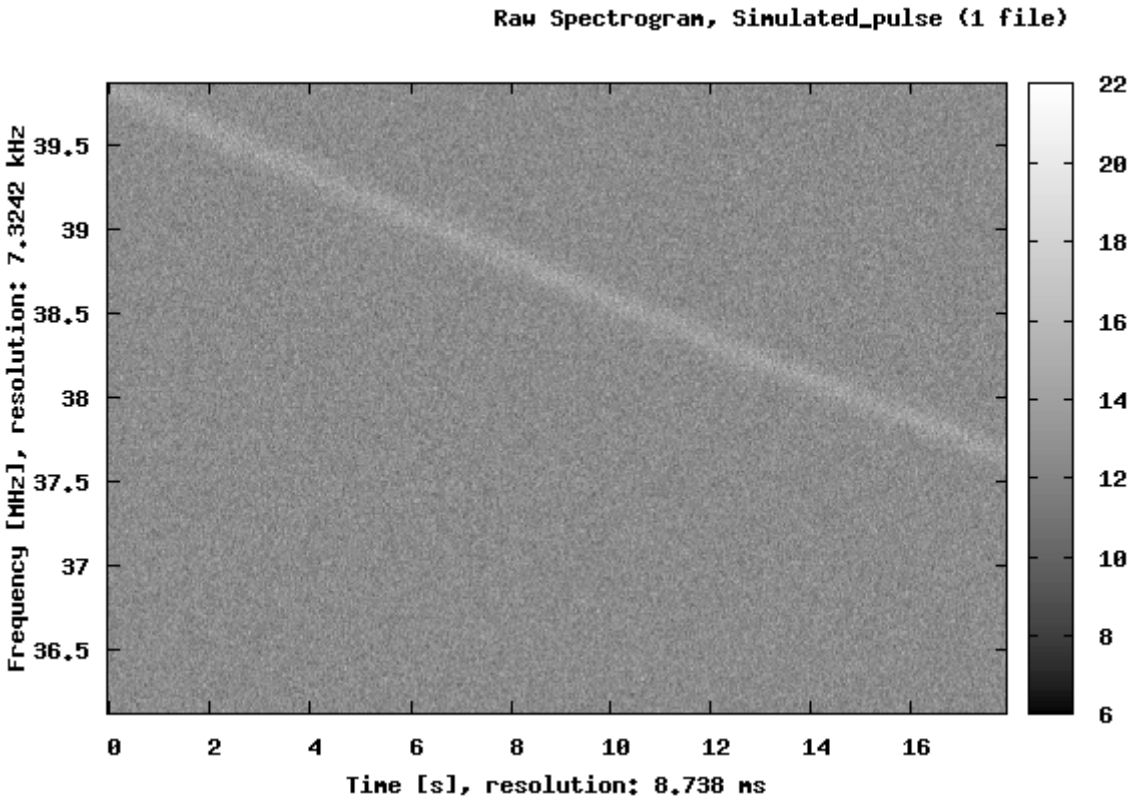

Figure 3: Same as Figure 2, except now FWHM = 1 s and noise is added.

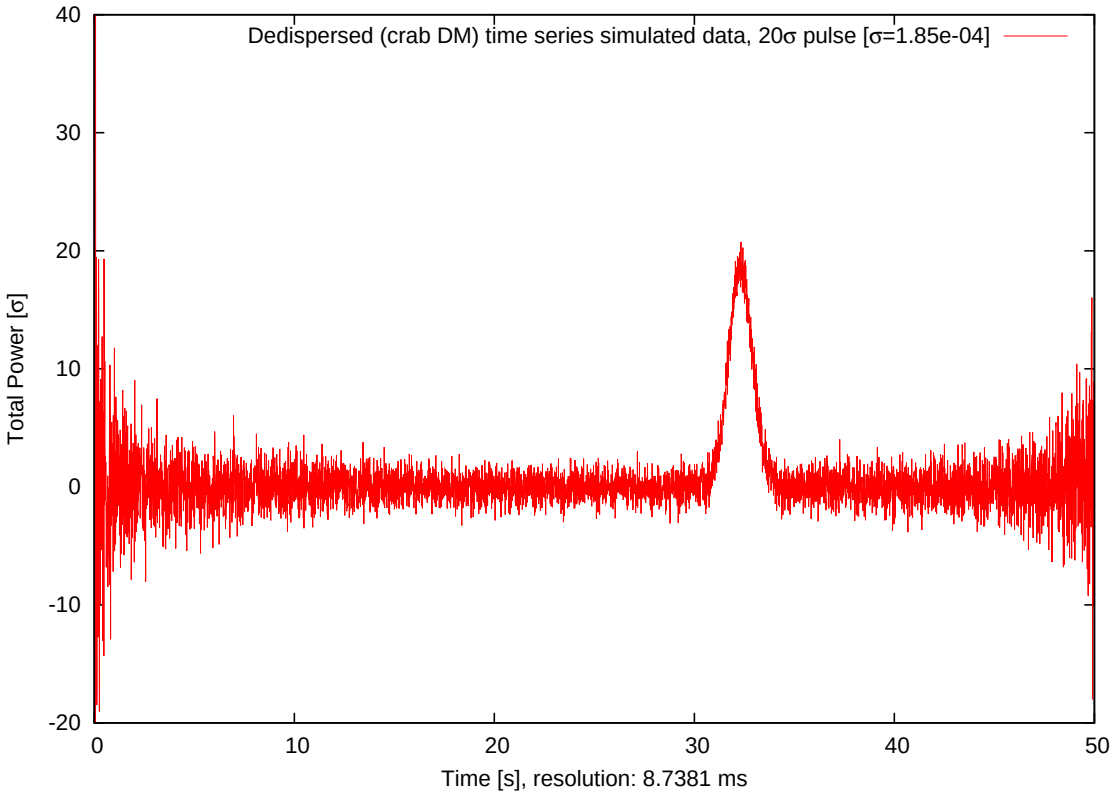

Figure 4: Dedispersed time series (at Crab DM) of the pulse from Figure 3. Fewer samples are averaged at the ends of the dedispersed time series, resulting in the larger variance at the edges.

References

[1] J. M. Cordes *et al.*, "The Brightest Pulses in the Universe: Multifrequency Observations of the Crab Pulsar's Giant Pulses," *Astrophysical Journal*, vol. 612, pp. 375 – 388, September 2004.

[2] K. B. Deshpande and S. W. Ellingson, "ETA Targeted DM Pulse Search Toolchain," Internal Report, Virginia Polytechnic Institute and State University, July 2009, available online: http://www.ece.vt.edu/swe/eta/.

[3] D. Lorimer and M. Kramer, *Handbook of Pulsar Astronomy*, Cambridge University Press, 2005.

[4] C. Patterson *et al.*, "Searching for Transient Pulses with the ETA Radio Telescope," *ACM Trans. Reconfigurable Technology & Systems*, vol. 1, no. 4, p. 19, January 2009.

A Appendix: Simulation Code

```
%%%%%%%%%%%%%%%%%%%%%%%%%%%%%%%%%%%%%%%%%%%%%%%%%%%%%%%%%%%%%%%%%%%%%%%
%% MATLAB Code to generate a coherent dispersed pulse %%
%% Developed by S.W.Ellingson, June 2009              %%
%% Modified by K.B.Deshpande, July 2009               %%
%%%%%%%%%%%%%%%%%%%%%%%%%%%%%%%%%%%%%%%%%%%%%%%%%%%%%%%%%%%%%%%%%%%%%%%

clear all;
close all;
more off;
% user-selectable parameters
DM =     56.791;  % [pc cm^{-3}]
FC =    38.0e+6;  % [Hz] center frequency of passband (as received)
FS =     7.5e+6;  % [samples per second]
T  =    17.8957;  % [s] duration of simulation
LFFT =     1024;  % size of FFT
p_amp =    0.65;  % amplitude of the pulse in time domain
t_half =      1;  % the FWHM of the pulse
% constants
alpha = 2.410e-16; % for DM in [pc cm^{-3}], time in [s], and frequency in
% [Hz]
beta = 1/log(2);
% derived parameters
dt  = 1/FS;       % Time domain sample period
df  = FS/LFFT;    % FFT bin width
dt2 = LFFT*dt;    % FFT period (how often we get a vector of LFFT output
% samples)
% more initializations
fbin = [ 0 : df : FS/2 - df , -FS/2 : df : -df ]; % [Hz] FFT bin center
% frequencies (at baseband)
fbin = fftshift(fbin);                            % fftshift into low-high
% order
f1 = FC + max(fbin)/2;                            % [Hz] start frequency
% (center freq of pulse at start of simulation)
t1 = DM/(alpha*(f1^2));                           % [s] reference delay for
% start freq (f1)
tbin = (DM./(alpha*((FC+fbin-df/2).^2))) - t1;    % [s] delay relative to
% t1 for lowest frequency in each bin
tbin = [ tbin (DM/(alpha*((FC+fbin(LFFT)+df/2).^2))) - t1 ]; % adding one
% more value to simplify algorithm below
num_scl = 1000;
X = zeros(1,LFFT);
```

```
x = zeros(1,LFFT);
xs = zeros(1,num_scl*LFFT);
t = 0;              % [s] initialize sim time
kmax = ceil(T/dt2); % number of FFT input blocks to process
fp = fopen('pulse.out','w');
k = 0;
k1 = 0; %count the number of FFT blocks to write
while k<kmax, % loop over FFT input blocks
  k=k+1;
  k1= k1+1;
  b = 1;        % count bins
  for f = fbin, % loop over FFT bins
    t2a = tbin(b+1);              % delay for max frequency in this bin
    t2b = tbin(b);                % delay for min frequency in this bin
%% Gaussian shaped pulse
    X(b) = exp(-(t-t2a)^2/(beta*t_half^2));
%% Impulse
%     X(b) = 0;
%     if ((t>t2a) & (t<=t2b)),    % are we in this time-frequency cell?
%      X(b) = 1;
%     end
    b = b + 1;
  end % for f
  t = t + dt2;          % update time
  X = fftshift(X);      % FFT shift into screwy FFT order
  x = ifft(X)*LFFT;     % Inverse FFT gives time domain
  xs(:,(k1-1)*LFFT+1:k1*LFFT)=x;
  if (k1 > num_scl)
      disp([t k]);
      k1 = 1;
      max_xs = max(abs(xs));
  for l=1:max(length(xs)),
% Write in ETA format
      xr = round(10*(p_amp*real(xs(l))/max_xs+randn()));
      xi = round(10*(p_amp*imag(xs(l))/max_xs+randn()));
      fwrite (fp,bitshift(xi,1),'schar',0,'ieee-be');
      fwrite (fp,bitshift(xr,1),'schar',0,'ieee-be');
   end % for l
  end %for k1
end % while k
fclose(fp);
return;
```

Appendix C

RFI Mitigation Algorithm for the Eight-meter-wavelength Transient Array

In this appendix, we present the complete technical report "RFI Mitigation Algorithm for the Eight-meter-wavelength Transient Array". The report was written in March 2009. This appendix is referred to from Section 4.1.5 of the thesis.

RFI Mitigation Algorithm for the Eight-meter-wavelength Transient Array

Kshitija Deshpande * and S.W.Ellingson

March 10, 2009

Contents

*Bradley Department of Electrical & Computer Engineering, 432 Durham Hall, Virginia Polytechnic Institute and State University, Blacksburg, VA 24061 USA. E-mail: kshitija@vt.edu

1 Introduction

We present here a radio frequency interference (RFI) mitigation algorithm and illustrate its use for the Eight-meter-wavelength Transient Array (ETA). ETA is a low frequency transient radio telescope consisting of 10 dual polarized active dipoles, located in the mountainous region near Balsam Grove, NC at the Pisgah Astronomical Research Institute (PARI) (35°12' N, 82°52' W). It is Galactic noise-limited over 29-47 MHz, has a center frequency of 38 MHz, and a coherent acquisition of 18 MHz from each dipole. The recorded data are sampled at 7.5 mega-samples per second (MSPS) with 7-bit I and 7-bit Q [1]. The processed bandwidth for the data is 3.75 MHz. The off-line data processing is done using the ETA toolchain [2]. In this report, we assume that data are already calibrated to remove variations due to instrumental frequency response and power level variations with time.

2 Need for RFI Excision and Limitations of Subjective Methods

Man-made RFI is a major problem in low frequency radio astronomy. This interference can be classified as narrowband, broadband, or intermittent. Figure 1 shows a spectrogram of an hour-long ETA acquisition with RFI visible.

A simple iterative procedure of time-frequency pixel blanking was used previous to the development of the algorithm presented in Section 3 of this report. This procedure was as follows:

1. Examine each pixel in the time-frequency matrix. Any pixel which is above a specified threshold is considered RFI. Find such pixels and set them equal to the mean power spectral density (PSD).

2. Obtain a time series by summing the frequency channels. Identify pixels associated

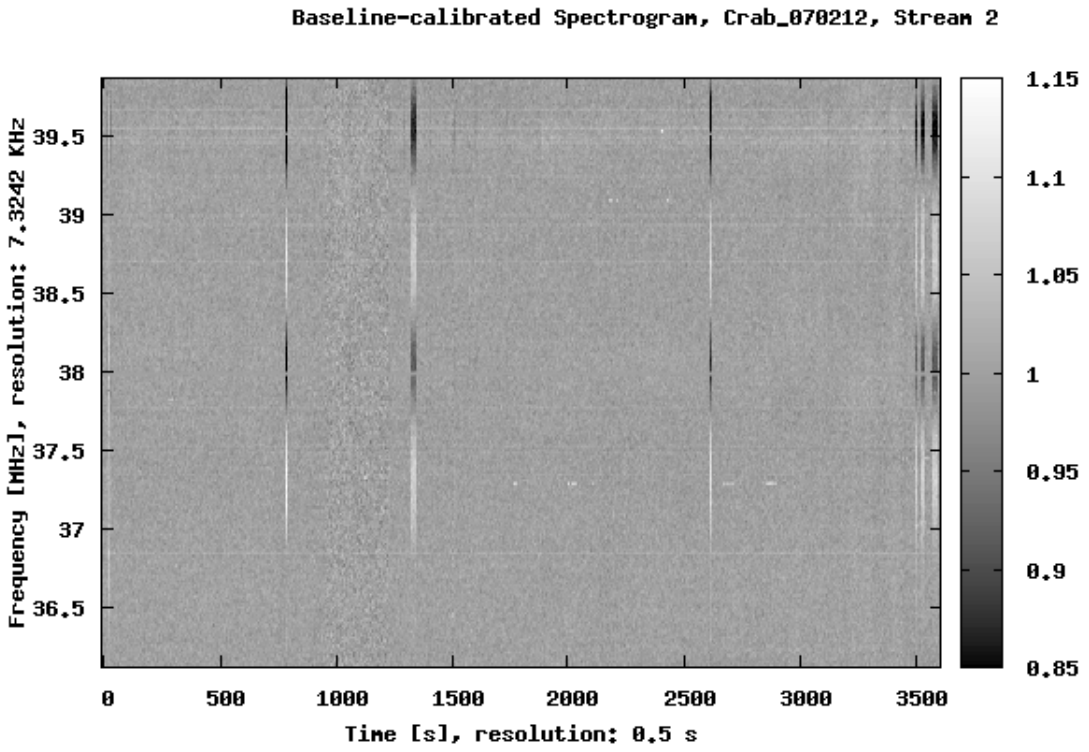

Figure 1: Baseline-calibrated spectrogram from one ETA antenna without RFI mitigation. Frequency resolution: 7.3242 kHz. Time resolution: 0.5 s. (Dataset Crab_070212, stream 2 (6Y).)

with times at which the total power is greater than a specified total power threshold, and set them equal to the mean value of the total power.

3. Obtain a spectrum by taking the spectrogram resulting from Step 2 and summing it over time. Search for frequency bins with total power greater than a specified threshold, and set the associated pixels to the mean value of the integrated spectrum.

4. Iterate steps 1 to 3, adjusting thresholds, until a satisfactory level of RFI excision is achieved.

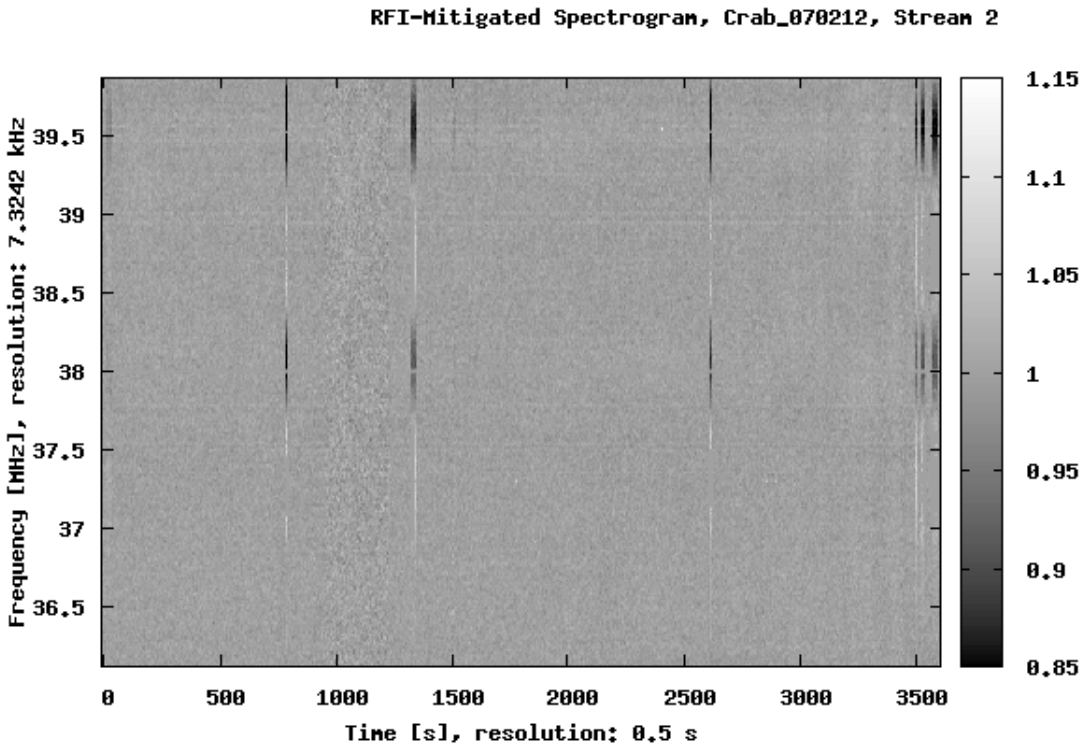

Figure 2: Result of RFI mitigation with old algorithm from Section 2. (Dataset Crab_070212, stream 2 (6Y).)

Figure 2 shows the resulting spectrogram. Figures 6(c) and 6(d) show the resulting time

series and frequency spectrum, for a particular choice of threshold values. The thresholds applied were 0.4, 0.03 and 0.02 in time-frequency, time, and frequency domains respectively. Thus, in the time-frequency domain, for instance, the pixels with magnitudes greater than 1.4 are blanked. Note that RFI is reduced but not eliminated. A more aggressive choice of thresholds could be more effective but that could also unacceptably damage underlying astronomy. Furthermore, the method is tedious and subjective; that is, different persons applying the algorithm are likely to prefer different thresholds, resulting in different and possibly inconsistent results. We therefore seek an algorithm that automates the process of excising RFI for all low frequency observations from the ETA telescope.

3 Methodology

The proposed RFI mitigation algorithm is described below.

1. Obtain a time series by averaging the spectrograms over frequency channels. Identify and blank the "dropouts" by visually inspecting the time series. Dropouts are high-power out-of-band RFI which cause gain compression in the receiver. These are the regions where the total power drops considerably. Figure(3(a)) shows the time series and Figure(3(b)) shows an example of a dropout. Since the receiver behaves nonlinearly when the dropouts occur, these regions must be identified and blanked a priori.

2. Replace the largest magnitude pixels in the time-frequency domain data obtained from previous step, by the mean PSD. Let this fraction of pixels replaced be n. An appropriate value of n is obtained later. This step removes very strong RFI, which otherwise creates problems in subsequent steps.

3. Compute the standard deviations in time-frequency (σ_{tf}), time (σ_t), and frequency (σ_f) domains for one relatively RFI-free interval. The convenient interval for ETA data is one file corresponding to 17.897 s.

4. Examine all time-frequency pixels and replace any pixel with magnitude greater than $m\sigma_{tf}$ by the mean value of PSD. An appropriate value of m is obtained below.

5. Obtain a time series by averaging over frequency channels. Set all pixels associated with times having power larger than $m\sigma_t$ equal to the mean power value.

6. Integrate over spectra and then set all pixels associated with frequencies having values larger than $m\sigma_f$ equal to the mean integrated spectrum value.

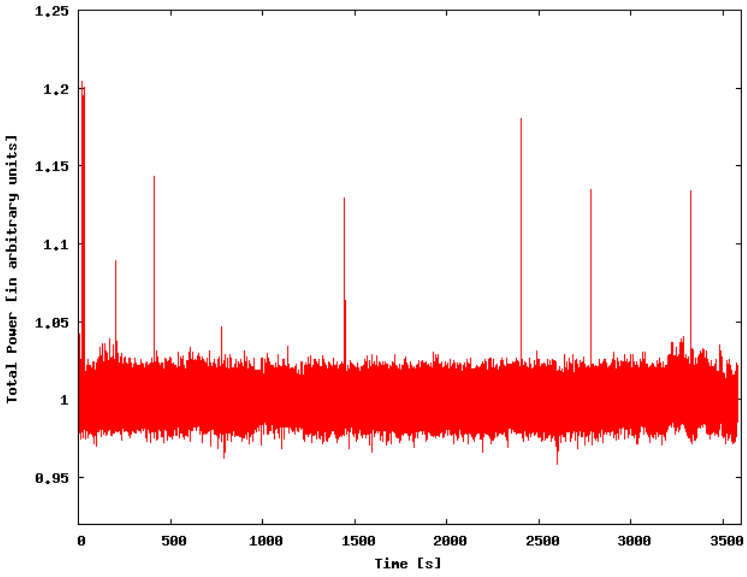

(a)

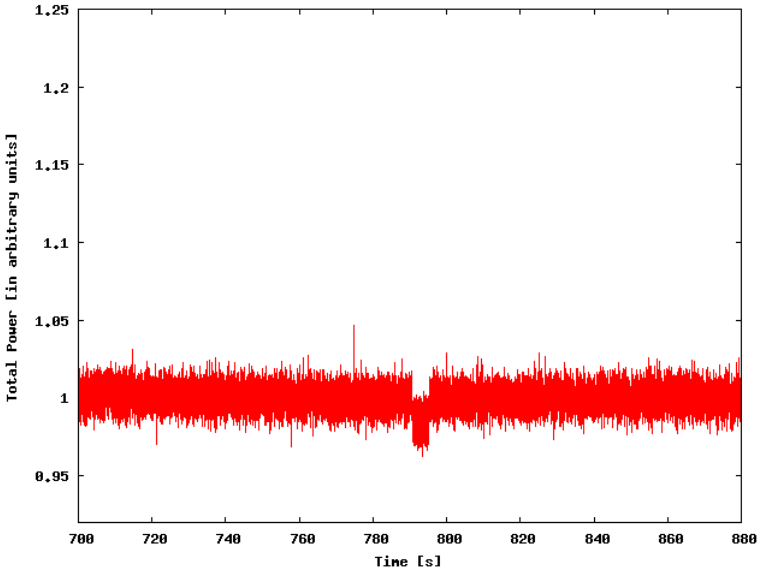

(b)

Figure 3: Figure (a) shows time domain result without RFI mitigation. Figure (b) is a close-up from Figure (a) showing a dropout. (Crab_070212 dataset, stream 2 (6Y).)

The above algorithm is similar to the original algorithm described in Section 2, but it has a better control over the amount of astronomical data loss. Now, we wish to determine values of m and n in a more thoughtful, yet automatic way.

The criterion for choosing n is that it should not be so large that it significantly affects RFI-free portions of the data. A nominal value of n was found by experimenting with $n = 0.1\%, 1\%$ and 10%. It was noticed that $n = 0.1\%$ was leaving behind unacceptable levels of RFI, whereas $n = 10\%$ was discarding an excessive amount of data in addition to RFI. Thus, our trials suggested $n = 1\%$ as a reasonable choice.

We now consider how m should be set. Figure 4 shows how the choice of m affects the fraction of data removed. $m = 1$ and $m = 2$ resulted in loss of more than 4.5% data. A threshold of 3-5σ seemed to work fine in the subsequent RFI mitigation steps. Further experiments with datasets of different degrees of RFI contamination showed that $m = 4$ and $m = 5$ leave some residual RFI. Thus, $m = 3$ was taken to be a reasonable choice.

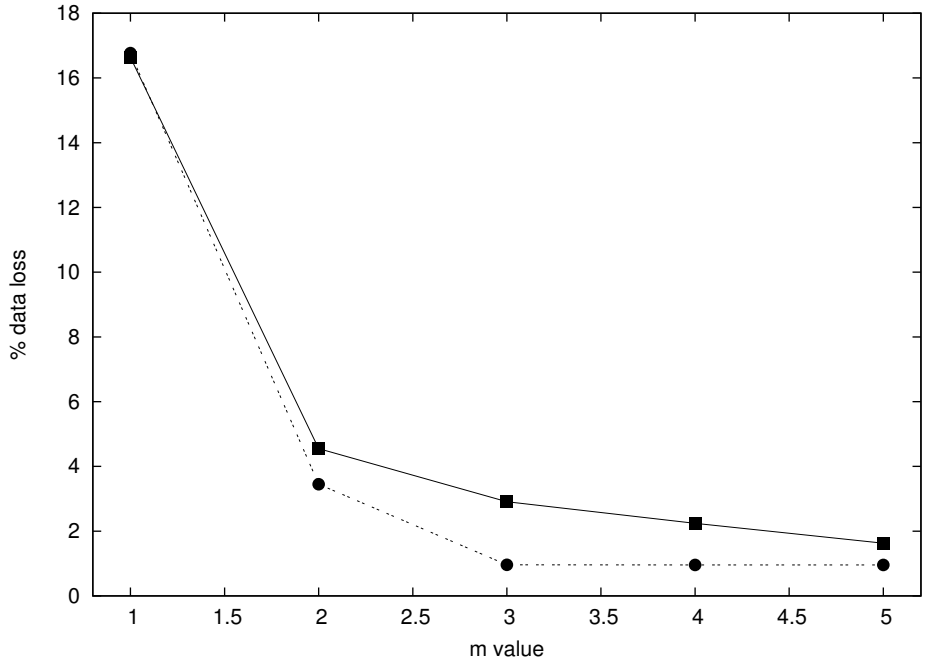

Figure 4: Fraction of data blanked for various values of m with $n = 1\%$ for Crab_070212 dataset, stream 2 (6Y) (*solid*) and simulated dataset, noise only (*dashed*).

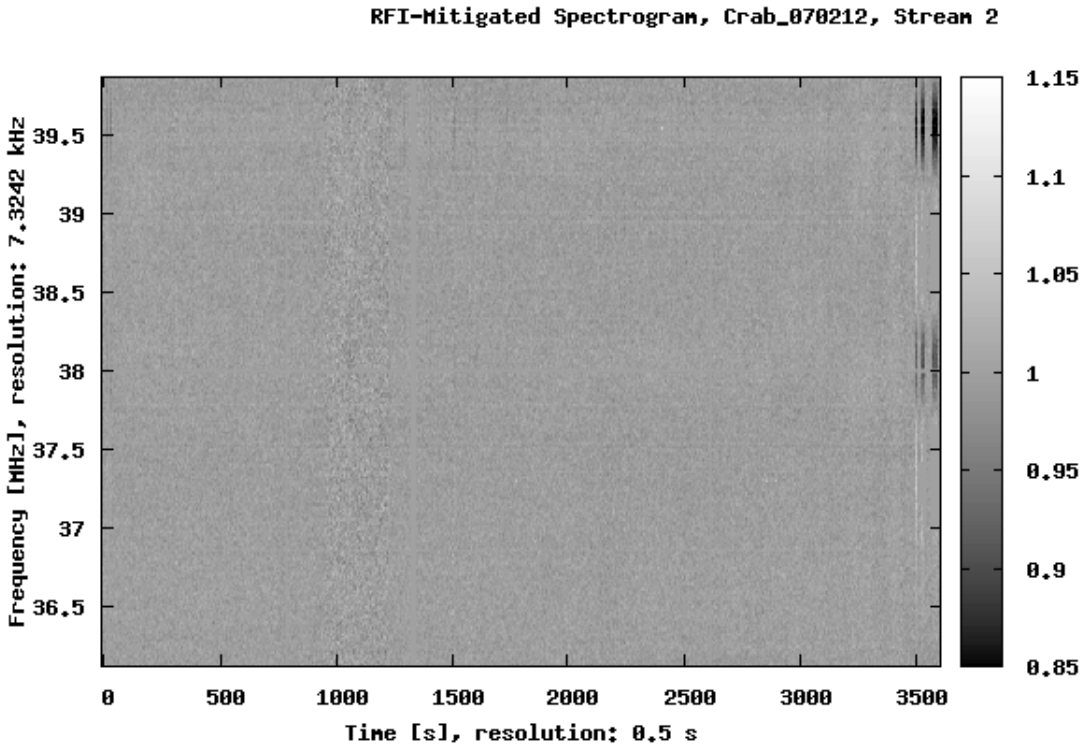

Figure 5: Result of RFI mitigation with algorithm proposed in Section 3. (Crab_070212 dataset, stream 2 (6Y).)

4 Results and Discussion

Figure 5 shows the spectrogram with proposed RFI mitigation algorithm applied. By comparing the outcomes (Figure 6) of RFI mitigation using algorithms from Section 2 and Section 3, it can be said that better level of RFI excision is achieved using the algorithm proposed in Section 3.

To demonstrate the effect of the algorithm on RFI-free data, the proposed algorithm was applied on simulated data containing only Gaussian noise. Figure 7 shows the result. The dashed curve in Figure 4 shows the fraction of data lost for various values of m. It can be said from this experiment that using the proposed algorithm and above-mentioned values of n and m, automation in RFI excision is achieved at the cost of losing 1.0% data.

Finally, it should be emphasized that although this algorithm mitigates most of the RFI, it cannot clean the files completely. This is due to the fact that in the operating frequency range of ETA, data are corrupted with some kinds of RFI which are not well-modeled as being localized strictly in the time domain or the frequency domain.

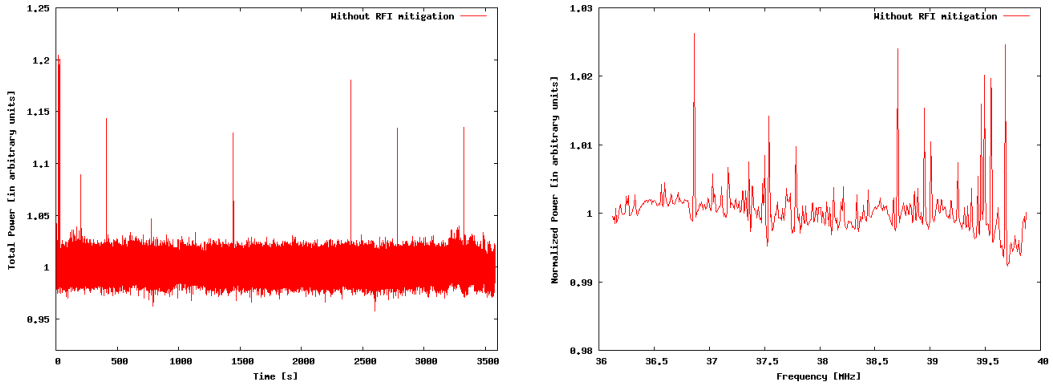

(a)

(b)

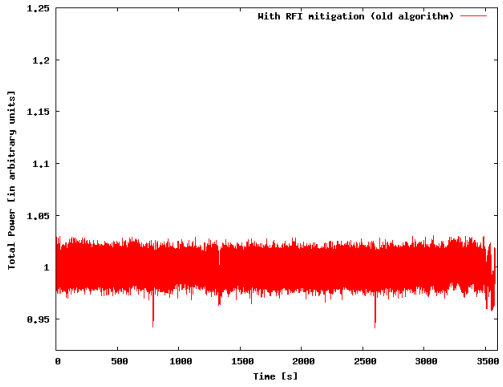

(c)

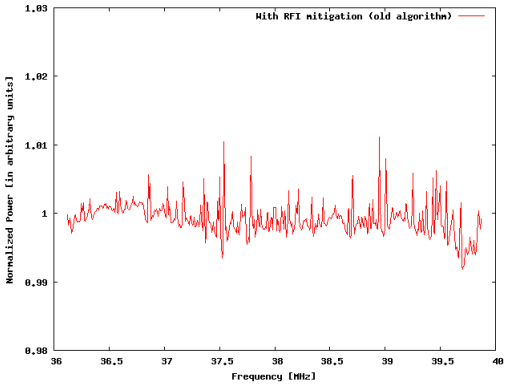

(d)

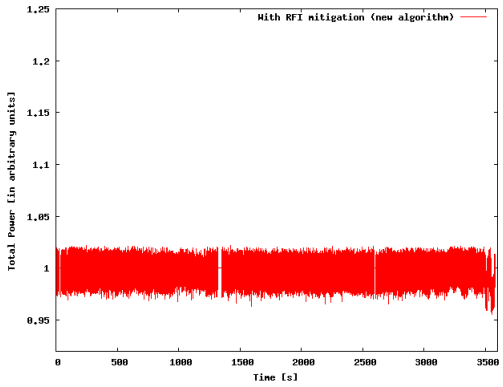

(e)

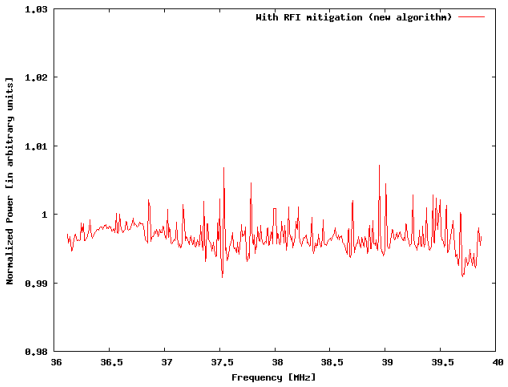

(f)

Figure 6: (a) and (b) show time and frequency domain results without RFI mitigation; results of RFI mitigation with the old algorithm (described in Section 2) are seen in (c) and (d); application of the proposed RFI mitigation algorithm from Section 3 results in (e) and (f). (Dataset Crab_070212, stream 2 (6Y).)

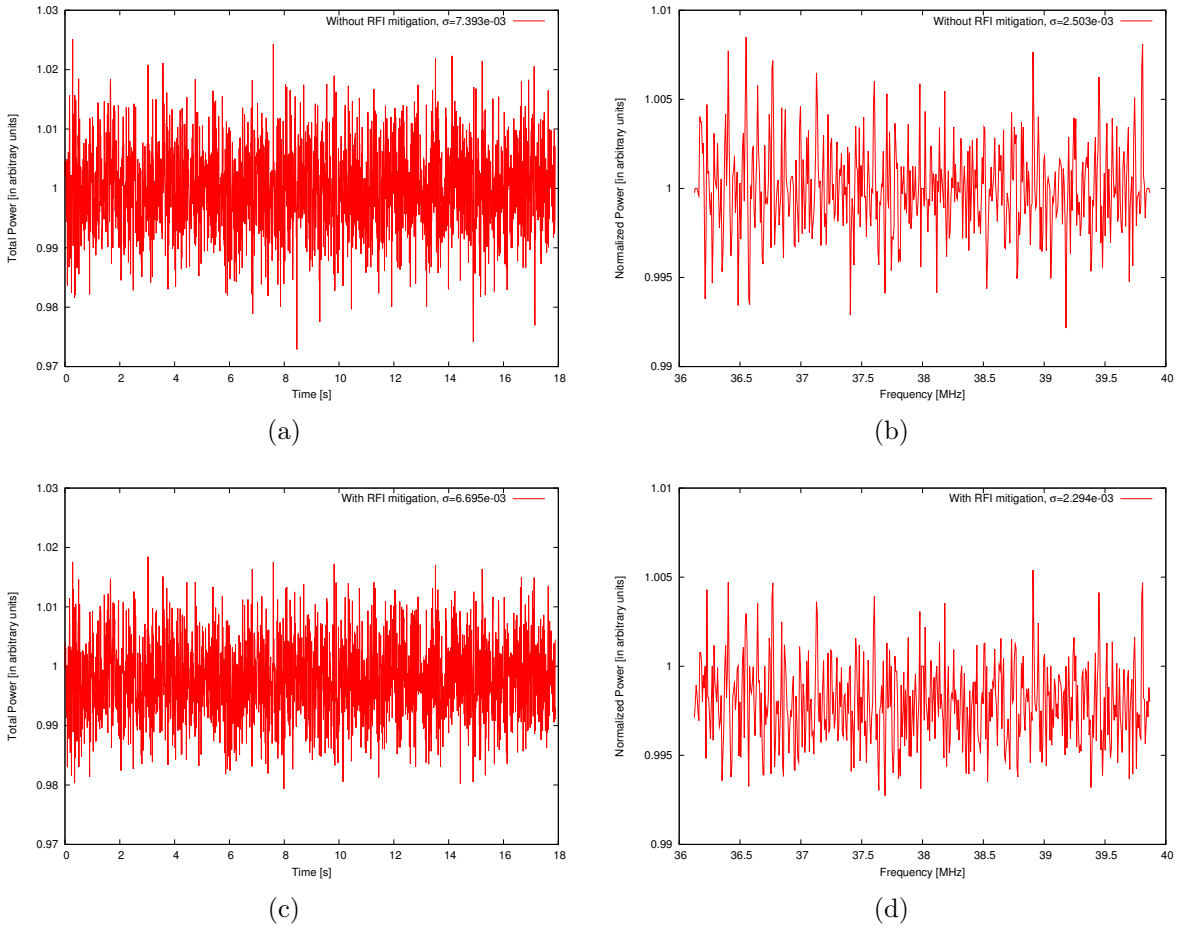

Figure 7: (a) and (b) show the time and frequency domain results without any RFI excision; (c) and (d) illustrate the outcome of RFI mitigation. (Simulated dataset, noise only.)

References

[1] C. Patterson, S. Ellingson, B. Martin, K. Deshpande, J. Simonetti, M. Kavic, and S. Cutchin, "Searching for Transient Pulses with the ETA Radio Telescope", *ACM Trans. Reconfigurable Technology & Systems*, Vol. 1, No. 4, Art. 20 (19pp), Jan. 2009.

[2] K. Deshpande and S. W. Ellingson,"ETA Toolchain", Internal Report Virginia Polytechnic Institute and State University.

Appendix D

ETA Data Collection

All datasets collected to date by ETA are listed in Table D.1, and also are summarized in Table 3.3. The columns of Table D.1 are explained below.

- **Dataset Name** : Name of the dataset with the acquisition date embedded in it.
- **Date Acquired** : Local date in yymmdd (year-month-date) format.
- **Start Time** : Local time of the beginning of the acquisition.
- **Duration** : Total acquisition in hours.
- **Antennas** : ETA antennas numbered as shown in Figure 3.2. B stands for north-south dipole while Y represents east-west dipole.
- **Campaign** : Main campaigns are PBH, CGP, and GCN-triggered.
- **RFI Level**: Rough estimates of unusable data in %. This estimation is based on the amount of data that were discarded after application of RFI mitigation algorithm or initial visual inspection.

Table D.1: Chronological arrangement of datasets collected. All datasets collected after July 2007 are with ground screens installed.

Dataset Name	Date Acquired	Start Time	Duration [h]	Antennas	Campaign	RFI Level
060912	060912	N/A		various	(diagnostic)	
061221	061221	04:00	0.75	6B, 6Y	PBH / B0950+08	
061222	061222	03:56	0.75	6B, 6Y	PBH / B0950+08	
061223	061223	03:52	0.75	6B, 6Y	PBH / B0950+08	
061224	061224	03:48	0.75	6B, 6Y	PBH / B0950+08	
061225	061225	03:44	0.75	6B, 6Y	PBH / B0950+08	
061226	061226	03:40	0.53	6B, 6Y	PBH / B0950+08	
061226add	061226	N/A	0.22	6B, 6Y	PBH / B0950+08	
061227	061227	03:36	0.56	6B, 6Y	PBH / B0950+08	
061227add	061227	N/A	0.19	6B, 6Y	PBH / B0950+08	
061228	061228	03:32	0.75	6B, 6Y	PBH / B0950+08	
061229	061229	03:28	0.75	6B, 6Y	PBH / B0950+08	
061230	061230	03:24	0.75	6B, 6Y	PBH / B0950+08	
061231	061231	03:20	0.75	6B, 6Y	PBH / B0950+08	
070102	070102	03:12	0.75	6B, 6Y	PBH / B0950+08	
070103	070103	03:08	0.75	6B, 6Y	PBH / B0950+08	
070104	070104	03:04	0.75	6B, 6Y	PBH / B0950+08	
070105	070105	03:00	0.75	6B, 6Y	PBH / B0950+08	
070106	070106	02:56	0.75	6B, 6Y	PBH / B0950+08	
GRB_070129	070129	18:37	1.00	6B, 6Y	GCN-triggered	
GRB_070208	070208	04:12	1.00	6B, 6Y	GCN-triggered	
Crab_070212	070212	19:58	1.00	6B, 6Y	CGP	$\sim 20-30\%$
Crab_070213	070213	20:00	1.00	6Y	CGP	$\sim 20-30\%$
B0950+08_070213	070213	00:27	1.00	2B, 6B	PBH / B0950+08	
CasA_070213	070213		0.28	2B, 6B	Cas A Fringes	
B0950+08_070214	070214	00:24	0.75	6Y	PBH / B0950+08	
CasA_070214	070214	12:45	0.22	2B, 6B	Cas A Fringes	
Interval_070214	070214	16:41	0.28	6Y	Diurnal Variation	
Crab_070214	070214	19:54	1.00	2B, 6B	CGP	$\sim 30-40\%$
B0950+08_070215	070215	00:15	0.75	2B, 6B	PBH / B0950+08	
Interval_070215a	070215	08:06	0.09	6Y	Diurnal Variation	
070215a	070215	09:53	0.52	6B, 6Y	Diurnal Variation	
Interval_070215b	070215	09:55	0.18	2B	Diurnal Variation	
CasA_070215	070215	13:39	0.25	2B, 6B	Cas A Fringes	
Crab_070215	070215	19:50	1.00	6Y	CGP	$\sim 30-40\%$
B0950+08_070216	070216	00:15	0.39	2B, 6B	PBH / B0950+08	
Crab_070216	070216	19:46	0.75	2B, 6B	CGP	$\sim 40-50\%$

Dataset Name	Date Acquired	Start Time	Duration [h]	Antennas	Campaign	RFI Level
B0950+08_070217	070217	00:11	0.75	6Y	PBH / B0950+08	
Crab_070217	070217	19:42	1.00	2B, 6B	CGP	$\sim 40-50\%$
B0950+08_070218	070218	00:07	1.00	6Y	PBH / B0950+08	
Crab_070218	070218	19:38	0.75	2B, 6B	CGP	$\sim 40-50\%$
GRB_070218	070218	20:20	1.00	6Y	GCN-triggered	
Crab_070219	070219	19:34	0.75	2B, 6B	CGP	$\sim 40-50\%$
GRB_070219	070219	23:51	1.00	6Y	GCN-triggered	
Crab_070220	070220	19:30	1.00	2B, 6B	CGP	$\sim 40-50\%$
Crab_070221	070221	19:26	0.75	2B, 6B	CGP	$\sim 20-30\%$
GRB_090222	070222	20:24	1.00	2B, 6B	GCN-triggered/CGP	
Crab_070228	070228	18:59	1.00	2B, 6B	CGP	$\sim 20-30\%$
Crab_070228b	070228	19:57	1.00	6Y	CGP	$\sim 20-30\%$
B0950+08_070228	070228	23:20	0.75	2B, 6B	PBH / B0950+08	
B0950+08_070228b	070301	00:03	0.75	6Y	PBH / B0950+08	
Crab_070308	070308	18:28	1.00	1B,4B,6B	CGP	$>\sim 50\%$
B0950+08_070308	070308	22:49	0.75	1B,4B,6B	PBH / B0950+08	
GRB_070309	070309	05:08	1.00	1B,4B,6B	GCN-triggered	
Crab_070323	070323	18:29	1.00	(1,4,6,2)B	CGP	
B0950+08_070323	070323	22:50	0.75	(1,4,6,2)B	PBH / B0950+08	
Crab_070324	070324	18:25	1.00	(1,4,6,2)B	CGP	
B0950+08_070325	070325	22:42	0.75	(1,4,6,2)B	PBH / B0950+08	
Crab_070326	070326	18:17	1.00	(1,4,6,2)B	CGP	$\sim 20-30\%$
B0950+08_070327	070327	22:34	0.75	(1,4,6,2)B	PBH / B0950+08	
B0950+08_070328	070328	22:30	1.00	(1,4,6,2)B	PBH / B0950+08	
B0950+08_070330	070330	22:26	0.75	(1,4,6,2)B	PBH / B0950+08	
B0950+08_070331	070331	22:22	1.00	(1,4,6,2)B	PBH / B0950+08	
B0950+08_070401	070401	22:18	0.75	(1,4,6,2)B	PBH / B0950+08	
B0950+08_070402	070402	22:14	1.00	(1,4,6,2)B	PBH / B0950+08	
day_0400_070408	070408	04:00	0.25	(1,4,6,2)B		
day_1558_070408	070408	15:58	0.25	(1,4,6,2)B		
day_0256_070409	070409	02:56	0.25	(1,4,6,2)B		
day_1454_070409	070409	14:54	0.25	(1,4,6,2)B		
day_0950_070410	070410	09:50	0.25	(1,4,6,2)B		
day_2048_070410	070410	20:48	0.25	(1,4,6,2)B		
day_0648_070411	070411	06:48	0.25	(1,4,6,2)B		
day_1146_070411	070411	11:46	0.25	(1,4,6,2)B		
day_1844_070411	070411	18:44	0.25	(1,4,6,2)B		
day_2342_070411	070411	23:42	0.25	(1,4,6,2)B		
day_0542_070412	070412	05:42	0.25	(1,4,6,2)B		
day_0842_070412	070412	08:42	0.25	(1,4,6,2)B		

Dataset Name	Date Acquired	Start Time	Duration [h]	Antennas	Campaign	RFI Level
day_1342_070412	070412	13:42	0.25	(1,4,6,2)B		
day_1742_070412	070412	17:42	0.25	(1,4,6,2)B		
day_2240_070412	070412	22:40	0.25	(1,4,6,2)B		
day_0440_070413	070413	04:40	0.25	(1,4,6,2)B		
day_0740_070413	070413	07:40	0.25	(1,4,6,2)B		
day_2138_070413	070413	21:38	0.25	(1,4,6,2)B		
071118_0600_2	071118	06:00	1.00	(1,8,6,9)B	PBH / B0950+08 / CGP	$\sim 10-20\%$
071118_0845_2	071118	08:45	0.50	(1,8,6,9)B	CGP	
071118_0600_4	071118	06:00	1.00	(1,3,C,4)Y	PBH / B0950+08 / CGP	$\sim 10-20\%$
071118_0845_4	071118	08:45	0.50	(1,3,C,4)Y	CGP	$\sim 10-20\%$
071118_1050_2	071118	10:50	1.00	(1,8,6,9)B		$\sim 20-30\%$
071118_1050_4	071118	10:50	1.00	(1,3,C,4)Y		
071118_1800	071118	18:00	0.25	(1,8,6,9)B		
071118_2100	071118	21:00	0.25	(1,8,6,9)B		
071119_0100	071119	01:00	0.25	(1,8,6,9)B	CGP	
071119_0400	071119	04:00	1.00	(1,8,6,9)B		
071119_2000_1	071119	20:00	0.50	2B,C1,C2,1B		$\sim 10-20\%$
071119_2000_2	071119	20:00	0.50	(1,8,6,2)B		
071120_0200_1	071120	02:00	1.00	2B,C1,C2,1B	CGP	
071120_0200_2	071120	02:00	1.00	(1,8,6,2)B	CGP	
071120_0500_1	071120	05:00	0.25	2B,C1,C2,1B		
071120_0500_2	071120	05:00	0.25	(1,8,6,2)B		
071120_1400_1	071120	14:00	0.25	(x,x,C,1B)		
071120_1400_2	071120	14:00	0.25	(1,8,6,2)B		
071120_1400_3	071120	14:00	0.25	(x,8Y,C,1Y)		
071120_1400_4	071120	14:00	0.25	(9B,4Y,1Y,3Y)		
071120_2200_2	071120	22:00	0.25	(1,8,6,2)B		
071120_2200_4	071120	22:00	0.25	(9B,4Y,1Y,3Y)		
071121_0200_2	071121	02:00	0.70	(1,8,6,2)B	CGP	$\sim 10-20\%$
071121_0200_4	071121	02:00	0.70	(9B,4Y,1Y,3Y)	CGP	$<\sim 10\%$
071121_0600_2	071121	06:00	0.70	(1,8,6,2)B	PBH / B0950+08	
071121_0600_4	071121	06:00	0.70	(9B,4Y,1Y,3Y)	PBH / B0950+08	
071121_0832_GRB_2	071121	08:32	1.00	(1,8,6,2)B	GCN-triggered	
071121_0832_GRB_4	071121	08:32	1.00	(9B,4Y,1Y,3Y)	GCN-triggered	
071122_1600_2	071122	16:00	0.07	(1,8,6,2)B		
071122_1600_4	071122	16:00	0.07	(9B,4Y,1Y,3Y)		
071124_0200_2	071124	02:00	0.75	(1,8,6,2)B	CGP	$\sim 10-20\%$
071124_0200_4	071124	02:00	0.75	(9B,4Y,1Y,3Y)	CGP	$\sim 10-20\%$
071125_0001_2	071125	00:01	0.07	(1,8,6,2)B	CGP	
071125_0001_4	071125	00:01	0.07	(9B,4Y,1Y,3Y)	CGP	

Dataset Name	Date Acquired	Start Time	Duration [h]	Antennas	Campaign	RFI Level
071201_0100_2	071201	01:00	1.00	(1,8,6,2)B	CGP	$\sim 10-20\%$
071201_0100_4	071201	01:00	1.00	(9B,4Y,1Y,3Y)	CGP	$\sim 10-20\%$
071202_0056_2	071202	00:56	0.95	(1,8,6,2)B	CGP	
071202_0056_4	071202	00:56	0.95	(9B,4Y,1Y,3Y)	CGP	
071203_0052_2	071203	00:52	0.95	(1,8,6,2)B	CGP	
071203_0052_4	071203	00:52	0.95	(9B,4Y,1Y,3Y)	CGP	
071204_0048_2	071204	00:48	0.95	(1,8,6,2)B	CGP	
071204_0048_4	071204	00:48	0.95	(9B,4Y,1Y,3Y)	CGP	
071205_0044_2	071205	00:44	0.95	(1,8,6,2)B	CGP	
071205_0044_4	071205	00:44	0.95	(9B,4Y,1Y,3Y)	CGP	

Appendix E

Calibrated and RFI Mitigated Spectrograms

In this appendix, we present the calibrated and RFI mitigated spectrograms of the antennas used in the data analysis of the datasets in which the CGP candidates were found. This appendix is referred to from Sections 5.2.1 and 5.2.2.

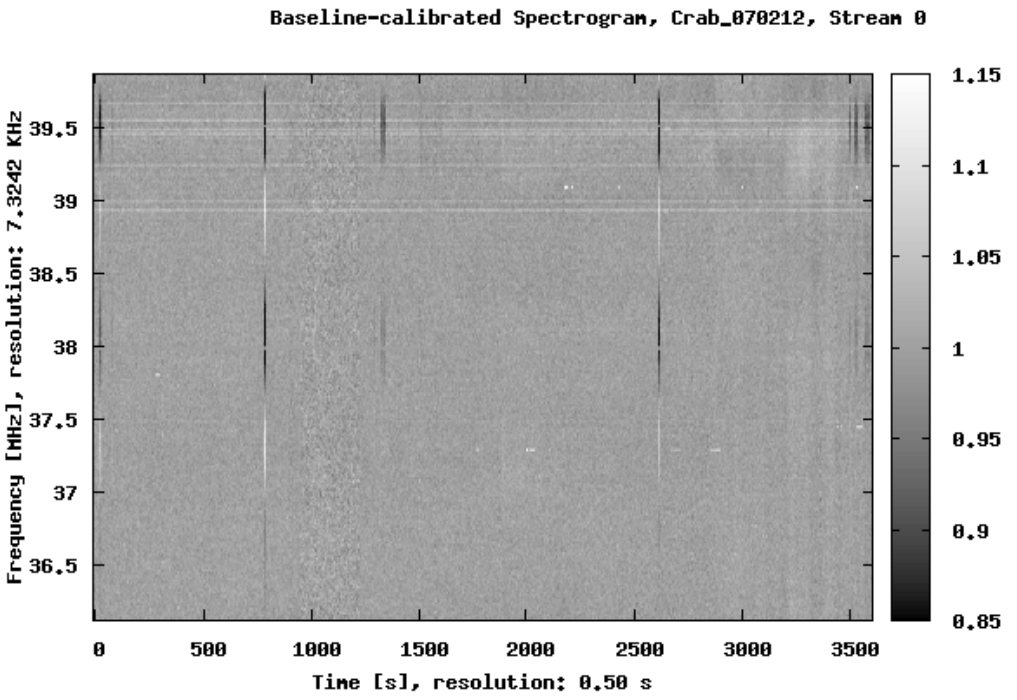

Figure E.1: Dataset: Crab_070212. Calibrated Spectrogram, stream 0 (6B).

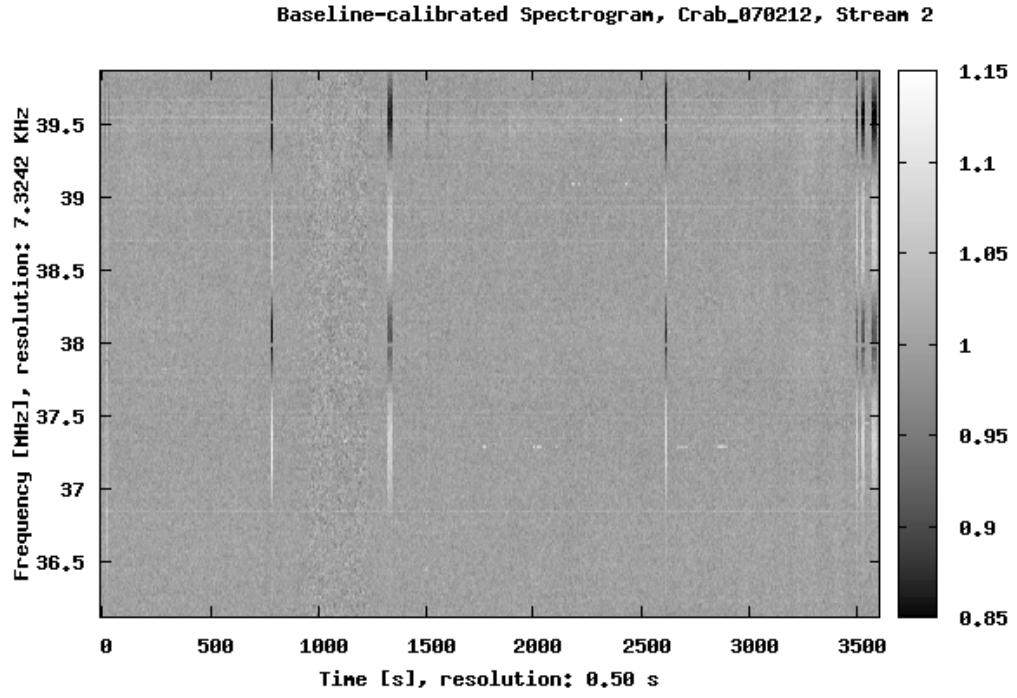

Figure E.2: Dataset: Crab_070212. Calibrated Spectrogram, stream 2 (6Y).

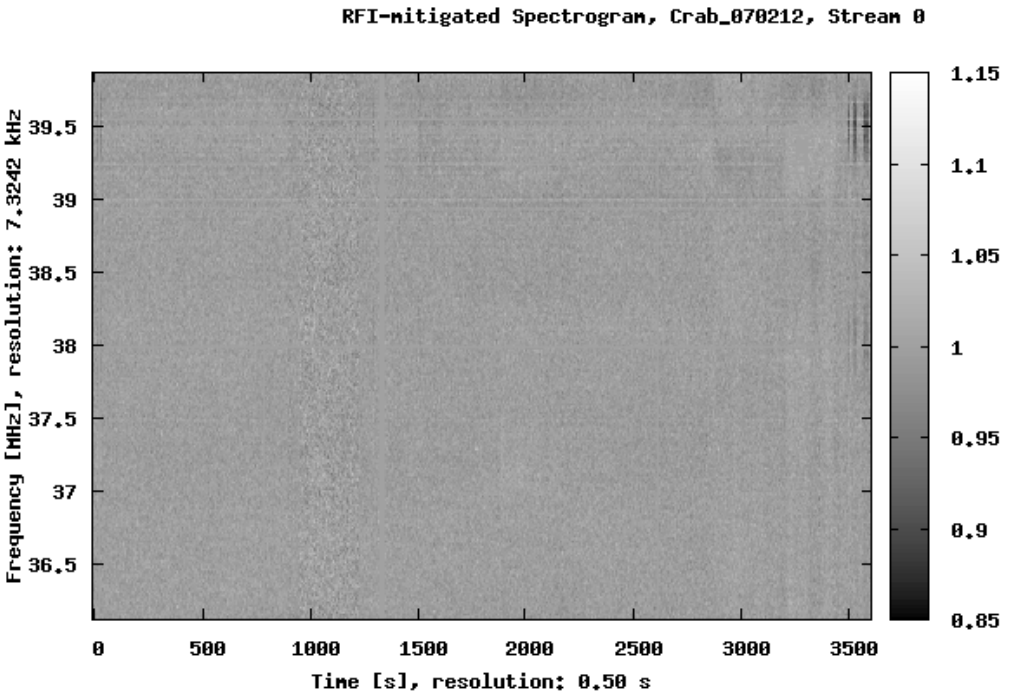

Figure E.3: Dataset: Crab_070212. Spectrogram after RFI mitigation, stream 0 (6B).

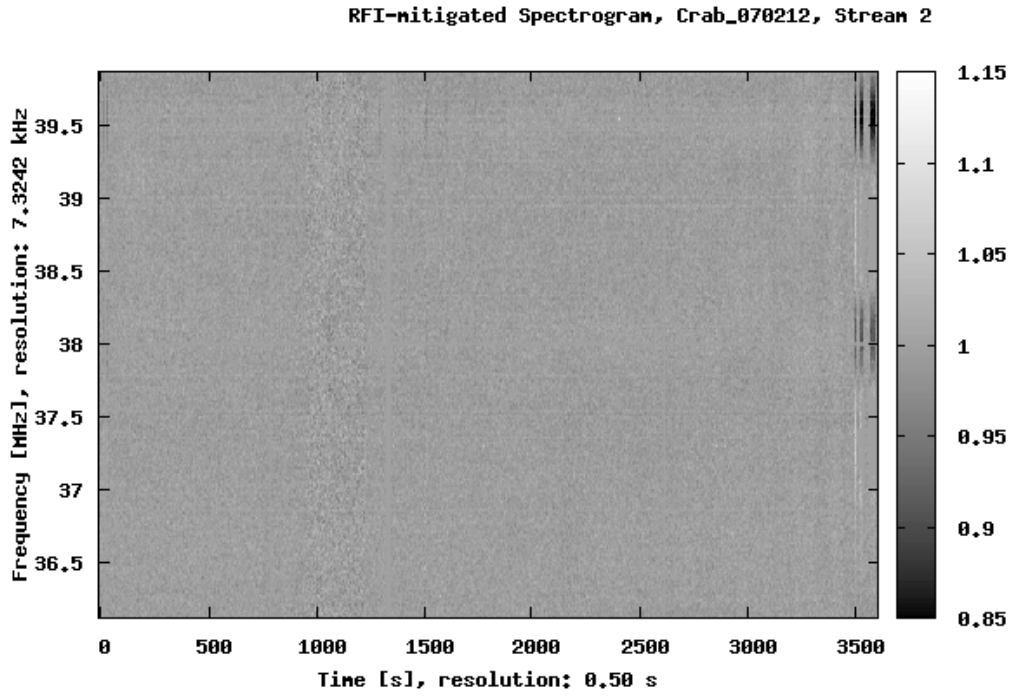

Figure E.4: Dataset: Crab_070212. Spectrogram after RFI mitigation, stream 2 (6Y).

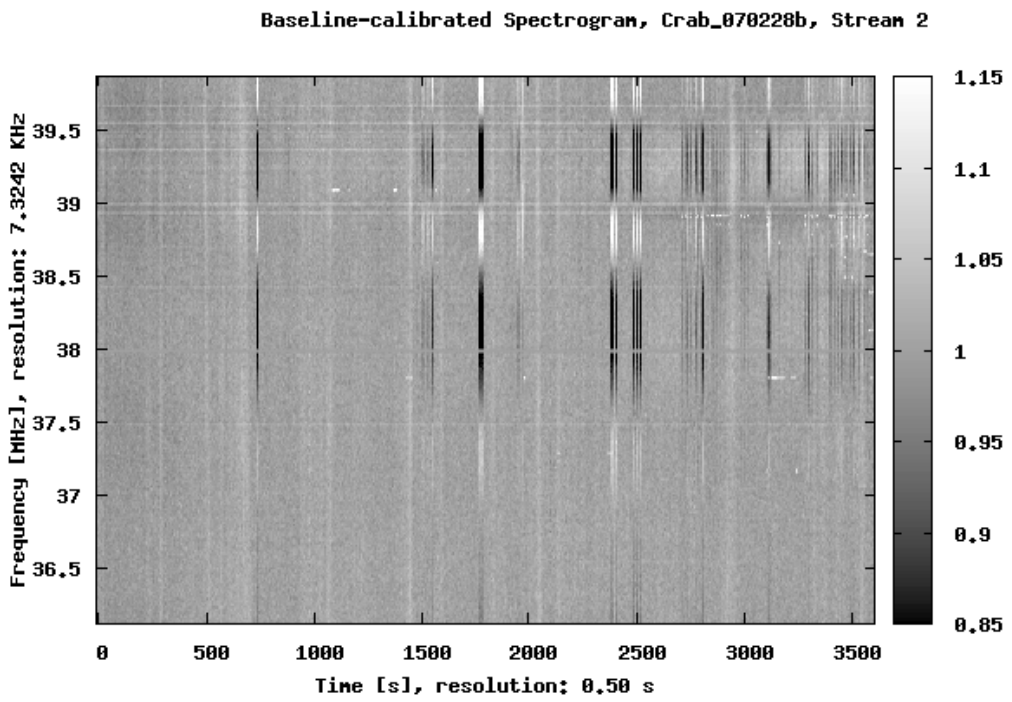

Figure E.5: Dataset: Crab_070228b. Calibrated Spectrogram, stream 2 (6Y).

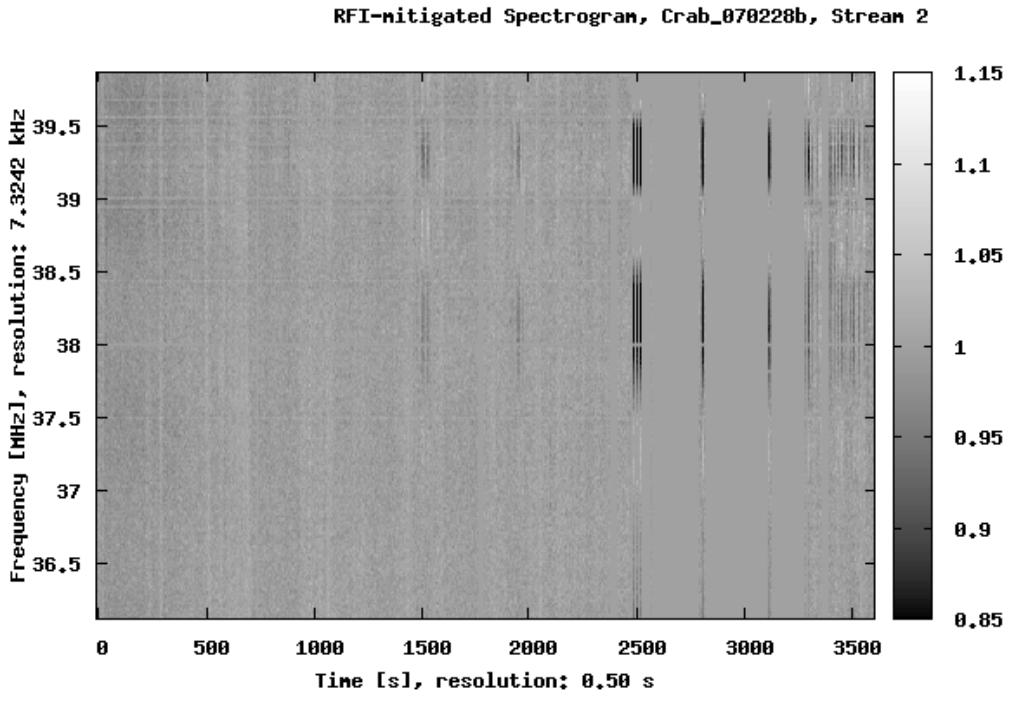

Figure E.6: Dataset: Crab_070228b. Spectrogram after RFI mitigation, stream 2 (6Y).

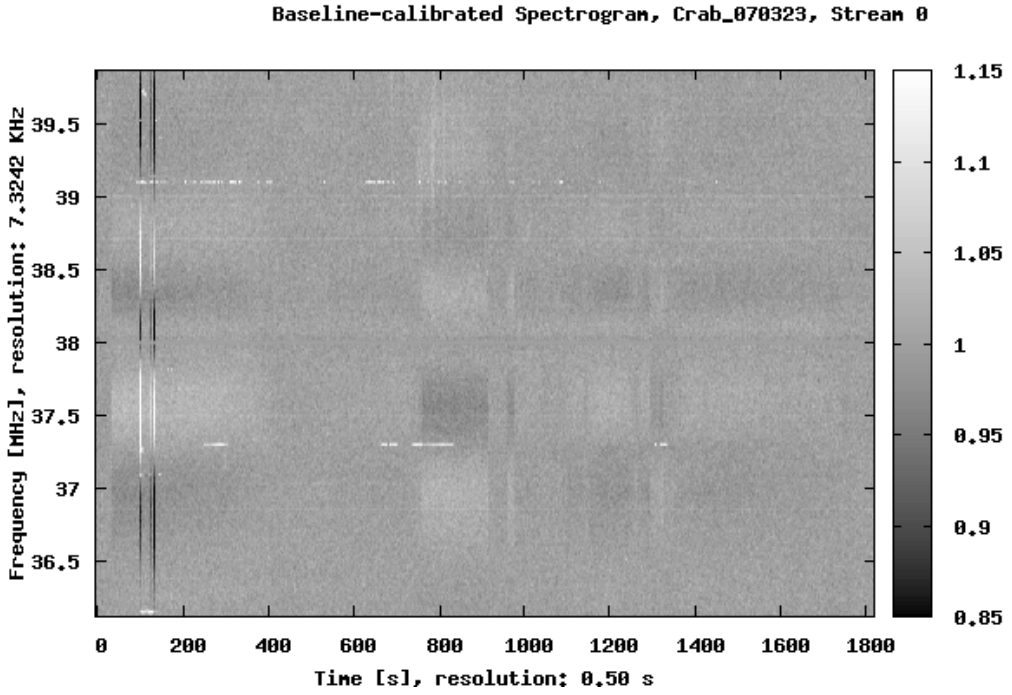

Figure E.7: Dataset: Crab_070323. Calibrated Spectrogram, stream 0 (1B).

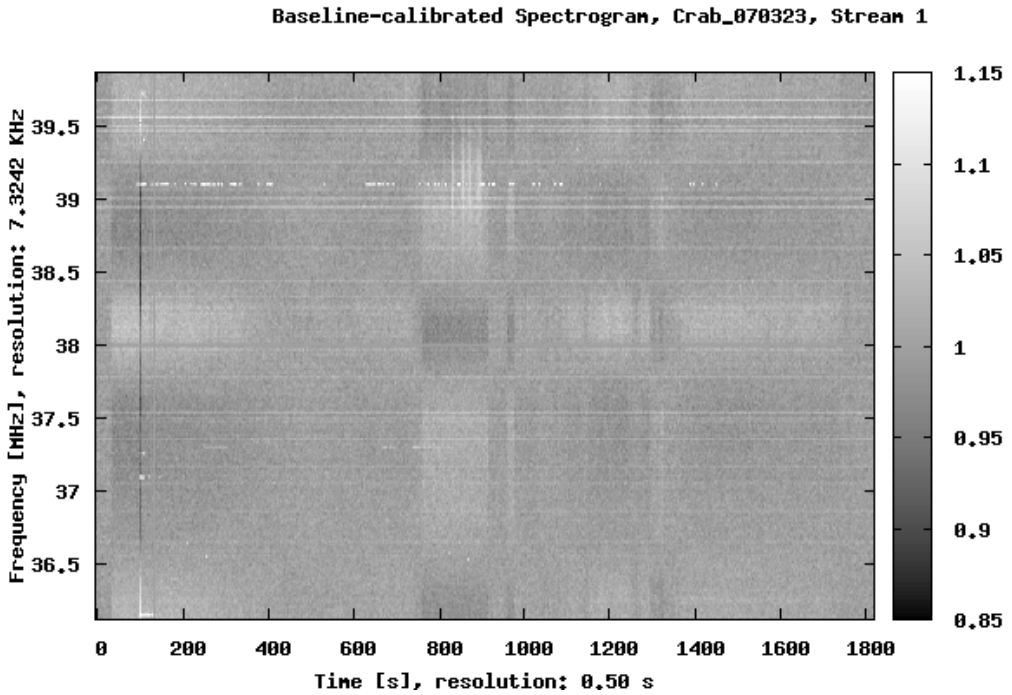

Figure E.8: Dataset: Crab_070323. Calibrated Spectrogram, stream 1 (4B).

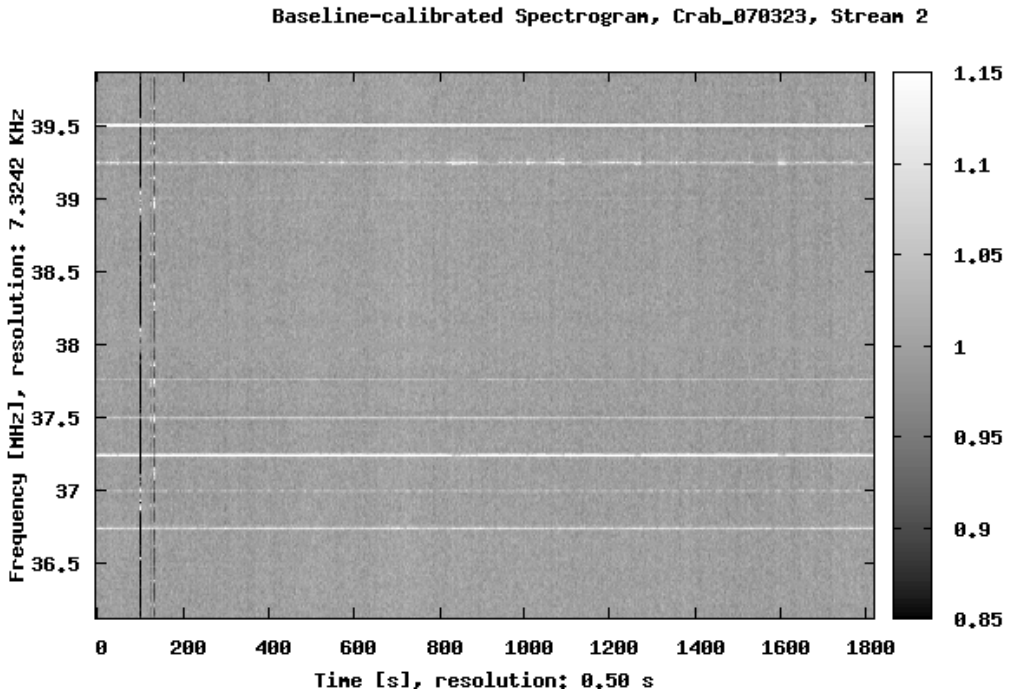

Figure E.9: Dataset: Crab_070323. Calibrated Spectrogram, stream 2 (6B).

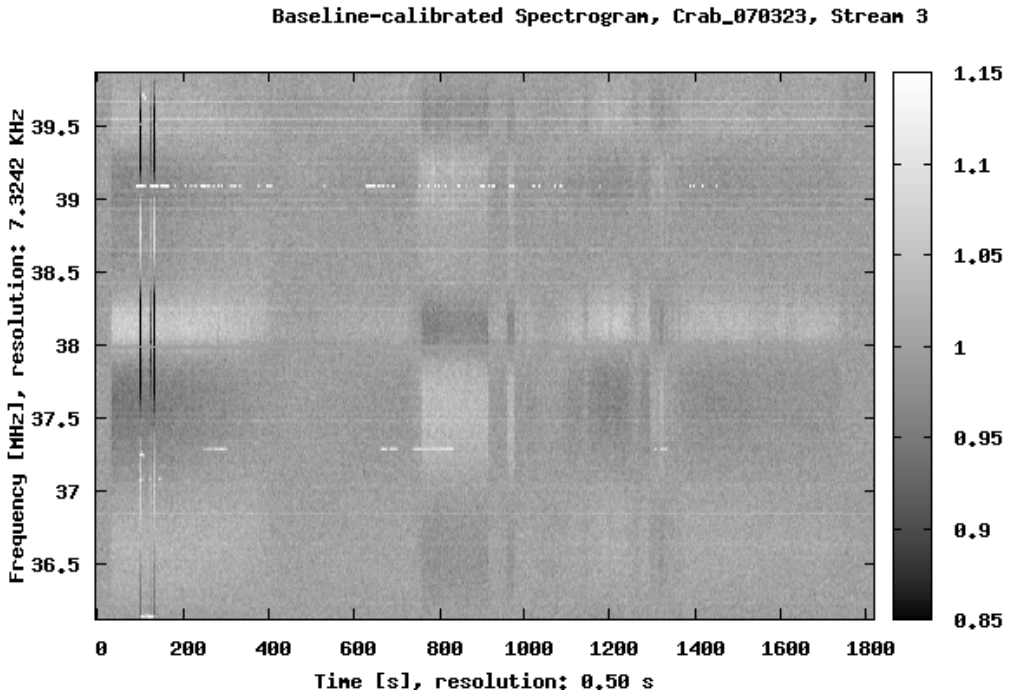

Figure E.10: Dataset: Crab_070323. Calibrated Spectrogram, stream 3 (2B).

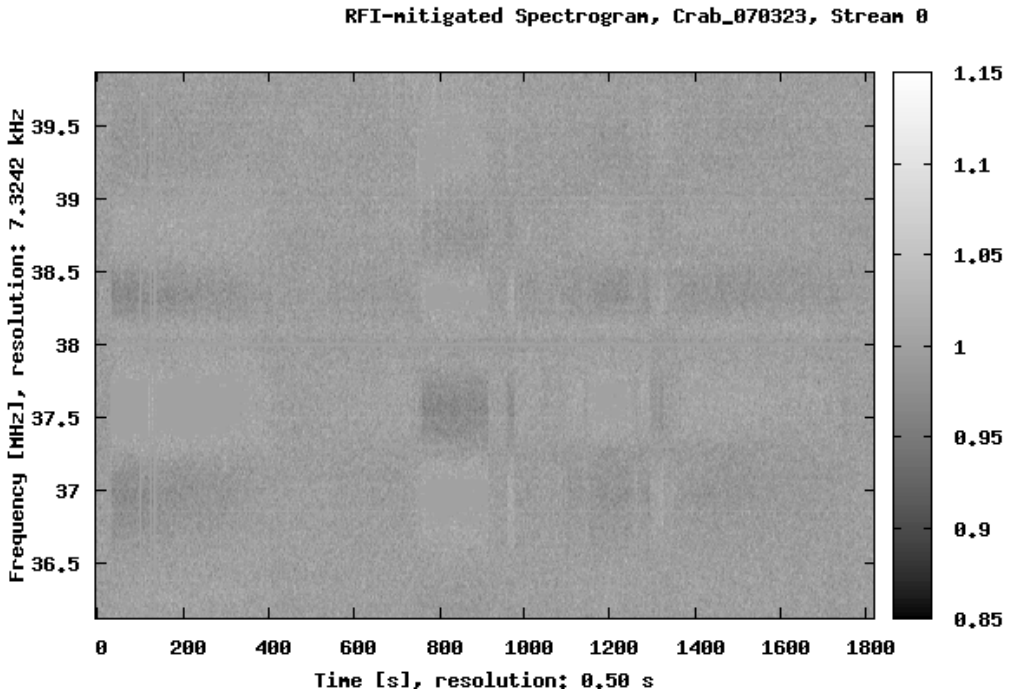

Figure E.11: Dataset: Crab_070323. Spectrogram after RFI mitigation, stream 0 (1B).

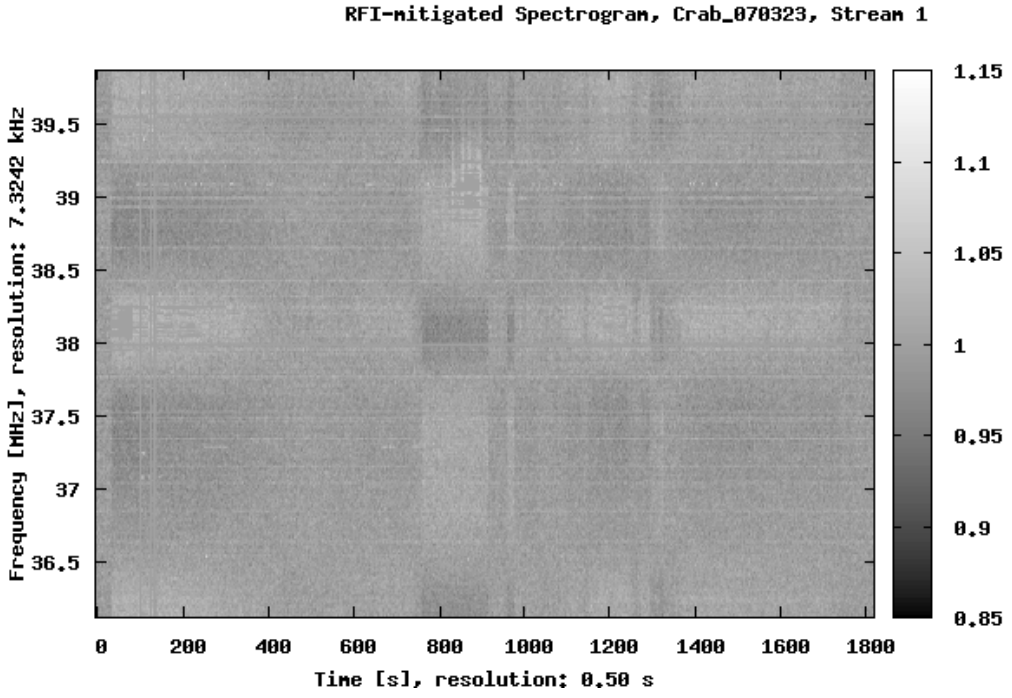

Figure E.12: Dataset: Crab_070323. Spectrogram after RFI mitigation, stream 1 (4B).

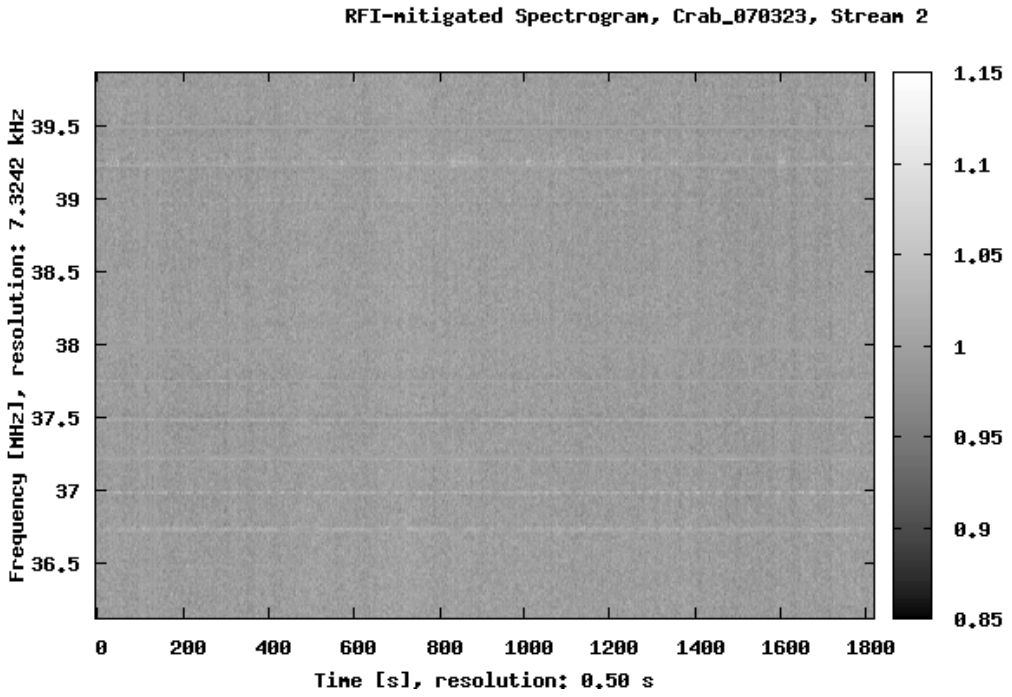

Figure E.13: Dataset: Crab_070323. Spectrogram after RFI mitigation, stream 2 (6B).

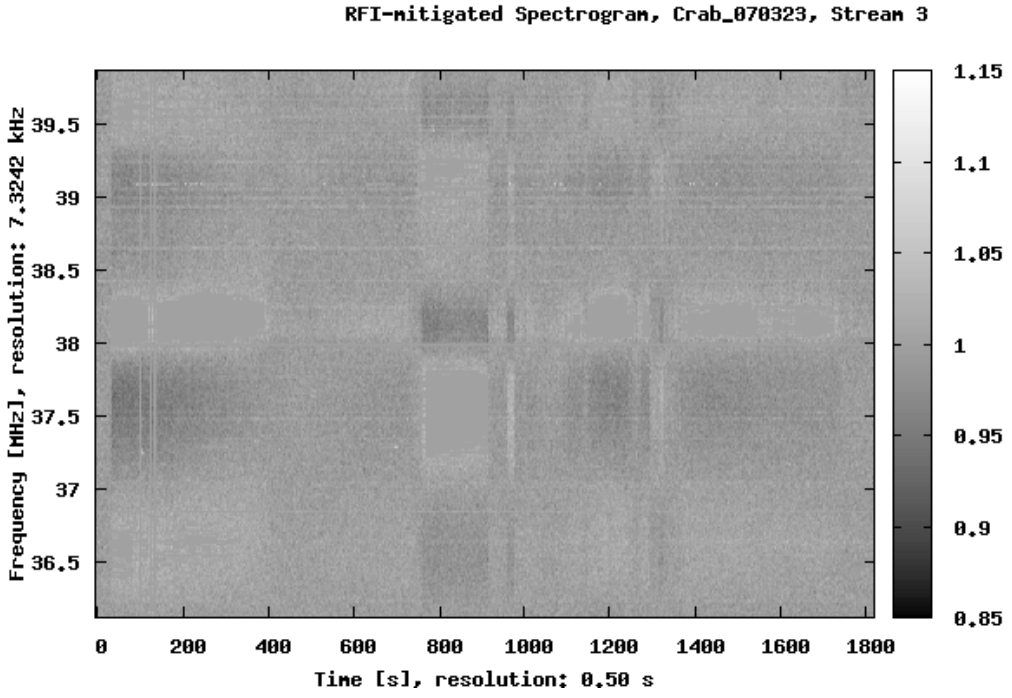

Figure E.14: Dataset: Crab_070323. Spectrogram after RFI mitigation, stream 3 (2B).

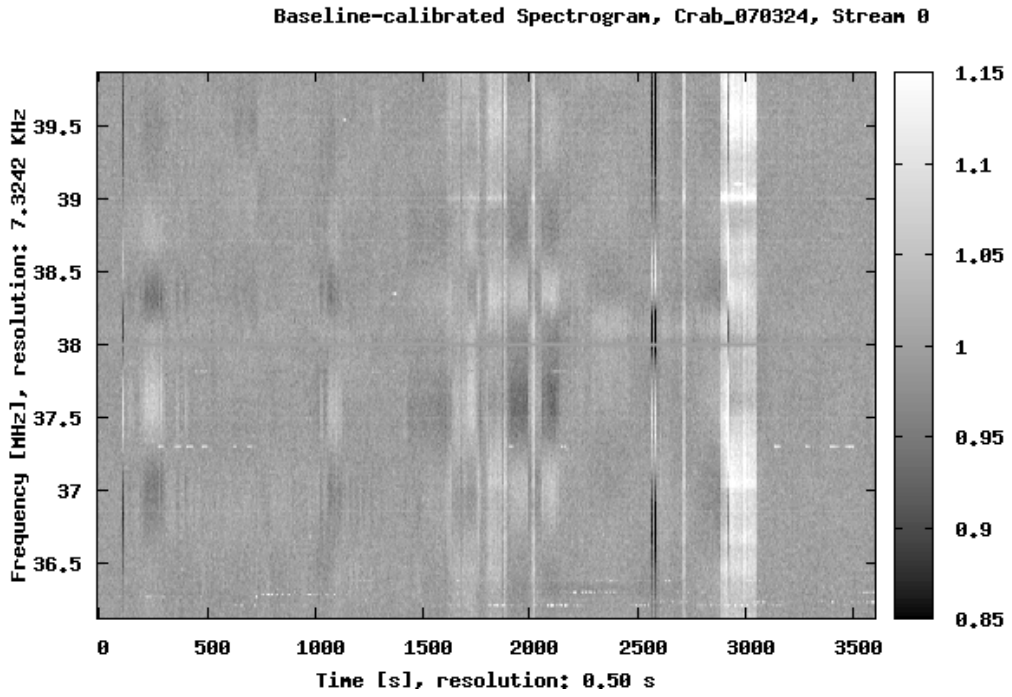

Figure E.15: Dataset: Crab_070324. Calibrated Spectrogram, stream 0 (1B).

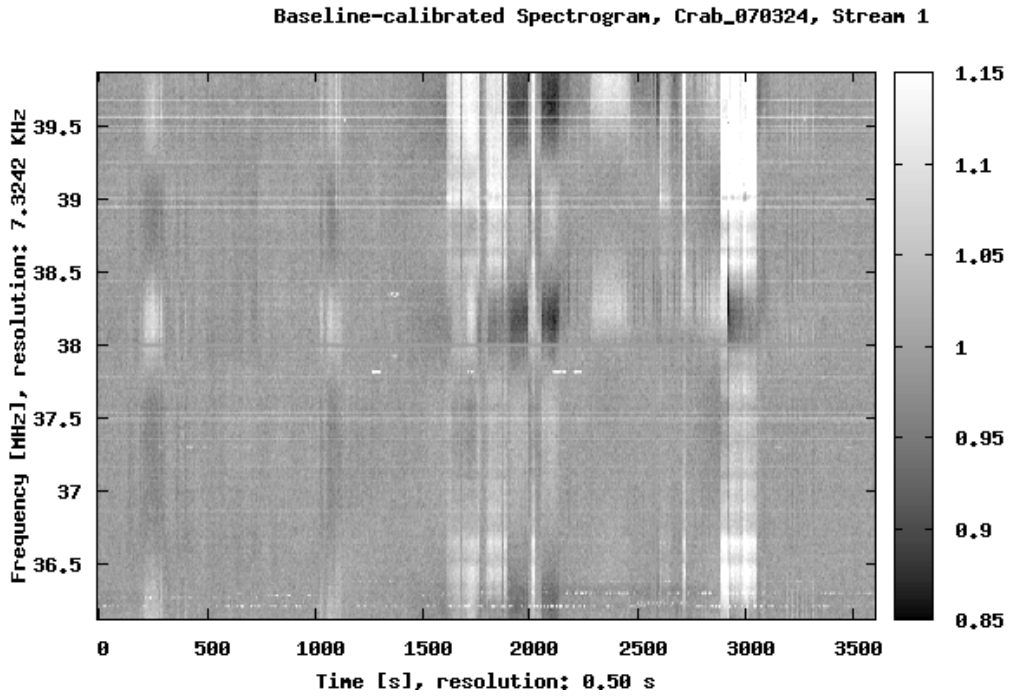

Figure E.16: Dataset: Crab_070324. Calibrated Spectrogram, stream 1 (4B).

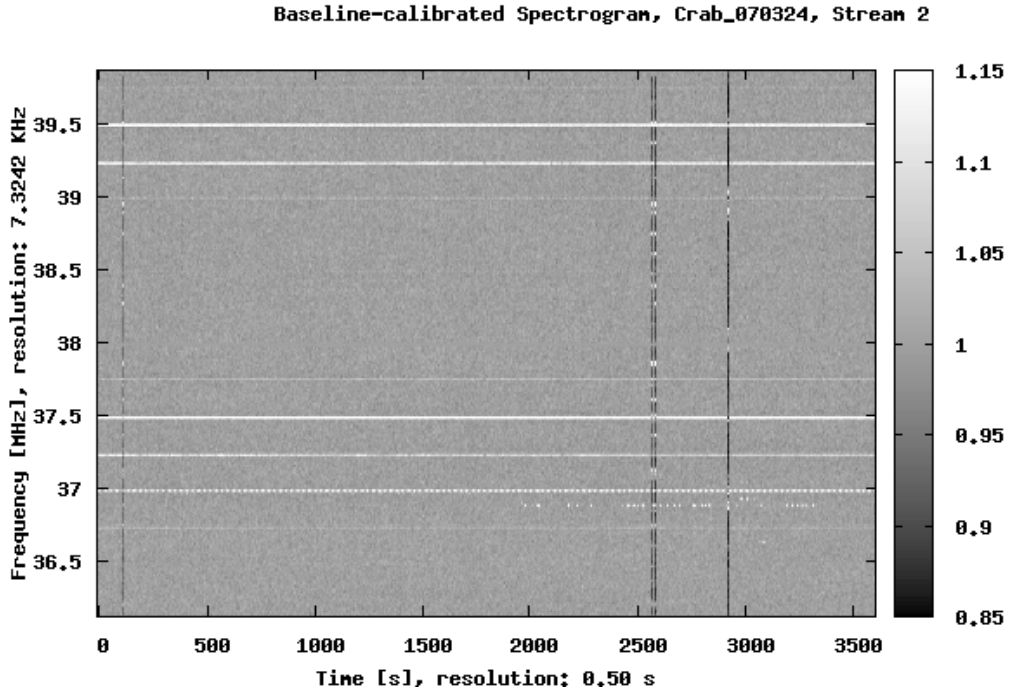

Figure E.17: Dataset: Crab_070324. Calibrated Spectrogram, stream 2 (6B).

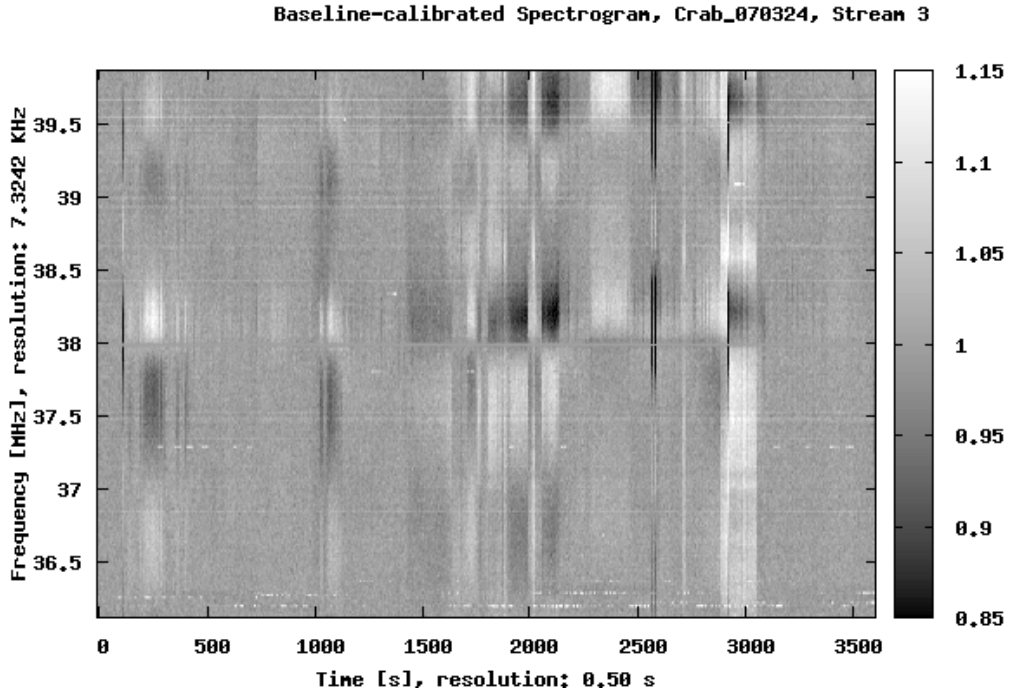

Figure E.18: Dataset: Crab_070324. Calibrated Spectrogram, stream 3 (2B).

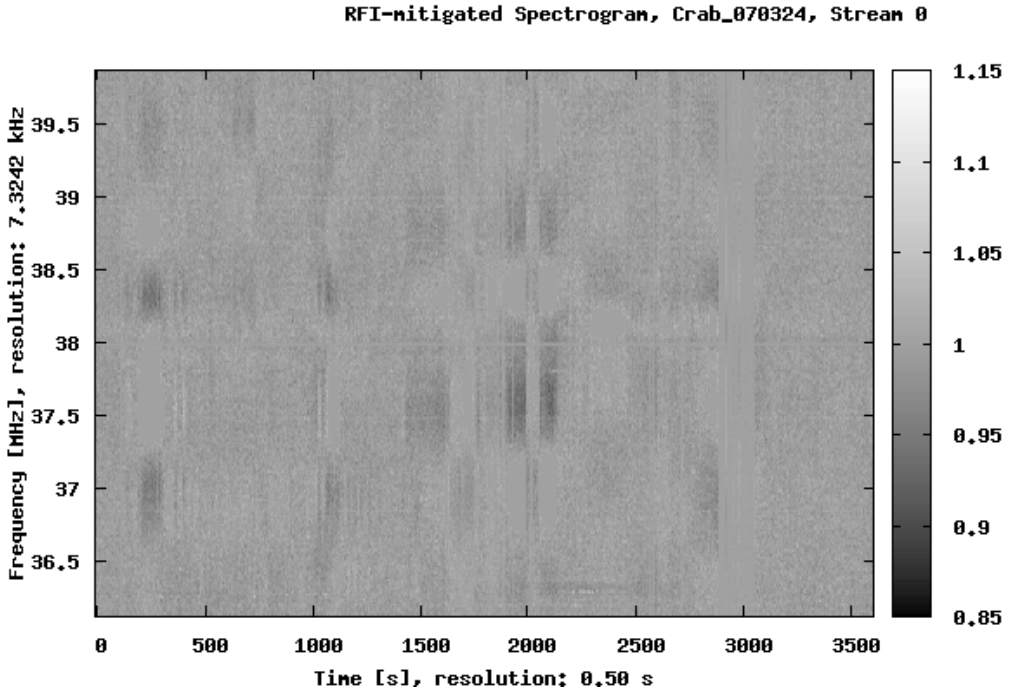

Figure E.19: Dataset: Crab_070324. Spectrogram after RFI mitigation, stream 0 (1B).

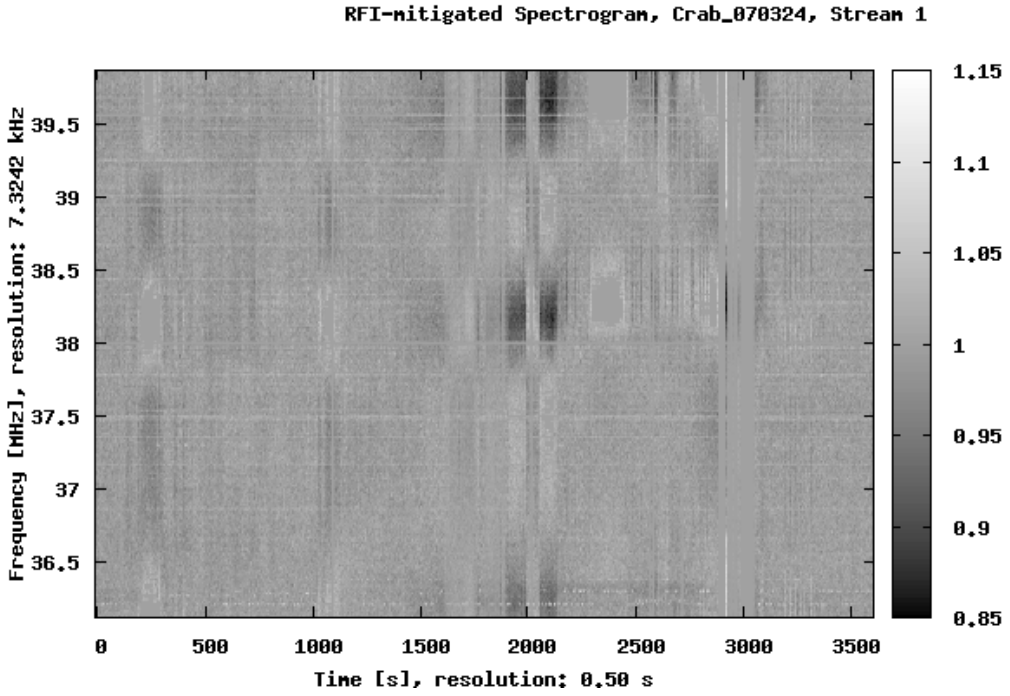

Figure E.20: Dataset: Crab_070324. Spectrogram after RFI mitigation, stream 1 (4B).

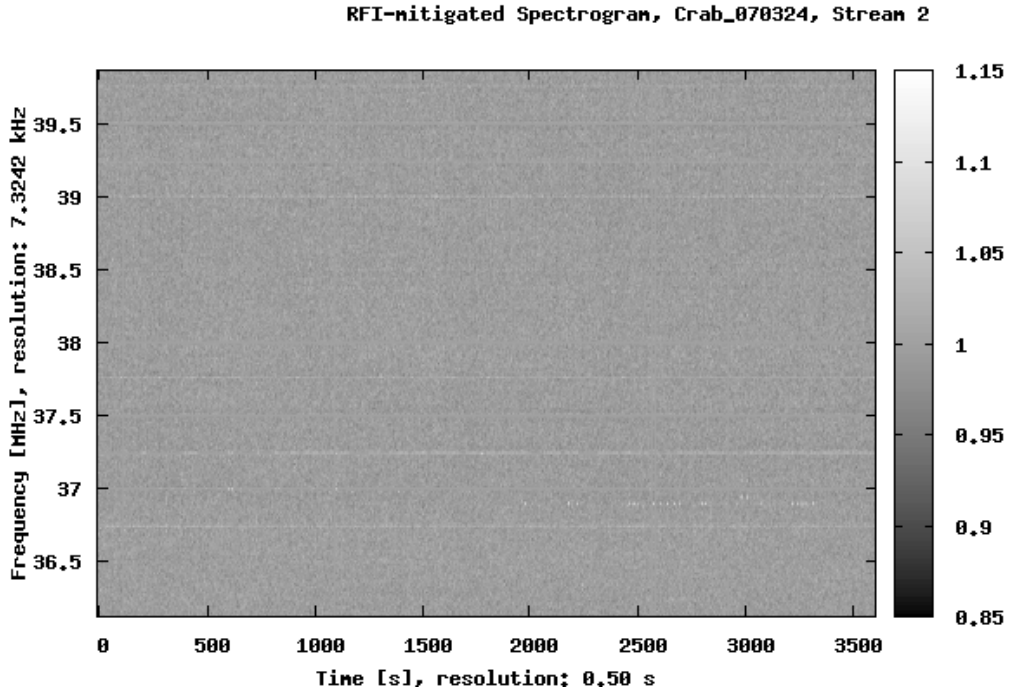

Figure E.21: Dataset: Crab_070324. Spectrogram after RFI mitigation, stream 2 (6B).

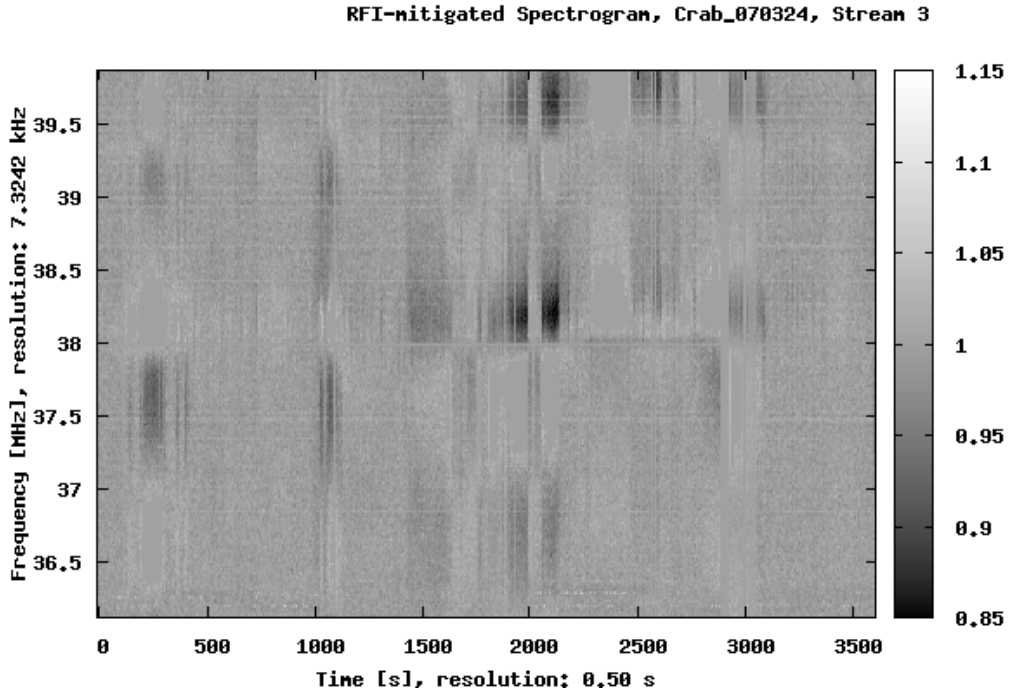

Figure E.22: Dataset: Crab_070324. Spectrogram after RFI mitigation, stream 3 (2B).

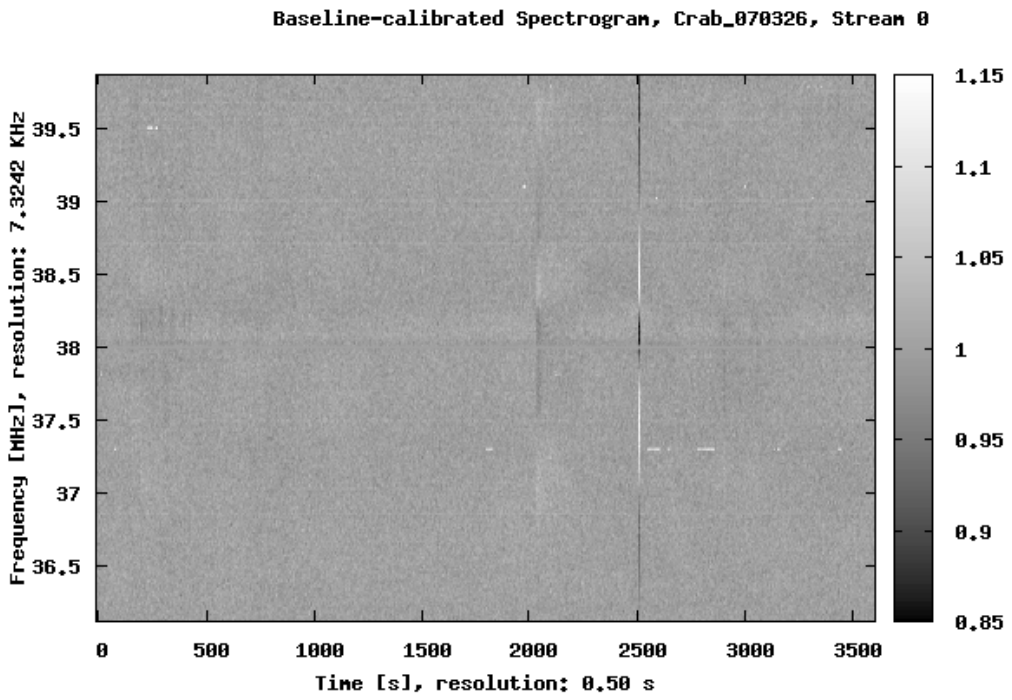

Figure E.23: Dataset: Crab_070326. Calibrated Spectrogram, stream 0 (1B).

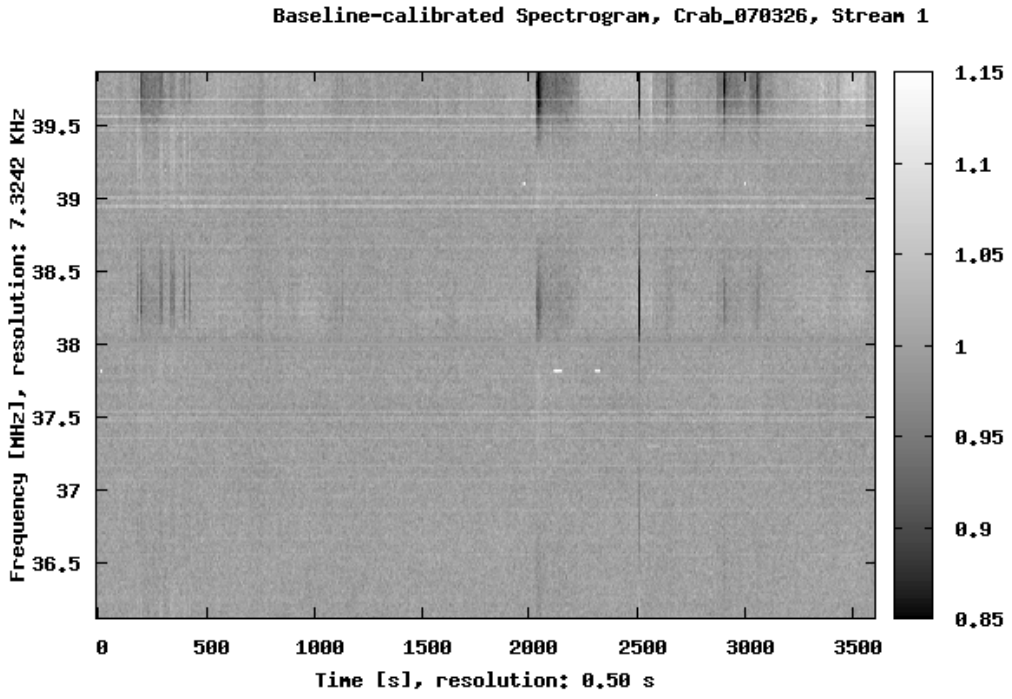

Figure E.24: Dataset: Crab_070326. Calibrated Spectrogram, stream 1 (4B).

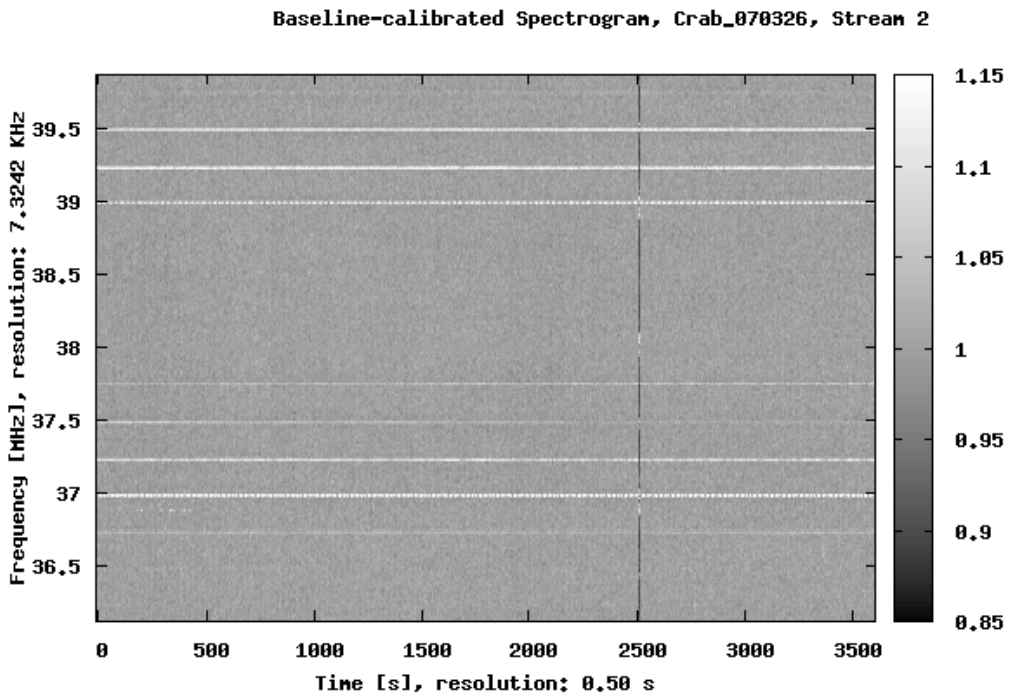

Figure E.25: Dataset: Crab_070326. Calibrated Spectrogram, stream 2 (6B).

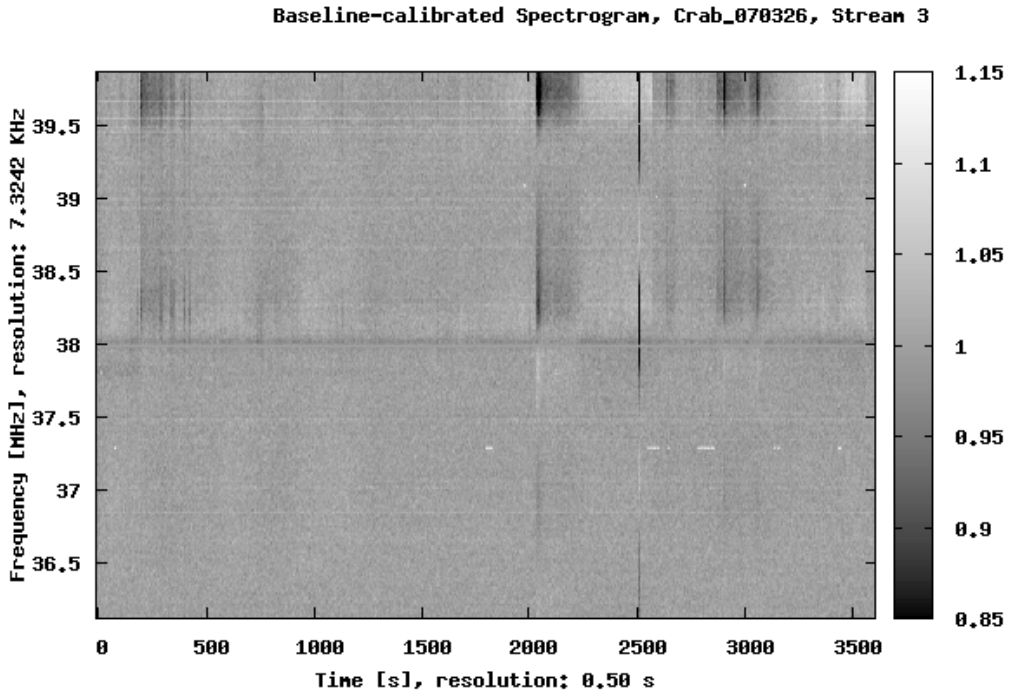

Figure E.26: Dataset: Crab_070326. Calibrated Spectrogram, stream 3 (2B).

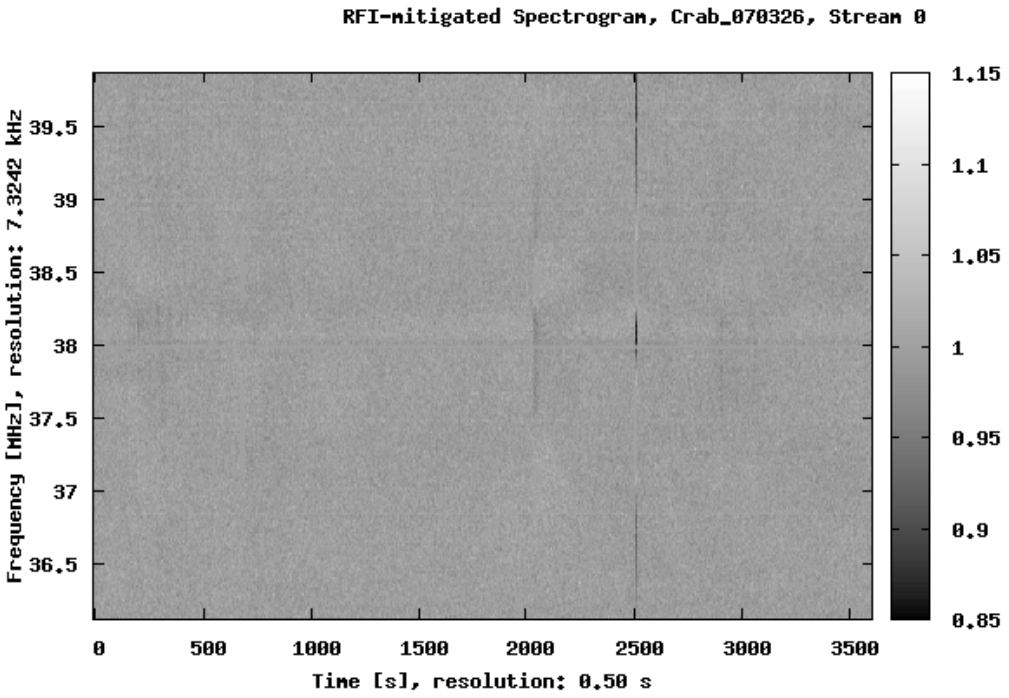

Figure E.27: Dataset: Crab_070326. Spectrogram after RFI mitigation, stream 0 (1B).

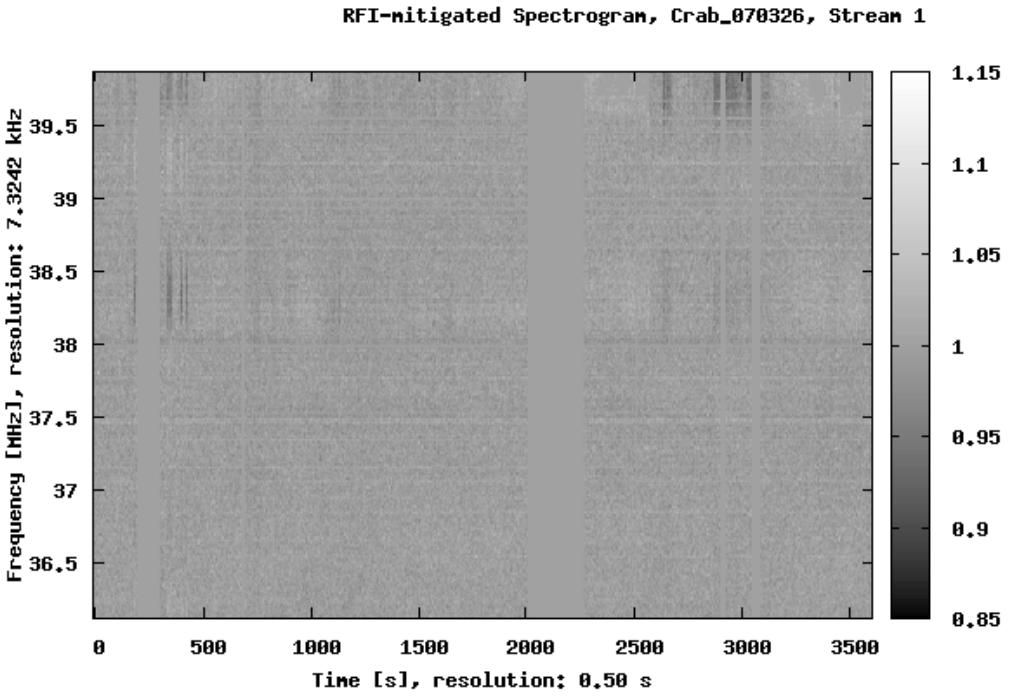

Figure E.28: Dataset: Crab_070326. Spectrogram after RFI mitigation, stream 1 (4B).

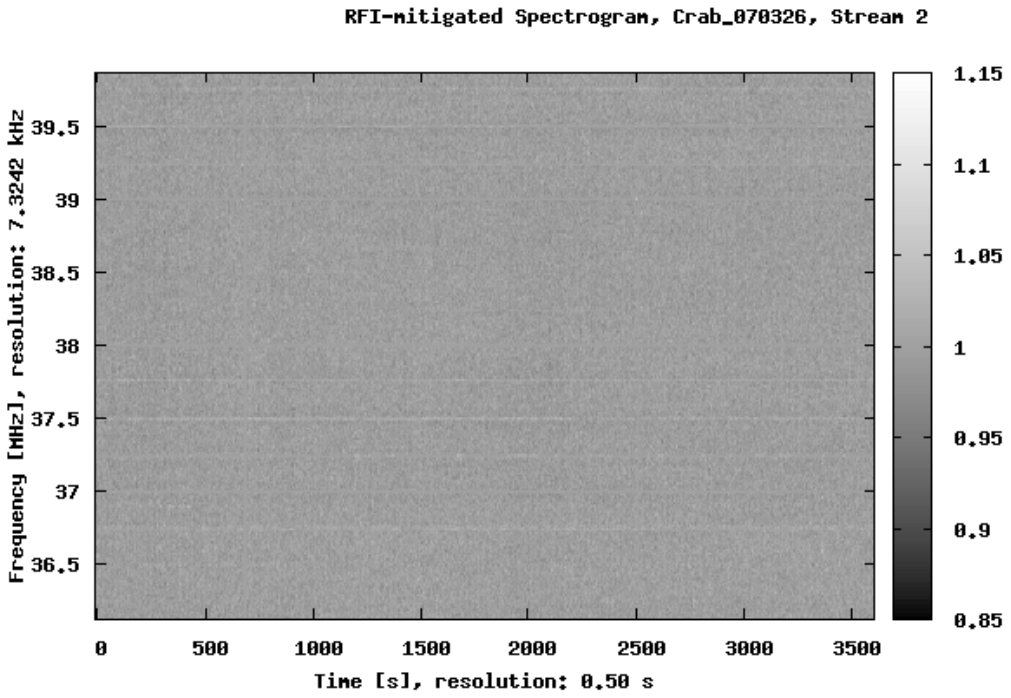

Figure E.29: Dataset: Crab_070326. Spectrogram after RFI mitigation, stream 2 (6B).

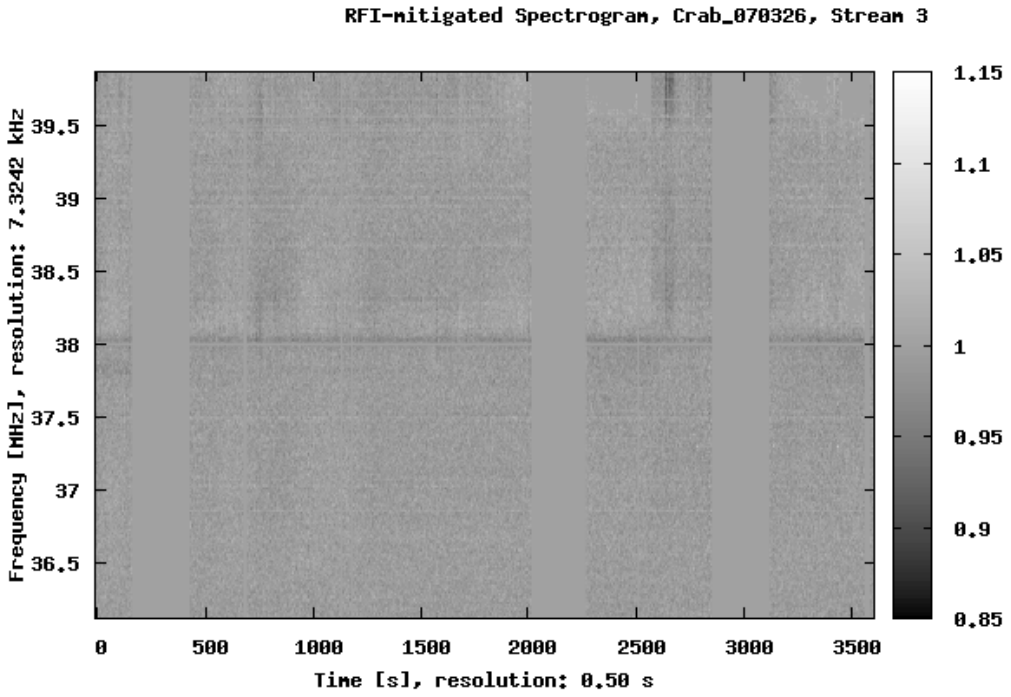

Figure E.30: Dataset: Crab_070326. Spectrogram after RFI mitigation, stream 3 (2B).

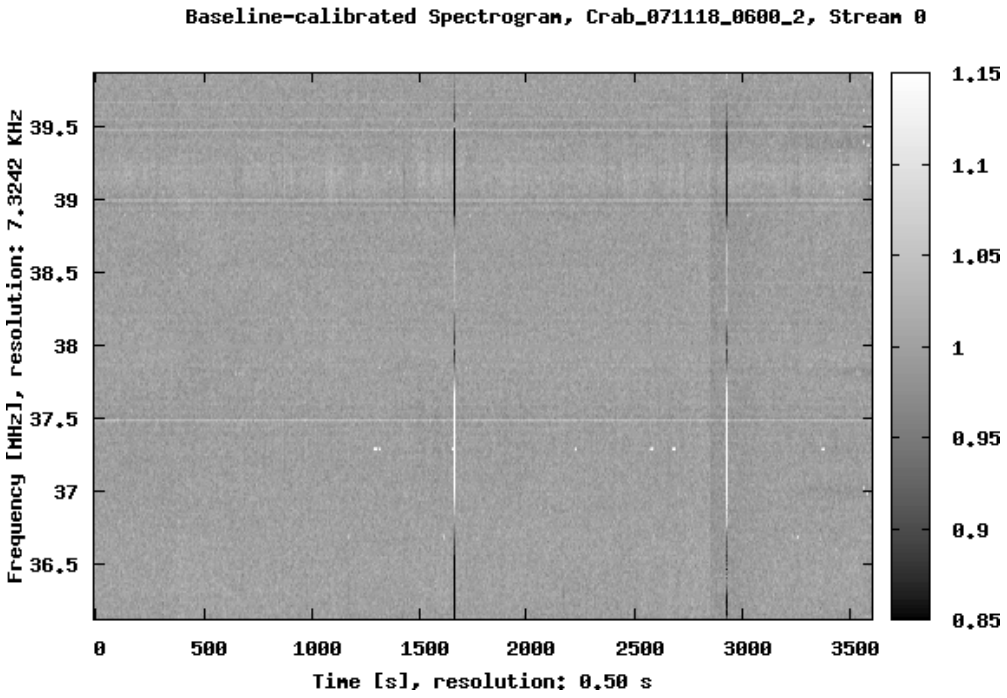

Figure E.31: Dataset: 071118_0600. Calibrated Spectrogram, stream 0 (1B).

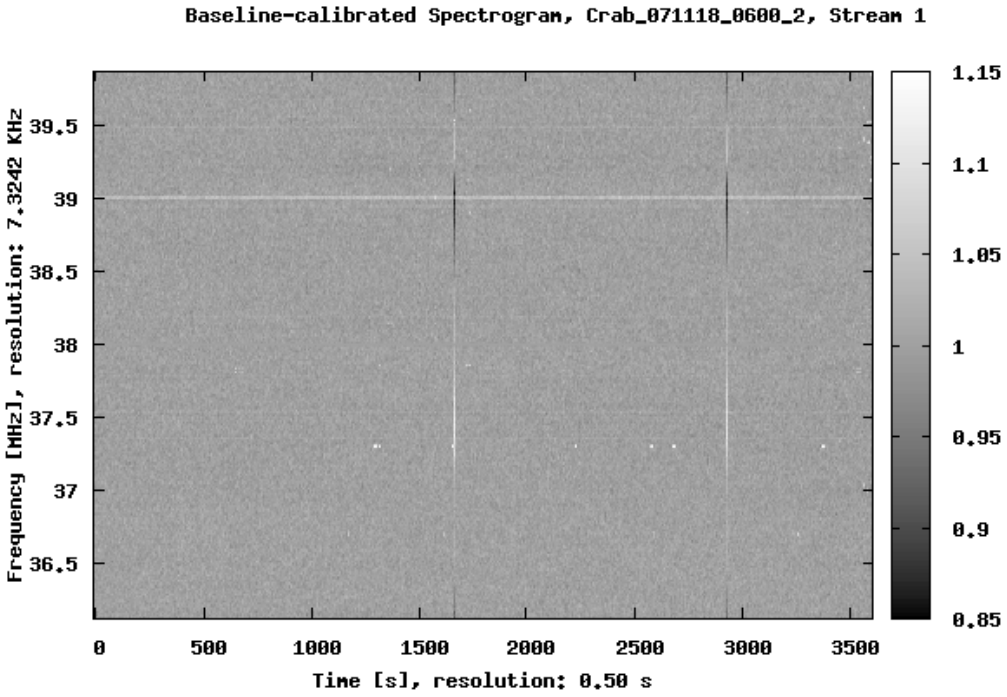

Figure E.32: Dataset: 071118_0600. Calibrated Spectrogram, stream 1 (8B).

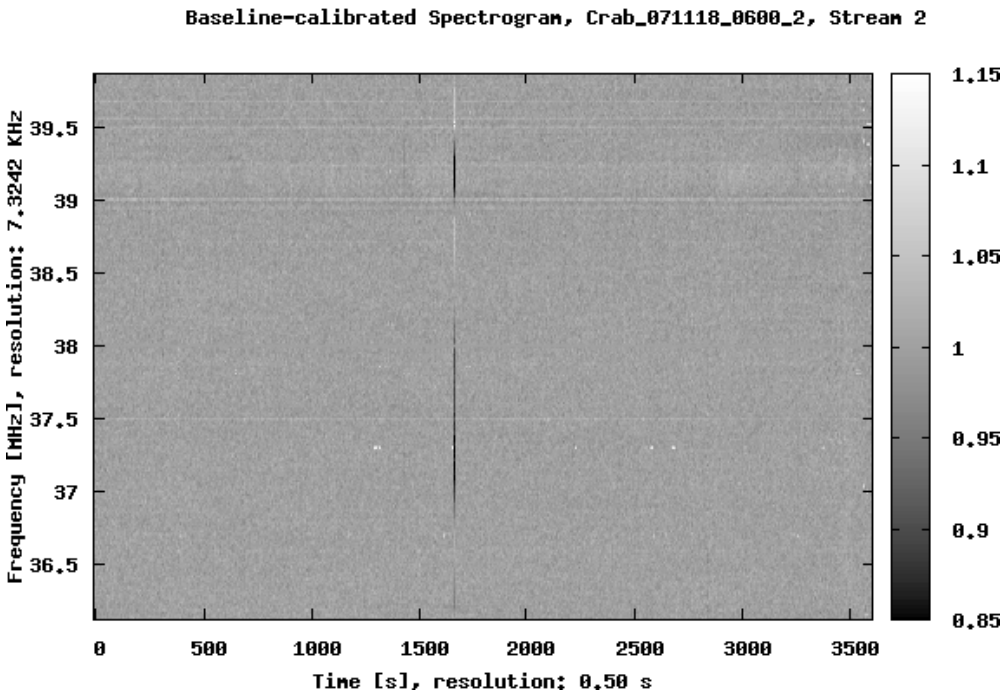

Figure E.33: Dataset: 071118_0600. Calibrated Spectrogram, stream 2 (6B).

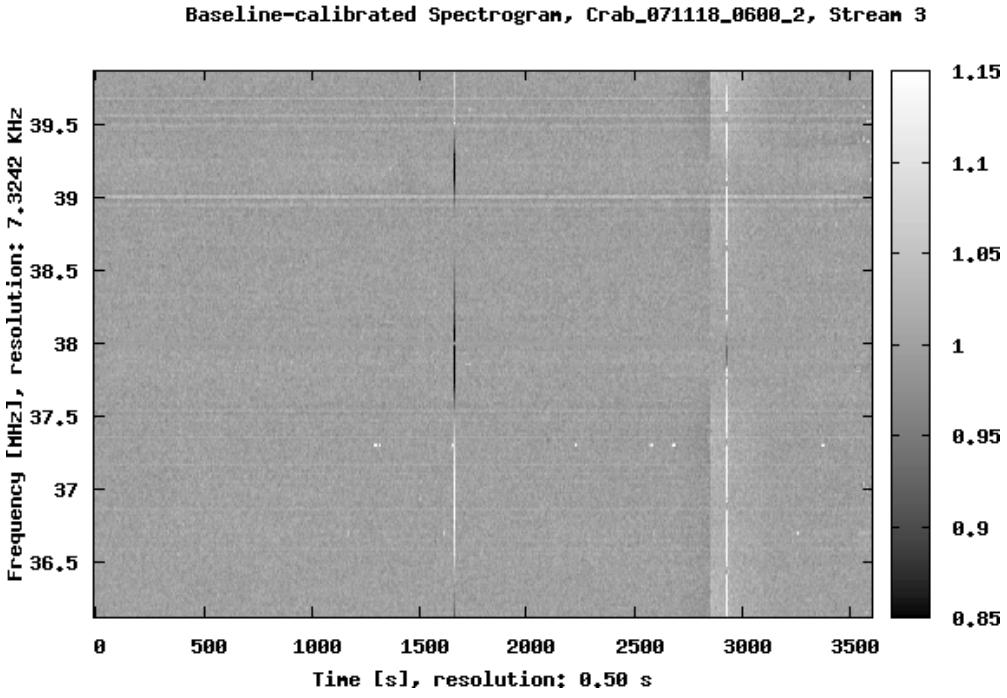

Figure E.34: Dataset: 071118_0600. Calibrated Spectrogram, stream 3 (2B).

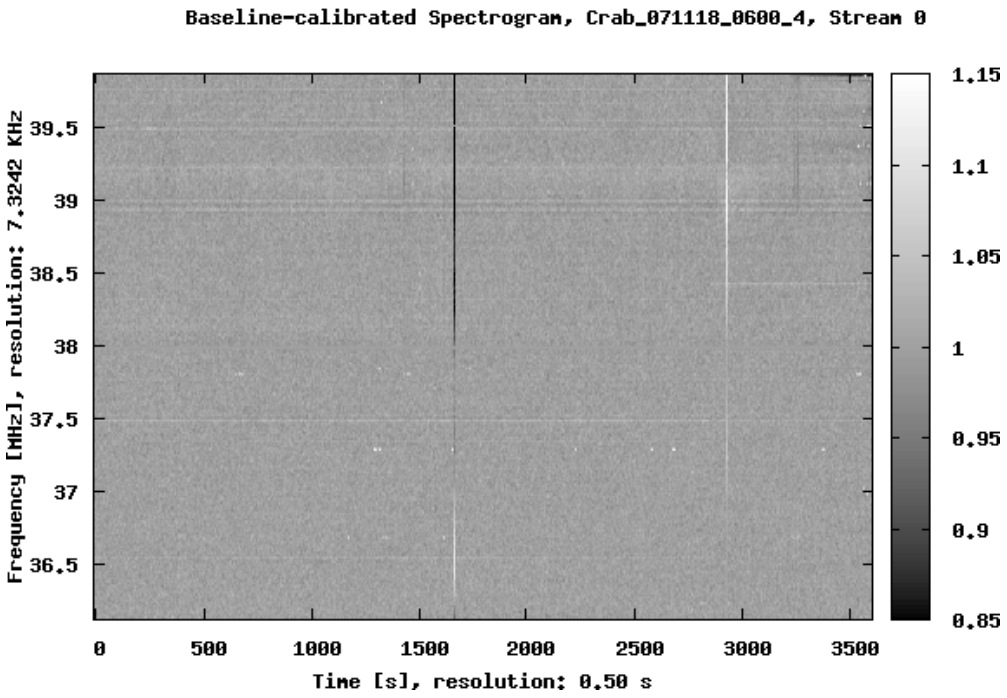

Figure E.35: Dataset: 071118_0600. Calibrated Spectrogram, stream 4 (9B).

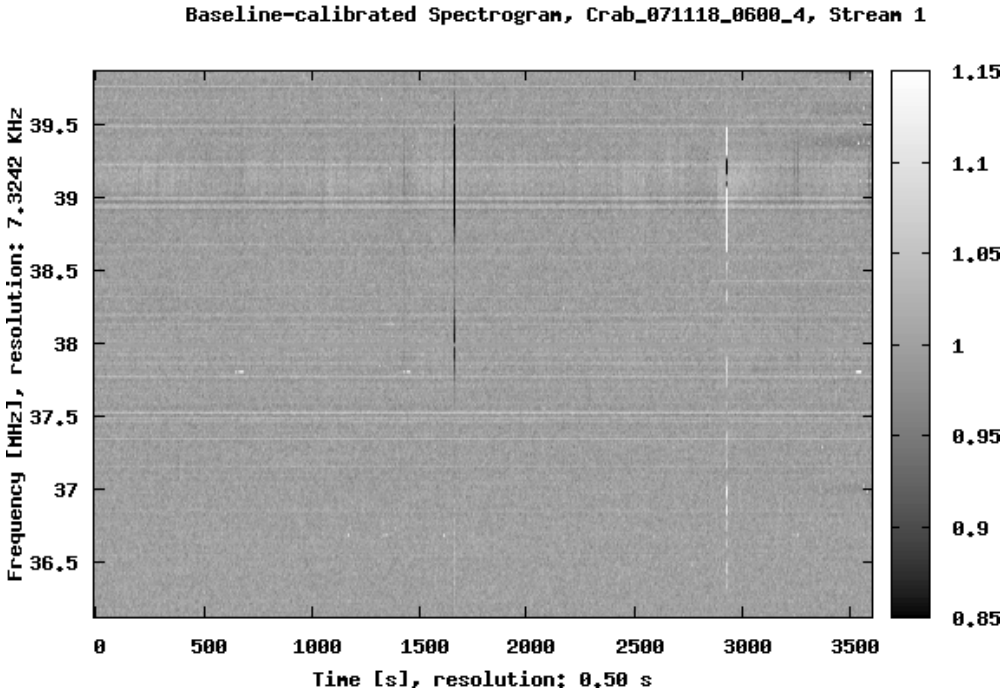

Figure E.36: Dataset: 071118_0600. Calibrated Spectrogram, stream 5 (4Y).

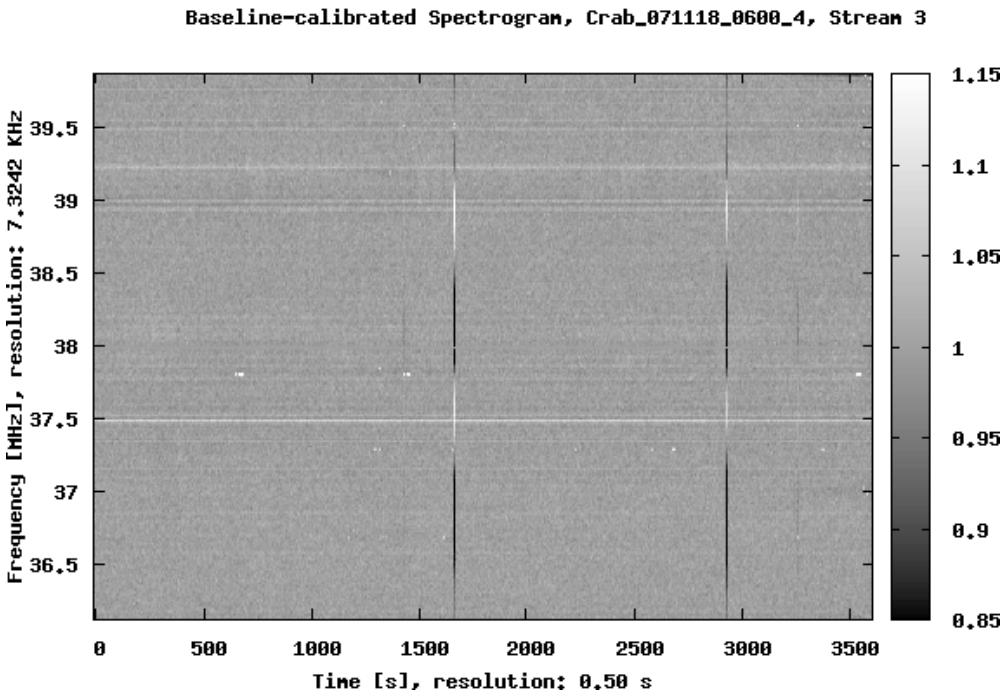

Figure E.37: Dataset: 071118_0600. Calibrated Spectrogram, stream 7 (3Y).

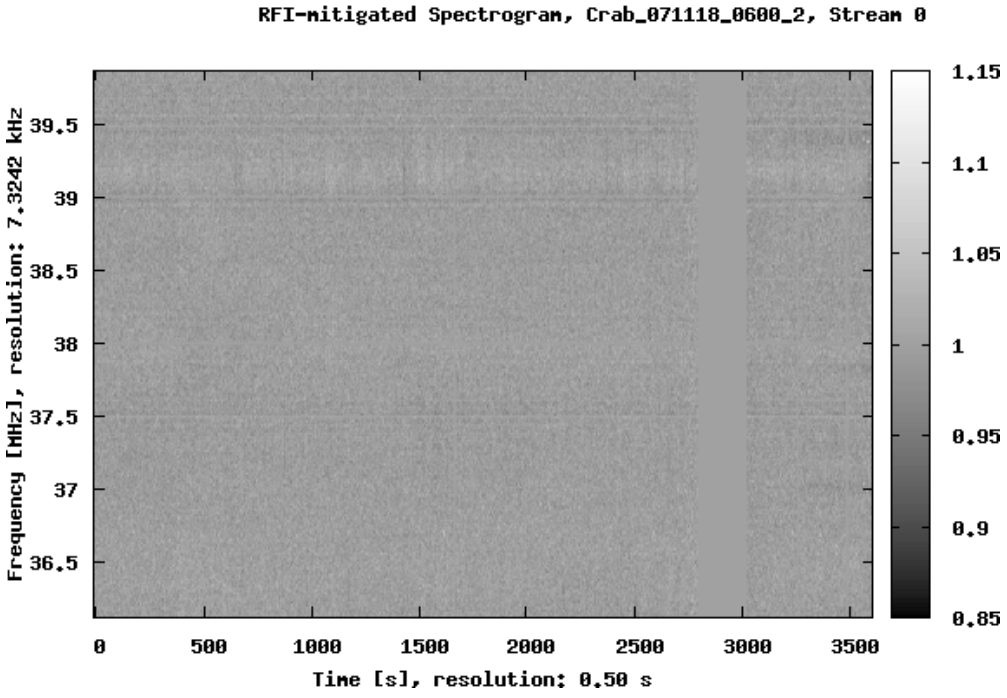

Figure E.38: Dataset: 071118_0600. Spectrogram after RFI mitigation, stream 0 (1B).

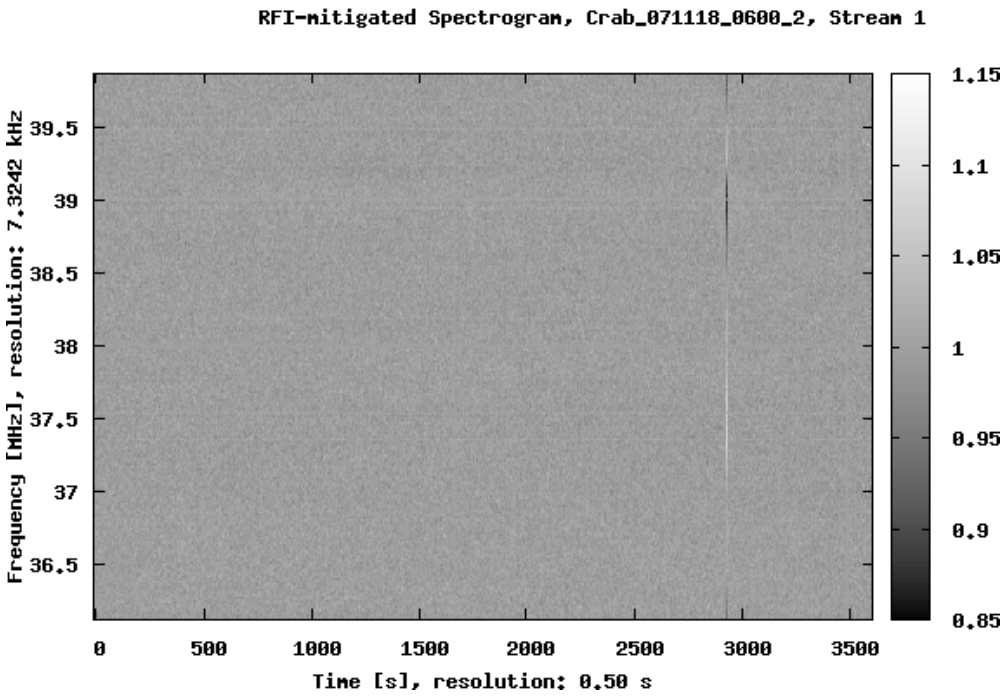

Figure E.39: Dataset: 071118_0600. Spectrogram after RFI mitigation, stream 1 (8B).

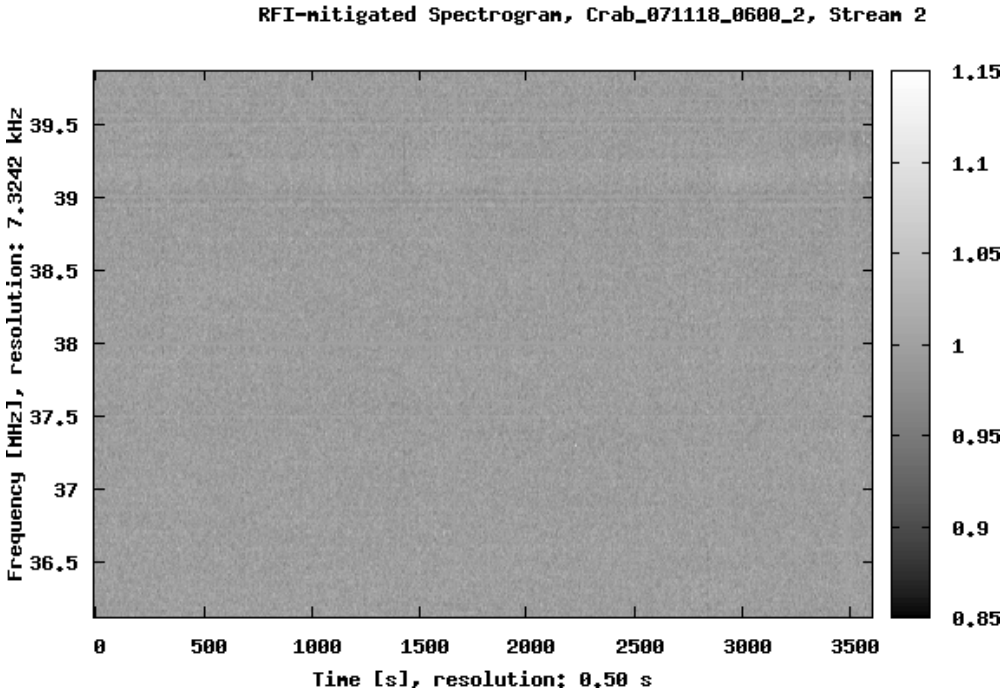

Figure E.40: Dataset: 071118_0600. Spectrogram after RFI mitigation, stream 2 (6B).

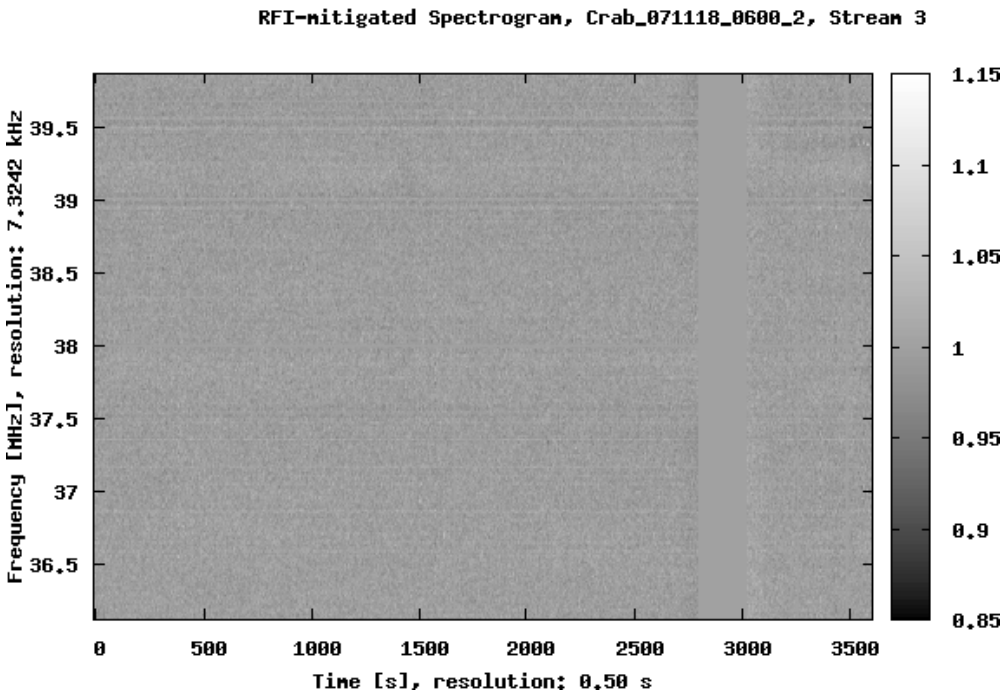

Figure E.41: Dataset: 071118_0600. Spectrogram after RFI mitigation, stream 3 (2B).

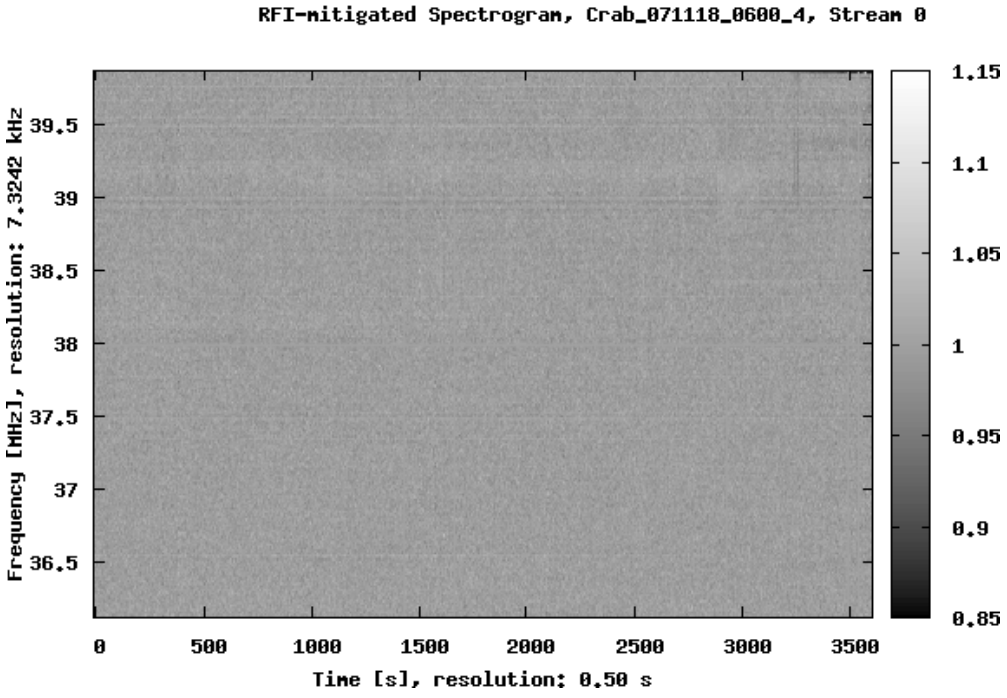

Figure E.42: Dataset: 071118_0600. Spectrogram after RFI mitigation, stream 4 (9B).

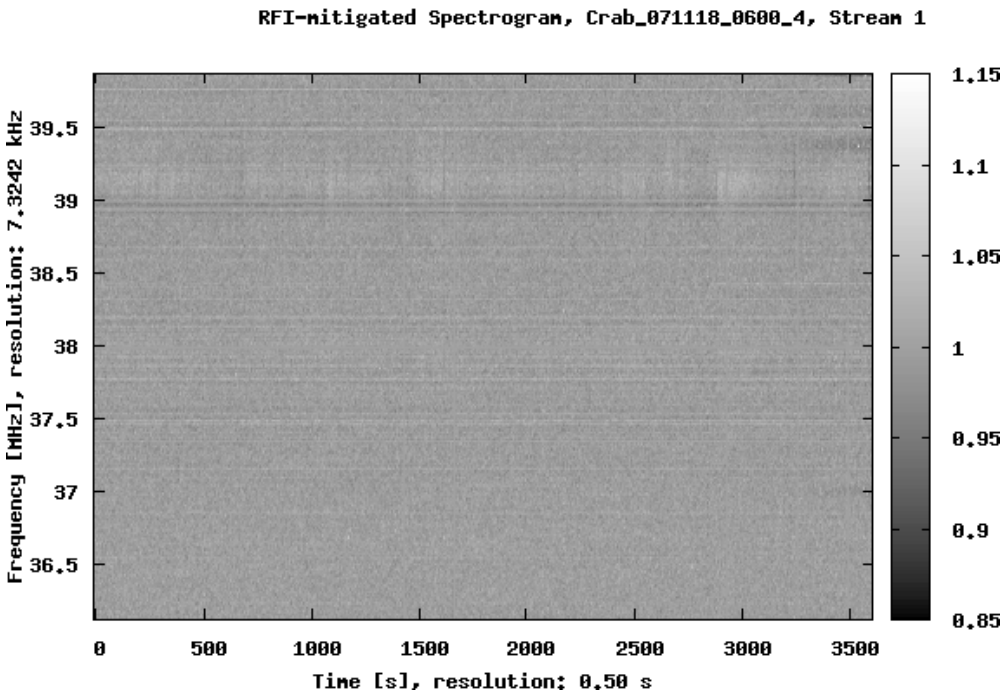

Figure E.43: Dataset: 071118_0600. Spectrogram after RFI mitigation, stream 5 (4Y).

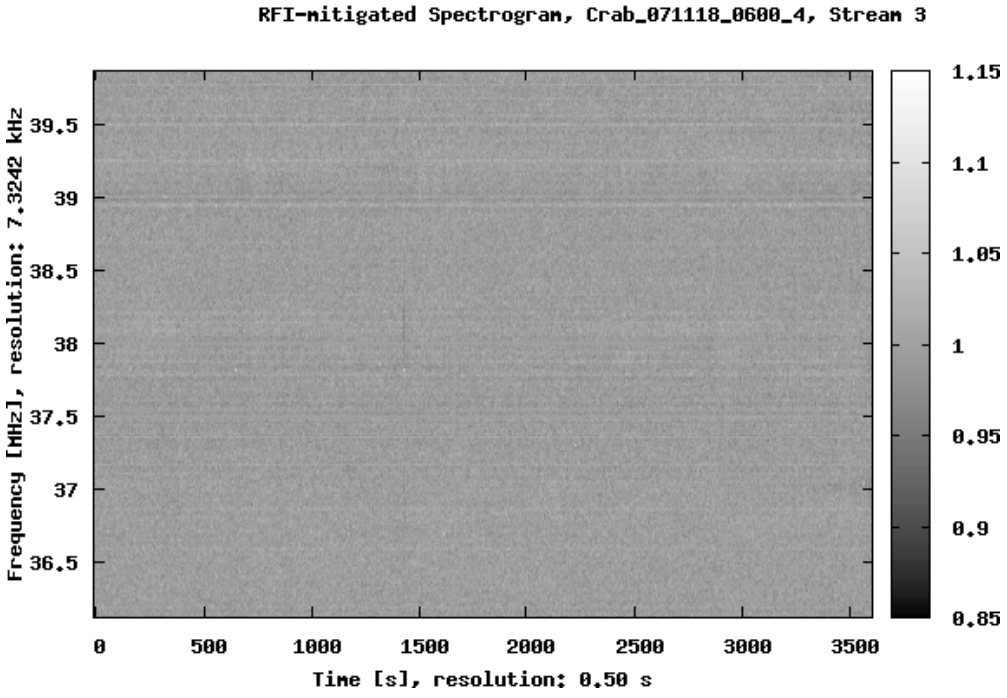

Figure E.44: Dataset: 071118_0600. Spectrogram after RFI mitigation, stream 7 (3Y).

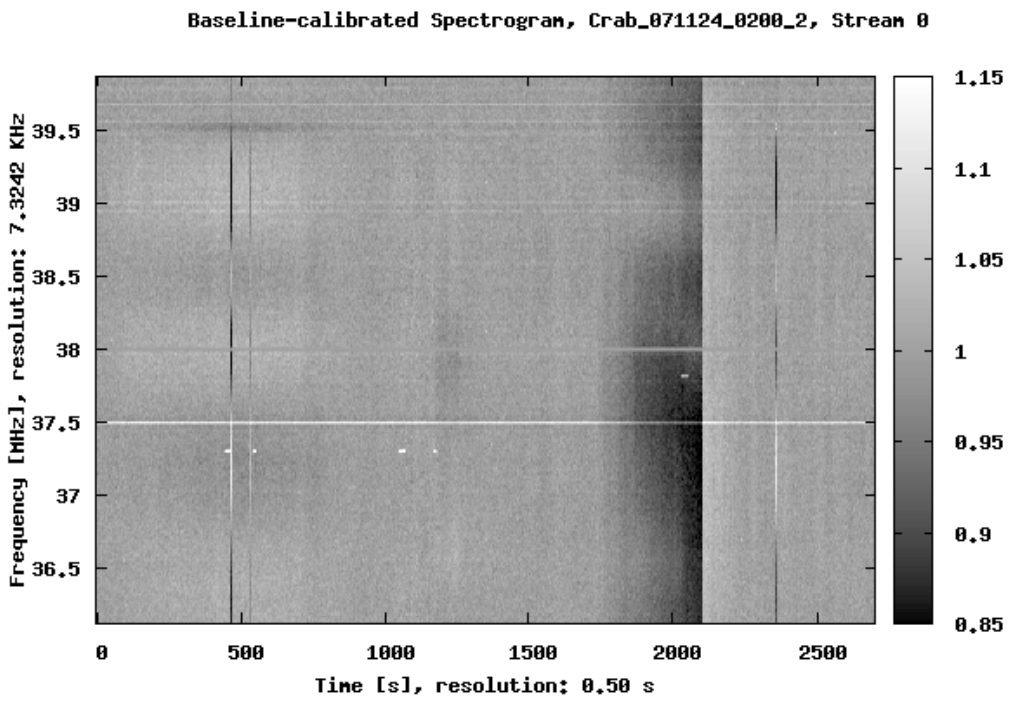

Figure E.45: Dataset: 071124_0200. Calibrated Spectrogram, stream 0 (1B).

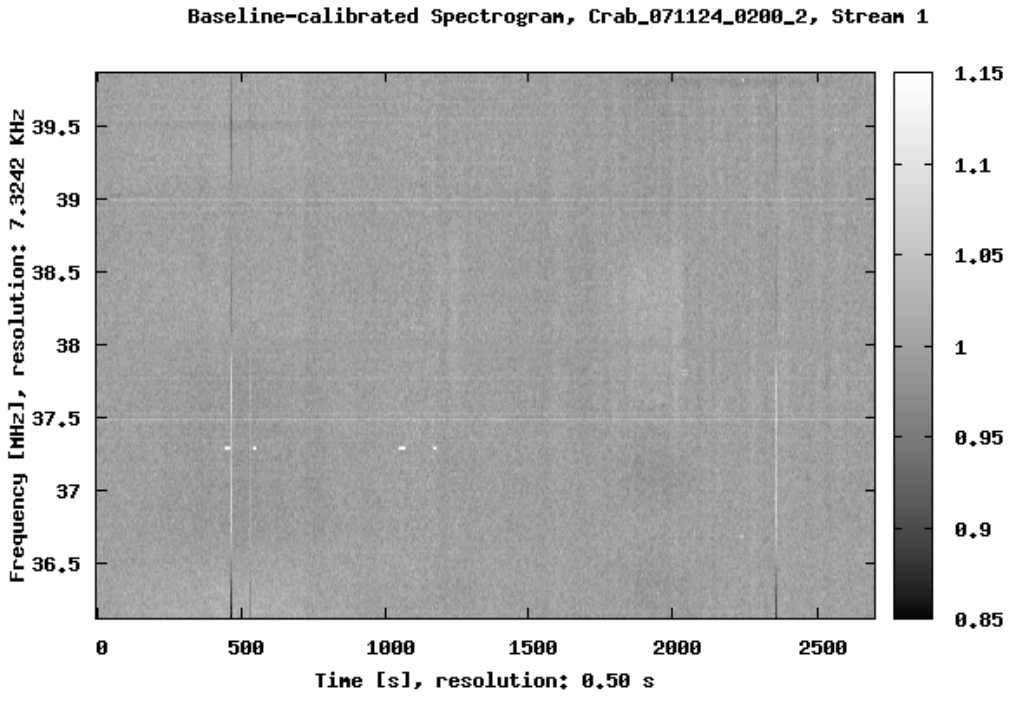

Figure E.46: Dataset: 071124_0200. Calibrated Spectrogram, stream 1 (8B).

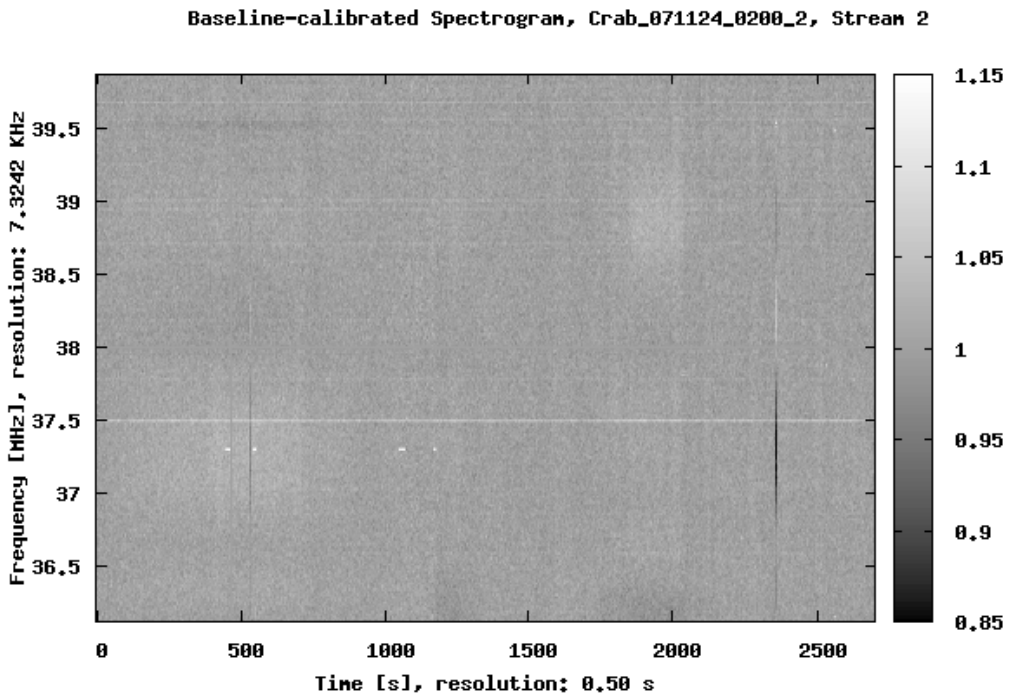

Figure E.47: Dataset: 071124_0200. Calibrated Spectrogram, stream 2 (6B).

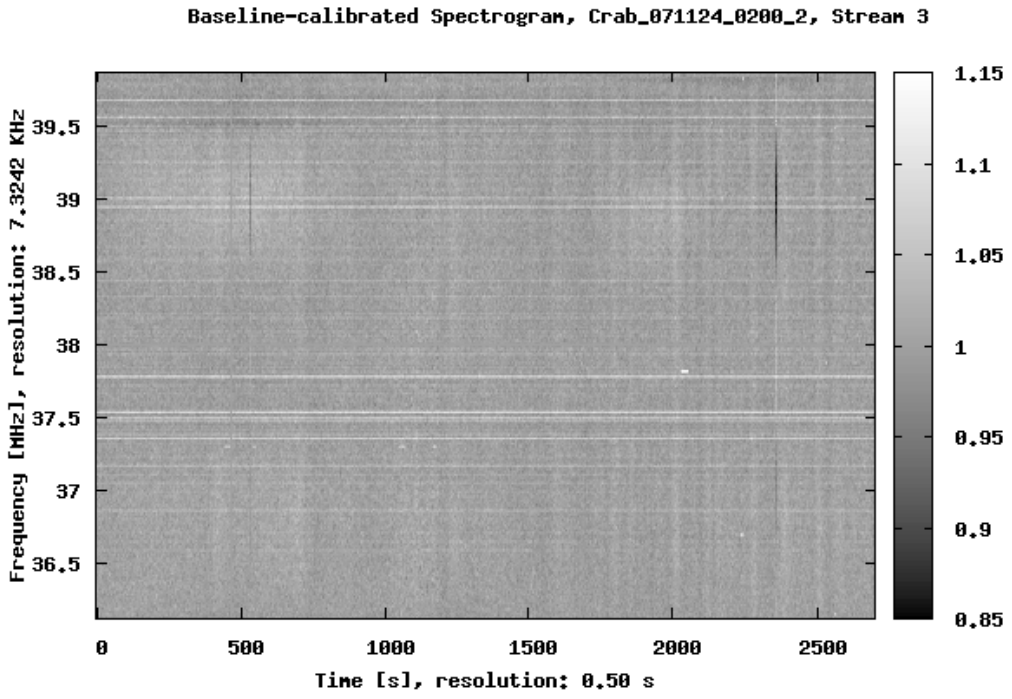

Figure E.48: Dataset: 071124_0200. Calibrated Spectrogram, stream 3 (2B).

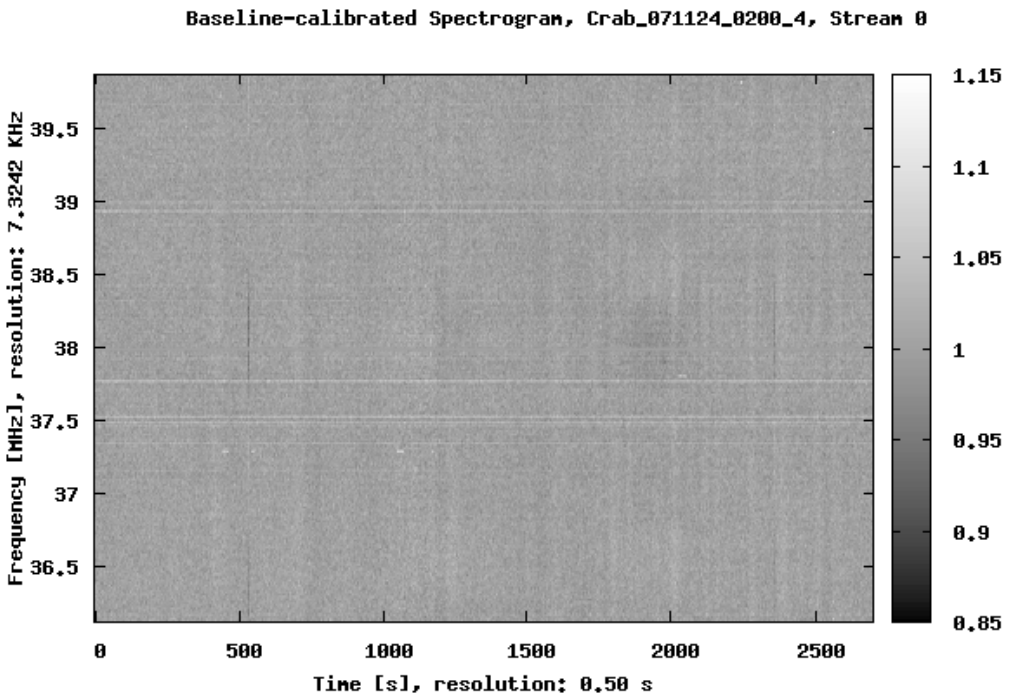

Figure E.49: Dataset: 071124_0200. Calibrated Spectrogram, stream 4 (9B).

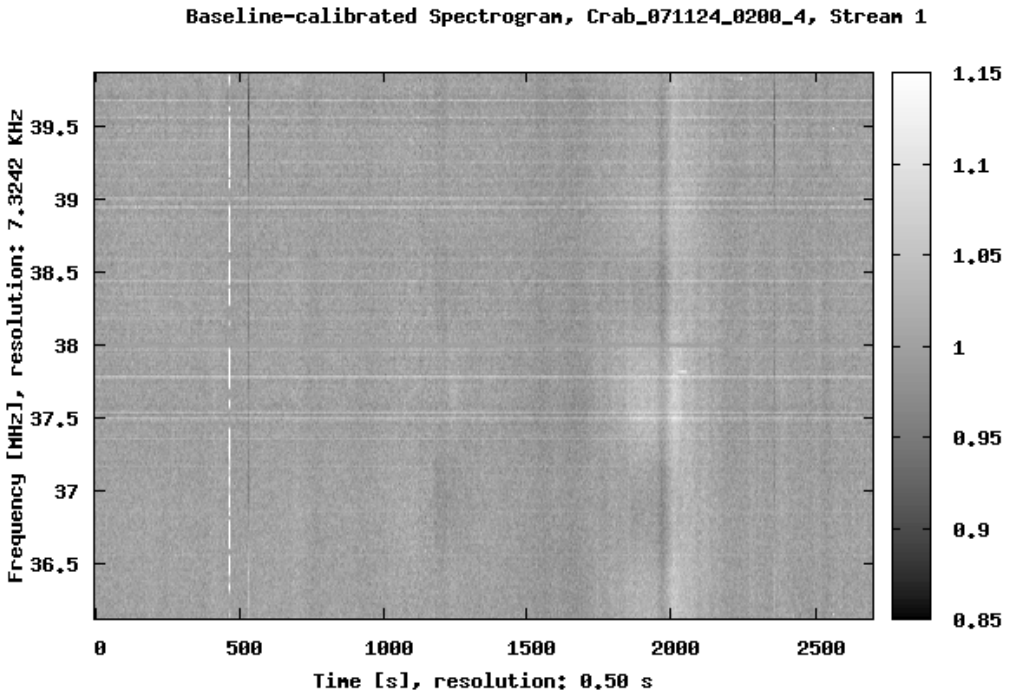

Figure E.50: Dataset: 071124_0200. Calibrated Spectrogram, stream 5 (4Y).

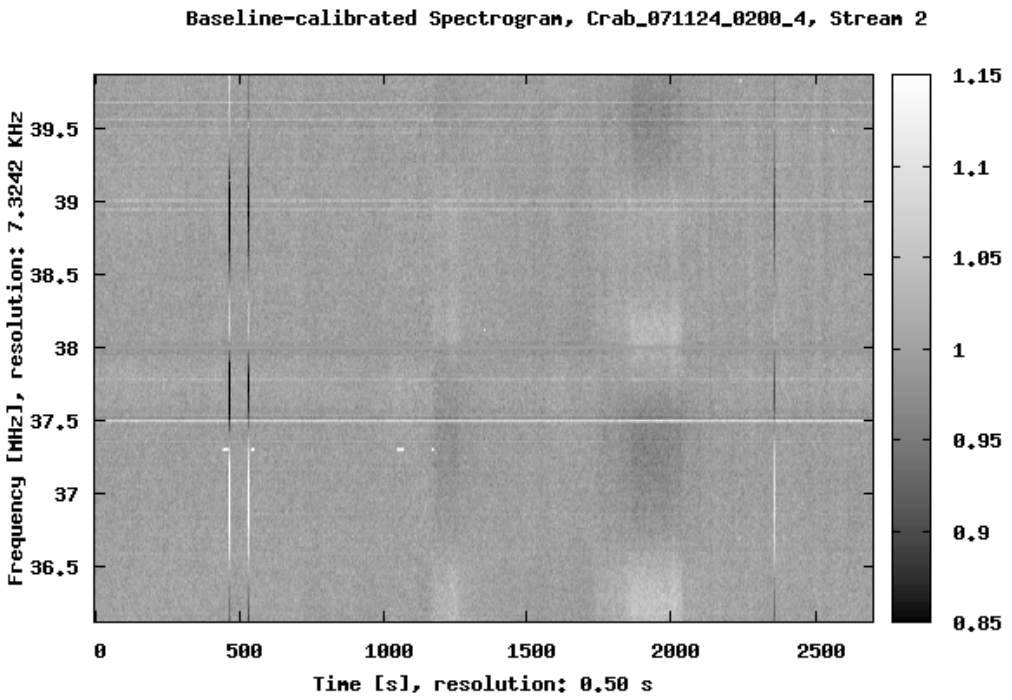

Figure E.51: Dataset: 071124_0200. Calibrated Spectrogram, stream 6 (1Y).

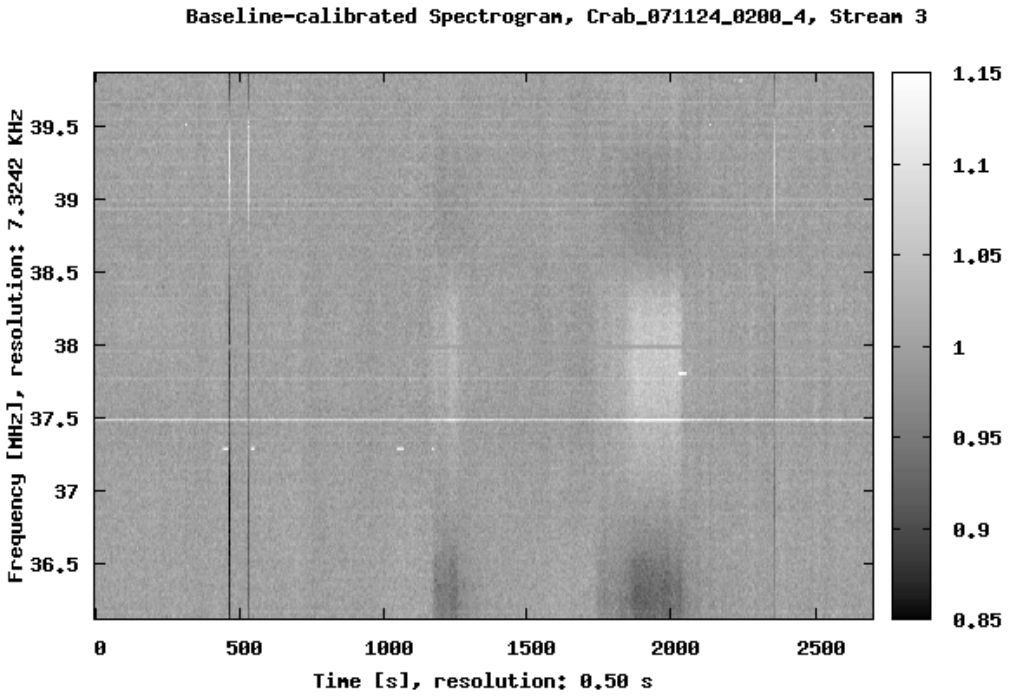

Figure E.52: Dataset: 071124_0200. Calibrated Spectrogram, stream 7 (3Y).

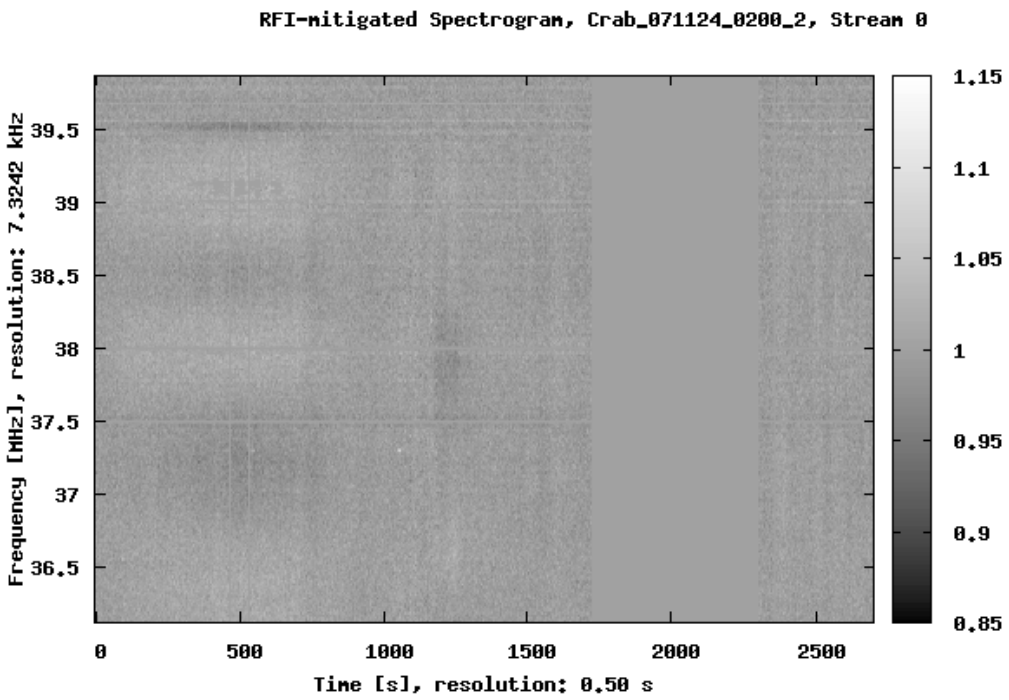

Figure E.53: Dataset: 071124_0200. Spectrogram after RFI mitigation, stream 0 (1B).

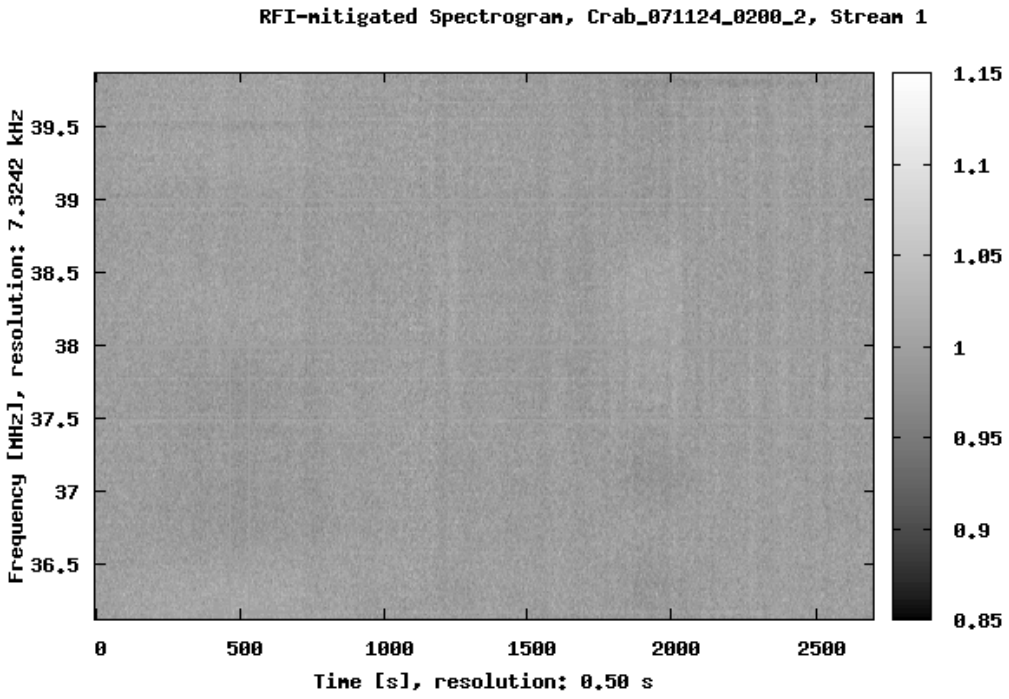

Figure E.54: Dataset: 071124_0200. Spectrogram after RFI mitigation, stream 1 (8B).

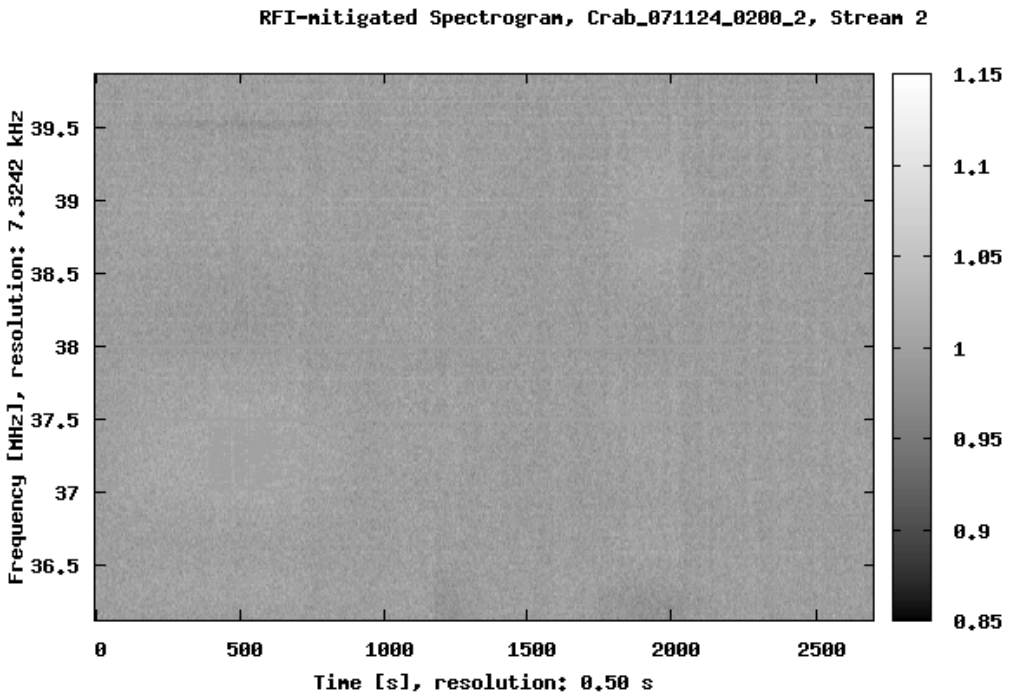

Figure E.55: Dataset: 071124_0200. Spectrogram after RFI mitigation, stream 2 (6B).

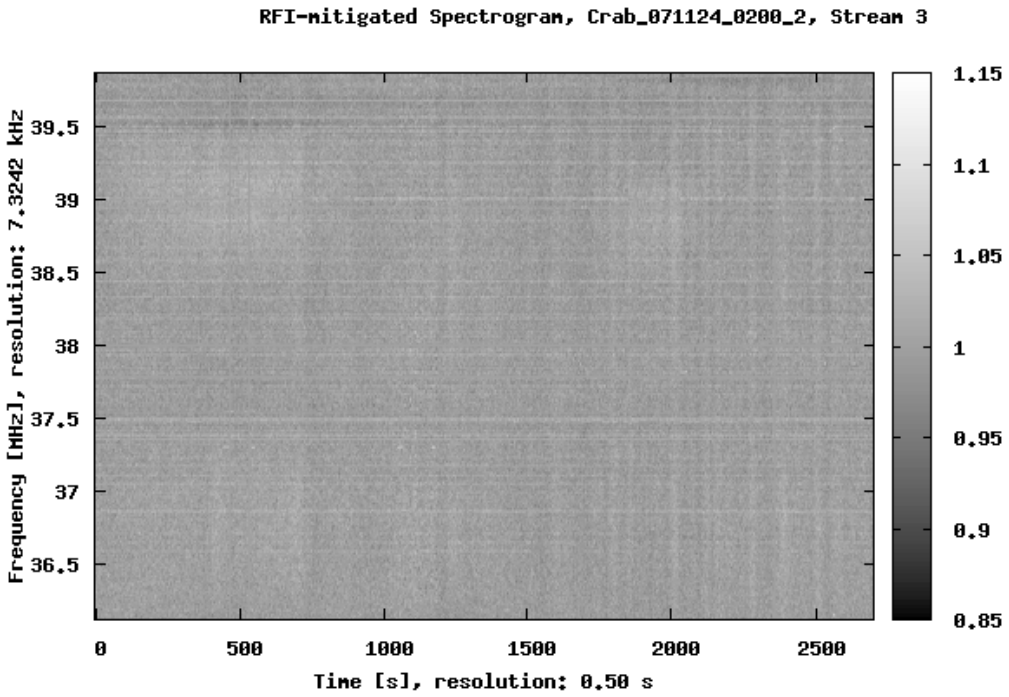

Figure E.56: Dataset: 071124_0200. Spectrogram after RFI mitigation, stream 3 (2B).

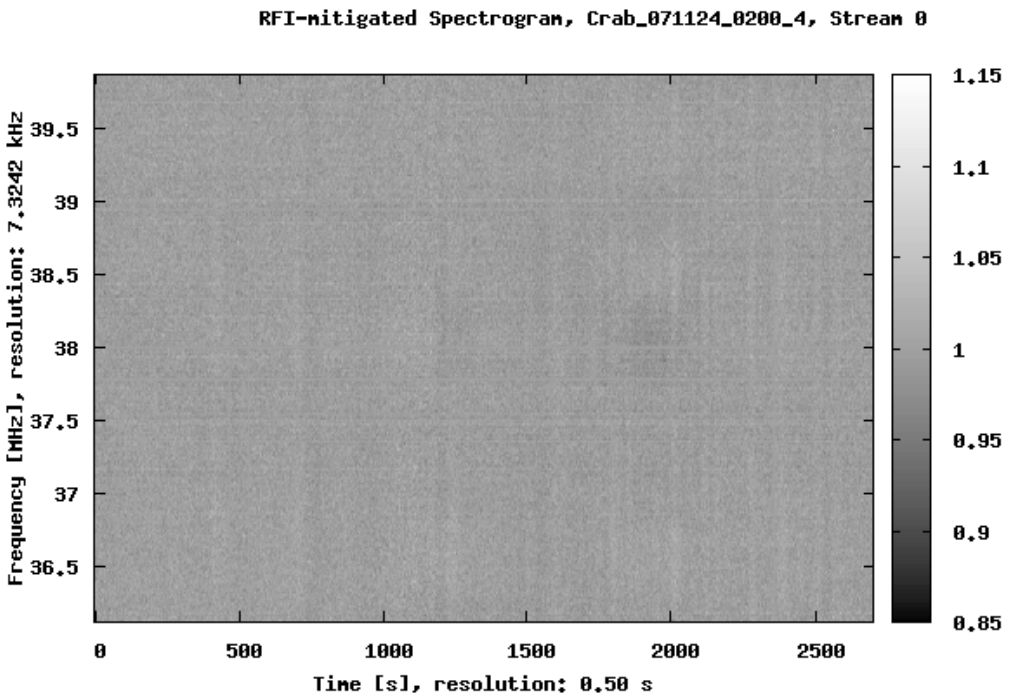

Figure E.57: Dataset: 071124_0200. Spectrogram after RFI mitigation, stream 4 (9B).

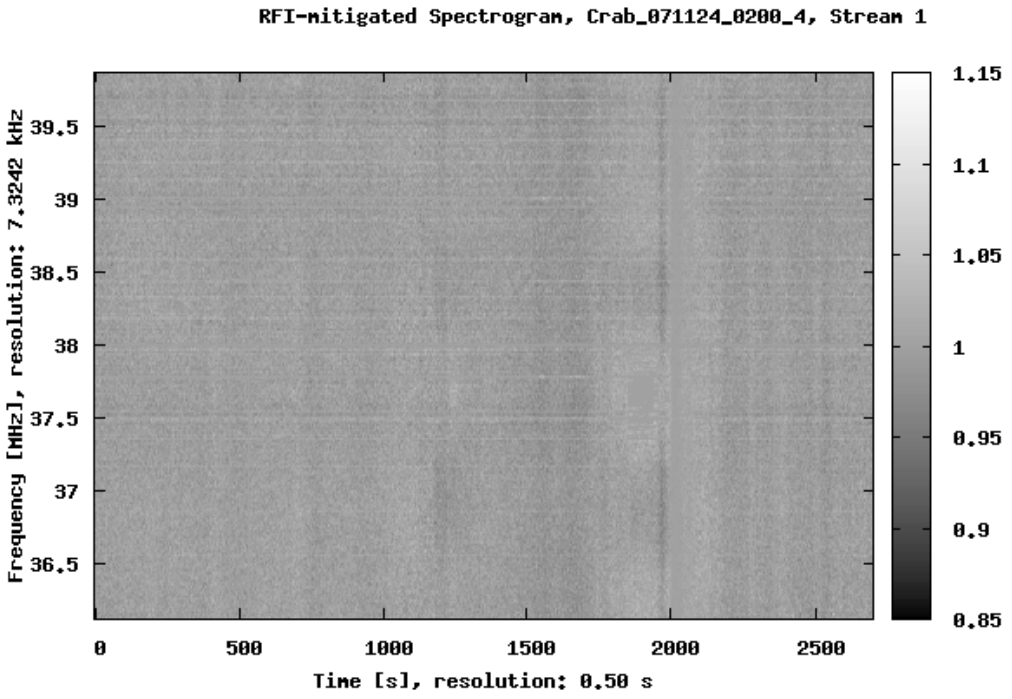

Figure E.58: Dataset: 071124_0200. Spectrogram after RFI mitigation, stream 5 (4Y).

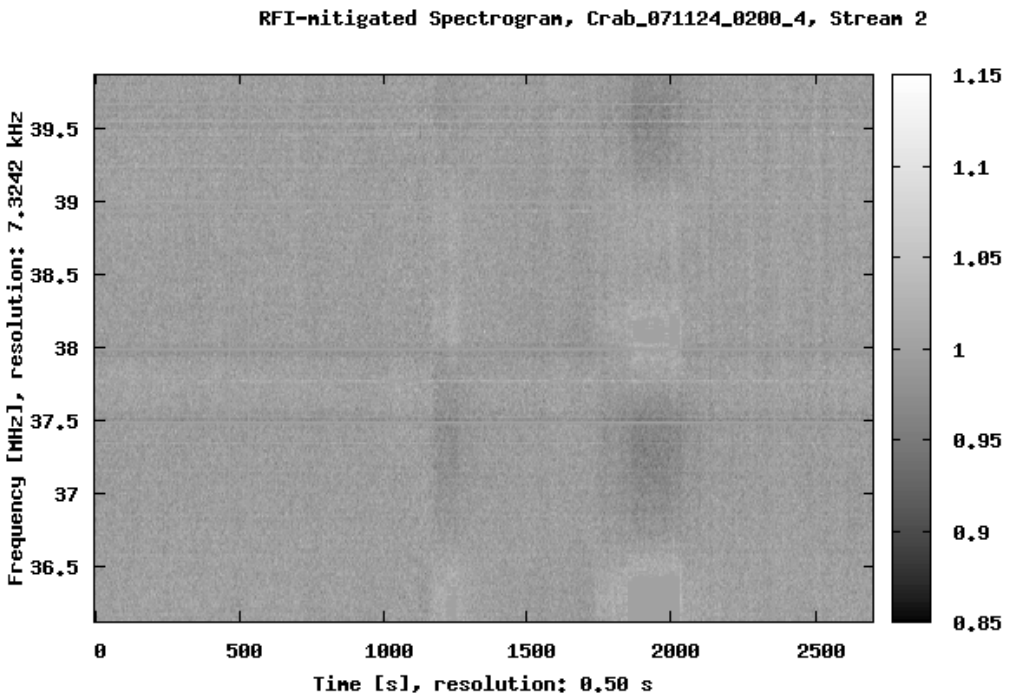

Figure E.59: Dataset: 071124_0200. Spectrogram after RFI mitigation, stream 6 (1Y).

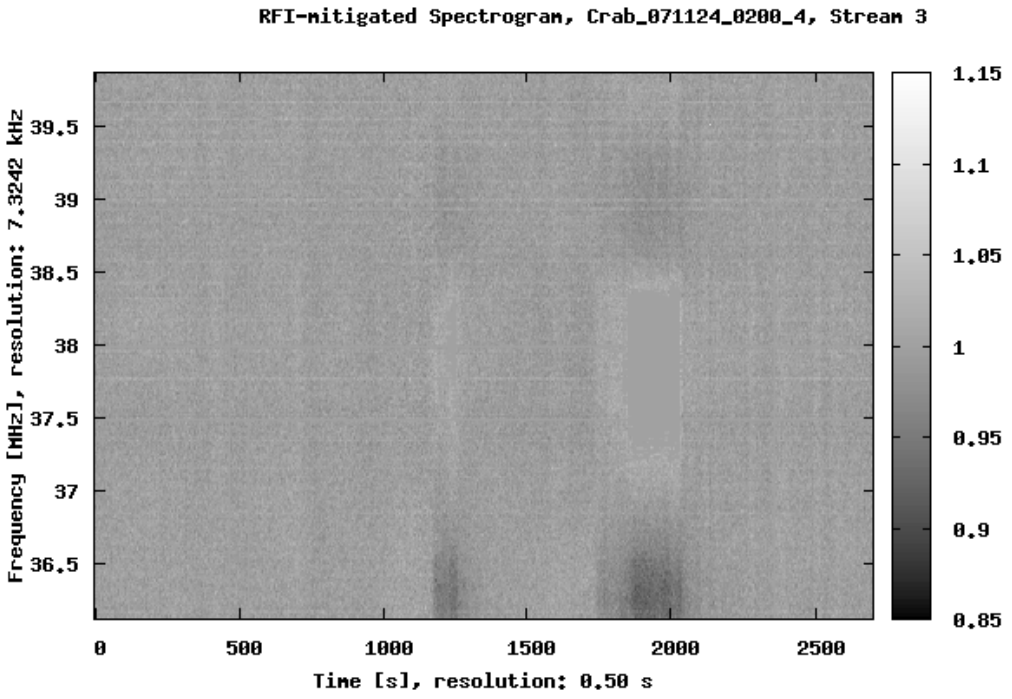

Figure E.60: Dataset: 071124_0200. Spectrogram after RFI mitigation, stream 7 (3Y).

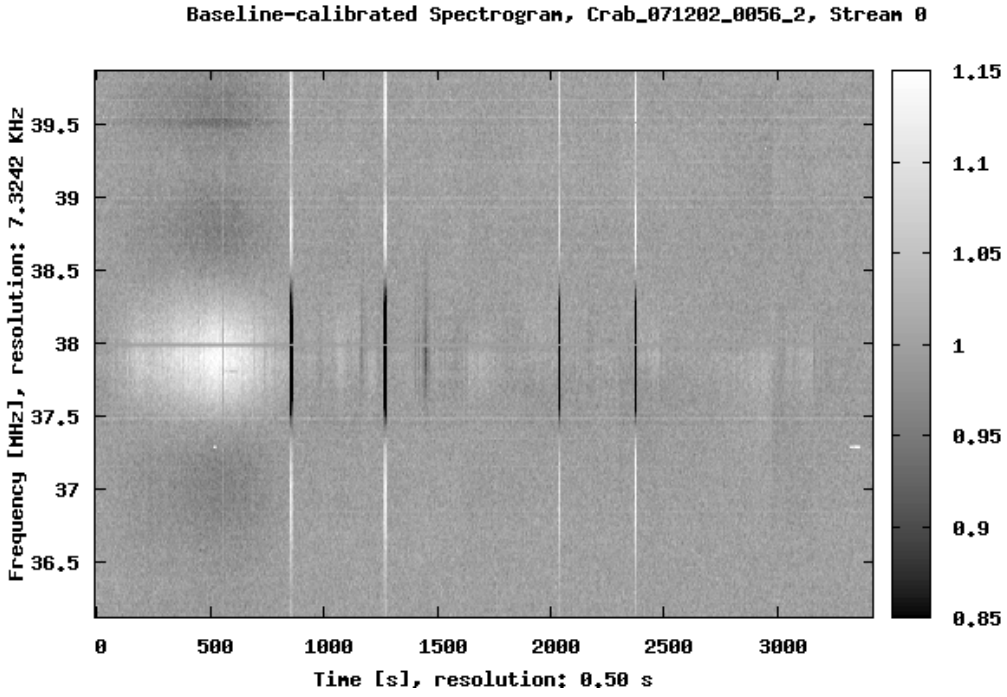

Figure E.61: Dataset: 071202_0056. Calibrated Spectrogram, stream 0 (1B).

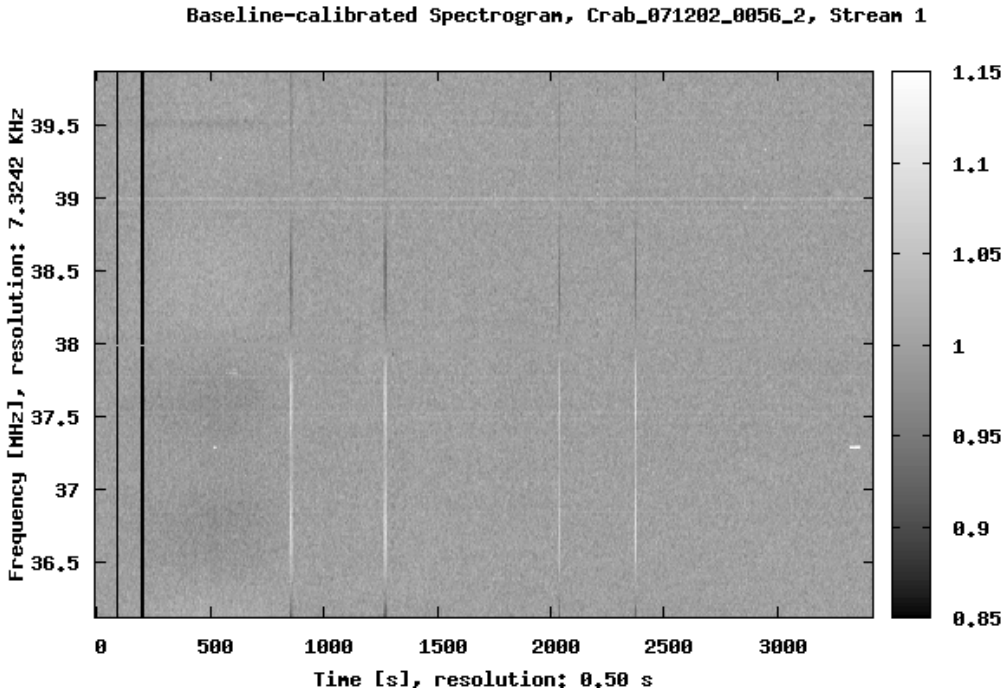

Figure E.62: Dataset: 071202_0056. Calibrated Spectrogram, stream 1 (8B).

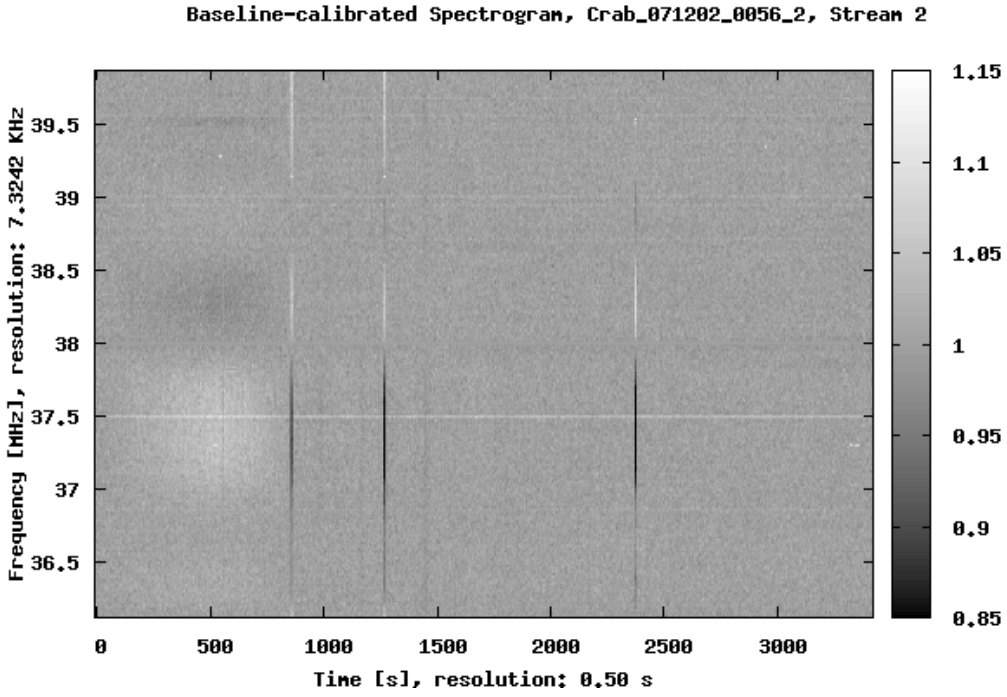

Figure E.63: Dataset: 071202_0056. Calibrated Spectrogram, stream 2 (6B).

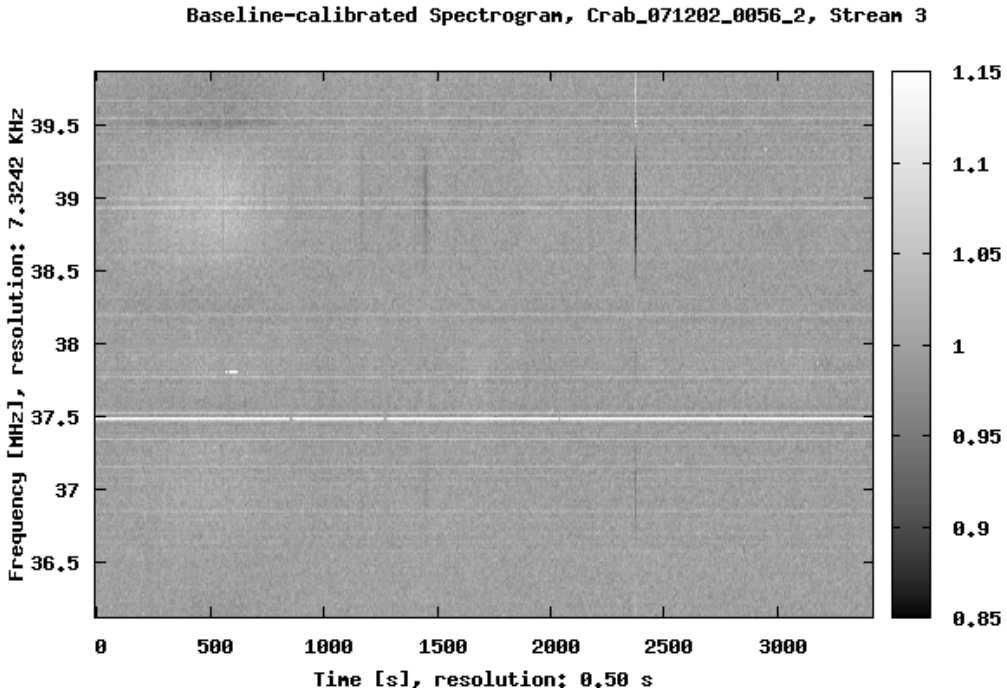

Figure E.64: Dataset: 071202_0056. Calibrated Spectrogram, stream 3 (2B).

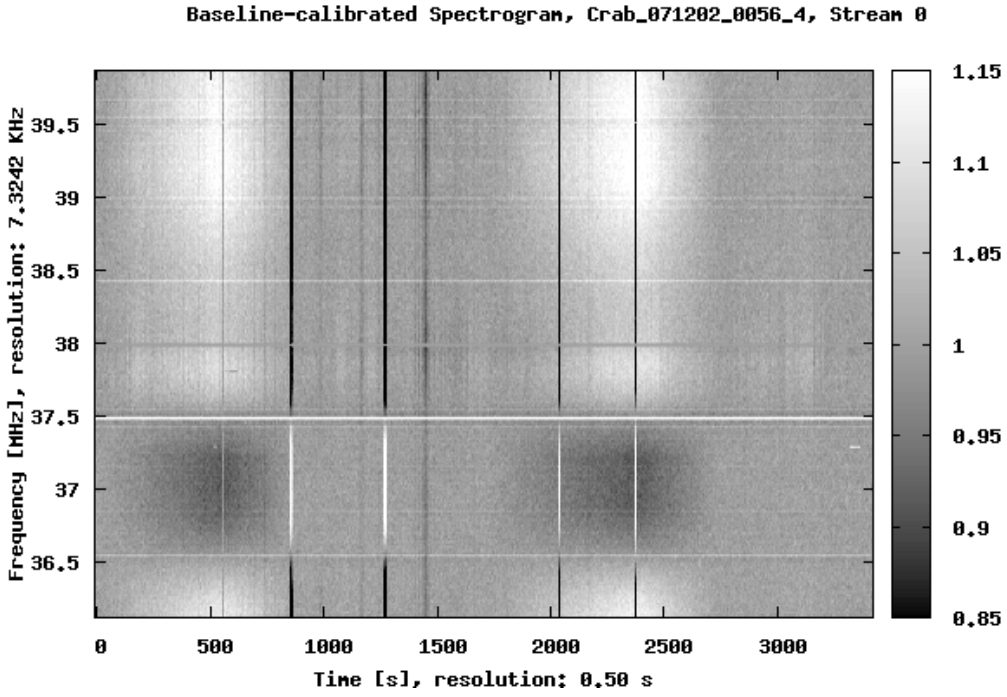

Figure E.65: Dataset: 071202_0056. Calibrated Spectrogram, stream 4 (9B).

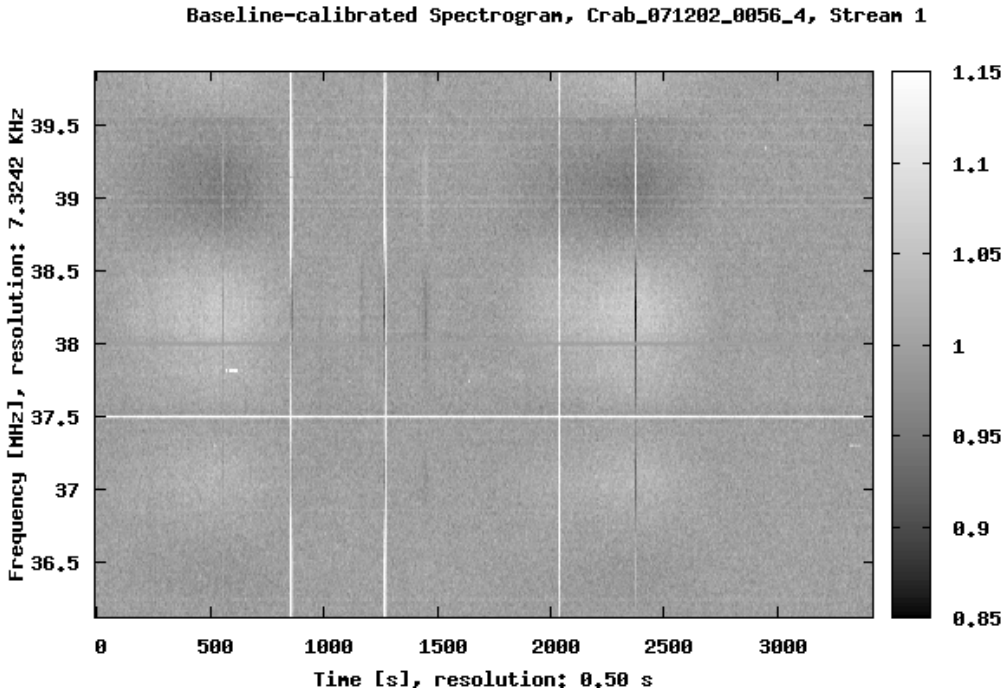

Figure E.66: Dataset: 071202_0056. Calibrated Spectrogram, stream 5 (4Y).

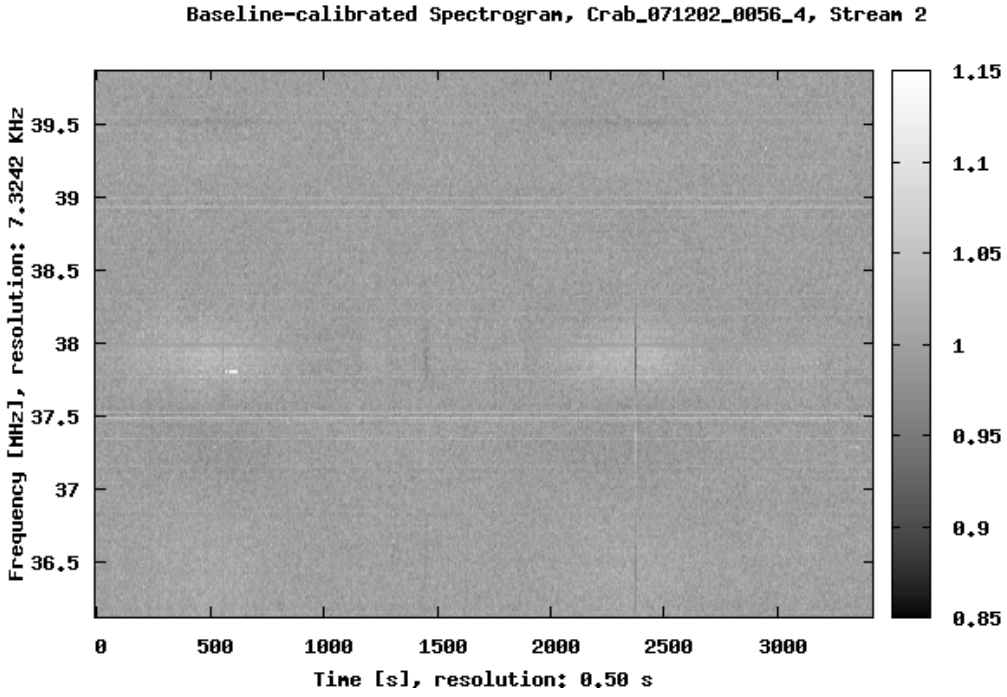

Figure E.67: Dataset: 071202_0056. Calibrated Spectrogram, stream 6 (1Y).

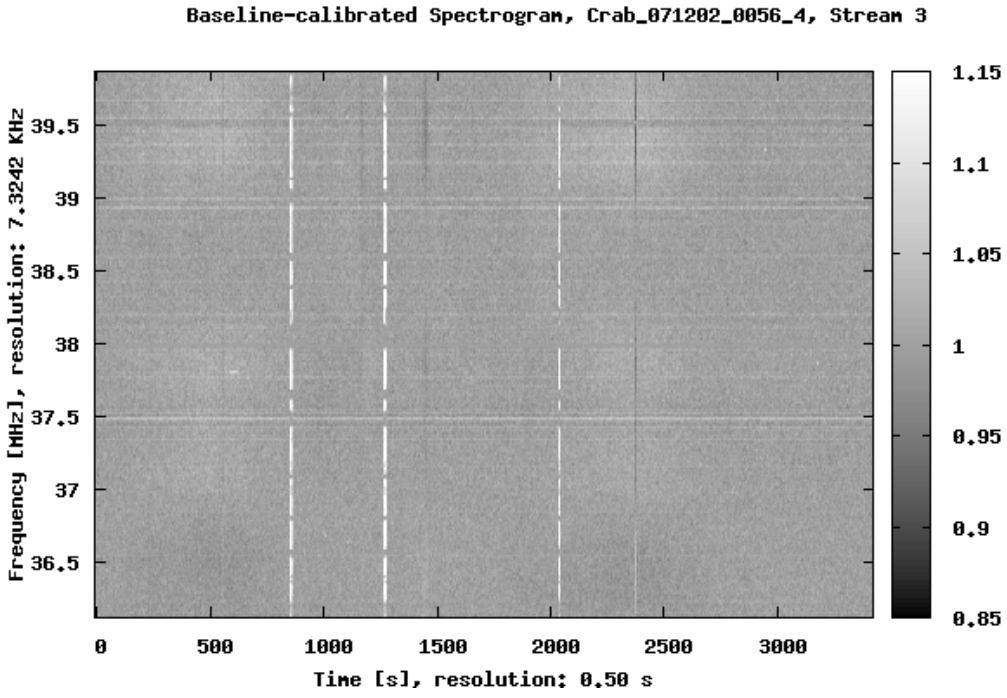

Figure E.68: Dataset: 071202_0056. Calibrated Spectrogram, stream 7 (3Y).

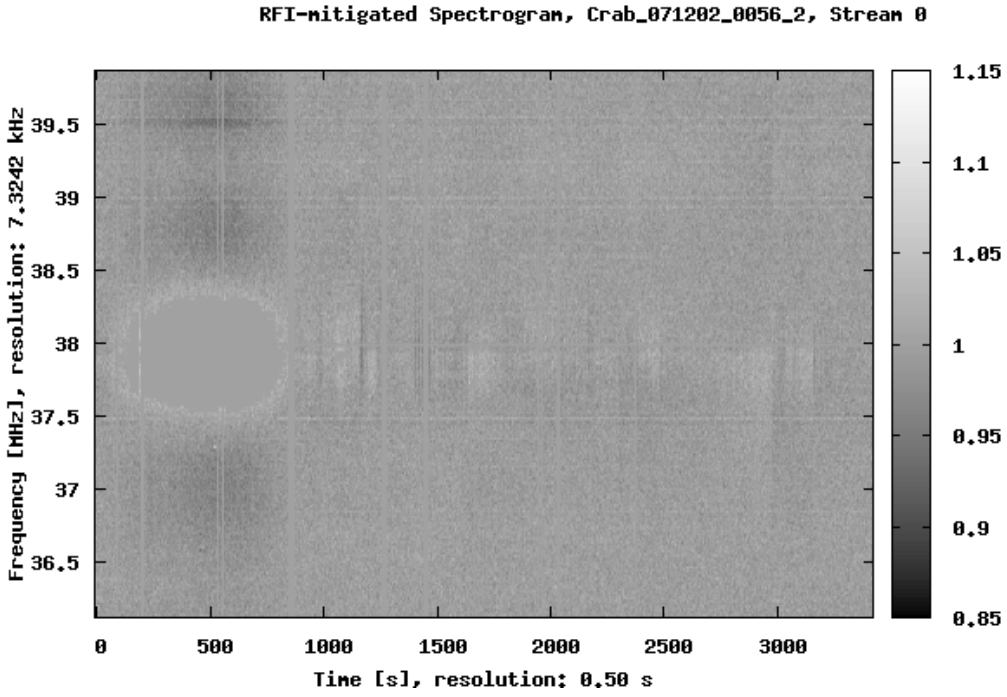

Figure E.69: Dataset: 071202_0056. Spectrogram after RFI mitigation, stream 0 (1B).

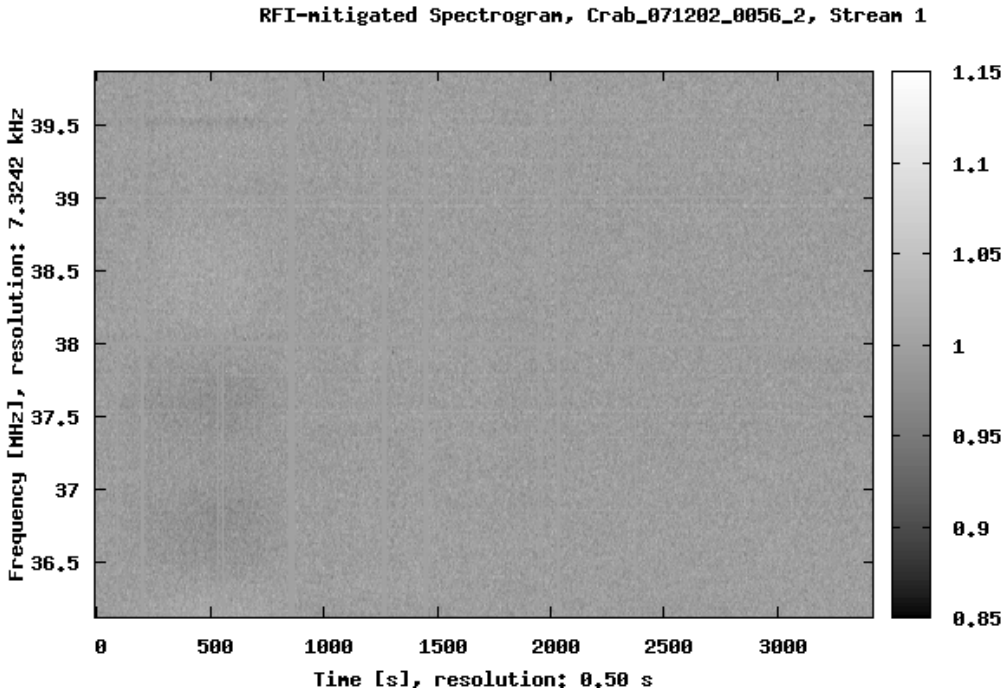

Figure E.70: Dataset: 071202_0056. Spectrogram after RFI mitigation, stream 1 (8B).

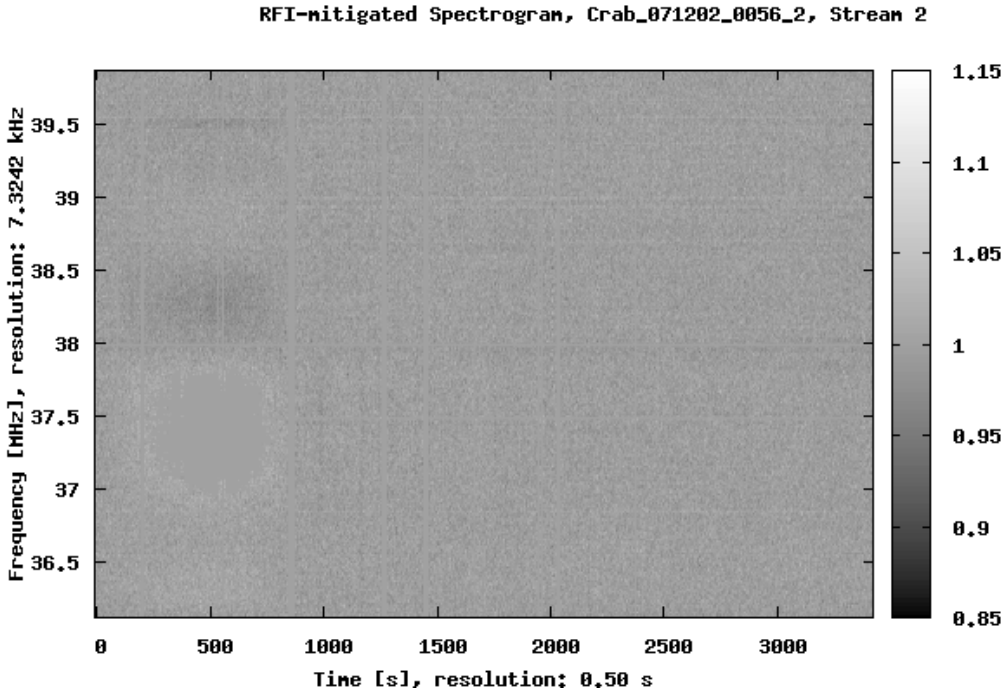

Figure E.71: Dataset: 071202_0056. Spectrogram after RFI mitigation, stream 2 (6B).

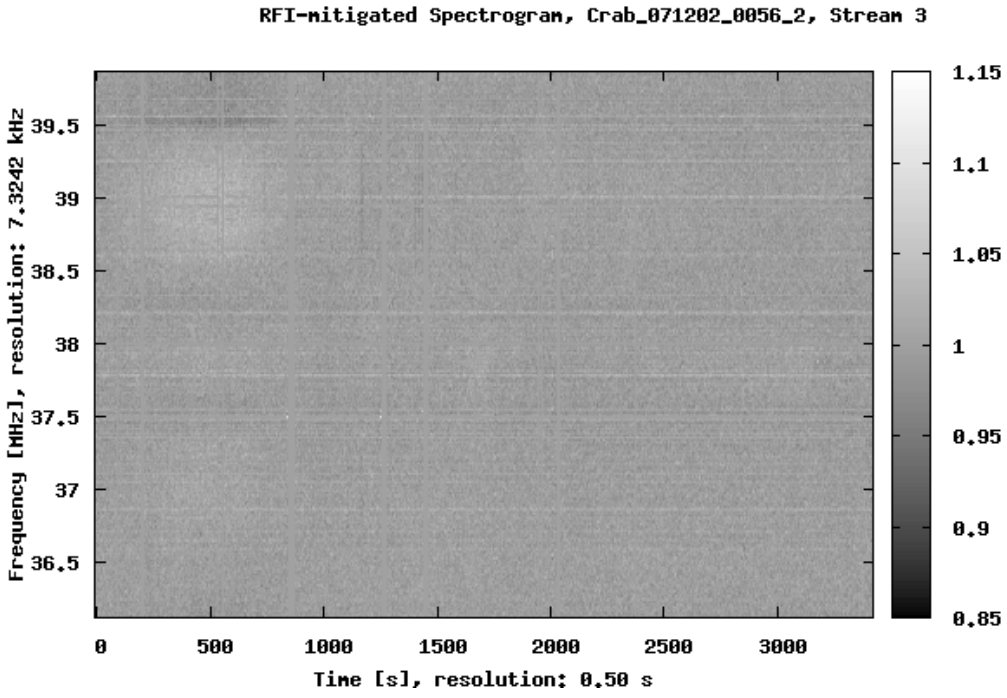

Figure E.72: Dataset: 071202_0056. Spectrogram after RFI mitigation, stream 3 (2B).

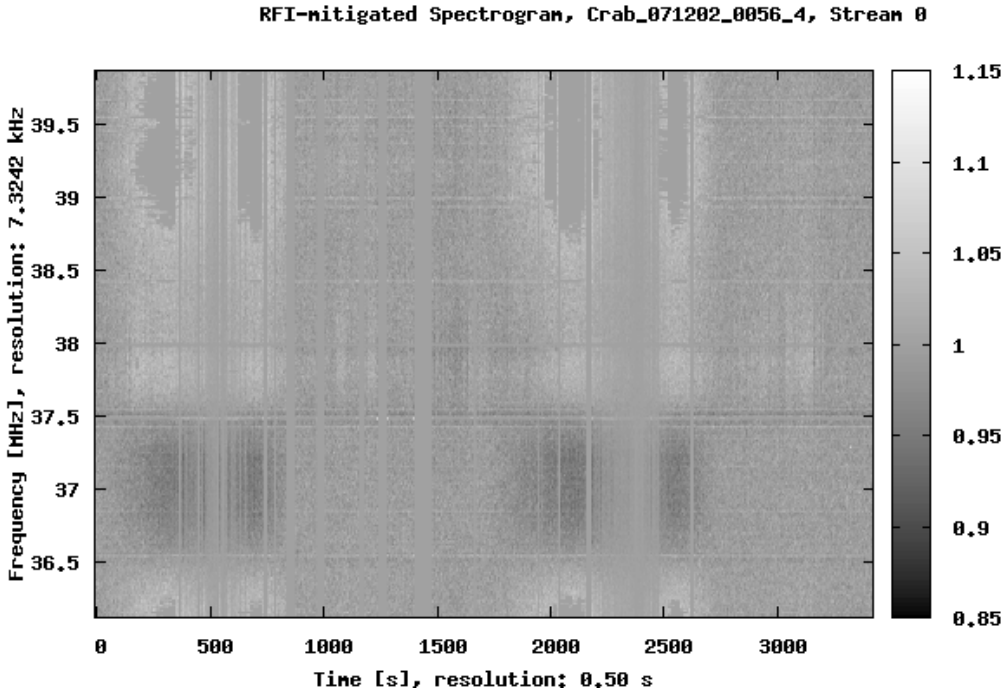

Figure E.73: Dataset: 071202_0056. Spectrogram after RFI mitigation, stream 4 (9B).

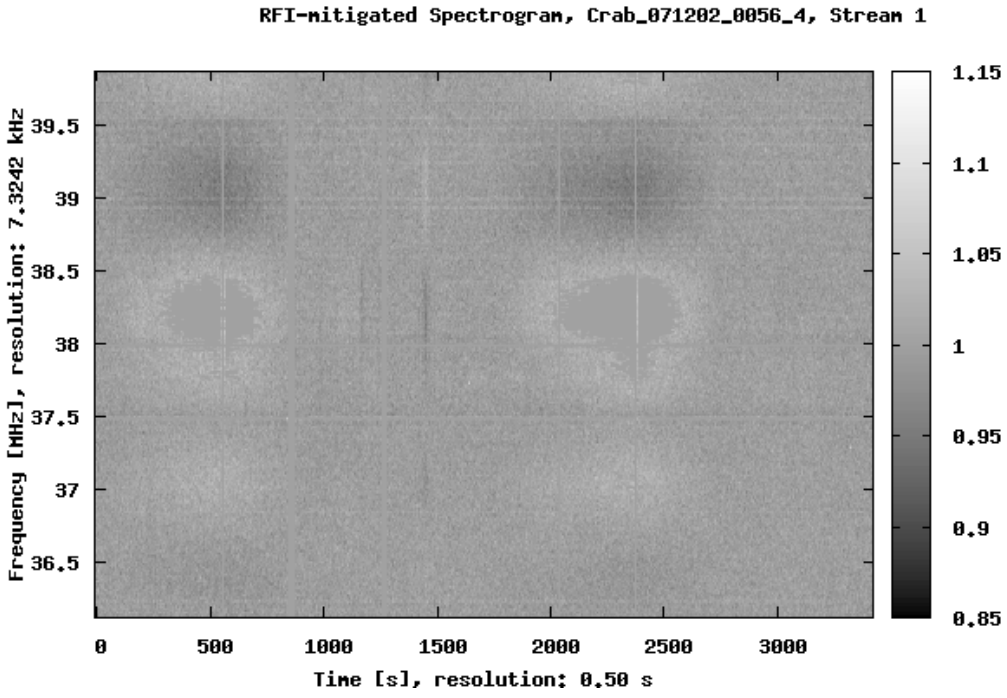

Figure E.74: Dataset: 071202_0056. Spectrogram after RFI mitigation, stream 5 (4Y).

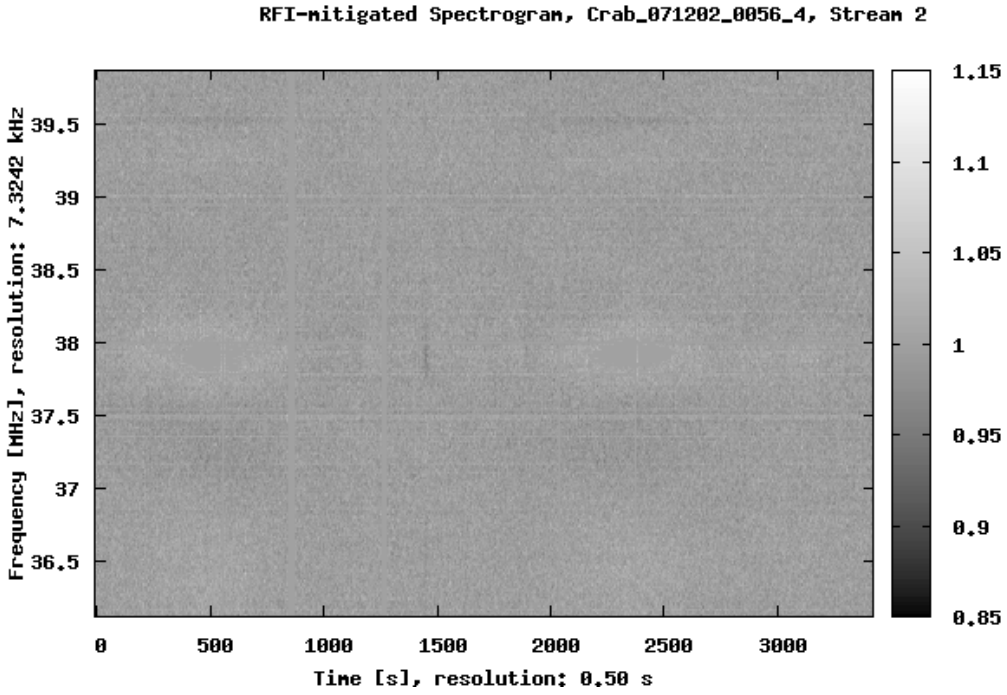

Figure E.75: Dataset: 071202_0056. Spectrogram after RFI mitigation, stream 6 (1Y).

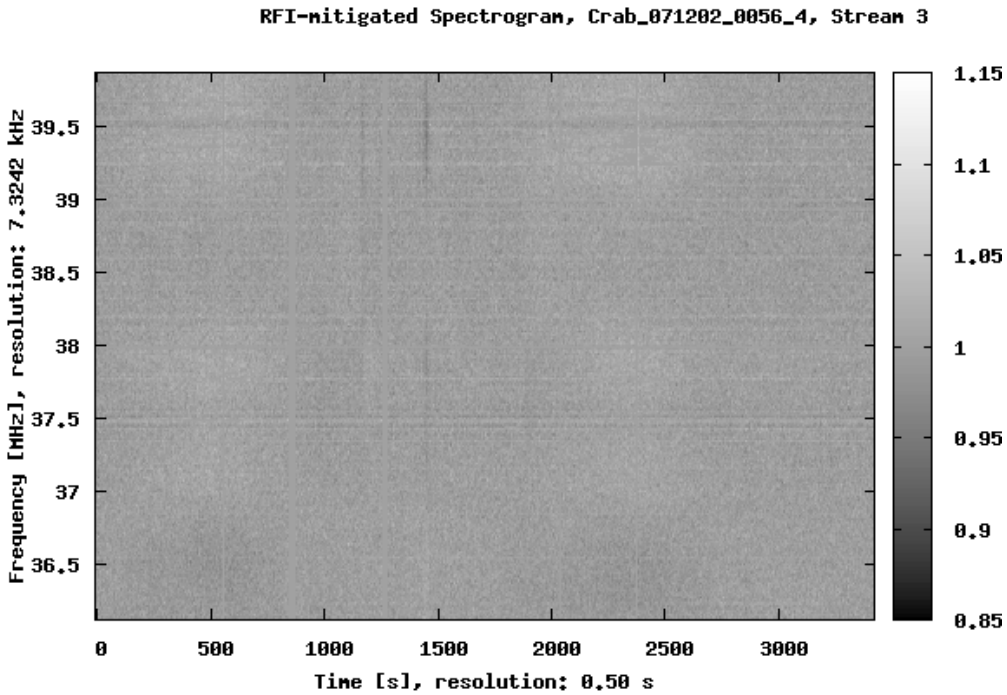

Figure E.76: Dataset: 071202_0056. Spectrogram after RFI mitigation, stream 7 (3Y).

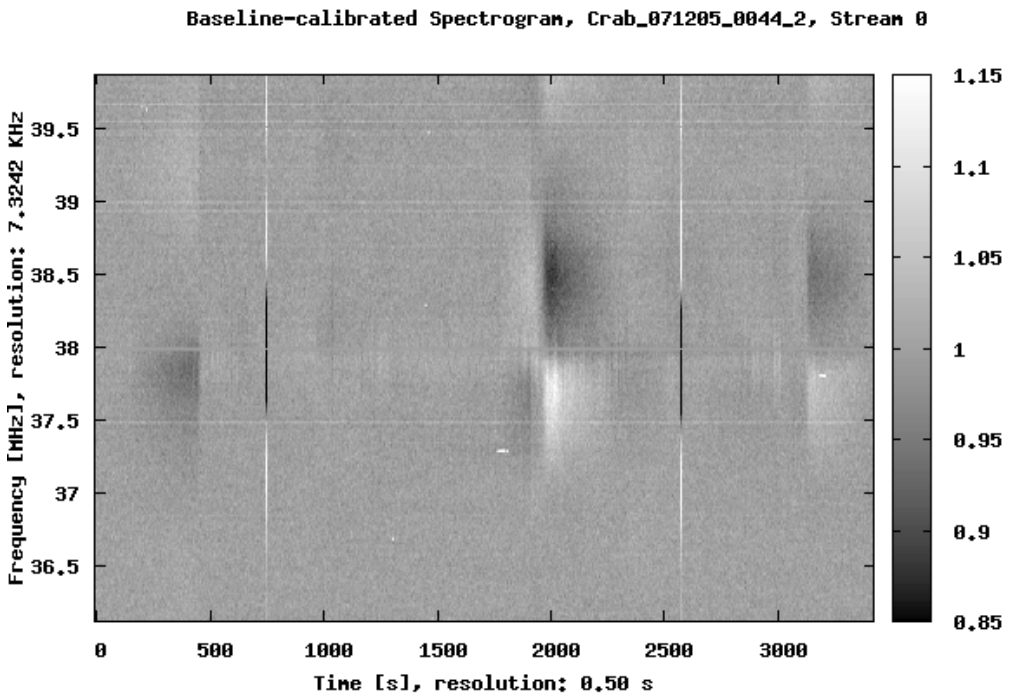

Figure E.77: Dataset: 071205_0044. Calibrated Spectrogram, stream 0 (1B).

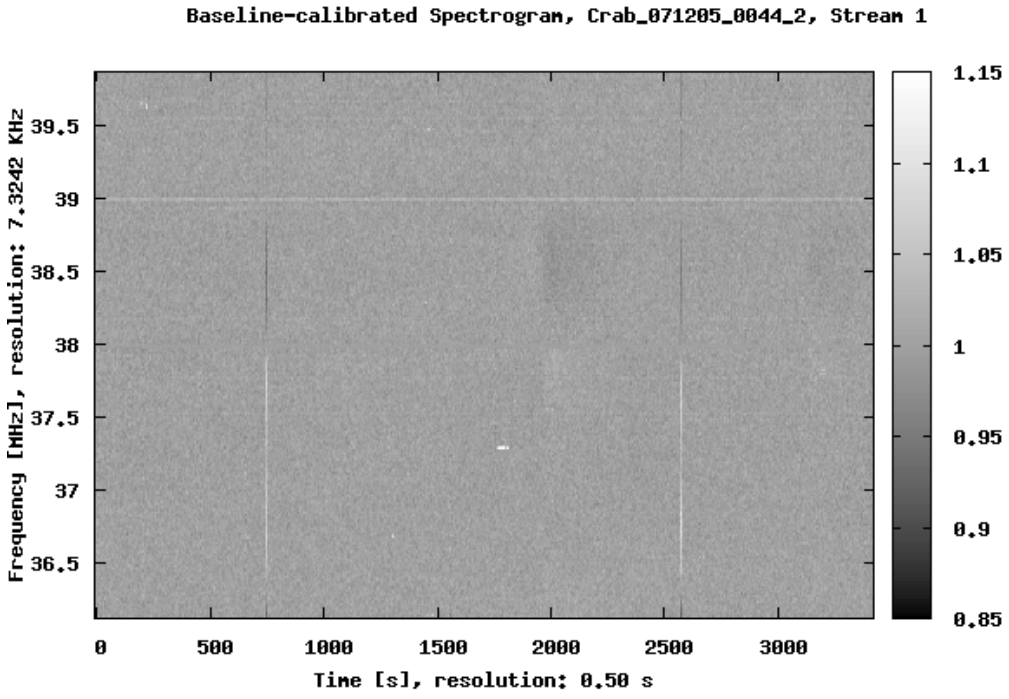

Figure E.78: Dataset: 071205_0044. Calibrated Spectrogram, stream 1 (8B).

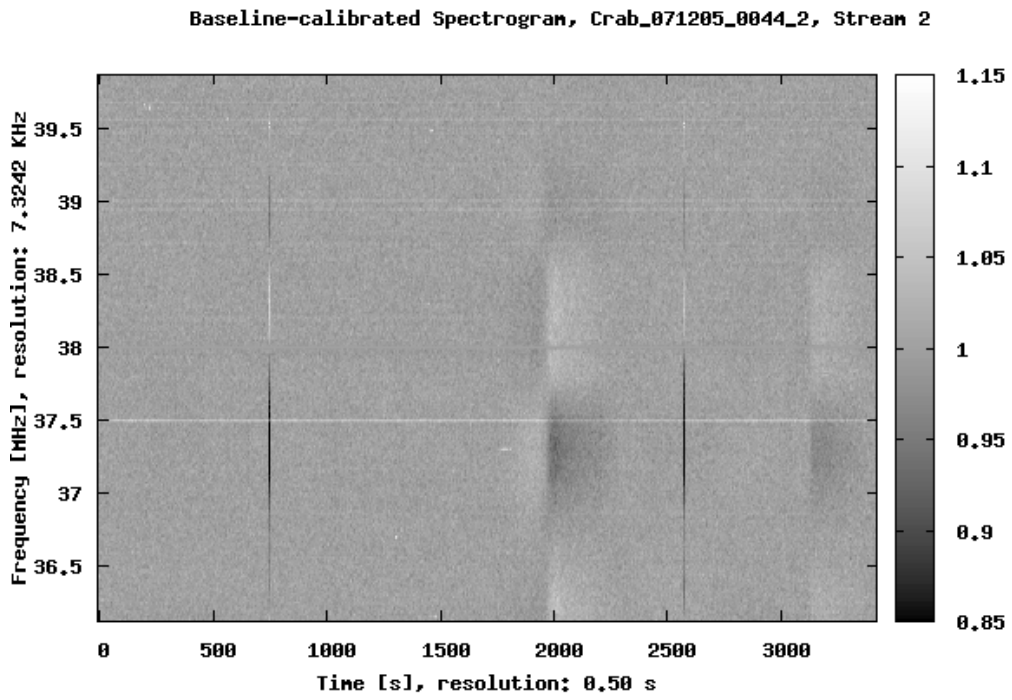

Figure E.79: Dataset: 071205_0044. Calibrated Spectrogram, stream 2 (6B).

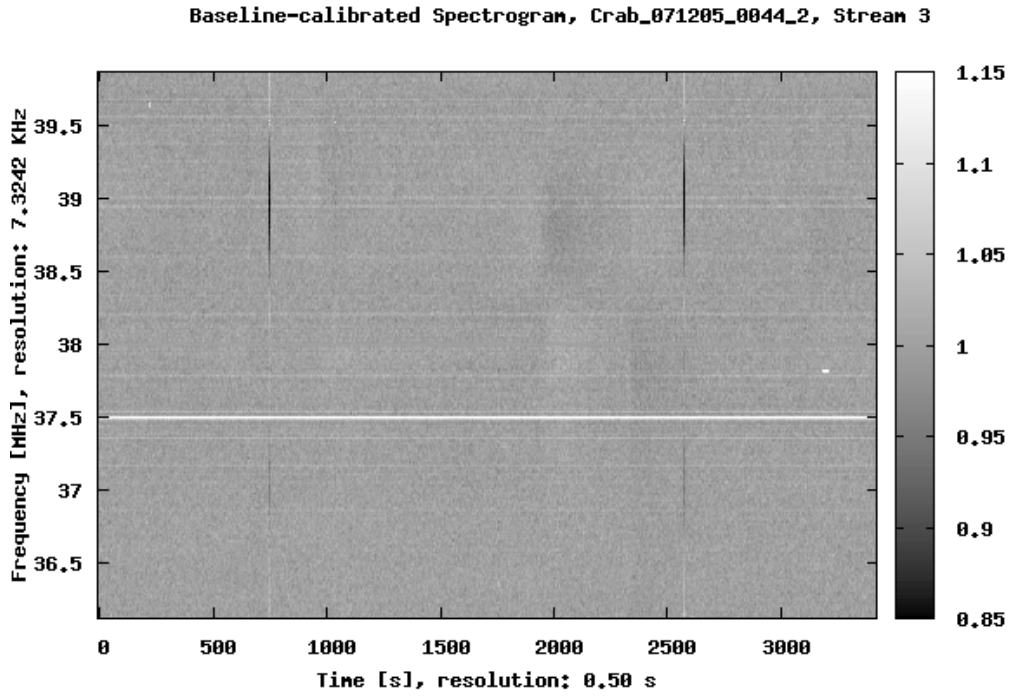

Figure E.80: Dataset: 071205_0044. Calibrated Spectrogram, stream 3 (2B).

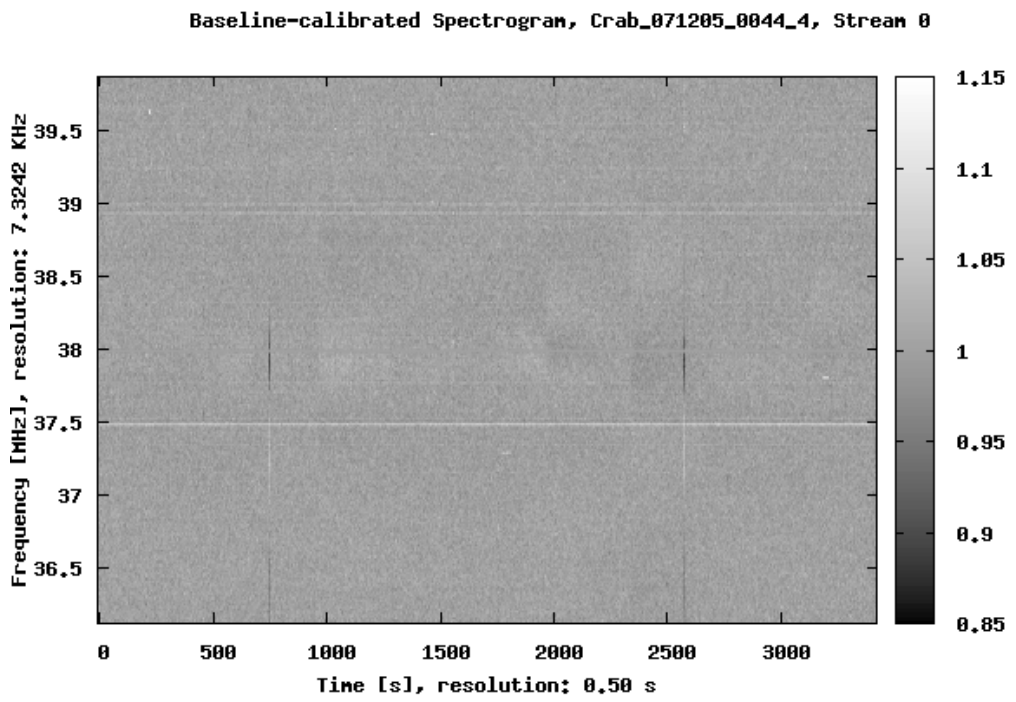

Figure E.81: Dataset: 071205_0044. Calibrated Spectrogram, stream 4 (9B).

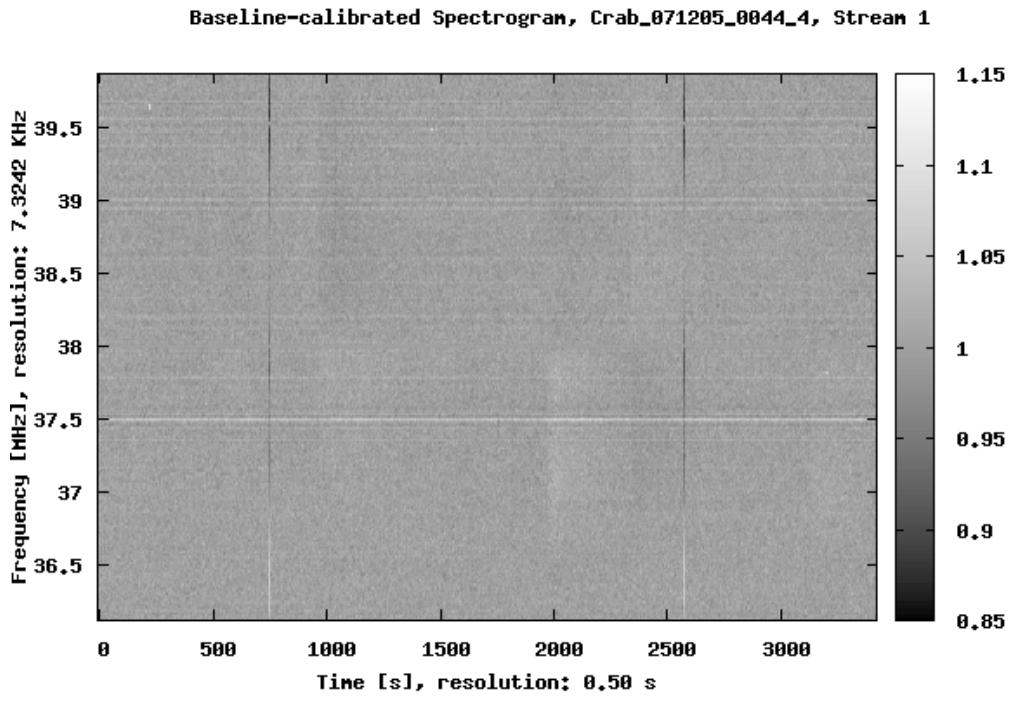

Figure E.82: Dataset: 071205_0044. Calibrated Spectrogram, stream 5 (4Y).

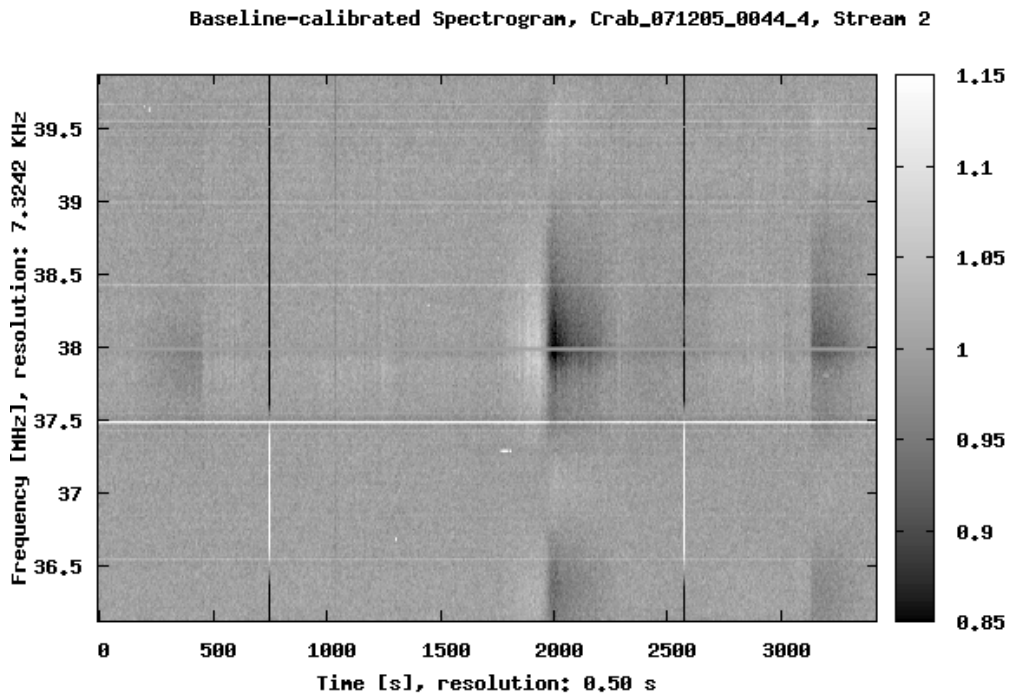

Figure E.83: Dataset: 071205_0044. Calibrated Spectrogram, stream 6 (1Y).

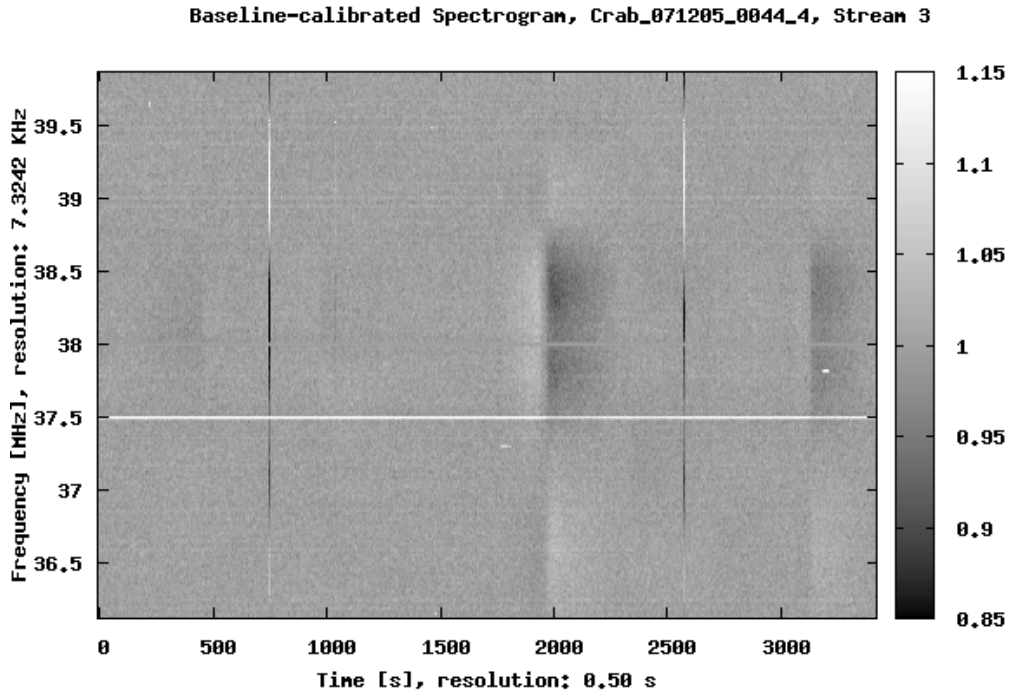

Figure E.84: Dataset: 071205_0044. Calibrated Spectrogram, stream 7 (3Y).

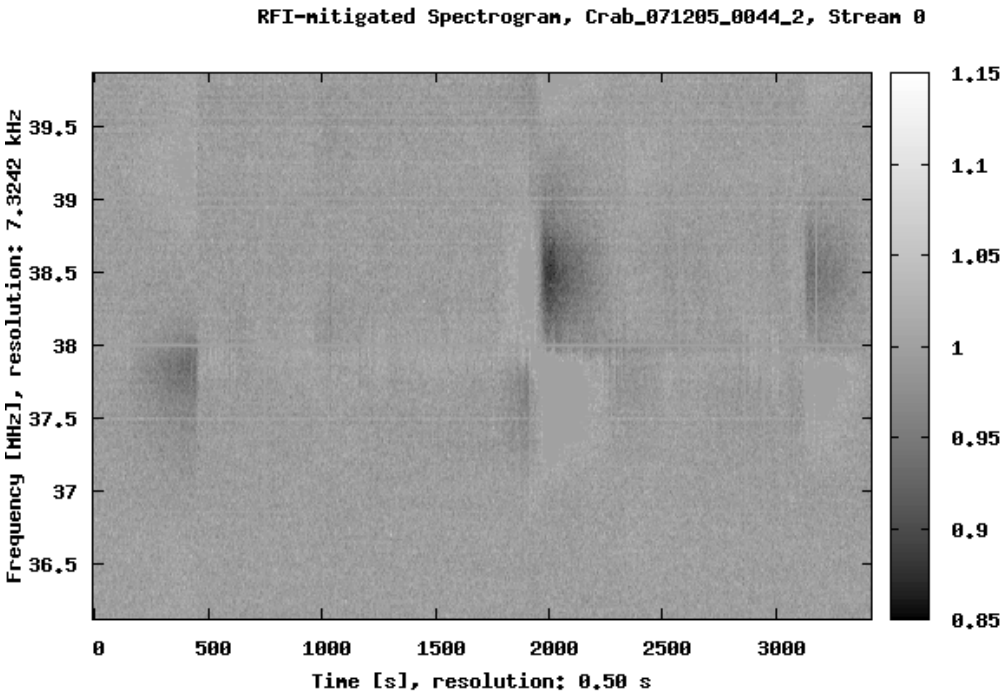

Figure E.85: Dataset: 071205_0044. Spectrogram after RFI mitigation, stream 0 (1B).

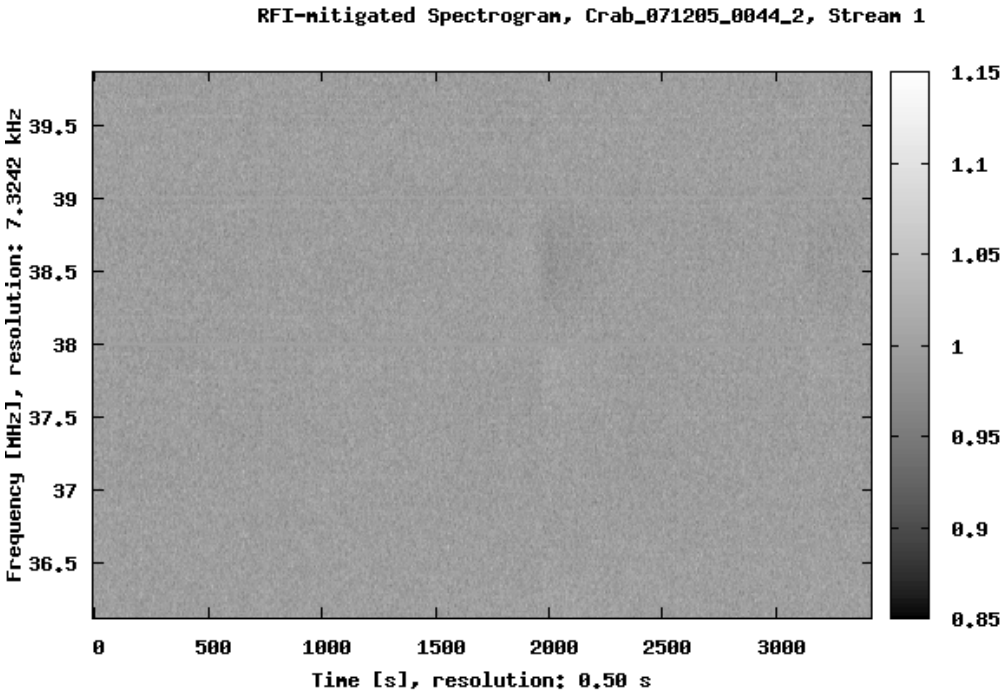

Figure E.86: Dataset: 071205_0044. Spectrogram after RFI mitigation, stream 1 (8B).

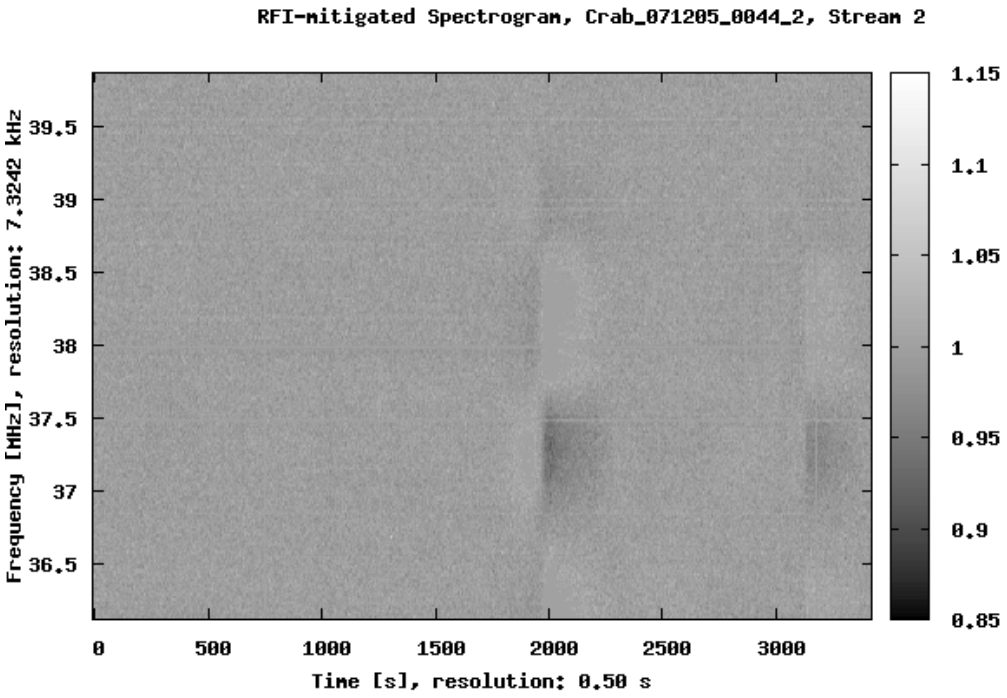

Figure E.87: Dataset: 071205_0044. Spectrogram after RFI mitigation, stream 2 (6B).

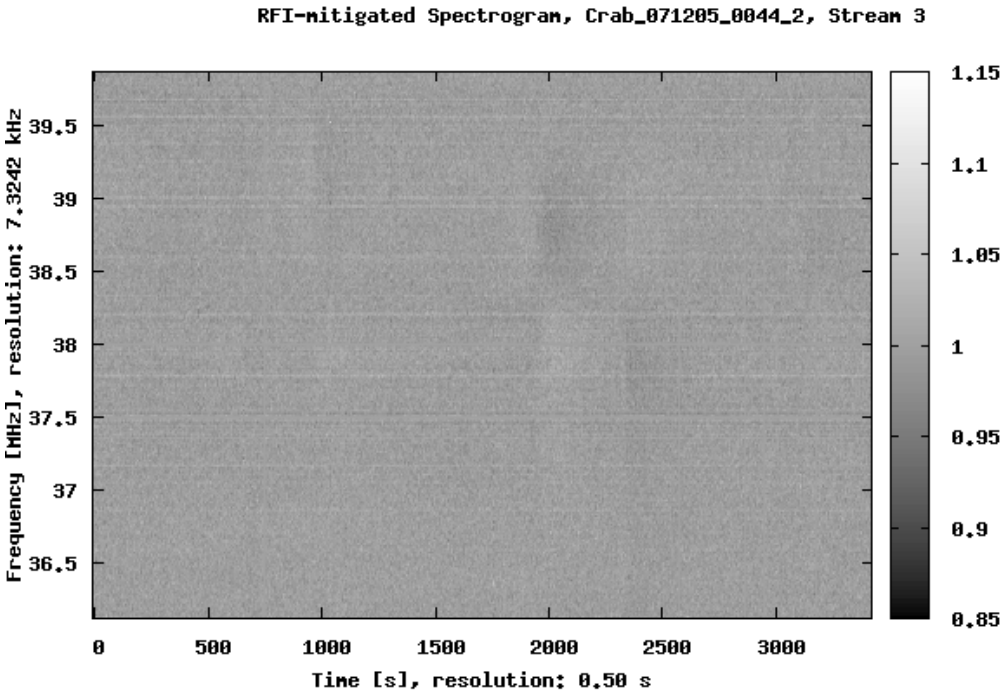

Figure E.88: Dataset: 071205_0044. Spectrogram after RFI mitigation, stream 3 (2B).

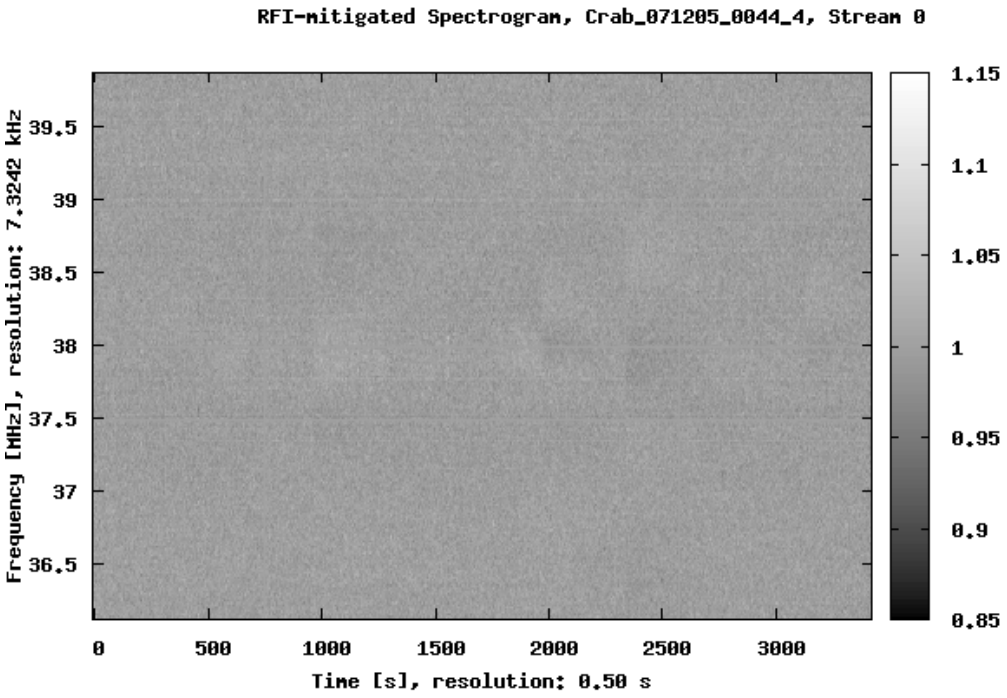

Figure E.89: Dataset: 071205_0044. Spectrogram after RFI mitigation, stream 4 (9B).

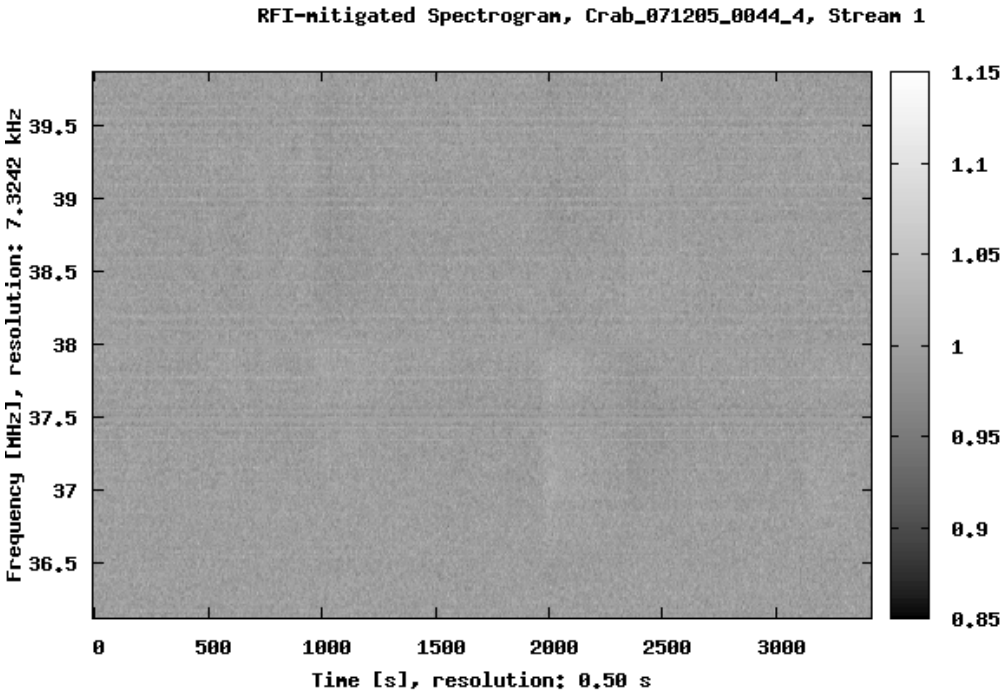

Figure E.90: Dataset: 071205_0044. Spectrogram after RFI mitigation, stream 5 (4Y).

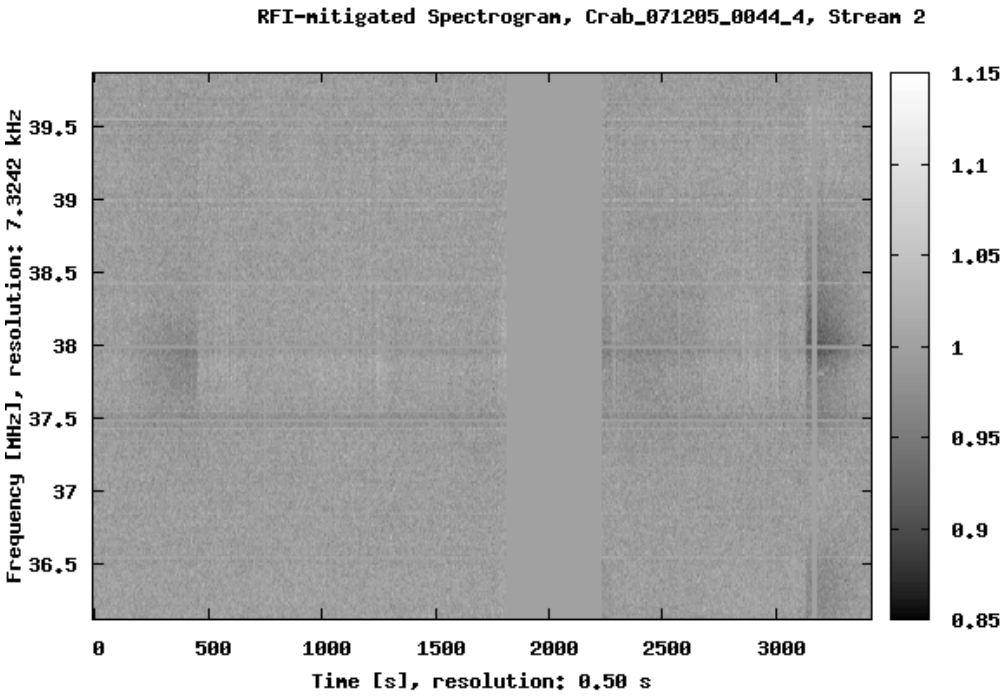

Figure E.91: Dataset: 071205_0044. Spectrogram after RFI mitigation, stream 6 (1Y).

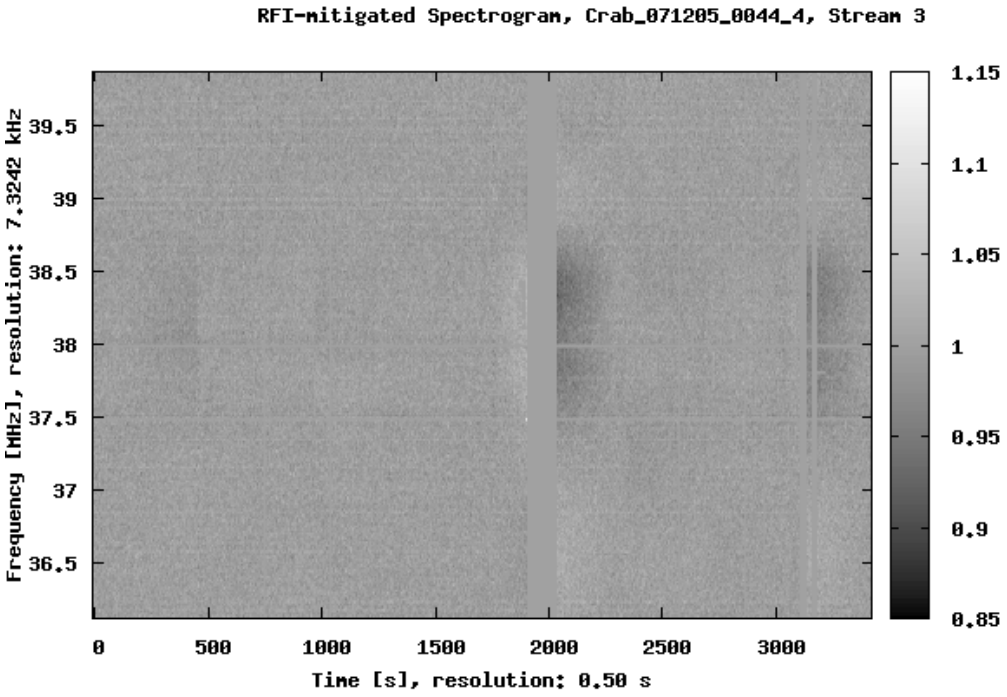

Figure E.92: Dataset: 071205_0044. Spectrogram after RFI mitigation, stream 7 (3Y).

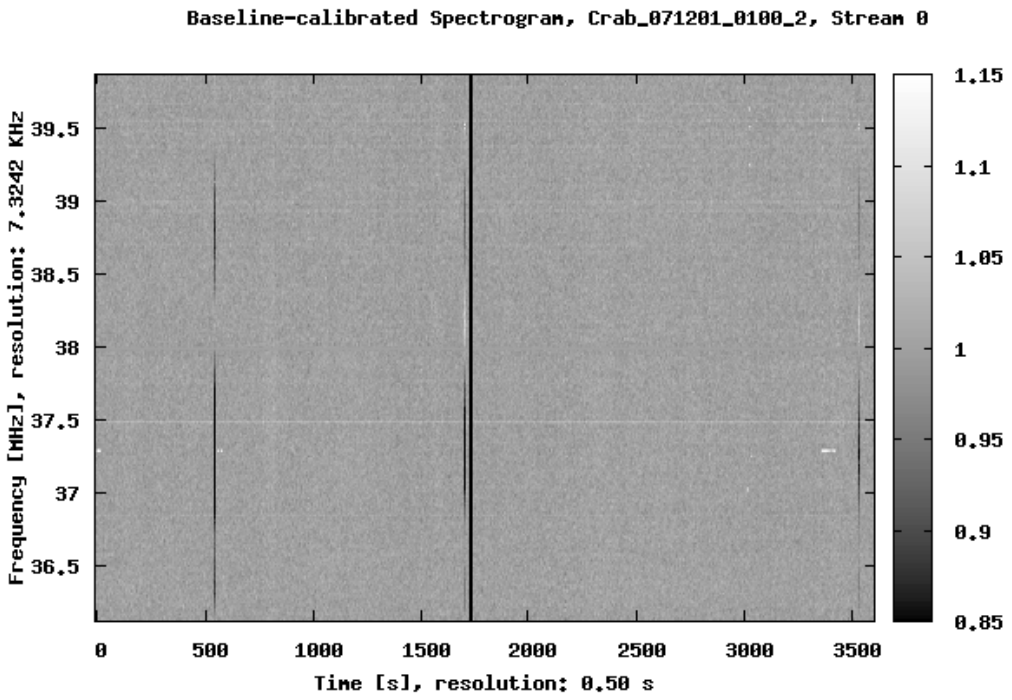

Figure E.93: Dataset: 071201_0100. Calibrated Spectrogram, stream 0 (1B).

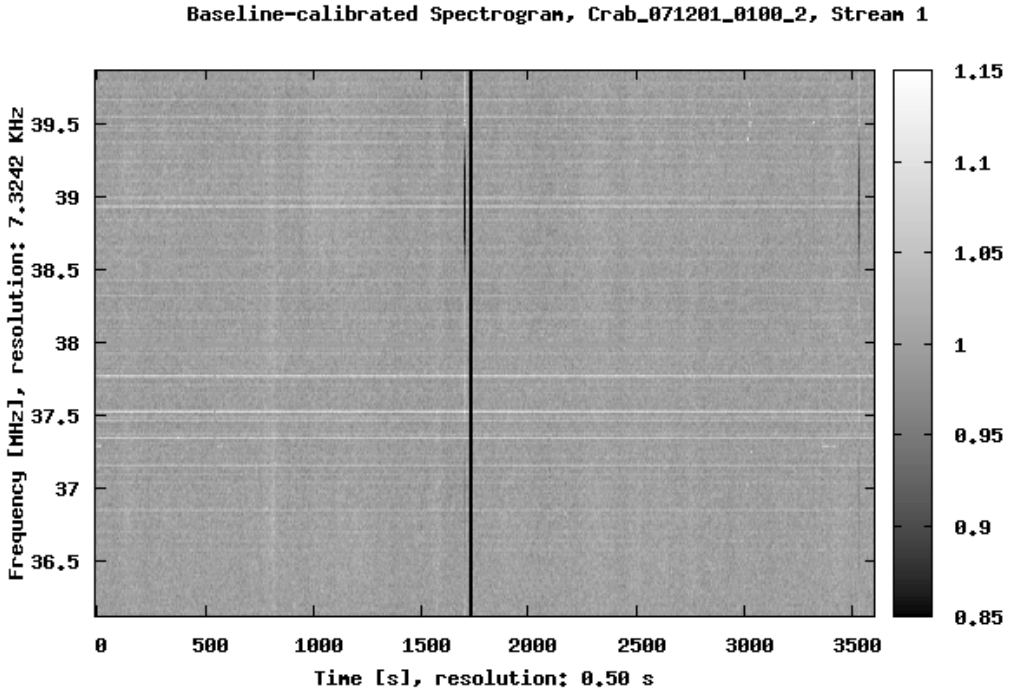

Figure E.94: Dataset: 071201_0100. Calibrated Spectrogram, stream 1 (8B).

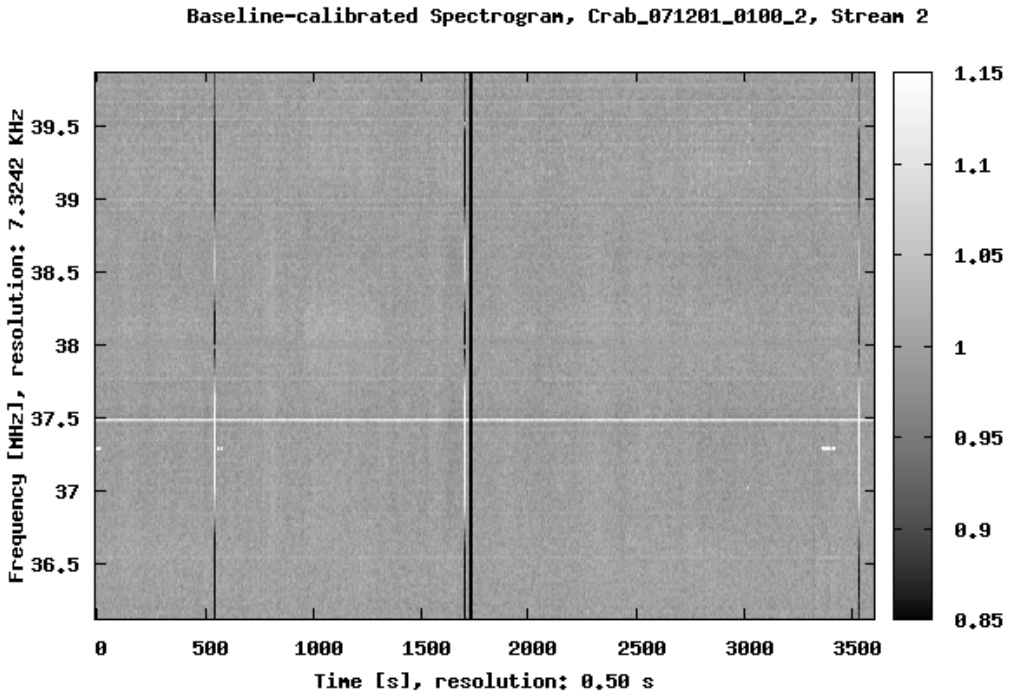

Figure E.95: Dataset: 071201_0100. Calibrated Spectrogram, stream 2 (6B).

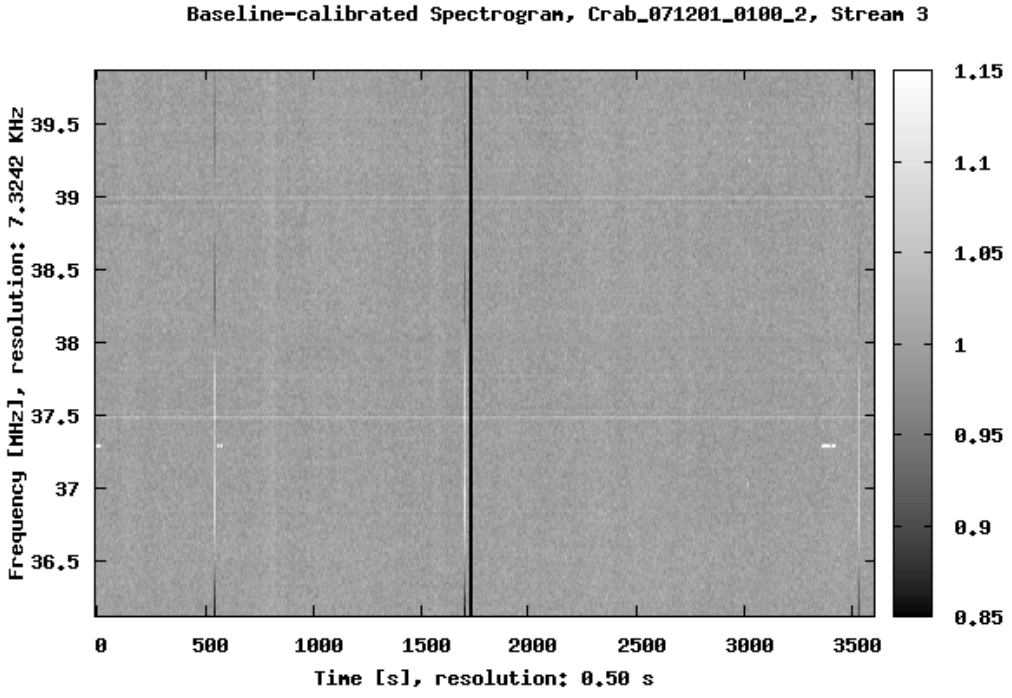

Figure E.96: Dataset: 071201_0100. Calibrated Spectrogram, stream 3 (2B).

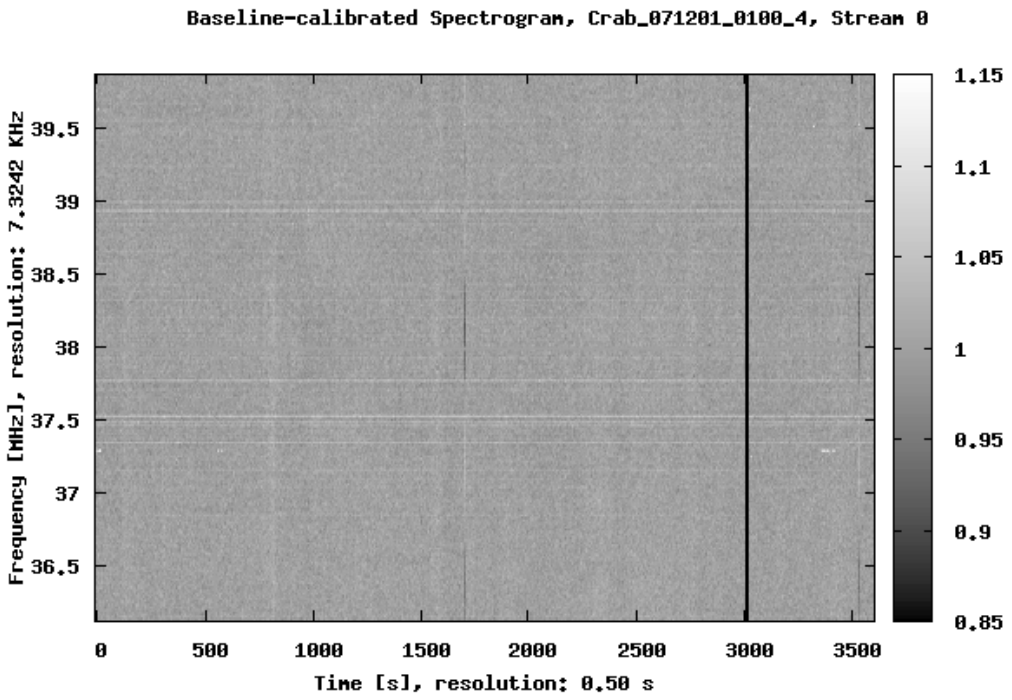

Figure E.97: Dataset: 071201_0100. Calibrated Spectrogram, stream 4 (9B).

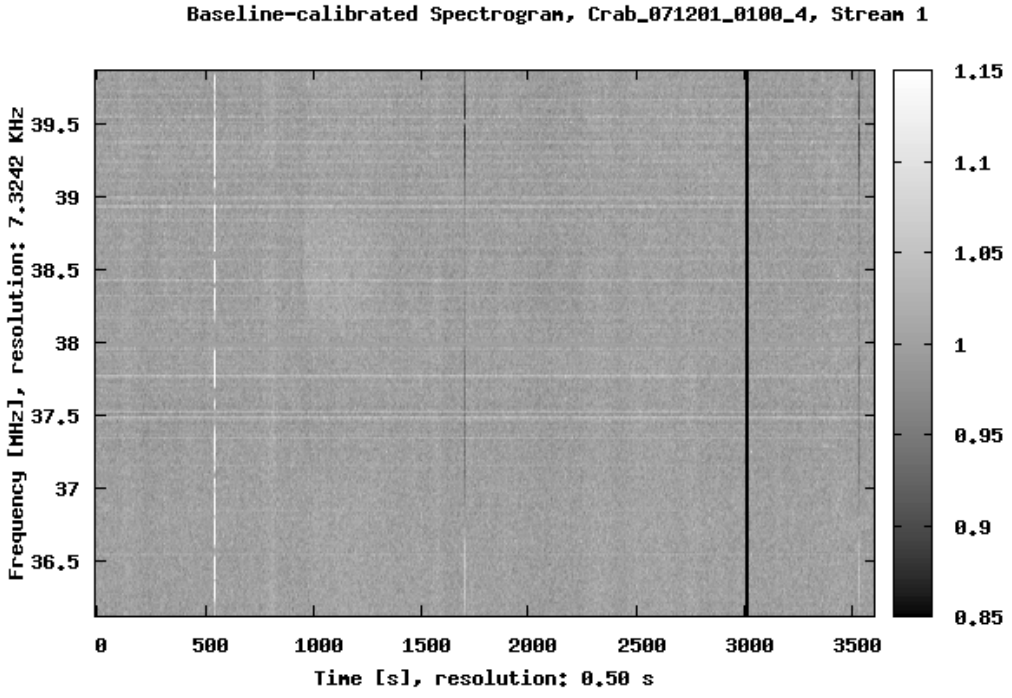

Figure E.98: Dataset: 071201_0100. Calibrated Spectrogram, stream 5 (4Y).

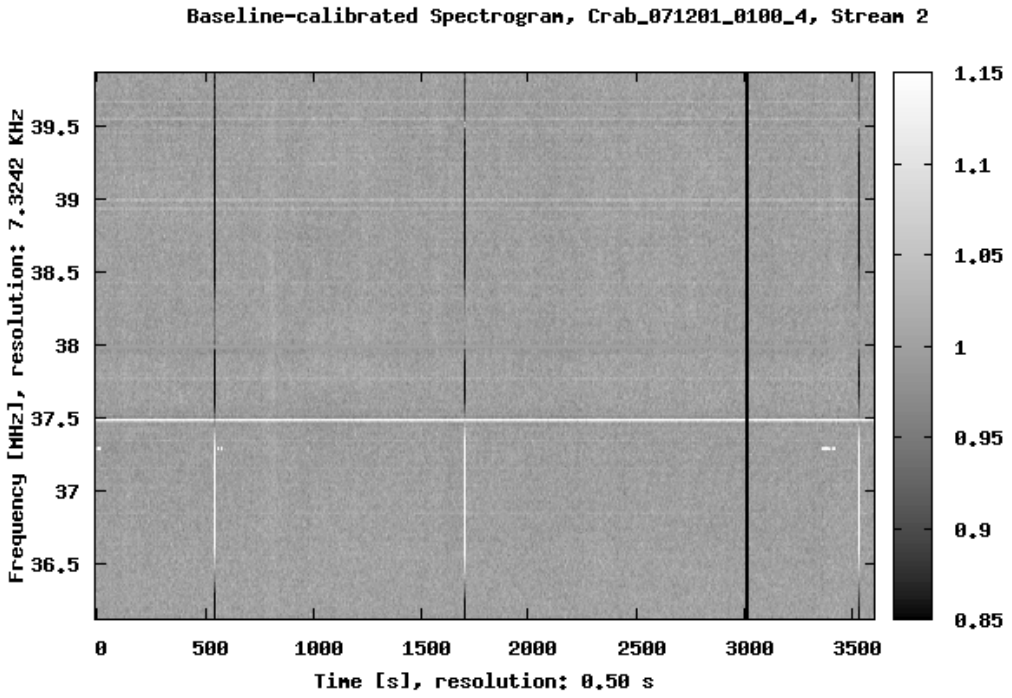

Figure E.99: Dataset: 071201_0100. Calibrated Spectrogram, stream 6 (1Y).

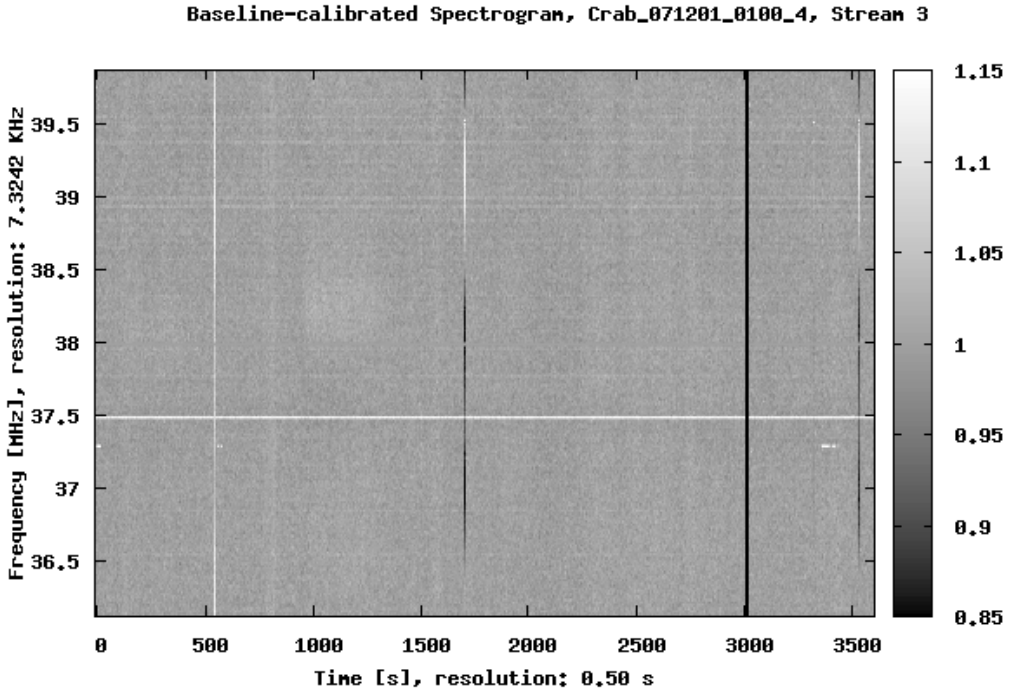

Figure E.100: Dataset: 071201_0100. Calibrated Spectrogram, stream 7 (3Y).

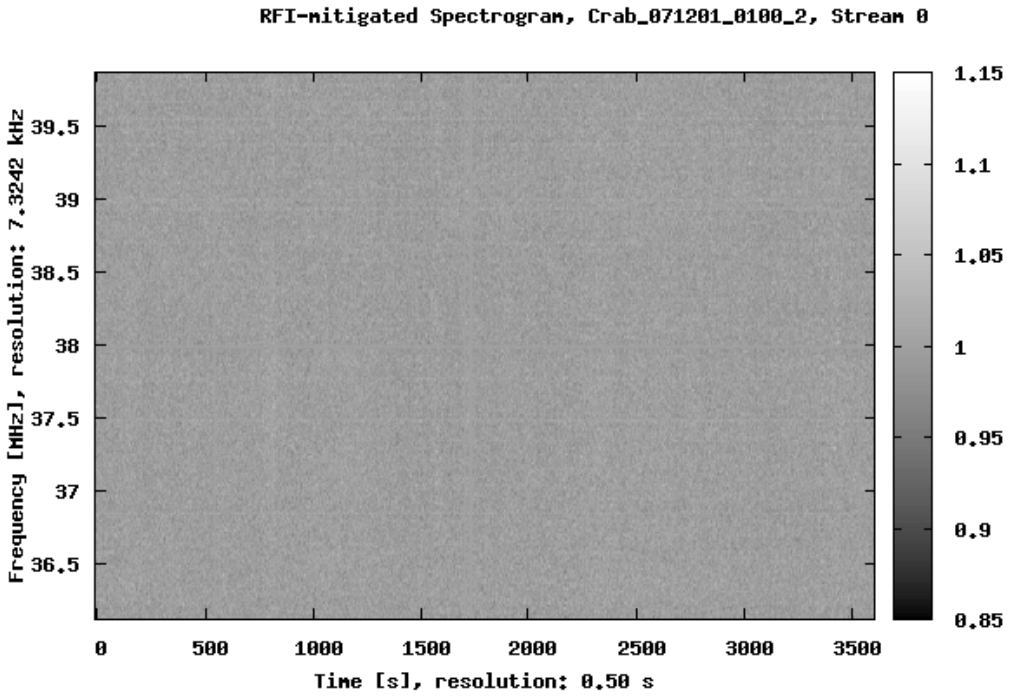

Figure E.101: Dataset: 071201_0100. Spectrogram after RFI mitigation, stream 0 (1B).

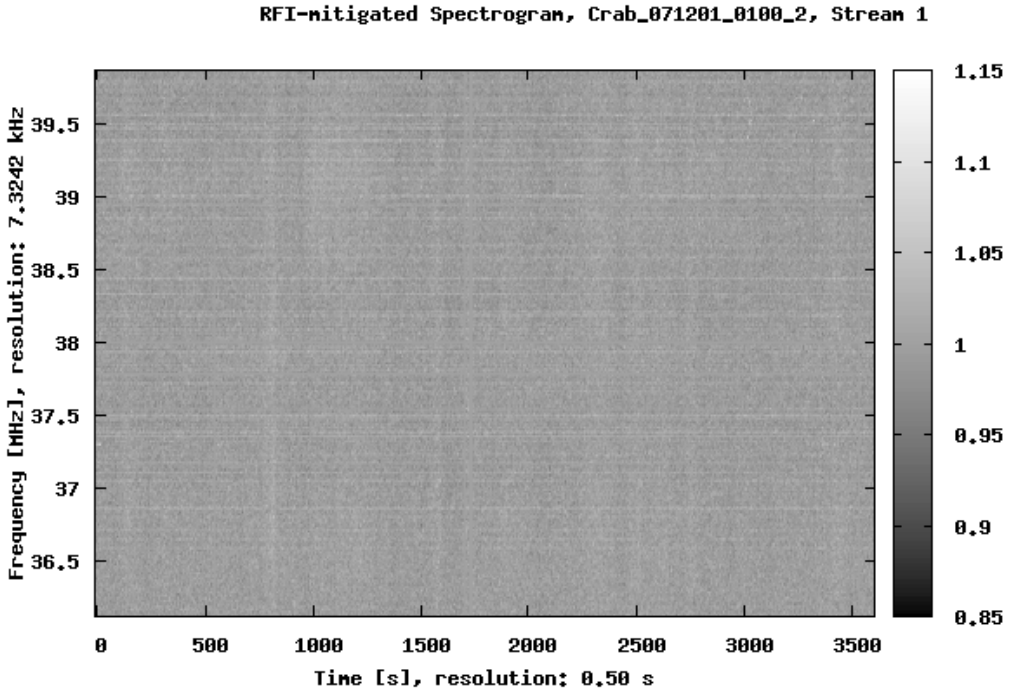

Figure E.102: Dataset: 071201_0100. Spectrogram after RFI mitigation, stream 1 (8B).

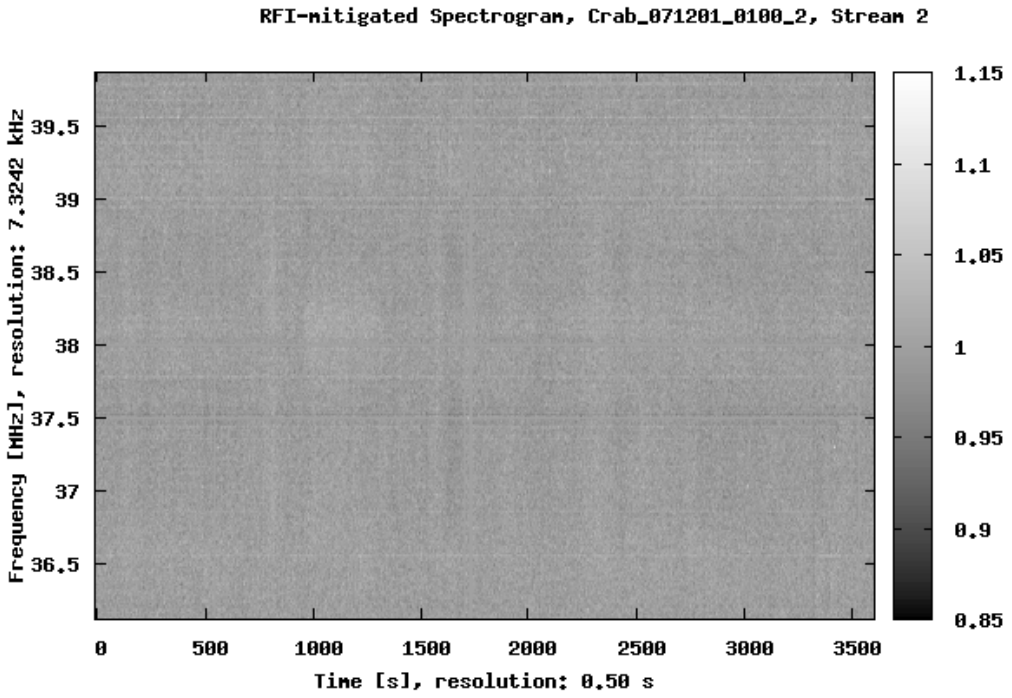

Figure E.103: Dataset: 071201_0100. Spectrogram after RFI mitigation, stream 2 (6B).

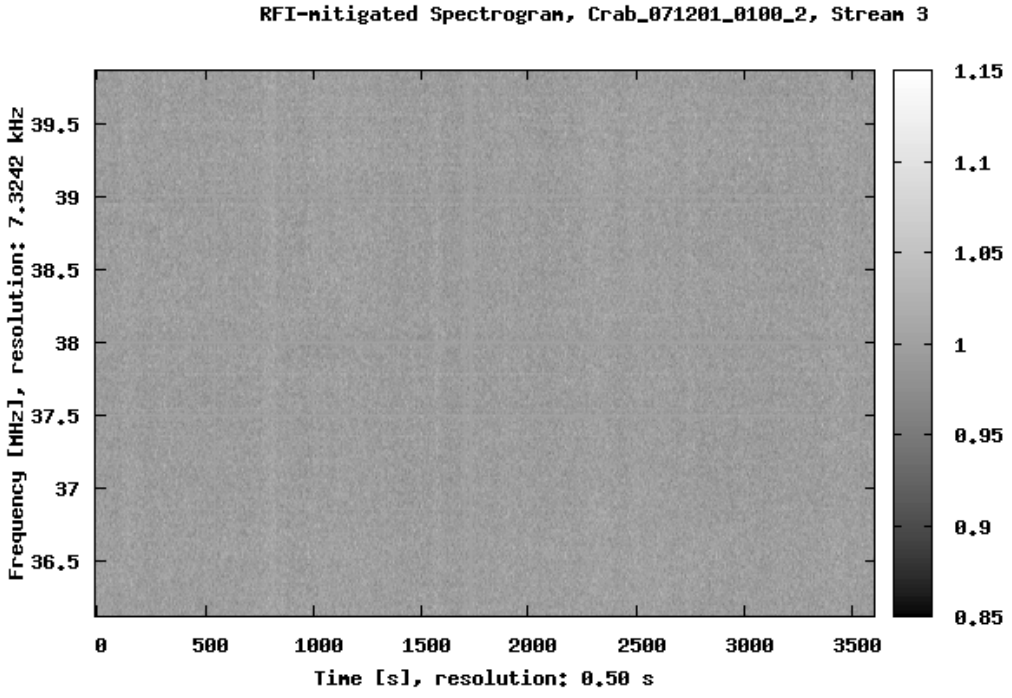

Figure E.104: Dataset: 071201_0100. Spectrogram after RFI mitigation, stream 3 (2B).

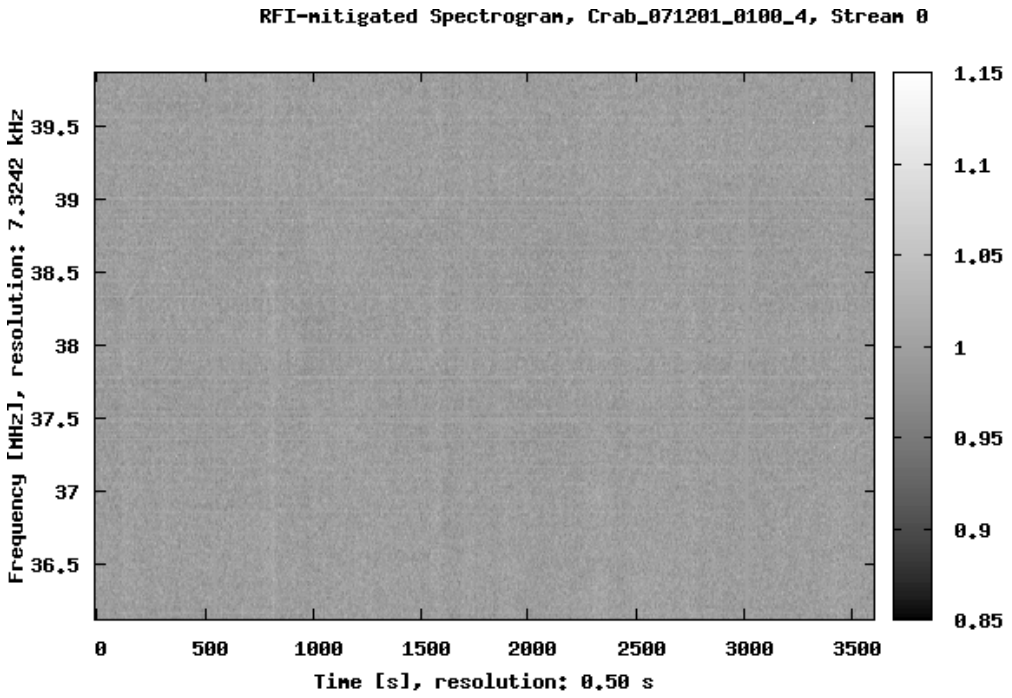

Figure E.105: Dataset: 071201_0100. Spectrogram after RFI mitigation, stream 4 (9B).

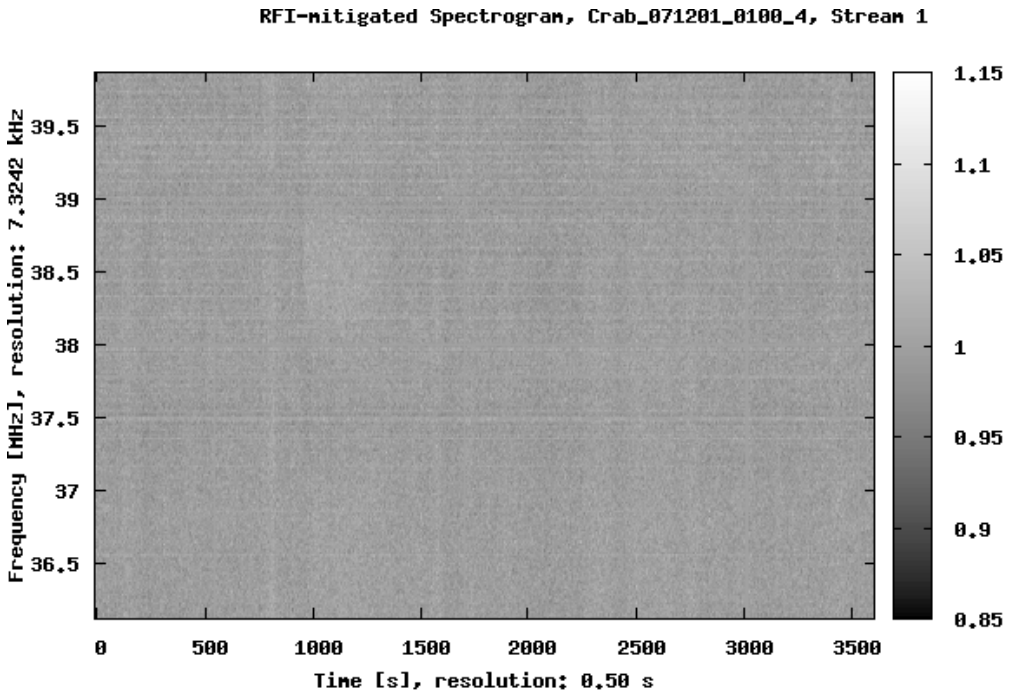

Figure E.106: Dataset: 071201_0100. Spectrogram after RFI mitigation, stream 5 (4Y).

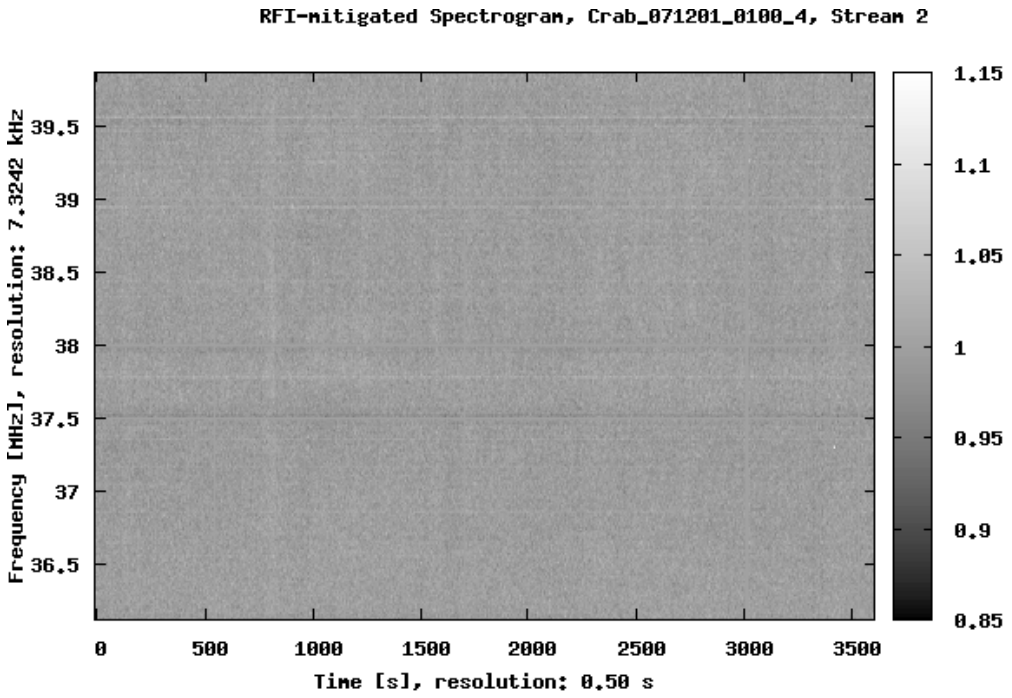

Figure E.107: Dataset: 071201_0100. Spectrogram after RFI mitigation, stream 6 (1Y).

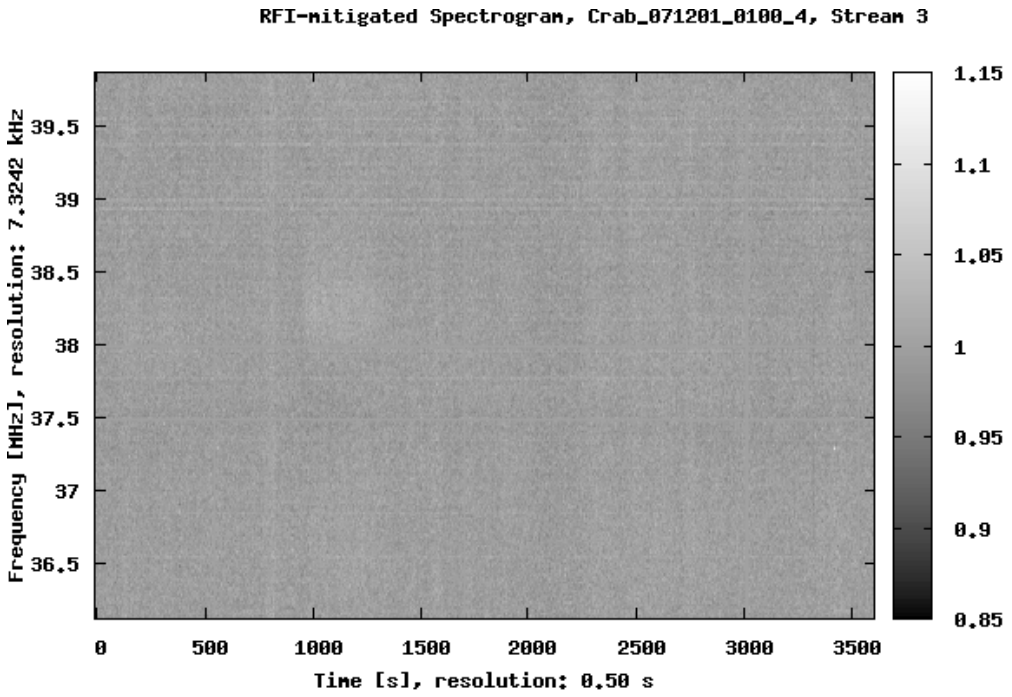

Figure E.108: Dataset: 071201_0100. Spectrogram after RFI mitigation, stream 7 (3Y).

Bibliography

[1] G. C. Bower, "Mining for the Ephemeral," *Science*, Vol. 318, pp. 759 − 760, Nov. 2007.

[2] D. H. Staelin and E. C. Reifenstein, "Pulsating Radio Sources near the Crab Nebula," *Science*, Vol. 162, pp. 1481 − 1483, Dec. 1968.

[3] J. M. Cordes *et al.*, "The Brightest Pulses in the Universe: Multifrequency Observations of the Crab Pulsar's Giant Pulses," *Astrophysical Journal*, Vol. 612, Issue 1, pp. 375 − 388, Sept. 2004.

[4] M. V. Popov *et al.*, "Instantaneous Radio Spectra of Giant Pulses from the Crab Pulsar from Decimeter to Decameter Wavelengths," *Astronomy Reports*, Vol. 50, pp. 562 − 568, Jul. 2006, also available as astro-ph/0606025v1.

[5] N. D. R. Bhat *et al.*, "Detection of Crab Giant Pulses Using the Mileura Widefield Array Low Frequency Demonstrator Field Prototype System," *Astrophysical Journal*, Vol. 665, pp. 618 − 627, Aug. 2007.

[6] A. A. Ershov and A. D. Kuzmin, "Detection of Giant Pulses from the Pulsar PSR B1112+50," *Astronomy Letters*, Vol. 29, pp. 91 − 95, Feb. 2003, also available as astro-ph/0212529v1.

[7] A. D. Kuzmin, A. A. Ershov and B. Ya. Losovsky, "Detection of Giant Pulses from the Pulsar PSR B0031-07," *Astronomy Letters*, Vol. 30, pp. 247 − 250, Apr. 2004, also available as astro-ph/0402425v1.

[8] S. W. Hawking, "Particle creation by black holes," *Commun. Math. Phys.*, Vol. 43, pp. 199 − 220, Aug. 1975.

[9] D. N. Page and S. W. Hawking, "Gamma Rays from Primordial Black Holes", *Astrophysical Journal*, Vol. 206, pp. 1 − 7, May 1976.

[10] M. Rees, "Better Way of Searching for Black-Hole Explosions?," *Nature*, Vol. 266, p. 333, Mar. 1977.

[11] R. D. Blandford, "Spectrum of a Radio Pulse from an Exploding Primordial Black Hole," *Monthly Notices of the Royal Astronomical Society*, Vol. 181, pp. 489 − 498, 1977.

[12] M. Kavic *et al.*, "Transient Pulses from Exploding Primordial Black Holes as a Signature of an Extra Dimension," *Journal Cosmology and Astroparticle Physics*, Issue 11, 017, Nov. 2008.

[13] S. Phinney and J. H. Taylor, "Sensitive Search for Radio Pulses from Primordial Black Holes and Distant Supernovae," *Nature*, Vol. 277, p. 117, Jan. 1979.

[14] D. Eichler *et al.*, "Nucleosynthesis, Neutrino Bursts and Gamma-rays from Coalescing Neutron Stars," *Nature*, Vol. 340, pp. 126 − 127, Jul. 1989.

[15] R. Mochkovitch, *et al.*, "Gamma-ray Bursts as Collimated Jets from Neutron Star/Black Hole Mergers," *Nature*, Vol. 361, pp. 236 − 237, Jan. 1993.

[16] S. E. Woosley, "Gamma-ray Bursts from Stellar Mass Accretion Disks Around Black Holes," *Astrophysical Journal*, Vol. 405, pp. 273 − 277, Mar. 1993.

[17] V. V. Usov and J. I. Katz, "Low frequency radio pulses from gamma-ray bursts?," *Astronomy and Astrophysics*, Vol. 364, pp. 655 − 659, Dec. 2000.

[18] A. Sagiv and E. Waxman, "Collective Processes in Relativistic Plasma and Their Implications for Gamma-Ray Burst Afterglows," *Astrophysical Journal*, Vol. 574, pp. 861 − 872, Aug. 2002.

[19] A. O. Benz and G. Paesold, "A Search For Prompt Radio Emission Of Gamma-Ray Bursts," *Astronomy and Astrophysics* Vol. 329, pp. 61 − 67, Jan. 1998.

[20] S. A. Colgate, "Electromagnetic Pulse from Supernovae," *Astrophysical Journal*, Vol. 198, p. 439, Jun. 1975.

[21] W. P. S. Meikle and S. A. Colgate, "Supernova Radio Pulse Searches and Possible Improvements in Sensitivity," *Astrophysical Journal*, Vol. 220, p. 1076, Mar. 1978.

[22] B. M. S. Hansen and M. Lyutikov, "Radio and X-ray Signatures of Merging Neutron Stars," *Monthly Notices of the Royal Astronomical Society*, Vol. 322, pp. 695 − 701, Apr. 2001.

[23] J. V. Jelley *et al.*, "Radio Pulses from Extensive Cosmic-Ray Air Showers," *Nature*, Vol. 205, pp. 327 − 328, Jan. 1965.

[24] H. Falcke *et al.*, "Detection and Imaging of Atmospheric Radio Flashes from Cosmic Ray Air Showers," *Nature*, Vol. 435, pp. 313 − 316, May 2005.

[25] H. V. Cane and W. C. Erickson, "Studies of Space Weather Using Solar Radio Bursts," in *Clark Lake to the Long Wavelength Array: Bill Ericksons Radio Science*, ASP Conf. Ser., Vol. 345, pp. 133 − 141, 2005.

[26] I. de Pater, "Low Frequency Planetary Radio Emissions," in *Clark Lake to the Long Wavelength Array: Bill Ericksons Radio Science*, ASP Conf. Ser., Vol. 345, pp. 154 − 166, 2005.

[27] D. R. Lorimer *et al.*, "A bright millisecond radio burst of extragalactic origin," *Science*, Vol. 318, pp. 777 − 780, Nov. 2007.

[28] J. M. Cordes and M. A. McLaughlin, "Searches for Fast Radio Transients," *Astrophysical Journal* Vol. 596, pp. 1142 − 1154, Oct. 2003.

[29] R. J. Balsano, "Search for Radio Emission Coincident with Gamma Ray Bursts," Ph.D. Dissertation, Princeton University, Jan. 1999.

[30] C. A. Katz *et al.*, "A Survey for Transient Astronomical Radio Emission at 611 MHz," *Publications of the Astronomical Society of the Pacific*, Vol. 115, Issue 808, pp. 675 − 687, Jun. 2003.

[31] K. Becker, "Courting Serendipity: The Search for Transient Radio Signals," M. S. Thesis, Cornell University, Jan. 2005.
www.astro.cornell.edu/∼cordes/kate.thesis.ps.gz.

[32] D. E. Wilson, "A Pilot Survey for Astronomical Low Frequency Radio Transients," M.S. Thesis, Virginia Polytechnic Institute and State University, Blacksburg, Virginia, Aug. 2005, http://scholar.lib.vt.edu/theses/available/etd-08232005-212614/.

[33] M. F. Morales *et al.*, "The GRB All-sky Spectrometer Experiment (GASE)," *Astronomical Society of the Pacific Conference Series*, Vol. 345, p. 512, Sept. 2005.

[34] A. Siemion *et al.*, "New SETI Sky Surveys for Radio Pulses," submitted Nov. 2008, *Acta Astronautica*, preprint available: astro-ph/0811.3046v1.

[35] J. Welch *et al.*, "The Allen Telescope Array: The First Widefield, Panchromatic, Snapshot Radio Camera for Radio Astronomy and SETI," *Proc. IEEE*, Vol. 97, No. 8, pp. 1438 − 1447, Aug. 2009.

[36] C. Patterson *et al.*, "Searching for Transient Pulses with the ETA Radio Telescope," *ACM Trans. Reconfigurable Technology & Systems*, Vol. 1, No. 4, Art. 20, p. 19, Jan. 2009.

[37] W. A. Coles, R. G. Frehlich and M. Kojima, "Design of a 74-MHz Antenna for Radio Astronomy," *Proc. IEEE*, Vol. 82, No. 5, pp. 697 − 704, May 1994.

[38] C. A. Katz *et al.*, "The STARE Project: A Progress Report," 1997, astro-ph/9712330v1.

[39] C. J. Lonsdale *et al.*, "The Murchison Widefield Array: Design Overview," *Proc. IEEE*, Vol. 97, No. 8, pp. 1497 − 1506, Aug. 2009.

[40] M. de Vos, A. W. Gunst, and R. Nijboer, "The LOFAR Telescope: System Architecture and Signal Processing," *Proc. IEEE*, Vol. 97, No. 8, pp. 1431 − 1437, Aug. 2009.

[41] C. Law *et al.*,"Searching for Low Frequency Radio Transients with LOFAR CS1," *Proc. of "Bursts, Pulses and Flickering: wide-field monitoring of the dynamic radio sky*, Kerastari, Tripolis, Greece, June 2007, available online: http://pos.sissa.it/archive/conferences/056/033/Dynamic2007_033.pdf.

[42] J. W. T. Hessels *et al*, "The Radio Sky on Short Timescales with LOFAR: Pulsars and Fast Transients," To appear in *The Low-Frequency Radio Universe*, ASP Conf. Ser., Vol. 407, p. 318, Dec. 2009, preprint available: astro-ph/0903.1447v1.

[43] S. Ellingson *et al.*, "The Long Wavelength Array," *Proc. IEEE*, Vol. 97, No. 8, pp. 1421 − 1430, Aug. 2009.

[44] J. M. Cordes and T. J. W. Lazio, "NE2001. I. A New Model for the Galactic Distribution of Free Electrons and its Fluctuations," Jan. 2003, astro-ph/0207156v3.

[45] J. M. Cordes and T. J. W. Lazio, "NE2001. II. Using Radio Propagation Data to Construct a Model for the Galactic Distribution of Free Electrons," Jan. 2003, astro-ph/0301598v1.

[46] D. Lorimer and M. Kramer, *Handbook of Pulsar Astronomy*, Cambridge University Press, 2005.

[47] N. D. R. Bhat *et al.*, "Multifrequency Observations of Radio Pulse Broadening and Constraints on Interstellar Electron Density Microstructure," *Astrophysical Journal*, Vol. 605, Issue 2, pp. 759 − 783, Apr. 2004.

[48] A. A. Deshpande and R. Ramachandran, "Improving Pulsar Distances by Modelling Interstellar Scattering," *Monthly Notices of the Royal Astronomical Society*, Vol. 300, No. 2, pp. 577 − 582, Oct. 1998.

[49] S. W. Ellingson, "Antennas for the Next Generation of Low Frequency Radio Telescopes," *IEEE Transactions on Antennas and Propagation*, Vol. 53, No. 8, pp. 2480 − 2489, Aug. 2005.

[50] W. Stutzman and G. Thiele, *Antenna Theory and Design*, Wiley Publication; Second Edition, 1998.

[51] S. W. Ellingson, "Sky Noise-Induced Spatial Correlation," Long Wavelength Array Memo Series No. 142, Oct. 2008, http://www.ece.vt.edu/swe/lwa/memo/.

[52] S. W. Ellingson, J. H. Simonetti, and C. D. Patterson, "Design and Evaluation of an Active Antenna for a 29-47 MHz Radio Telescope Array," *IEEE Transactions on Antennas and Propagation*, Vol. 55, No. 3, pp. 826 − 831, Mar. 2007.

[53] S. W. Ellingson and A. Kerkhoff, "Comparison of two candidate elements for a 30-90 MHz radio telescope array," *IEEE Int'l Ant. and Prop. Symp.*, Washington, DC, Vol. 1A, pp. 590 − 593, Jul. 2005.

[54] M. Harun and S. Ellingson, "A Prototype Analog Receiver for LWA," Long Wavelength Array Memo Series No. 82, Mar. 2007, http://www.ece.vt.edu/swe/lwa/memo/.

[55] E. Polisensky, "LFmap: A Low Frequency Sky Map Generating Program," Long Wavelength Array Memo Series No. 111, Sept. 2007, http://www.ece.vt.edu/swe/lwa/memo/.

[56] S. D. Barthelmy *et al.*, "Progress with the Real-Time GRB Coordinates Distribution Network (BACODINE)," *AIP Conf. Proc.*, Vol. 384, pp. 580 − 584, 1996.

[57] J. Chennamangalam, Y. Maan and A. Deshpande, "Software Data-Processing Pipeline for Transient Detection," *Astronomical Society of the Pacific Conference Series*, Vol. 407, Dec. 2009, astro-ph/0905.0888v1.

[58] E. Argyle and J. F. R. Gower, "The Pulse Height Distribution for NP 0532," *Astrophysical Journal*, Vol. 175, L89 − L91, Jul. 1972.

[59] B. J. Rickett and J. H. Seiradakis, "The Flux of the Crab Pulsar at 74 MHz from 1971 to 1981," *Astrophysical Journal*, Vol. 256, pp. 612 − 616, May 1982.